Star Formation in the Gould Belt: A Submillimetre Perspective

Christopher Mowat

Submitted by Christopher Mowat to the University of Exeter as a thesis for the degree of Doctor of Philosophy in Physics, June, 2018.

I certify that all material in this thesis which is not my own work has been identified and that no material has previously been submitted and approved for the award of a degree by this or any other University.

Signed: .....

Christopher Mowat

Date: .....

Abstract

1st Supervisor: Dr. Jennifer Hatchell 2nd Supervisor: Prof. Matthew R. Bate

This thesis presents my work characterising star formation in Gould Belt molecular clouds using submillimetre observations from SCUBA-2 on the James Clerk Maxwell Telescope (JCMT). I use these observations alongside data from previously published surveys using instruments including the *Spitzer* Space Telescope. I investigate the effect of including submillimetre data on the numbers, classifications and lifetimes of Young Stellar Objects (YSOs) in Gould Belt molecular clouds, particularly protostars.

Following a literature review, I use SCUBA-2 450 and 850 μm observations to characterise star formation in the Lupus I molecular cloud. A total of eleven previously identified YSOs are detected with SCUBA-2, as well as eleven starless cores. Two cores have masses greater than the Jeans mass, and one has a virial parameter of 1.1 ± 0.4, meaning these cores could be unstable against collapse. I use submillimetre emission to calculate disk masses, and find that one YSO has a disk mass greater than the minimum mass solar nebula. I find that Lupus I has a high percentage of both protostars and Very Low Luminosity Objects (VeLLOs). I also fit YSO Spectral Energy Distributions (SEDs) with models, allowing protostellar envelope masses and temperatures to be calculated, and interstellar extinction to be constrained for some YSOs. The signs of recent and future star formation support the hypothesis that a shock has triggered a star forming event in Lupus I.

I also use SCUBA-2 data in conjunction with archival *Spitzer* and *Herschel* data to produce SEDs for five new candidate First Hydrostatic Cores (FHSCs) in Serpens South. These observations were then fit with models by the first author of this work, Alison Young. This work was able to identify two of the FHSC candidates as probable FHSCs, and constrain the rotation rate and inclination of one of them.

I use JCMT Gould Belt Survey (GBS) observations of ten molecular clouds to produce an updated catalogue of protostars in these clouds. I use the FellWalker algorithm to find

individual sources in the SCUBA-2 maps, and match them to the *Spitzer* YSO catalogue of Dunham et al. (2015). I use bolometric temperature to classify 362 out of 592 candidates as Class 0 or Class I protostars - a factor of two increase compared to the *Spitzer* catalogue due to improved submillimetre coverage. I find that protostellar lifetimes of 0.59 – 0.89 Myr - approximately 25 % longer than previously estimated. I also calculate protostellar luminosities, envelope masses, and envelope temperatures, and examine the distributions. Finally, I newly identify 19 protostars as VeLLOs, and increase the number of known VeLLOs in these clouds by a factor of two.

Contents

List of Figures

List of Tables

Declaration

This thesis contains work published or pending publication as papers. Chapter 2 and Chapter 3 are primarily based on a paper published in the Monthly Notices of the Royal Astronomical Society (MNRAS), Volume 467, pp. 812 – 835, May 2017 (DOI:10.1093/mnras/stx042). I am first author of this paper, with co-authors partaking supervisory and / or data reduction roles. The work of Chapter 4 is based on a paper published in MNRAS, Volume 474, pp. 800 – 823, February 2018 (DOI:10.1093/mnras/stx2669). I am third author on this paper, contributing observational data. The main body of work was done by the first author (AY) under the supervision of MRB. The work of Chapter 5 and Chapter 6 is pending submission to MNRAS as work I carried out as first author. Chapters 3 to 6 make use of archival data, the sources of which are explicitly stated.

Acknowledgements

I'd like to start by thanking my supervisor, Dr. Jenny Hatchell. I applied late for the Ph.D., and Jenny was willing to take a chance on the possible incompetence implied by such a start. Over the next four years Jenny has been a huge help in guiding my development as a researcher, so I am very glad she did take that chance.

Furthermore, I have been significantly helped by research collaborators including, but not limited to, Helen Kirk, James Di-Francesco, and Doug Johnstone, from Victoria, B.C. Their input has aided not only the implementation of my research, but also the clarity of my writing.

I would also like to acknowledge (and apologise to) the people I have been fortunate enough to share office space with. In particular, Lewis Ireland (SBD) has been a constant, entertaining thorn in my side and I'm proud to have been able to join him in our collective descent into madness. In addition, Sam Morell has always been willing to lend a hand, expecting nothing more than frivolity in return.

Moreover, I have lived variously with several people over the last four years that deserve thanks for putting up with me: Sam Shelley, Toby Octon, Tim Spicer, and Tom Graham. It's been a pleasure.

Finally, I'd like to thank my family, who have always been there, ready to provide long-distance support if ever needed.

Chris F Mowat

Exeter, U.K.

18th June 2018

Chapter 1

Introduction

"Let's roll..."

— C.M.Burns

Understanding the processes which give rise to star formation is one of the fundamental goals of astrophysics. Ever increasing computational power means that the large scales, huge masses and multitude of physical processes involved in star formation are now able to be simulated (e.g. Bate 2009, 2012). Moreover, ever larger and more technologically impressive instruments are able to probe star-forming regions at increased resolutions and sensitivities, revealing fundamental processes and structures (e.g. ALMA Wootten and Thompson 2009 and JWST Gardner et al. 2006).

My association with star formation is from the observational perspective, as a member of the James Clerk Maxwell Telescope (JMCT) Gould Belt Survey (GBS, Ward-Thompson et al. 2007). The JCMT GBS was initiated to map all of the low and intermediate-mass star forming regions within 500 pc of the Sun that are accessible to the JCMT. These regions lie mainly within the Gould Belt (see Section 1.1.1. What all of these regions have in common is that they are actually large agglomerations of gas and dust, known as molecular clouds. These clouds appear as dark patches of extinction at visible wavelengths, but are very bright in the far-infrared and submillimetre regimes (see Figure 1.1).

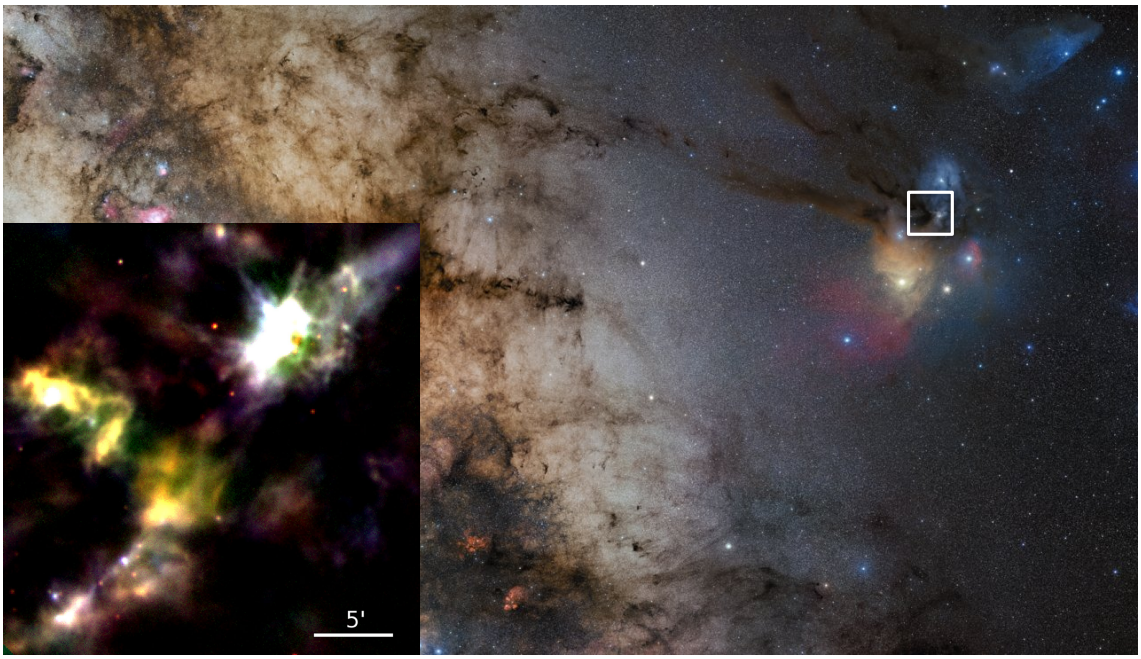

Figure 1.1: Optical and submillimetre images of the Ophiuchus molecular cloud. The larger optical image combines B, V, and R band photos of the ρ Ophiuchi molecular cloud complex. Areas of molecular gas are seen as dark areas of extinction. The smaller image (reproduced from Pattle et al. 2015) is a three-colour image incorporating SCUBA-2 450 and 850 µm and *Herschel* 250 µm observations of the L 1688 cloud core (also marked using a rectangle). What appeared dark in the optical image is now seen brightly in these submillimetre wavebands. Image credit: ESO/S. Guisard, source http://www.eso.org/public/images/eso0934a/.

1.1 Molecular Clouds

Star formation occurs in Giant Molecular Clouds (GMCs), with masses up to 10^6 $M_\odot$. GMCs are typically very cold, with temperatures of approximately 10 K (Shu, Adams, and Lizano 1987). GMCs are mostly formed of molecular hydrogen, but as H_2 does not have a dipole moment, dipole transitions cannot be observed. Therefore, when observing molecular clouds tracer molecules - such as isotopologues of CO - are observed (Dame and Thaddeus 1985). The assumed ratio of CO/H_2 is used to convert back to overall masses (Dame, Hartmann, and Thaddeus 2001).

As well as molecular hydrogen, GMCs consist of approximately 1 % interstellar dust.

This dust largely consists of graphite and silicates (Weingartner and Draine 2001a). The presence of this dust is important in astrophysics. The majority of molecular hydrogen is formed on dust grains (Gould and Salpeter 1963) and these grains provide the raw material for planet formation. In addition, photoelectric emission from dust is responsible for much of the heating of molecular clouds (Weingartner and Draine 2001b). Dust emits thermal continuum emission, allowing it to be observed by instruments such as the Submillimetre Common-User Bolometer Array 2 (SCUBA-2, Holland et al. 2013) on the JCMT.

Typically, a molecular cloud will have very low densities. For example, the *Spitzer* c2d Legacy survey found a mean number density, averaged over five star forming cloud complexes, of 389 particles cm^{-3} (Evans et al. 2009). Molecular clouds, however, are not quiescent. Motions of gas in these clouds create turbulent structure, which allows regions of higher density to form (Padoan and Nordlund 2002).

Turbulence in molecular clouds plays a key role in star formation (McKee and Ostriker 2007). It creates regions of higher density that undergo collapse and acts to counter gravity in such regions. Larson (1981) found that the internal velocity dispersion of molecular clouds was well correlated with their size and mass, via power law distributions. Kritsuk, Lee, and Norman (2013) show that these distributions can be interpreted as resulting from supersonic turbulence.

1.1.1 The Gould Belt

The ring of nearby O and B stars inclined at 17.2° ± 0.5° to the Galactic Plane (Perrot and Grenier 2003) is known as the Gould Belt (Herschel 1847; Gould 1874). Centred ~ 200 pc from the Sun, the Gould Belt has an approximate 'diameter' of ~ 700 - 1000 pc (Clube 1967; Stothers and Frogel 1974; Olano 1982). The Gould Belt contains most of the well-known nearby star-forming regions, including Orion (Bally 2008), Serpens (Eiroa, Djupvik, and Casali 2008), Taurus-Auriga (Kenyon, Gómez, and Whitney 2008), Perseus (Bally et al. 2008), ρ Ophiuchi (Wilking, Gagné, and Allen 2008), and Lupus (Comeron 2008). Due to the youth of the Gould Belt, and indeed the ongoing star formation, there are ~ 3 times as many O-B2 stars per square parsec in the Gould Belt compared to the Galactic belt (Stothers and

Frogel 1974). A census of the stellar constituents of nearby OB associations is presented by de Zeeuw et al. (1999), with Gould Belt sources included. The census data includes measured distances to the associations based on mean Hipparcos parallaxes.

The origin of the Gould Belt is not yet certain. Olano (1982) proposes that stellar winds and/or supernovae originating from the Cassiopeia-Taurus group could have birthed the 'ring' of the Gould Belt $\sim 3 \times 10^7$ years ago, with it since expanding to its current state. The work of Perrot and Grenier (2003) also supports the idea of an initial injection of energy from supernovae producing the Gould Belt. However, in Olano (2001), he proposes that the braking and compression of gas in a supercloud of $\sim 2 \times 10^7$ $M_\odot$ as it entered a major spiral arm of the galaxy formed the Gould Belt, as well as the local arm. Comerón and Torra (1992) and Comeron and Torra (1994) propose that a large high-velocity cloud (HVC) collided with the Galactic Plane, causing the appearance of a layer of gas inclined with respect to it.

1.2 Star Formation

1.2.1 The Jeans Mass

Before star formation can occur, a 'core' of gas and dust must collapse under gravity. For a cloud to collapse it needs to be unstable. Jeans (1902) looked at stability perturbations in a uniform gaseous cloud of infinite extent. He was able to show that a cloud would have a characteristic length scale at which it was stable to perturbations, but that an increase over this would lead to instability (resulting in a collapse). This characteristic scale is known as the Jeans length, given by

$$\lambda_J = \left(\frac{\pi {c_s}^2}{G \rho_0} \right)^{1/2}, \tag{1.1}$$

where c_s is the isothermal sound speed and ρ_0 is the density of the uniform isothermal gas. The relation can also be written as

$$\left(\frac{\lambda_J}{\mathrm{pc}} \right) = 0.19 \left(\frac{T}{10\mathrm{K}} \right)^{1/2} \left(\frac{\langle n(H_2) \rangle}{10^4 \mathrm{cm}^{-3}} \right)^{-1/2}, \tag{1.2}$$

where T is temperature in Kelvin and $\langle n(H_2) \rangle$ is the number density of molecular hydrogen. The corresponding mass associated with this length scale is known as the Jeans mass, given by

$$M_J = \frac{1.18 c_s^3}{\sqrt{\rho_0 G^3}}. \tag{1.3}$$

This relation can also be written as

$$\frac{M_J}{M_\odot} = 1.2 \left(\frac{T}{10\,\mathrm{K}} \right)^{3/2} \left(\frac{\langle n_0 \rangle}{10^4\,\mathrm{cm}^{-3}} \right)^{-1/2}, \tag{1.4}$$

where $\langle n_0 \rangle$ is the average number density of molecules - assumed to be hydrogen and helium (Chabrier 2003). Notably, as the Jeans mass depends inversely on density, and increase in density will cause a corresponding decrease in the Jeans mass. This means that once a cloud starts to collapse its Jeans mass will decrease further, so it will not be able to return to the previous equilibrium, and any perturbations can lead to the cloud fragmenting to form dense cores. A cloud with a mass equal to the Jeans Mass is not necessarily in equilibrium. Additional mechanisms for support or collapse such as magnetic fields and pressure confinement can affect this equilibrium.

1.2.2 The Virial Theorem

An estimate of the stability of a cloud can be obtained via the virial theorem, first introduced by Clausius (1870) and reviewed in Collins (1978). The virial theorem is used to quantify how the gravitational potential energy of a system balances with thermal motions, stating that the total kinetic energy (K) is equal to $-1/2$ times the gravitational potential energy of a system in virial equilibrium (with negligible magnetic and surface forces) (U) via the relation

$$2K + W = 0. \tag{1.5}$$

Applying this to a molecular cloud, the kinetic energy due to the thermal motions of the constituent atoms of the cloud is given by

$$K = \frac{3}{2} N k_B T, \tag{1.6}$$

where N is the number of atoms in the cloud and T is the temperature. If the cloud is assumed to be isothermal, this will be the same everywhere. Additionally, the potential energy of the cloud is given by

$$U = -\frac{3}{5}\frac{GM^2}{R}, \tag{1.7}$$

where M is the total mass of the cloud and R is the radius, assuming the cloud is spherical. Re-writing the virial theorem thus gives

$$3Nk_{\mathrm{B}}T = \frac{3}{5}\frac{GM^2}{R}. \tag{1.8}$$

If the left and right hand sides are equivalent, then the system is in virial equilibrium. If the left hand side is greater, thermal energy wins out and the cloud will expand. If, however, the right hand side dominates, then the cloud will collapse.

In order to find the characteristic mass beyond which a cloud will collapse, we first recognise that $N = M/\mu m_{\mathrm{H}}$, the total mass of the cloud divided by the average mass per particle. Additionally, assuming constant density throughout the cloud, the size of the cloud is given by

$$R = \left(\frac{3M}{4\pi\rho}\right)^{1/3}, \tag{1.9}$$

with ρ signifying the mass density of the cloud. Substituting these new expressions for N and R back into equation (4) gives the critical mass of a cloud, above which the cloud will collapse:

$$M_{\mathrm{crit}} = \left(\frac{5k_{\mathrm{B}}T}{G\mu m_{\mathrm{H}}}\right)^{3/2}\left(\frac{3}{4\pi\rho}\right)^{1/2}. \tag{1.10}$$

However, this form of the virial theorem is assuming that kinetic energy originating from thermal motions is the only supporting force against gravity. Knowledge of the gas velocity dispersion within a core of a known size allows for the calculation of the virial mass of a core via the relation

$$M_{\mathrm{vir}} = \frac{5}{3}\frac{(\Delta v)^2 R}{\mathrm{G}}, \tag{1.11}$$

where R is the radius of a core when treated as spherical, and G is the gravitational constant. Δv is the three-dimensional velocity dispersion of an observed tracer molecule in the cloud. This accounts for support from non-thermal motions. Chabrier and Hennebelle (2011)

demonstrate the importance of the addition of non-thermal turbulent support in order to recover the observed stellar initial mass function (IMF). I use this form of the virial theorem to examine the stability of dense cores in Lupus I in Chapter 3.

As with the Jeans Mass, the above form of the virial theorem does not necessarily mean that a true equilibrium is present when the equality is satisfied. It does not take into account, for example, magnetic support in the cloud. Magnetic fields have a significant effect on star formation, including regulating whether a binary system can occur (Lewis and Bate 2017). In addition, external gas pressure can act to confine dense cores (Pattle et al. 2015). Taking these additional mechanisms into account, the virial theorem can be written as

$$\frac{1}{2}\ddot{I} = 2\Omega_{\rm K} + \Omega_{\rm G} + \Omega_{\rm M} + \Omega_{\rm P}, \tag{1.12}$$

where $\ddot{I}$ is the second derivative of the moment of inertia. If this is 0, the core is in virial equilibrium. If $\ddot{I} < 0$ the core is collapsing, and if $\ddot{I} > 0$ the core is unbound and will disperse. Ω terms correspond to kinetic energy, gravitational potential, magnetic energy, and energy from external gas pressure, respectively (Pattle et al. 2015). An overview of some of the issues found with the virial theorem may be found in Ballesteros-Paredes (2006).

1.2.3 Protostellar Collapse - Early Models

While the Jeans analysis assumes that pressure is constant and equal inside and outside the cloud, Ebert (1955) and Bonnor (1956) independently and concurrently produced a model describing the case of a net external pressure from a medium acting on a constant-mass sphere of isothermal gas. These Bonnor-Ebert spheres are in hydrostatic equilibrium; gravity and external pressure inward are balanced by a pressure outwards produced by an ideal gas equation of state ($P = \rho T$). The mass enclosed by a Bonnor-Ebert sphere is approximated by

$$M_{BE} \simeq \frac{c_s^4}{\sqrt{G^3\rho}}, \tag{1.13}$$

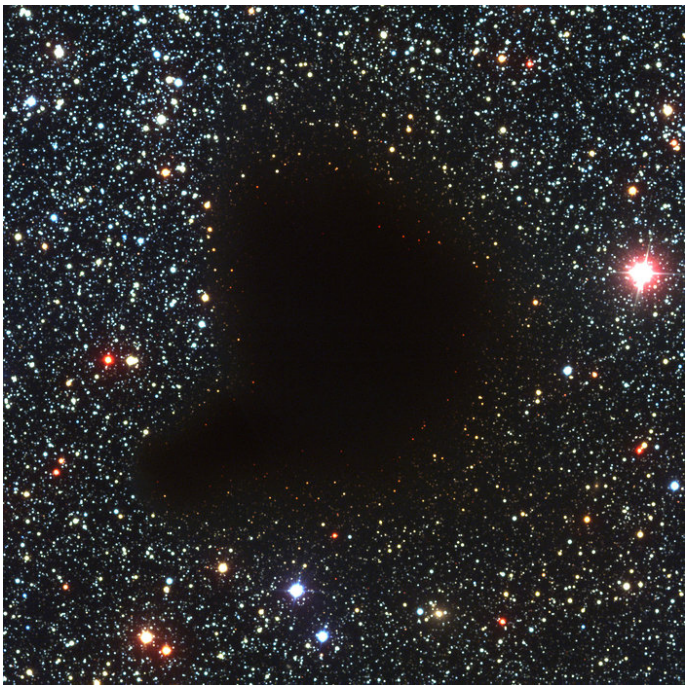

Figure 1.2: Three colour image of B68, in B, V, and I bands. Credit ESO, image source https://www.eso.org/public/images/eso9924a/.

where c_s is the isothermal speed of sound (for an ideal gas), $c_s = \sqrt{P/\rho}$. Whereas only some of the material within a sphere with a diameter given by λ_J will collapse, a Bonnor-Ebert sphere fully contains material of higher density than the surrounding medium, and thus more closely models a cloud differentiated from its surroundings.

A Bok globule (Bok and Reilly 1947) is a type of dense, dark and cold molecular cloud that is able to form stars. Alves, Lada, and Lada (2001) studied the Bok globule Barnard 68 (Figure 1.2), and are able to show that it is well characterised by a Bonnor-Ebert sphere with $\xi_{max} = 6.9 \pm 0.2$ (see figure 1.3), where ξ_{max} is the value of the non-dimensional radial parameter (ξ) at the outer boundary of the sphere ($r = R$),

$$\xi_{max} = \frac{R}{c_s}\sqrt{4\pi G \rho_c}. \tag{1.14}$$

Here ρ_c is the central volume density. The value of ξ_{max} seems to place Barnard 68 just over the boundary between hydrostatic equilibrium and instability to gravitational collapse.

Also related to the sound speed is the sound crossing time, $t_c = L/c_s$, with L denoting the size of the cloud. The sound crossing time is the time taken for a sound wave to travel

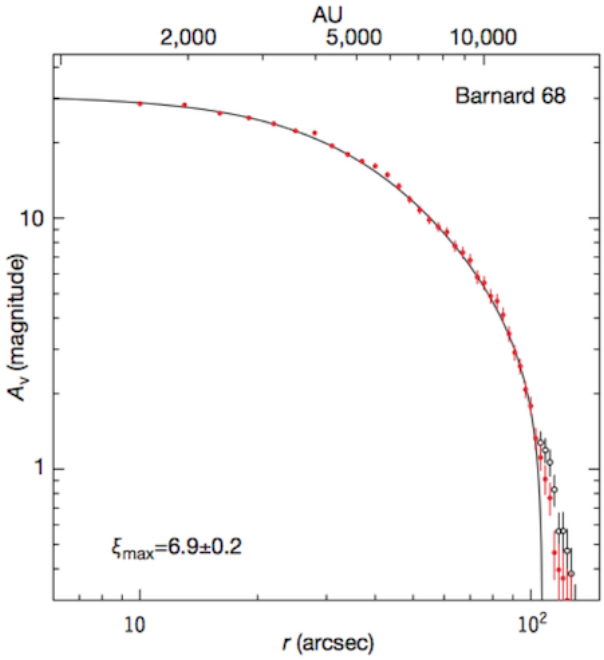

Figure 1.3: Figure reproduced from Alves, Lada, and Lada (2001), showing the azimuthally averaged radial dust column density profile of Barnard 68 (red). The open circles also include a prominence to the southeast of the cloud. The solid line shows the best fit of a Bonnor-Ebert sphere to the data.

across the cloud, and thus the timescale over which different parts of the cloud are able to communicate.

To quantify the collapse of a molecular cloud, we introduce the free-fall time t_{ff}, the time taken for a body to collapse under gravity if no forces oppose the collapse:

$$t_{ff} = \left(\frac{3\pi}{32G\rho}\right)^{1/2}. \tag{1.15}$$

More formally, this is the time taken for a homogeneous sphere with zero internal pressure to collapse to a point. This requires the cloud to be isothermal, so that any radiation released from gravitational contraction is able to escape. Once the sound crossing time becomes less than the free-fall time, pressure is sufficient to support the cloud core against collapse. Free-fall times of Gould Belt clouds are typically $\sim 10^4 - 10^5$ years (Curtis, Richer, and Buckle 2010; Könyves et al. 2015). Such durations are shorter than the ages of Gould Belt clouds, which are typically of order 10^6 years. Star formation in Gould Belt regions has been ongoing for much longer than this - $\sim$ 3 Myr in Lupus I, for example (Hughes et al. 1994). This demonstrates that support mechanisms are countering gravitational

collapse in these regions.

If a sphere of gas is sufficiently cold, then internal pressure may be neglected, as shown by Penston (1969). This assumption breaks down once the rise in density - due to collapse - causes opacity to become high enough such that the energy released from collapse is unable to radiate away. This means that collapse is now adiabatic, not isothermal (Larson 1969). In this case, the core heats up, allowing pressure to counter gravity and forming the First Hydrostatic Core (FHSC).

Prior to the work of Larson (1969) and Penston (1969) it had been assumed that the collapse of a cloud was homologous. However, the numerical calculations of Larson (1969) on a spherically symmetric collapsing protostar, assuming no rotation, no magnetic fields and no internal turbulence, demonstrate that collapse is extremely non-homologous. A small fraction of the total mass concentrated at the centre will reach high density and stop collapsing long before the rest of the cloud, since free-fall time is inversely proportional to density (equation (8)). This solution is known as the Larson-Penston solution, and exhibits self-similarity (where an object is exactly or approximately similar to a part of itself).

Another self similar solution is that of Shu (1977). In this treatment, an infinitesimal protostar in the centre of an isothermal sphere begins to accrete mass. Outside the accreting region the sphere is initially unchanged, until a wave expanding radially outwards (signalling the increasing size of the accreting region) meets these outer parts of the envelope. Again, this leaves a stellar-density region around the protostar long before much of the cloud has collapsed. Though this model starts marginally unstable, and hence is unphysical, it is the only fully analytic model of collapse. This treatment is expanded on by Terebey, Shu, and Cassen (1984) via the inclusion of an initially uniform and slow rotation of the isothermal sphere. Observations of 'starless cores' by Ward-Thompson et al. (1994) failed to show the $1/r^2$ radial density profile characteristic of the Shu model all the way to the centre of the cores. Instead, they found a flattening of the power law, consistent with, e.g., magnetic support of the cores.

Myers (2005) shows that the pressure-free collapse of a Bonnor-Ebert sphere under gravity is still able to match many observed properties of starless cores. However, turbulence

and magnetism are important mechanisms in star formation that cannot be ignored. Core turbulence increases with importance as the mass of a star-forming core increases (McKee and Ostriker 2007). Indeed Myers and Fuller (1992) find that, when these non-thermal motions have a radial dependence, the inclusion of turbulence in massive cores makes a significant difference to the formation of stars. The difference in low mass cores, however, is unimportant. The inclusion of magnetic fields is also an important step, as magnetic support can be a significant counter to gravity, and is demonstrated in a non-rotating case by Basu (1997). Krasnopolsky and Königl (2002) include the effects of both magnetism and rotation to describe the evolution of a collapsing core once a protostar has formed in the centre. Reviews of numerical modelling of star formation can be found in McKee and Ostriker (2007) and Padoan et al. (2013).

1.2.4 Filamentary Structure

Most stars do not form in isolation, but instead in regions of significant star-forming activity. In these regions, feedback plays a key role, with hot stellar winds, jets / outflows, and radiation all changing local conditions and influencing nearby star formation (Krumholz et al. 2014). If clusters are able to continue to accrete material whilst star formation is already well under way, then filaments provide a mechanism by which gas can be channelled to star-forming cores. Kirk et al. (2013) show that the southern filament in the Serpens South region has a flow of material of $\sim 30\,M_\odot\,Myr^{-1}$ along the filament towards the central cluster, while material radially accretes onto the filaments at a rate of $\sim 130\,M_\odot\,Myr^{-1}$ This demonstrates the ability of filamentary accretion into a central region to provide mass for, and indeed increase the rate of, star formation. Additionally, they show that in gravitationally supercritical regions of the filaments themselves, there is ongoing star formation signalled by the presence of protostars and pre-stellar cores.

Peretto et al. (2013), however, present observations the dark cloud SDC335.579-0.272 by ALMA demonstrating that not all star forming cores may require accretion via filaments. They identify two massive star-forming cores at the centre of the cloud, where 6 cold (15K) and dense ~ parsec-long filaments converge. They find that although some gas is

collapsing along these filaments, most is not. Thus, most of the core mass could have arisen from an overall large-scale collapse of the parent cloud, rather than relying on flow through the filaments.

Complementing observations, Myers (2011) produces models of star forming condensations in clusters, where cores are nodes of filamentary networks. Neighbouring filaments will blend as they converge, and filaments are also able to branch out into sub-filaments. If filaments are massive and widely spaced then they may gravitationally fragment. However, if filaments are densely layered then it is expected that global gravity will dominate. The models show that, with nodes as cores, dense stellate condensations are analogous to a multiple protostar-forming clump gathering material via a filamentary configuration. Figure 1.4 shows two snapshots from a radiation hydrodynamical simulation of star cluster formation (Bate 2012). Filamentary structure can clearly been seen evolving, with high column density filaments channeling into the central area of structure.

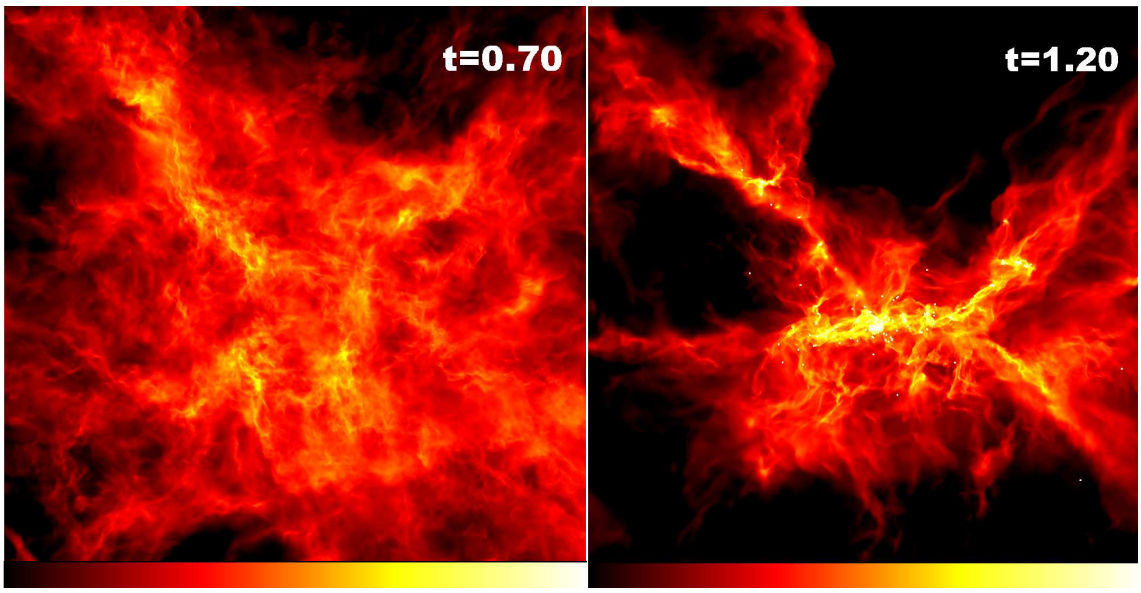

Figure 1.4: Reproduced from Figure 2 of Bate (2012). Two snapshots of a radiation hydrodynamical simulation of star cluster formation in a 0.6 pc box. Time is given in units of initial free-fall time (1.90 $\times 10^5$ years). Panels show log column density.

1.2.5 Young Stellar Objects

Protostars are the first main stage in evolution of Young Stellar Objects (YSOs) which form from the collapse of dense cores of gas and dust in molecular clouds (Larson 2003; McKee

and Ostriker 2007). They represent the stage of star formation during which a centrally accreting object is still embedded within the dense core. Once a dense core has collapsed into a protostar, evolution towards the main sequence can begin. The spectral evolution of low mass YSOs is introduced by Adams, Lada, and Shu (1987), based on the work of Lada and Wilking (1984).

Physically, the first evolutionary stage of a protostar is known as Stage 0. In this stage, the mass of the central object is lower than that of the surrounding envelope. This stage is typically reached at $\sim 10^4$ years. Once the mass of the protostar exceeds the envelope mass, the source is in the Stage I phase (André, Ward-Thompson, and Barsony 2000). At this stage, emission is still dominated by the envelope, with ongoing active accretion (e.g. Wilking, Lada, and Young (1989)).

Observationally, protostellar evolution is typically split into two phases. The Class 0 phase was first defined by André, Ward-Thompson, and Barsony (1993) after the detection of VLA 1623. Class 0 sources are deeply embedded, and characterised by a low ratio of bolometric to submillimetre luminosity, $L_{\rm bol}/L_{\rm smm}$ (André, Ward-Thompson, and Barsony 1993). Class I sources are still deeply embedded, but these objects have a greater amount of flux in the infrared regime, and a higher ratio of $L_{\rm bol}/L_{\rm smm}$. The methods used in this thesis for classifying YSOs are discussed in Section 1.3. The term 'YSO' refers to any object beyond the first core stage that has not yet reached the main sequence. 'Protostar', however, refers exclusively to Class 0 and Class I objects.

Most observationally-classified Class 0/I objects correspond to Stage 0/I protostars, as the characteristic long wavelength emission arises from their cold envelopes. However, the effects of geometry, extinction, and accretion mean that there is not a one-to-one correspondence between Class 0/I and Stage 0/I (Whitney et al. 2003; Robitaille et al. 2006; Crapsi et al. 2008; Dunham et al. 2010a; Furlan et al. 2016; Yang et al. 2017). For example, a protostar viewed at high inclinations ($> 70°$) may appear more evolved due to the presence of an outflow cavity. Therefore, not all protostars will be classified as Class 0/I objects, and such a classification is no guarantee of evolutionary stage. Presuming a correspondence between observational class and physical stage, SEDs and pictorial representations of Class 0 and Class I protostars are shown in Figure 1.5.

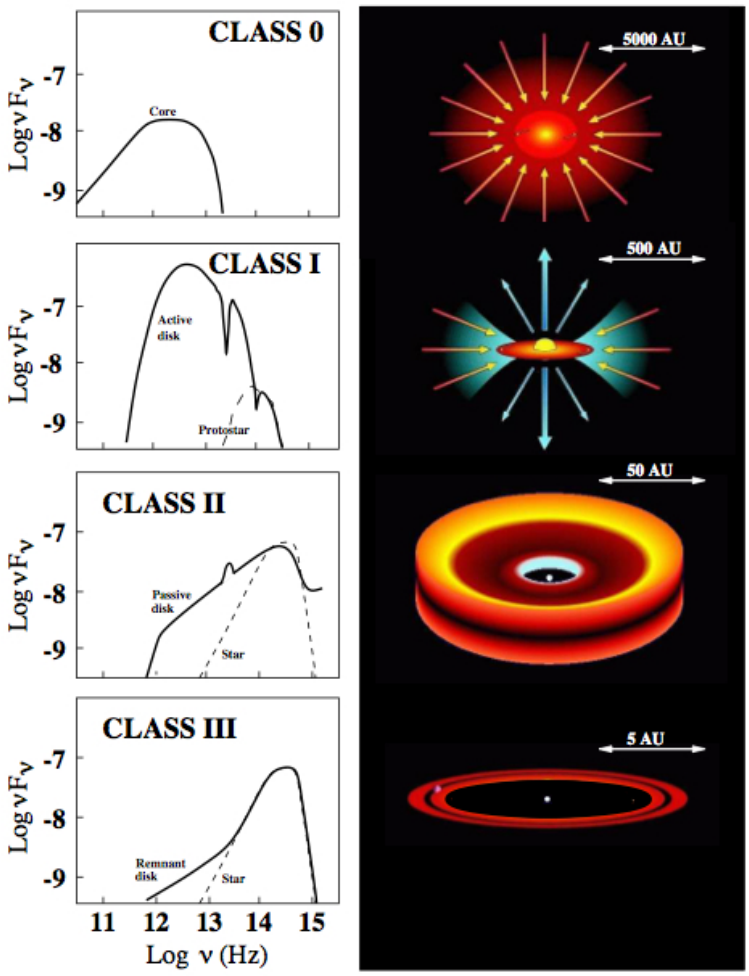

Figure 1.5: Figure reproduced from Isella (2006) showing, on the left, SEDs and, on the right, cartoons of the system geometry for a protostar at each point in its evolutionary classification. Horizontal axis units of frequency mean that colder material is to the left. The vertical axis units of $\log(\nu F_\nu)$ are equivalent to units of $\mathrm{Log}(\lambda F_\lambda)$.

At the end of Stage 1, after $\sim 10^6$ years, the star will have accreted most of its final mass (André and Montmerle 1994). A Class II object remains (Lada 1987). The envelope will have largely dissipated, so the emission is now dominated by the star and a circumstellar accretion disc (see Figure 1.5). This is known as a classical T Tauri star, after the prototype T Tauri. Class IIs are still YSOs, but they are no longer protostars.

As the young star continues to evolve into a Class III star, the disc will dissipate and accretion will diminish. This will lead to an SED with little or no IR excess (little or no disc emission, see Figure 1.5), as well as low levels of Hα emission indicating a low accretion rate. Thus, stars at this stage of evolution are often known as weak-line T Tauri stars, and indeed Padgett et al. (2006) find that only a small fraction of the weak-line T

Tauri stars have discs. At this stage, emission will be dominated by this pre-main sequence star, with some IR excess due to remnants of the star formation process that have yet to dissipate (Wilking, Lada, and Young 1989). Many Class III 'YSOs' have been found to be contaminant background galaxies (Dunham et al. 2015).

Observationally, Flat spectrum objects lie between Class I and II objects. This does not correspond to a distinct physical stage, with Flat-spectrum objects actually split approximately evenly between Class I and Class II YSOs (Heiderman and Evans 2015).

Massive young stars cannot be classified in the same way, as they reach the main sequence over shorter timescales. They will begin hydrogen burning before they have finished accreting material, and the most massive stars will supernova after ~ 3 Myr (before low-mass stars have even reached the main sequence, Zinnecker and Yorke 2007). However, intermediate mass Herbig Ae/Be stars, though more massive than T Tauri stars, are still analogous to lower mass stars (Hillenbrand et al. 1992).

1.2.6 Initial mass function

A further important characterisation of a star forming region is stellar density as a function of mass; in other words, the distribution of masses for newly formed stars. This was first characterised for stars of greater than one Solar mass by Salpeter (1955), and is of power law form

$$\frac{dN}{dm} \propto m^{-\alpha} \tag{1.16}$$

where $\alpha = 2.35$ is the Salpeter value. This relationship is known as the Salpeter initial mass function, and shows that the frequency of stars decreases as mass increases above $1\,M_\odot$. For reviews on determination of the IMF for larger stars ($M \geq 1\,M_\odot$), see Miller and Scalo (1979), and Scalo (1986).

More recently, determination of the mass function has been extended through lower mass stars down to the brown dwarf regime. This has demonstrated that the Salpeter slope does not hold at lower masses as, for example, the number of brown dwarfs observed is too low (see (Chabrier 2003)). Newer models for the IMF include those of Miller and

Scalo (1979), Kennicutt (1983), Scalo (1986), Kroupa, Tout, and Gilmore (1993), Kroupa (2001), Baldry and Glazebrook (2003), and the lognormal form of Chabrier (2003). Chabrier and Hennebelle (2011) use dimensional analysis to show that non-thermal support from turbulent velocity is required to produce the Salpeter slope, otherwise the drop-off at high masses is too great.

The IMF is additionally important in the context of star formation, as André et al. (2010) show that it bears a strong resemblance to the pre-stellar core mass function (CMF), first recognised by Motte, Andre, and Neri (1998). In other words, stellar mass could already be largely fixed by fragmentation before collapse in molecular clouds. Goodwin et al. (2008) show that the match between the CMF and the IMF is better when all stars form in binary or multiple-star systems, when compared to low-mass stars mainly forming in single systems. Hatchell et al. (2005) find that more massive cores are more likely to be protostellar. In Hatchell and Fuller (2008), they find that this can be explained by the fast evolution of massive cores and the continued accretion of mass onto these protostellar cores. They discuss that the pre-stellar CMF should be steeper than the IMF. This situation is not incompatible with the observed similarities between the CMF and IMF provided, for example, that massive cores can fragment into multiple systems. See figure 1.6 for the comparison between CMF and IMF from André et al. (2010). The Salpeter slope in the context of the $\mathrm{d}N/\mathrm{dlog}M$ format used in this figure is -1.35.

1.2.7 Mass Segregation

Massive stars are more likely to be found near the centre of stellar clusters (Hillenbrand and Hartmann 1998; Kirk and Myers 2011). This mass segregation can either be dynamical (a post-birth evolution of the stellar cluster that preferentially sends higher mass stars near the centre of the cluster) or primordial (present at the birth of the stellar cluster e.g. in dense cores formed from fragmentation). The dynamical timescale (or crossing time) is the characteristic time taken for stars to significantly move within a stellar cluster, given by $t_{\mathrm{cross}} = R/v$, where R is the radius of the system and v is the average stellar velocity relative to the cluster as a whole. If the dynamical timescale is longer than the observed age of

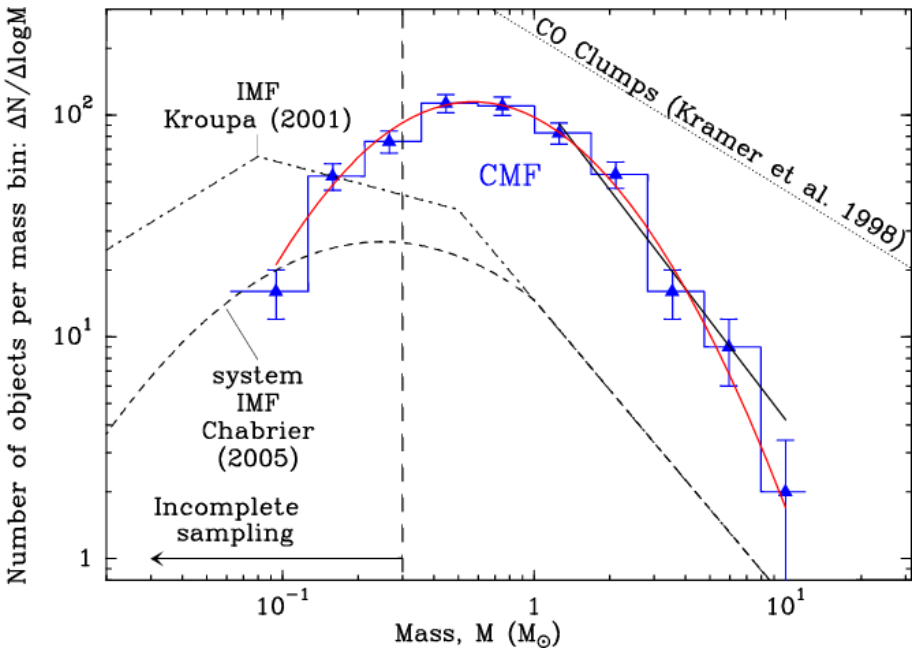

Figure 1.6: Figure reproduced from André et al. (2010) showing the CMF (blue histogram) of the Aquila region derived from SPIRE/PACS observations. The red curve shows a lognormal fit, and the black line a power law fit at high mass (-1.5 ± 0.2). The Kroupa (2001) IMF for single stars, the systems IMF of Chabrier (2005) and the typical mass spectrum of a CO clump (Kramer et al. 1998) are also shown. The similarity between CMF and IMF can clearly be seen.

the stellar cluster then it is assumed that massive stars have not had time to preferentially travel to the centre, and hence that primordial mass segregation is important (Bonnell and Davies 1998). Though observations have shown evidence for primordial mass segregation (e.g. Bontemps et al. (2010b) Kirk and Myers (2011), Polychroni et al. (2013), Kryukova et al. (2014)), there is not a consensus, and Allison et al. (2009) argue that stars of $\geq 4M_{\odot}$ can dynamically mass segregate over a shorter timescale than the ages of their parent clusters (e.g. Orion Nebula). Additionally, X-ray observations of the Cygnus OB2 association (Wright et al. 2014) show no evidence for mass segregation, demonstrating that it is not a universal property of star formation.

Two models have been suggested to allow the formation of these high mass stars: Monolithic collapse and competitive accretion. Described by McKee and Tan (2003), monolithic collapse explains the formation of very massive stars in isolation. In this model, fragmentation of a molecular cloud into individual dense cores will largely fix the final masses of the stars within. Protostars will form from the collapse of these massive, turbulent cores, accreting matter via an accretion disc.

Bonnell et al. (1997) introduce the concept of competitive accretion via smoothed-particle hydrodynamics (SPH) simulations of small, young stellar clusters. When accretion is competitive, each star's accretion rate depends on the local gas density and the square of the accretion radius (Bonnell et al. 2001). Low mass stars will accrete most mass during a gas-dominated phase, but most of the accretion of higher mass stars will happen during a stellar-dominated phase. In other words, stars will continue to accrete matter based on the gravitational potential of the entire cloud, competing for the as yet unbound gas. See Zinnecker and Yorke (2007) for an overview on the debate between monolithic collapse and competitive accretion.

1.2.8 Star formation efficiency

If cores have accreted most of their final mass before the majority of the cloud has collapsed (as with Shu 1977), this would suggest that the fraction of material from molecular clouds that actually ends up as stars is low. This requires the cloud to be unbound and prevented from ultimate collapse by, e.g., supersonic turbulence (Mac Low and Klessen 2004) as well as thermal support. Indeed, Myers et al. (1986) find a star formation efficiency over a sample of 54 molecular cloud complexes of approximately 2%. Similarly, Evans et al. (2009) find a current star formation efficiency in molecular clouds sampled by the Spitzer Space Telescope of 3% – 6%, with the potential to reach 15% – 30% if star formation rates stay constant for 10 Myr. Low star formation efficiencies are another indicator that non-thermal support is preventing gravitational collapse in molecular clouds.

1.3 Deriving Quantities from Observations

1.3.1 Submillimetre Dust Continuum Emission

Wien's displacement law states that the radiation emitted by a black body per unit wavelength peaks at the wavelength $\lambda_{\max} = b/T$, where T is the temperature of the black body and Wien's displacement constant $b \approx 2.898 \times 10^{-3}$ m K. For wavelengths in the submillimetre regime, corresponding emission temperatures are of the order 10 K. This means

that submillimetre continuum emission traces cold dust grains. Hence, submillimetre continuum emission is only able to trace protostars and YSOs when they are still surrounded by dust. This can take the form of an envelope (Rygl et al. 2013) or circumstellar disks. The dust will absorb radiation from the YSO, and re-emit continuum flux that is bright at submillimetre wavelengths (approximately 100 – 1000 µm).

We are able to use continuum emission maps of molecular clouds to extract information which includes overall mass, column densities, dust temperature and the dust emissivity index, β, which gives information on the frequency dependence of opacity. Dust continuum emission is a thermal emission that varies relatively slowly with frequency. At wavelengths greater than ~ 200 μm, clouds are found to be optically thin (optical depth $\tau \ll 1$). This allows emission from all depths in the cloud to be sampled with approximately equal efficiency.

1.3.2 Column density and mass

As the dust can be assumed to be optically thin, the flux density from the dust can be written as

$$S_\nu = \int_\Omega B_\nu(T, \nu)\tau d\Omega, \tag{1.17}$$

where $B_\nu(T, \nu)$ is the Planck function and $d\Omega$ is the solid angle. For dust, $\tau = \kappa_\nu N_{\mathrm{H_2}} \mu \mathrm{m_p}$, where κ_ν is the opacity coefficient with units of $\mathrm{cm^2 g^{-1}}$, $N_{\mathrm{H_2}}$ is the column number density of molecular hydrogen, μ is the mean molecular weight per $\mathrm{H_2}$ molecule and $\mathrm{m_p}$ is the mass of a proton. This allows the equation of radiative transfer to be re-written:

$$S_\nu = \int_\Omega B_\nu(T, \nu)\kappa_\nu N_{\mathrm{H_2}} \mu \mathrm{m_p} d\Omega. \tag{1.18}$$

Thus, flux per pixel is given by

$$S_{\nu,\mathrm{p}} = B_\nu(T, \nu)\kappa_\nu N_{\mathrm{H_2}} \mu \mathrm{m_p} \Omega_\mathrm{p}, \tag{1.19}$$

where pixel solid angle $\Omega_p = (\theta_p)^2$ and θ_p is the dimension of a pixel in arcseconds. This can be rearranged to find column density:

$$N_{H_2} = \frac{S_{\nu,p}}{B_\nu(T,\nu)\kappa_\nu \mu m_p \Omega_p}. \tag{1.20}$$

Similarly, the total mass within a region can be found by substituting in area, $dA = d^2 d\Omega$, and recognising that $N_{H_2}\mu m_p dA$ gives mass, giving

$$M = \frac{S_\nu d^2}{B_\nu(T,\nu)\kappa_\nu} \tag{1.21}$$

where d is the distance to the region (Hildebrand 1983). Hence, masses can be calculated assuming a temperature and opacity for an area.

A fit to the observed SED (provided data at a minimum of two wavelengths are available) will allow dust temperature to be estimated, within constraints. To obtain an SED fit for a cold star-forming region, dust can be assumed to emit as an opacity-modified blackbody. Such emission can be fitted pixel-by-pixel to recover variations in dust properties (e.g Peretto et al. (2010)).

Model fitting will typically be achieved via a minimisation of χ^2 (least-squares), where

$$\chi^2 = \sum_{i=1}^{n} \left(\frac{d_i - m_i^2}{\sigma_i} \right). \tag{1.22}$$

Here, d is a data point, m is an expected value from a model, and σ is the uncertainty. The model that minimises χ^2 is said to have maximum likelihood. A χ^2 fitting procedure is used to derive envelope masses and temperatures for protostars in Chapter 3 and Chapter 6, with the procedure outlined in Section 3.2.5.

1.3.2.1 Dust emissivity index

In order to derive mass, we need to know opacity longward of ~ 300 µm, or fit it as a free parameter to SEDs. A simplified opacity assumes a power law such that $\kappa_\nu \sim \nu^\beta$, where β is the dust emissivity index. In the higher density environment around protoplanetary

disks, typically $\beta < 1$ (Draine 2006). This compares with larger values found in dense protostellar cores and filamentary regions of molecular clouds of $\beta \geq\sim 1.6$ and $\beta \approx 2$, respectively (Sadavoy et al. 2013; Chen et al. 2016). On discovering a lower than expected dust emissivity index in the Orion Molecular Cloud 2/3 region, Schnee et al. (2014) discuss possible reasons for this discrepancy, including the presence of mm-sized dust grains. It should be noted that there is not actually a strict power-law relationship between opacity and frequency over all frequencies. The relation does, however, approximate to a power law in the submillimetre regime (Ossenkopf and Henning 1994; Juvela et al. 2015).

1.3.3 Mid Infrared Spectral Index

First defined in Wilking, Lada, and Young (1989) and expanded upon by Greene et al. (1994), the mid infrared spectral index (a or α) provides a measure of the 'slope' of the SED between 2.2 and 25 µm. It is calculated using the relation

$$a = \frac{d\log(\lambda F_\lambda)}{d\log\lambda}, \tag{1.23}$$

where λF_λ is flux density and λ is wavelength.

Mid infrared spectral index is used to classify YSOs. Values for a of > 0.3 correspond to Class 0/I protostars - it cannot reliably distinguish between the two. Values of -0.3 $\geq a \geq$ -1.6 result in a Class II classification, leaving values of 0.3 $\geq a \geq$ -0.3 to indicate a Flat-spectrum YSO. Any YSO with an a value of $\leq$ -1.6 is considered as Class III. Though not explicitly included in these calculations, a value of a significantly greater than 0 can be indicative of a Class 0 protostar (André, Ward-Thompson, and Barsony 1993; Enoch et al. 2009). The method for calculating the mid-infrared spectral index using observed fluxes is detailed in Section 3.2.3.

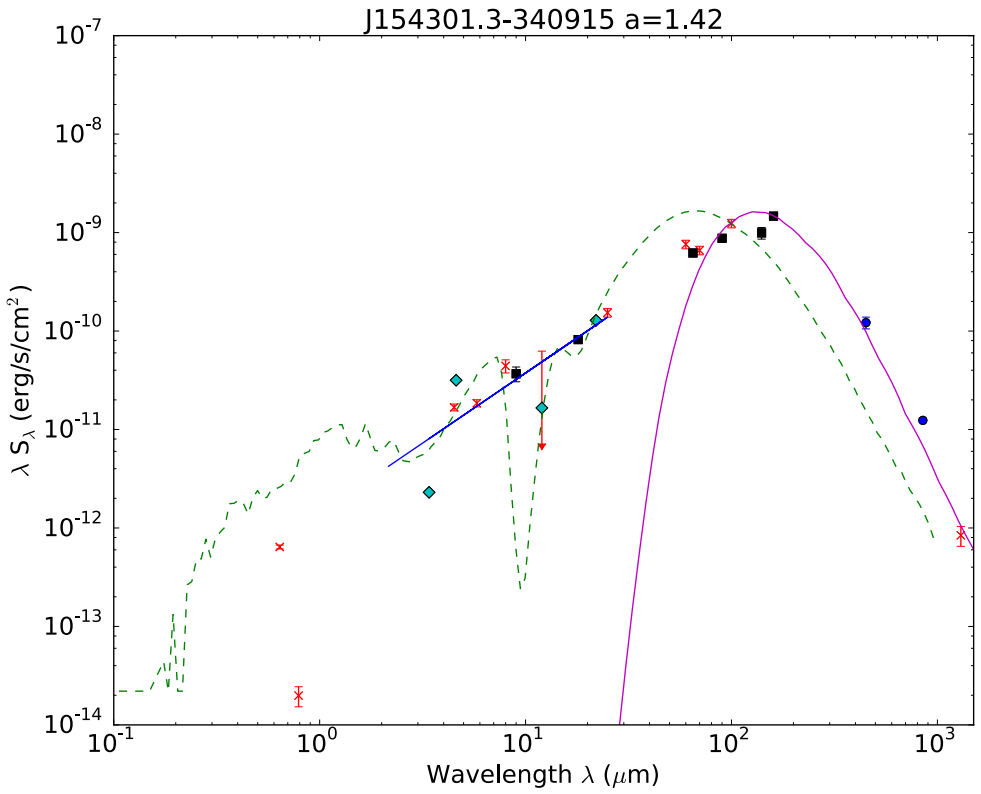

Figure 1.7: Example SED, with fit for mid-infrared spectral index shown as a blue line. The value obtained for this source is $a = 1.42$. This SED is the object L1YSO 7 from Chapter 3, a Class 0 protostar.

1.3.4 Bolometric Temperature

The bolometric temperature ($T_{\rm bol}$) of a source is the temperature of a black body with the same flux-weighted mean frequency as the source SED (Myers and Ladd 1993), defined as

$$T_{\rm bol} = 1.25 \times 10^{-11} \langle \nu \rangle {\rm K}, \tag{1.24}$$

where mean frequency $\langle \nu \rangle$ is defined as

$$\langle \nu \rangle = \frac{\int \nu S_\nu d\nu}{\int S_\nu d\nu}. \tag{1.25}$$

$T_{\rm bol}$ can be used to estimate the observational class of a protostar (Chen et al. 1995; Enoch et al. 2009). A Class 0 object will have $T_{\rm bol} \leq 70$ K, and a Class I YSO will have 70 K $< T_{\rm bol} \leq 650$ K. A Class II YSO will have 650 K $< T_{\rm bol} \leq 2800$ K, with Class IIIs having values greater than this. Overall, the closer $T_{\rm bol}$ is to the effective temperature of a main sequence star, the more evolved the YSO is. The calculation of $T_{\rm bol}$ for an observational dataset is

detailed in Section 3.2.4.

1.3.5 Bolometric Luminosity

Bolometric luminosity is the amount of energy emitted by an object per unit time, across all wavelengths. This allows a cold object - luminous at submillimetre wavelengths - to be compared to a more evolved YSO. The bolometric luminosity ($L_{\rm bol}$) of an object is calculated by integrating flux S_ν over frequency:

$$L_{\rm bol} = 4\pi d^2 \int S_\nu d\nu. \tag{1.26}$$

$L_{\rm bol}$ is typically provided in units of Solar luminosity ($L_\odot$), where 1 $L_\odot$ = 3.828×10^{26} W. The calculation of $L_{\rm bol}$ for an observational dataset is also detailed in Section 3.2.4.

1.3.5.1 The Luminosity Problem

First presented by Kenyon et al. (1990), the luminosity problem describes the situation whereby constant accretion models of protostellar formation produce luminosities far in excess of the observed luminosities of embedded protostars. Other, more complex models of star formation incorporating, for example, variable bursts of accretion of stellar material have since been used to explain this (Dunham and Vorobyov 2012). However, if the observed lifetimes of protostars do not match the timescale produced by models the problem remains. It is, therefore, very important to accurately know how long-lived protostars are, and recent observational estimates using large source counts produce lifetimes in the range of 0.54 – 0.72 Myr (Heiderman and Evans 2015; Dunham et al. 2015).

1.4 Instrumentation

This thesis makes use of data taken with a number of telescopes and instruments around the world and in space.

1.4.1 James Clerk Maxwell Telescope (JCMT)

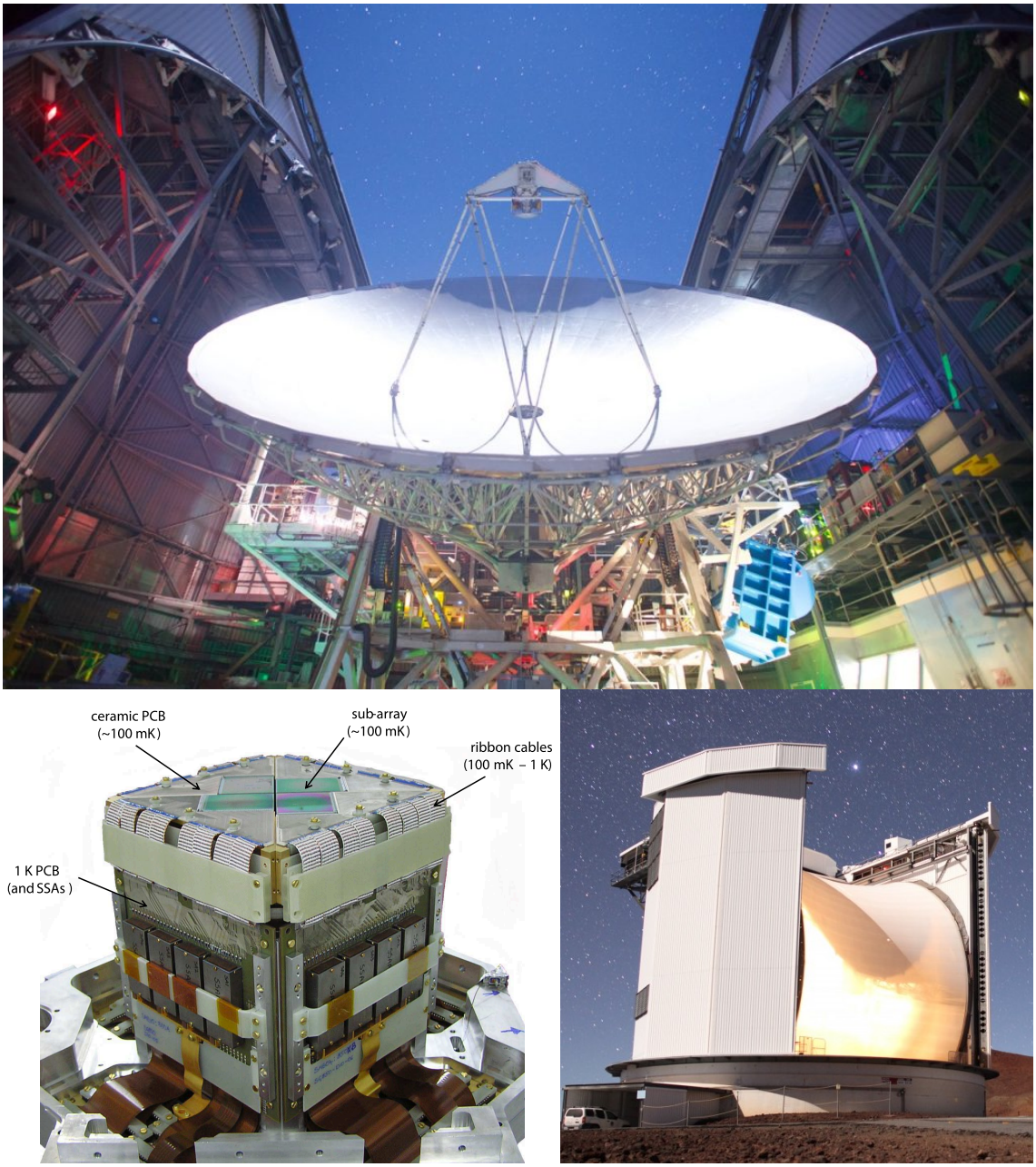

Figure 1.8: Top: Image of the 15 m dish of the JCMT. SCUBA-2 is visible as the blue box at the bottom right. Credit Will Montgomerie. Bottom Left: Focal plane unit of SCUBA-2. The four sub-arrays are indicated. Reproduced from Holland et al. (2013). Bottom right: External image of the JCMT, with the wind shield covering the dish. Credit Will Montgomerie.

The JCMT, located on Mauna Kea in Hawaii (which is situated at approximately 19° north of the Equator), is a 15 m telescope designed for submillimetre wavelength observations (Matthews and Leech 2004). The high altitude (4092m), dry atmosphere and low level of clouds make Mauna Kea an excellent site for infrared and submillimetre observations.

The telescope has instrumentation for both continuum and spectral line detections. The top and bottom right panels of Figure 1.8 show internal and external views of the JCMT, respectively.

1.4.1.1 SCUBA-2

SCUBA-2 (Holland et al. 2013) is a wide-field, 10,000 pixel bolometric camera used for observations of submillimetre continuum emission. Incident electromagnetic radiation causes a response from a bolometer when it heats a material with temperature-dependent resistance. This allows the power of the radiation to be measured (Richards 1994). SCUBA-2 operates in the atmospheric windows at 450 and 850 µm, with a field of view of 43 square arc-minutes (Dempsey et al. 2012). SCUBA-2 takes observations at both 450 and 850 µm simultaneously, using four sub-arrays at each wavelength. The combined four sub-arrays consist of 5120 bolometers - though typically only $\sim$ 65 % are operational - and are cooled to temperatures of 100 – 200 mK. These sub-arrays can be seen on the image of a SCUBA-2 focal plane unit in the bottom left panel of Figure 1.8. There are two focal plane units in total, one for observations at each wavelength.

The majority of the observations undertaken as part of the JCMT GBS used SCUBA-2 (Holland et al. 2013). SCUBA-2 is capable of producing maps of submillimetre continuum emission over extended areas of the sky. The young objects found in regions where star formation is ongoing are able to be traced by emission at 450 and 850 µm. The Gould Belt survey aimed to use SCUBA-2 to detect all Class 0 and Class I protostars, as well as pre-stellar cores, to allow large-number statistics to be obtained on the various stages of star formation. Figure 1.9 shows a map of Perseus B1, produced using SCUBA-2 at 850 µm. SCUBA-2 observations and data reduction are discussed in detail in Chapter 2, and used throughout this thesis.

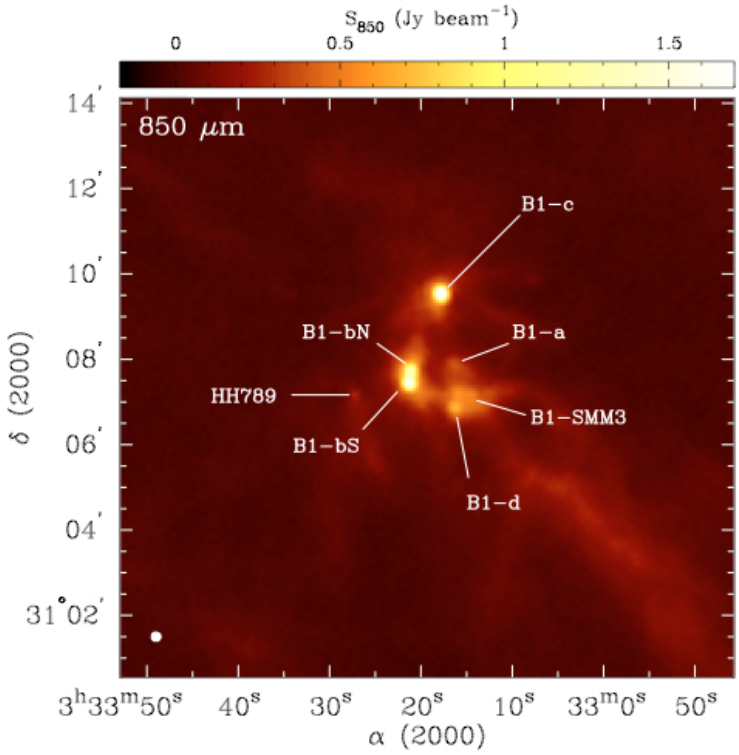

Figure 1.9: Figure reproduced from Sadavoy et al. (2013) showing a continuum map of the Perseus B1 clump observed with SCUBA-2 at 850 µm, with an observed resolution of ~ 14″. Known sources in the region, from Jørgensen et al. (2007) and Hatchell et al. (2007), are marked.

1.4.1.2 HARP

The Heterodyne Array Receiver Programme, as well as the Auto-Correlation Spectral Imaging System (ACSIS) is used to observe molecular lines in the submillimetre regime. As the submillimetre band contains many spectral lines, HARP/ACSIS allows the study of space densities, velocities, chemical structure and gaseous excitation (Buckle et al. 2009).

HARP is used to map many of the sources seen by SCUBA-2 in CO isotopologues. These include the J = 3 → 2 transitions of ^{12}CO, ^{13}CO and C^{18}O. These spectral line measurements allow for velocity measurements, crucial for understanding feedback processes such as molecular outflows from protostars (Drabek-Maunder et al. 2016). Line measurements are also required to quantify the line contamination present in SCUBA-2 observations. The contribution to continuum flux from molecular lines is usually under 20 %, but can be as high as 79 % near outflows (Drabek et al. 2012). HARP observations are used to remove this contamination from SCUBA-2 maps used in Chapter 5 and 6 when possible.

1.4.1.3 POL-2

POL-2 is a polarimeter for SCUBA-2 designed to detect polarised submillimetre radiation. This traces absorption, emission or scattering events, since light emitted from a star is not polarised (Bastien et al. 2011). POL-2 was initially hoped to produce polarisation maps of 100 bright sources found in the SCUBA-2 survey, to provide valuable information on the importance of magnetic fields and turbulence in star formation. Due to delays, however, the GBS itself has been unable to acquire POL-2 observations of Gould Belt clouds. Instead, more recent surveys of Gould Belt clouds with POL-2 have been undertaken, including the B-fields in STar-forming Region Observations (BISTRO) Survey Ward-Thompson et al. (2017).

1.4.2 Other Instruments

1.4.2.1 *Spitzer* Space Telescope

The *Spitzer* Space Telescope (Werner et al. 2004) has an 85 cm primary mirror able to observe between 3.6 and 160 µm. It is able to provide both images and spectroscopy, and is responsible for, among other science, the discovery of many previously unknown young stellar objects and even entire molecular cloud complexes (Gutermuth et al. 2008). *Spitzer* comprises two main instruments.

The Multiband Imaging Photometer for Spitzer (MIPS, Rieke et al. 2004) is used for observations at 24, 70, and 160 µm. Resolution at these wavelengths is approximately 6, 18, and 40″, respectively. Additionally, observations at 3.6, 4.5, 5.8 and 8.0 µm are implemented with the Infrared Array Camera (IRAC, Fazio et al. 2004). Resolution in the IRAC bands is 1.6, 1.6, 1.8, and 1.9″, respectively.

Several surveys with *Spitzer* were commissioned to map molecular clouds in the Gould Belt. These include the 'From Molecular Cores to Planet-Forming Disks' (c2d, Evans et al. 2003; Evans et al. 2009), 'Gould Belt' (GB) Legacy (Dunham et al. 2015), Orion (Megeath et al. 2012) and Taurus (Rebull et al. 2010) surveys.

Spitzer data are used in Chapter 3 to inform observations of YSOs in Lupus I and to provide fluxes to construct SEDs. They are used in Chapter 4 to provide 24 µm fluxes for First Hydrostatic Core (FHSC) candidates in Serpens South. They are also used to provide the list of protostellar candidates in Chapters 5 and 6.

1.4.2.2 *Herschel* Space Observatory

Herschel (Pilbratt et al. 2010) was a space telescope with a 3.5 m diameter, offering observing capabilities between 55 and 671 µm. *Herschel*was able to carry out spectroscopy over the entire wavelength range, as well as imaging in five main bands (out of a possible six) with the PACS (Poglitsch et al. 2010) and SPIRE (Griffin et al. 2010) instruments. The central wavelengths of the five main bands are at approximately 70, 160, 250, 350, and 500 µm, with resolutions ranging between approximately 5 and 36 µm. Observations of star-forming regions with *Herschel* have been undertaken by the *Herschel* Gould Belt Survey (GBS) (André et al. 2010). These have allowed SCUBA-2 mapping to focus on the most promising regions with high extinction ($A_V > 3$), where cores are found and star formation is ongoing.

Herschel data are used as part of the data reduction procedure in Chapter 2, and they are used to provide 160 and 250 µm fluxes for FHSC candidates in Chapter 4.

1.5 Selected Molecular Clouds Observed in this Study

The following section introduces the molecular clouds of the Gould Belt that I have worked on while producing this thesis. It begins with an outline of the Lupus I molecular cloud, which is the subject of a dedicated chapter (Chapter 3). Observations of Serpens South are used in Chapter 4, and data from all clouds in Section 1.5 are used in Chapters 5 and 6.

1.5.1 Lupus I

Lupus (Latin for wolf) is one of the 48 ancient constellations listed by Ptolemy in the second century A.D. It represents a wolf being killed by the nearby centaur of Centaurus. Within

this region of the southern sky lies the Lupus molecular cloud complex. The Lupus cloud comprises nine individual sub-clouds (Hara et al. 1999). Low mass protostars and YSOs of all evolutionary classifications can be found in the Lupus complex (Merín et al. 2008).

One of the largest of the Lupus sub-clouds was first identified as B228. B228 was catalogued by Barnard (1927), as a vacant (dark) region in the sky extending from the NW to the SE. More recently the ridge, as well as additional nearby structure, has been collectively referred to as Lupus I (Comeron 2008). This molecular cloud is one of the closest regions of star formation to Earth. The most recent estimate of the distance to Lupus I has yielded a value of 182^{+7}_{-6} pc (Galli et al. 2013), although other work has produced lower estimates (e.g., the value of 155 ± 8 pc, Lombardi, Lada, and Alves 2008). As the value from Galli et al. (2013) is recent, well-constrained, and calculated specifically for Lupus I (as opposed to the whole Lupus complex), this is adopted here as the distance to Lupus I.

Extinction maps of the region (Cambrésy 1999) as well as large-scale CO molecular line surveys of the complex (Murphy, Cohen, and May 1986; Tachihara et al. 2001) point to a total mass of molecular gas in Lupus I of the order 10^4 $M_\odot$. Assumption of distance, as well as the method of estimating mass, can significantly affect the mass estimates for molecular clouds in Lupus. This can be seen in the mass estimates for individual clouds in Lupus derived from extinction in Chapman et al. (2007), where a distance of 200 pc is assumed for Lupus I, being 3 times lower than from the rotational transition observations in Tachihara et al. (1996) and Hara et al. (1999), where 150 pc is assumed for all regions of Lupus.

Lupus I sits on the edge of the Scorpius-Centaurus OB association, a nearby group of high-mass stars (see, e.g., Preibisch et al. 2002). The median age of stars in the closest subgroup of Sco-Cen, Upper Centaurus-Lupus, is estimated at 16 Myr (Pecaut, Mamajek, and Bubar 2012). Thus the association is older than the YSOs in Lupus I itself, for which Hughes et al. (1994) found an age range of between 0.76 and 3.16 Myr.

There is also ongoing star formation in the region, an example being the Class 0 protostar IRAS 15398-3359 (Oya et al. 2014). In addition, Rygl et al. (2013) observed Lupus I as part of the *Herschel* Gould Belt Survey. They were able to demonstrate that Lupus I is

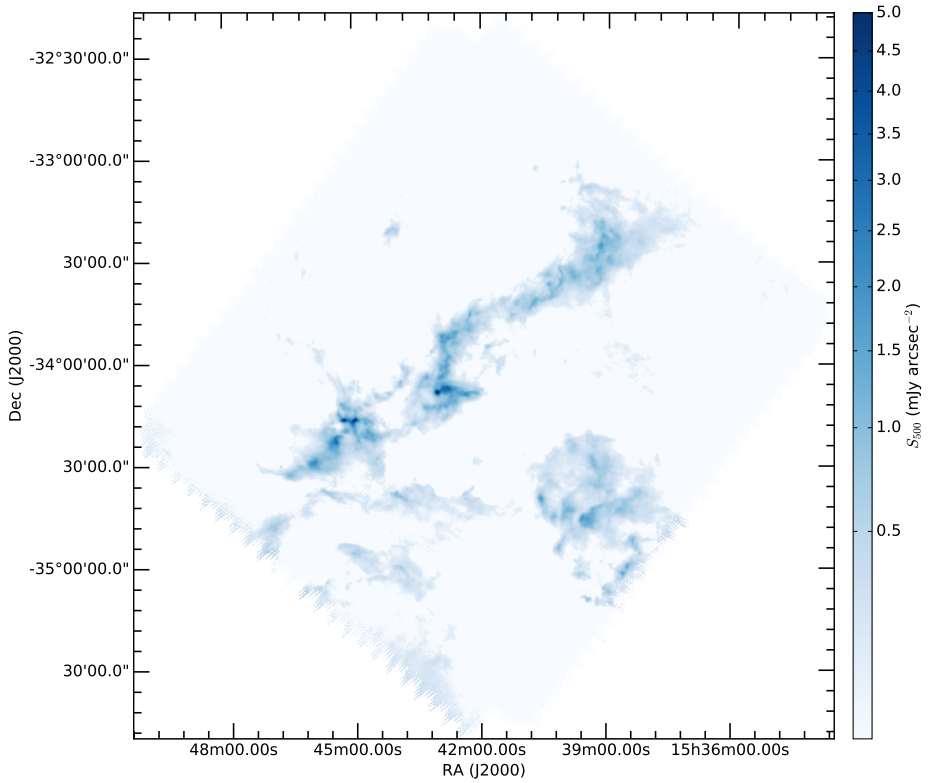

Figure 1.10: *Herschel* 500 µm continuum map of the Lupus I molecular cloud, previously published by Rygl et al. (2013) as part of the *Herschel* Gould Belt Survey. Data available at http://www.herschel.fr/cea/gouldbelt/en/Phocea/Vie_des_labos/Ast/ast_visu.php?id_ast=66

experiencing an increase in star formation due to the amount of high-extinction material and the large number of prestellar objects. The *Herschel* 500 µm map of Lupus I is shown in Figure 1.10. Stars in Lupus I are also noted by Hughes et al. (1994) to be younger than those of Lupus III; Tachihara et al. (1996) suggest this could be the result of a shock from Sco-Cen across Lupus I, which is closer to Sco-Cen than Lupus III.

1.5.2 Serpens / Aquila

The Serpens / Aquila molecular cloud complex is a large region consisting of several smaller clouds and subclouds located near the galactic plane. These clouds are located in the vicinity of the ancient constellations of Serpens and Aquila. Aquila (Latin for eagle) represents the eagle that carried the thunderbolts of Zeus / Jupiter, while Serpens (the snake) represents a snake being held by the healer Asclepius (depicted by the constellation

Ophiuchus). The constellation of Serpens is thus split into two separate parts about Ophiuchus: the head (caput) and the tail (cauda). Most of the molecular clouds of Serpens / Aquila are located in the relatively small area defined by Serpens Cauda. 'Aquila' largely refers to the Aquila Rift, a band of high extinction (Cambrésy 1999) and an alternative name for the entire agglomeration. The Aquila Rift contains a large number of YSOs; approximately 50 % of the YSOs catalogued by the *Spitzer* GB and c2d surveys are located in Serpens / Aquila (Dunham et al. 2015).

Serpens Main (often just Serpens) was first recognised to be a site of active star formation by Strom, Grasdalen, and Strom (1974). Since then, it has been well-studied (Harvey, Wilking, and Joy 1984; Eiroa and Casali 1992; Hogerheijde et al. 1999; Harvey et al. 2007; Graves et al. 2010). Serpens comprises three clusters: The Core, or Cluster A, is furthest north. South of The Core lies Cluster B, also known as Serpens NH3. The third cluster is further to the south situated around the star VV Ser (Eiroa, Djupvik, and Casali 2008). The *Spitzer* Space Telescope observed over 200 YSOs within Serpens - the majority of which lie outside the main clusters (Harvey et al. 2007).

The distance to the Serpens cloud has been controversial, but recent work by Ortiz-León et al. (2017a) has constrained the distance to 436 ± 9.2 pc. The mass of the main core of Serpens (Cluster A) has been calculated as approximately 250 – 300 $M_\odot$ (McMullin et al. 2000), though this was calculated using a smaller distance value of roughly 220 pc. Adjusting the mass based on this would provide a total mass of order 10^3 $M_\odot$. Observations of Serpens have been obtained as part of the JCMT GBS, but have not yet been published in a first look paper.

Westerhout 40 (W40) is an HII region first catalogued by Westerhout (1958). Adjacent to this HII region is a molecular cloud with a mass of order 200 $M_\odot$ for the cloud core and 10^4 $M_\odot$ for the entire complex (Dobashi et al. 2005; Rodney and Reipurth 2008; Mallick et al. 2013). The region contains a stellar cluster dominated by three OB stars responsible for exciting the HII region (Smith et al. 1985).

W40 appears to be spatially associated with the nearby Serpens clouds, also at a distance of 436 ± 9.2 pc (Ortiz-León et al. 2017a). This recent distance determination helped

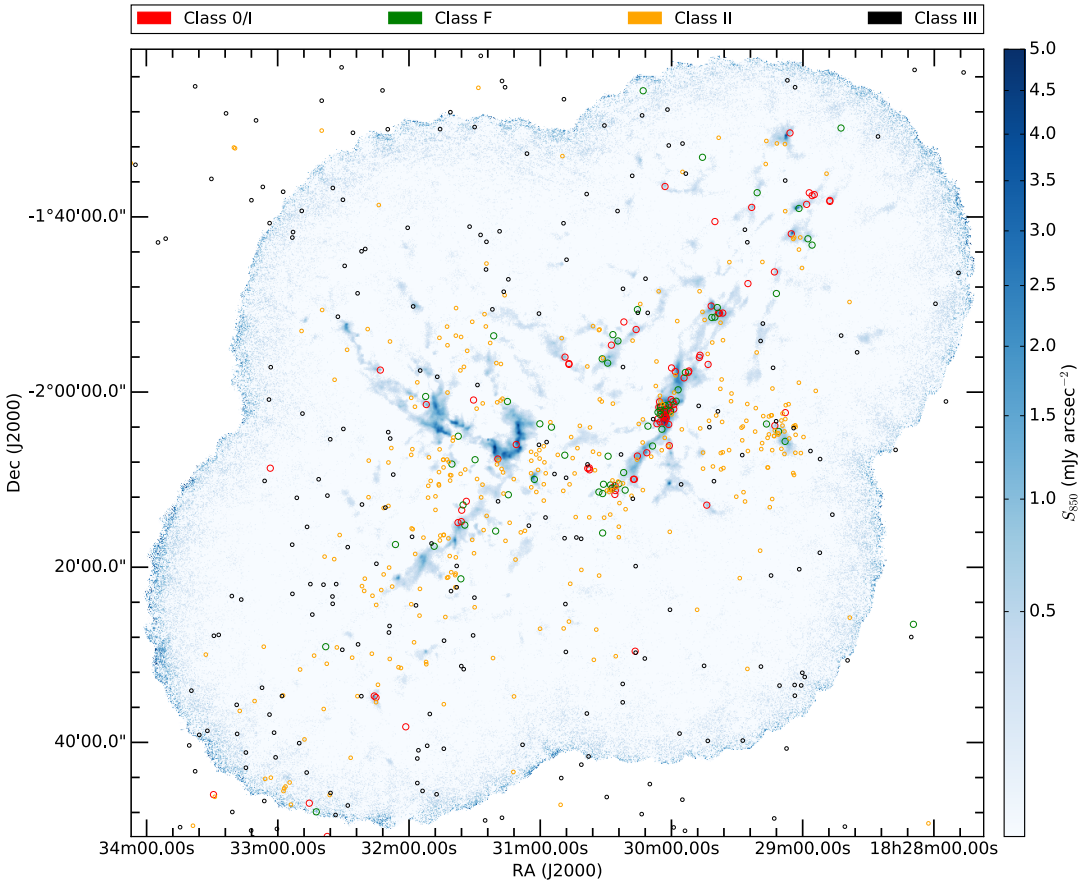

Figure 1.11: SCUBA-2 850 µm map of W40 and Serpens South, with *Spitzer* YSOs from Dunham et al. (2015) marked using colour-coded circles. Class 0/I and Flat-Spectrum sources are shown using larger circles. The continuum image is shown using square-root scaling.

clarify the association of W40 with Serpens / Serpens South, which had previously been uncertain Rumble et al. (2016). The region contains a large number of YSOs from the *Spitzer* catalogue (Dunham et al. 2015), but this count is likely incomplete due to oversaturation in the *Spitzer* IRAC bands. Indeed, the X-ray observations of Kuhn et al. (2010) have revealed a number of YSOs missed by *Spitzer*. The W40 region is shown alongside Serpens South in the SCUBA-2 850 µm map of Aquila (Figure 1.11). The positions of the known *Spitzer* YSOs marked. W40 is located to the east of Serpens South, in the left half of the image. Note the areas of bright submillimetre emission without any YSOs marked.

Serpens South contains a large number of YSOs but was not discovered until the Aquila Rift was mapped by the *Spitzer* Space Telescope (Gutermuth et al. 2008), despite lying just 3° south of Serpens Main. Since then, it has been the subject of studies at multiple continuum wavelengths (Bontemps et al. 2010a; Maury et al. 2011; Könyves et al. 2015) as

well as molecular line emission (e.g., Nakamura et al. 2011; Kirk et al. 2013). These have aimed to characterise the population of prestellar and protostellar cores in the cloud. It has been revealed as a dense filament of molecular gas undergoing a significant star formation event. Figure 1.11 shows that *Spitzer* identified a large number of Class 0/I protostars in Serpens South, particularly in the central region.

Much like W40, the distance to Serpens South was until recently uncertain. Some studies indicated a distance of approximately 250 pc (Straizys, Cernis, and Bartasiūtė 2003; Maury et al. 2011) while others calculated distances of over 400 pc (Dzib et al. 2010). The larger estimates have recently been confirmed by Ortiz-León et al. (2017a), and the distance of 436 ± 9.2 pc can now be used for Serpens South. The central filament has a mass of approximately 610 $M_\odot$ (Maury et al. 2011), with the cloud at large having a mass of order 10^5 $M_\odot$ (Dame and Thaddeus 1985). The star formation rate (SFR) is high, at approximately 23 $M_\odot$ Myr^{-1}.

The JCMT GBS also observed other single fields in the Aquila Rift. MWC 297 is an intermediate mass star with associated molecular gas and dust as well as YSOs (Rumble et al. 2015). Serpens North (named by GBS) is a region further east in the Aquila Rift compared to Serpens Main. It also contains a number of YSO catalogued by Dunham et al. (2015).

1.5.3 Ophiuchus

The ρ Ophiuchi molecular cloud complex (also known as Ophiuchus) is located in the Southern Sky within the constellation of Ophiuchus (the healer Asclepius). Like Lupus I, Ophiuchus is found at the edge of the Sco-Cen OB association, in the Upper Scorpius subgroup (Preibisch and Mamajek 2008). A dark cloud in the vicinity was recognised by Barnard (1919) as B42. Later, Lynds (1962) catalogued the dark nebulae in Ophiuchus and provided the names for the sub-clouds that are still in use. The main cloud, L1688, is a well-studied site of ongoing star formation (Wilking, Gagné, and Allen 2008; Pattle et al. 2015). As well as L1688, the less-active L1689 lies to the east. The cloud complex, and a zoomed-in image of L1688, is shown in Figure 1.1.

Away from L1688 and L1689, there are further sub-clouds collectively known as Ophiuchus North. There is little star formation activity in Ophiuchus North, with only 12 YSOs identified by the *Spitzer* GBS (Hatchell et al. 2012). By contrast, L1688 and L1689 contain approximately 300 YSOs (Padgett et al. 2008). Ophiuchus is one of the closest regions of star formation to Earth, with a distance to L1688 of 137.3 ± 1.2 pc (Ortiz-León et al. 2017b). L1689 appears further away, at 147.3 ± 3.4 pc, but further observations are required before this can be confirmed.

1.5.4 Perseus

The Perseus molecular cloud is situated in the Northern Sky in the constellation of Perseus (a Greek hero). Perseus consists of several sites of active star formation with a combined mass of approximately 10^4 $M_\odot$, and is one of the most well-studied star forming regions Jørgensen et al. (2006), Rebull et al. (2007), and Bally et al. (2008). Perseus contains nearly 400 YSOs (Dunham et al. 2015), including a larger than usual fraction of young protostars (see Chapter 6).

The complex has two main sites of star formation. NGC 1333 was first discovered by Schönfeld in 1855 and was first recorded in literature by Hubble (1922a, 1922b). The associated dark cloud was subsequently catalogued by Barnard (1927). NGC is undergoing a significant star forming event - it is the most active region within Perseus (Walawender et al. 2008) and contains a large number of Class 0 protostars (Sadavoy et al. 2014). NGC 1333 is shown within the Perseus West region in Figure 1.12.

IC 348 was first recognised by Dreyer (1895), whose catalogue gives the region its name. Like NGC 1333, it was then included in the work of Barnard (1927). IC 348 has been well-studied and despite being a compact region it contains multiple sources representing the various stages of star formation, from starless and protostellar cores to molecular outflows (Herbst 2008).

Whether the sub-clouds of Perseus are co-distant or spatially distinct remains uncertain. Indeed, there is evidence to suggest that IC 348 may be approximately ten per cent

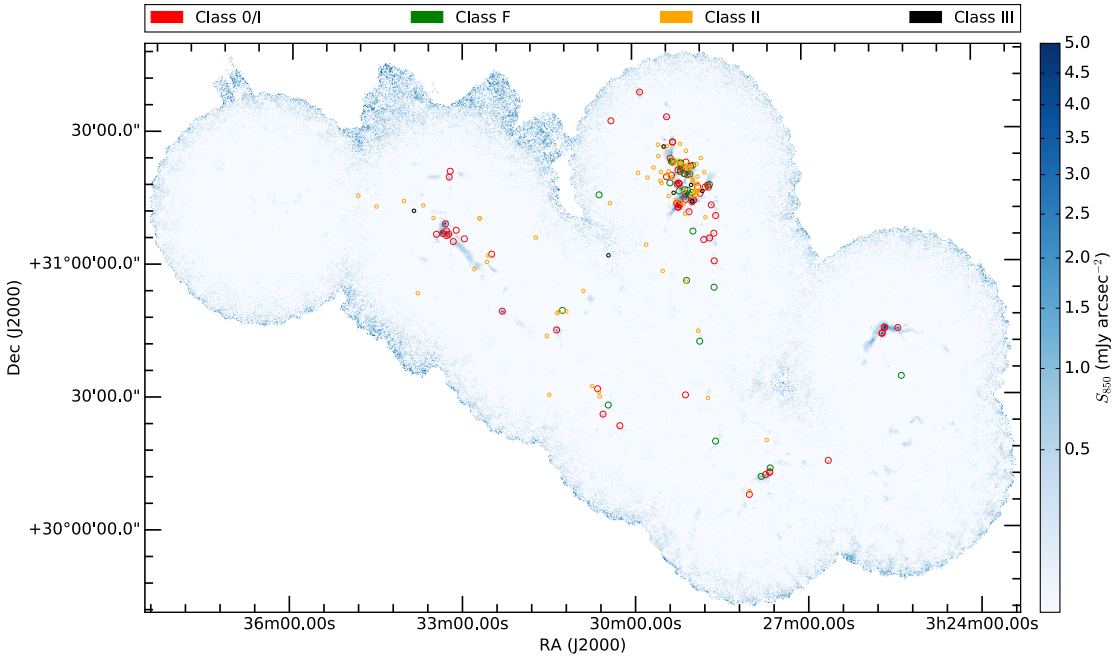

Figure 1.12: SCUBA-2 850 µm map of the western part of the Perseus molecular cloud, with *Spitzer* YSOs from Dunham et al. (2015) marked using colour-coded circles. Class 0/I and Flat-Spectrum sources are shown using larger circles. The continuum image is shown using square-root scaling. The largest cluster of YSOs is NGC 1333. Other sub-clouds include the B1 protostellar cluster (Sadavoy et al. 2013), L1448, L1451, and L1455 (Chen et al. 2016).

more distant than the western part of the cloud containing, e.g., NGC 1333 (Ĉernis 1990, 1993). For both the western and eastern parts of Perseus, however, we adopt a distance of 250 pc. This is consistent within uncertainties with both the closer distances of Hirota et al. (2008) and Hirota et al. (2011) (235 ± 18 pc and 232 ± 18 pc, respectively) and the greater Gaia parallax distance of 270 pc Herczeg et al. (2017).

1.5.5 Auriga / California

The Auriga / California molecular cloud is located within the constellation of Auriga (the charioteer) in the Northern Sky. The variable stars RW Aur and UY Aur were discovered by Ceraski (1906) and Leavitt and Pickering (1907), respectively. Later, Barnard catalogued the dark nebulae in the vicinity that represent the sites of star formation in Barnard (1919). The cloud is often associated with the nearby Taurus cloud, as Taurus-Auriga (Kenyon, Gómez, and Whitney 2008), but as part of the JCMT GBS we treat these clouds separately (Buckle et al. 2015; Broekhoven-Fiene et al. 2017).

The name Auriga / California itself was first used by Harvey et al. (2013), as the Auriga clouds lie in close proximity to the California nebula. Auriga / California contains a large population of ~ 166 YSOs which are predominantly concentrated around the LkHα 101 cluster (Broekhoven-Fiene et al. 2014). Auriga / California is one of the more distant Gould Belt regions, at a distance of 450 ± 23 pc (Lada, Lombardi, and Alves 2009).

1.5.6 Cepheus

The Cepheus Flare (Hubble 1934) is a large agglomeration of molecular clouds (Kun, Kiss, and Balog 2008) found in the Northern Sky in the constellation of Cepheus (a mythological Greek king). Many of the molecular clouds within Cepheus were catalogued by Barnard (1927), but it is the Lynds (1962) catalogue of dark nebulae that gives many of the individual clouds their names. For example, the JCMT GBS observed six such clouds, namely L1228, L1251, and L1147/58 and L1172/74. The final four clouds are collectively referred to as Cepheus South (Pattle et al. 2017).

Due to the separation of individual sub-clouds, different parts of Cepheus are found at different distances. L1228 and L1251 are found at 200 and 300 pc, respectively (Kun, Kiss, and Balog 2008). For the sub-clouds that comprise Cepheus South, we adopt a mean distance of 306.5 pc (Straizys et al. 1992). Cepheus is an active site of star formation with over 100 YSOs (Kirk et al. 2009; Dunham et al. 2015).

1.5.7 Corona Australis

The Corona Australis molecular cloud complex is situated in the constellation of Corona Australis (Southern Crown) in the Southern Sky. A large number of variable stars were observed in the region by, e.g., van Gent (1933) and later Herbig (1960) concluded that the nebula in Corona Australis was young.

At the heart of the Corona Australis cloud is the Coronet protostellar cluster (Neuhäuser and Forbrich 2008) and the cloud as a whole contains approximately 100 YSO candidates (Peterson et al. 2011). Corona Australis is one of the closest star forming regions to Earth,

at a distance of approximately 130 pc (Neuhäuser and Forbrich 2008).

1.5.8 IC 5146

IC 5146 is a reflection nebula and HII region (Herbig and Reipurth 2008) first identified by Wolf (1904) and also observed as a dark cloud by Barnard (1927). It is located in the Northern Sky in the constellation of Cygnus (Swan). IC 5146 contains over 100 known YSOs including over twenty protostars (Harvey et al. 2008; Dunham et al. 2015).

IC 5146 is more distant than other Gould Belt regions. Harvey et al. (2008) derive a distance to the cloud of 950 ± 80 pc, and other studies have indicated a distance of more than 1 kpc (Herbig and Reipurth 2008). Though the distance to IC 5146 is not yet certain, we adopt a distance of 950 pc for the JCMT GBS studies (Johnstone et al. 2017).

1.5.9 Other Molecular Clouds in the Gould Belt

The molecular clouds outlined above are the ones that I have worked during the course of this PhD. These molecular clouds are not the only ones observed by the JCMT GBS. Other clouds were observed that were not part of the *Spitzer* c2d and GB surveys. These are now briefly summarised.

The Orion Molecular Cloud Complex is the nearest region where both low and high mass star formation is ongoing (Bally 2008). It is also the region in the Gould Belt that contains the most known YSOs (Megeath et al. 2012). Taurus (also summarised by Kenyon, Gómez, and Whitney 2008) is a nearby low-mass star forming region that was the subject of a dedicated *Spitzer* survey (Rebull et al. 2010). The Pipe Nebula is a nearby (~ 130 pc) site of star formation with dark nebulae first identified by Barnard (1919). It has been the subject of fewer studies that most other Gould Belt clouds (Alves, Lombardi, and Lada 2008).

1.6 Thesis Outline

This thesis consists of seven chapters as well as an appendix. In this introduction I discuss molecular clouds, particularly the Gould Belt molecular clouds studied in this thesis. I outline star formation models, and observational tools used to determine the properties of YSOs. Finally, I briefly review some of the instrumentation used to obtain the observations that made this work possible, particularly SCUBA-2 and *Spitzer*.

In Chapter 2 I outline the procedure used to reduce SCUBA-2 data into continuum maps. I then detail the changes I made to the standard JCMT GBS data reduction parameters in order to improve the recovery of faint emission in the maps of the Lupus I molecular cloud.

In Chapter 3 I present the results of my study of Lupus I. This includes characterising both YSOs and starless cores in the cloud, for example, by calculating masses of cores and protostellar envelopes. I also fit model SEDs to YSOs to investigate properties such as temperature and determine whether model SED grids are able to constrain the properties of the YSOs in Lupus I.

Chapter 4 details work I did as part of a University of Exeter collaboration investigating the SEDs of First Hydrostatic Core candidates. I discuss how I produced observed SEDs for five new candidates, and the results fitting models to these observations were able to provide.

Chapters 5 and 6 present the work undertaken to produce an updated catalogue of protostars in ten Gould Belt clouds. Chapter 5 discusses the process of finding sources in SCUBA-2 maps and matching these sources to YSOs to produce a catalogue of 450 and 850 μm fluxes for protostellar candidates. Chapter 6 then uses these new and / or updated fluxes to reclassify these candidates and calculate the properties of protostars including their lifetimes, luminosities, and envelope masses.

Chapter 7 then summarises the findings of this thesis before discussing how I would like to continue this work in the future. Finally, the appendix presents the full tables of results for all protostellar candidates investigated in Chapters 5 and 6.

Chapter 2

SCUBA-2 Observations and Data Reduction

> *"This is a thousand monkeys working at a thousand typewriters. Soon they'll have written the greatest novel known to man."*
>
> — *C.M.Burns*

In this chapter I discuss the work I carried out to improve the reduction of the JCMT GBS SCUBA-2 observations of Lupus I. As a member of the JCMT GBS team, my first project was to produce a 'first look' paper using the GBS observations of the Lupus I molecular cloud. To do this, I first investigated the process of reducing the data from raw observations into useable maps. Lupus I contains areas of very faint submillimetre emission. Therefore, I tested different data reduction parameters with the aim of improving the recovery of this faint emission.

First, I outline the general observation procedure in Section 2.1 before discussing the process of reducing SCUBA-2 data in Section 2.2. I then introduce the observations of the Lupus I molecular cloud and describe the changes I made to improve the recovery of faint source emission in these maps in Section 2.3.

2.1 JCMT Observations

When observing a chosen target the JCMT will typically observe the same field multiple times. This improves the signal-to-noise ratio (SNR) in the final maps. Each continuum observation for the JCMT GBS was made using the PONG mapping pattern (Kackley et al. 2010) at both 850 µm and 450 µm. To produce a PONG map, the telescope scans across the sky and changes direction when it reaches the edge of a specified field. This allows maps to be larger than would be produced by a static instrument. In our case, 30' diameter maps were obtained. Each of these observations took approximately 40 – 50 minutes to be completed, and each individual field was scanned 4 – 7 times.

SCUBA-2 raw data takes the form of a time series. The power at each bolometer varies with time, so this signal is subsequently averaged. The SCUBA-2 data acquisition writes these data to an output file every 30 seconds, with a separate file written for each of the eight bolometer arrays (Thomas 2015). Figure 2.1 shows an example snapshot of the raw output data files for each of the four 850 µm sub-arrays. These are the 32^{nd} output file for observation 68 of the Lupus I E field (see Table 2.1).

Observing conditions vary between observations, both within one night and on different nights. This affects GBS observations as molecular clouds usually comprise multiple fields. One property that varies between observations is τ_{225}, the opacity in the atmosphere at 225 GHz as measured at the nearby Caltech Submillimetre Observatory (CSO, though this instrument has since been decommissioned). τ_{225} is also informed by the JCMT water vapour monitor, which measures at 183 GHz. τ_{225} is related to precipitable water vapour (PWV) via the relation $\tau_{225} = 0.04\mathrm{PWV}_{\mathrm{zenith}} + 0.017$ (Dempsey et al. 2013). Lower values of τ_{225} indicate drier observing conditions and reduced opacity in the submillimetre bands. The amount of water vapour in the atmosphere affects observations at 450 and 850 µm differently. While observations at 850 µm can be successfully carried out in band 3 ($0.08 < \tau_{225} < 0.12$) or even band 4 ($0.12 < \tau_{225} < 0.2$) weather, 450 µm observations can begin to degrade even in band 2 conditions ($0.05 < \tau_{225} < 0.08$). In band 2 weather the atmospheric transmission at 450 µm drops to 30 % or below, shown in Figure 2.2. In contrast, transmission at 850 µm in band 2 is approximately 80 %.

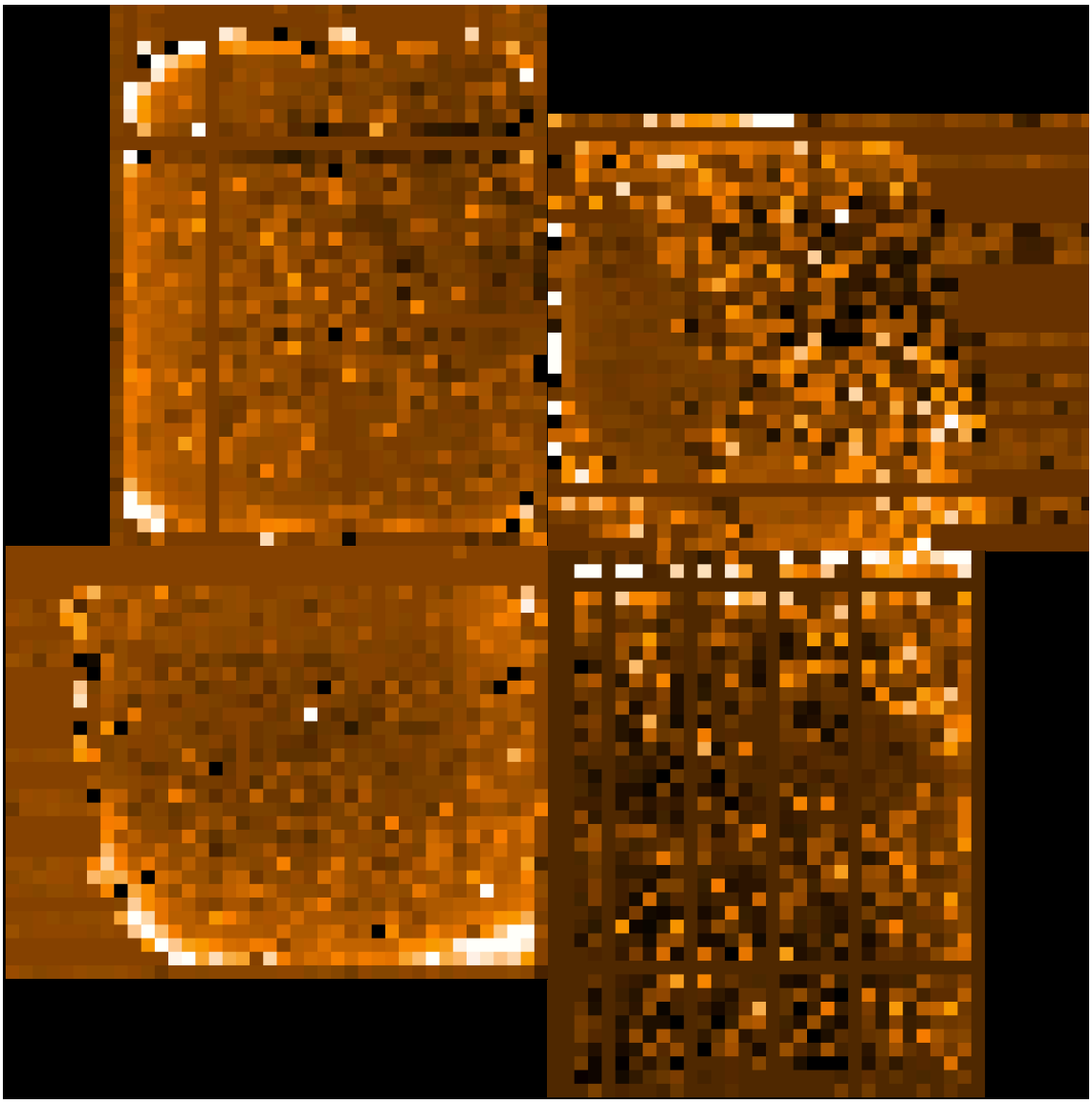

Figure 2.1: Image of individual sub-array output files for a SCUBA-2 850 µm observation of Lupus I. Clockwise from top left are the s8a, s8b, s8c and s8d sub-arrays. Each pixel corresponds to an individual bolometer.

To account for the differences in observing conditions, atmospheric extinction is corrected for using the most recent measurement of opacity taken by the JCMT. The extinction correction at 850 µm is found using the relation $\tau_{850} = 4.6(\tau_{225} - 0.0043)$, while the correction at 450 uses the relation $\tau_{450} = 26.0(\tau_{225} - 0.012)$. The JCMT will also regularly observe calibration sources with known fluxes, such as CRL 618 (Dempsey et al. 2013). These observations provide a flux conversion factor (FCF) which is then used on the raw data. The FCF converts from power on the array (pW) to astrophysical units (mJy/beam or mJy/arcsec^2 - JCMT GBS maps use units of mJy/arcsec^2). The FCFs at 850 and 450 µm

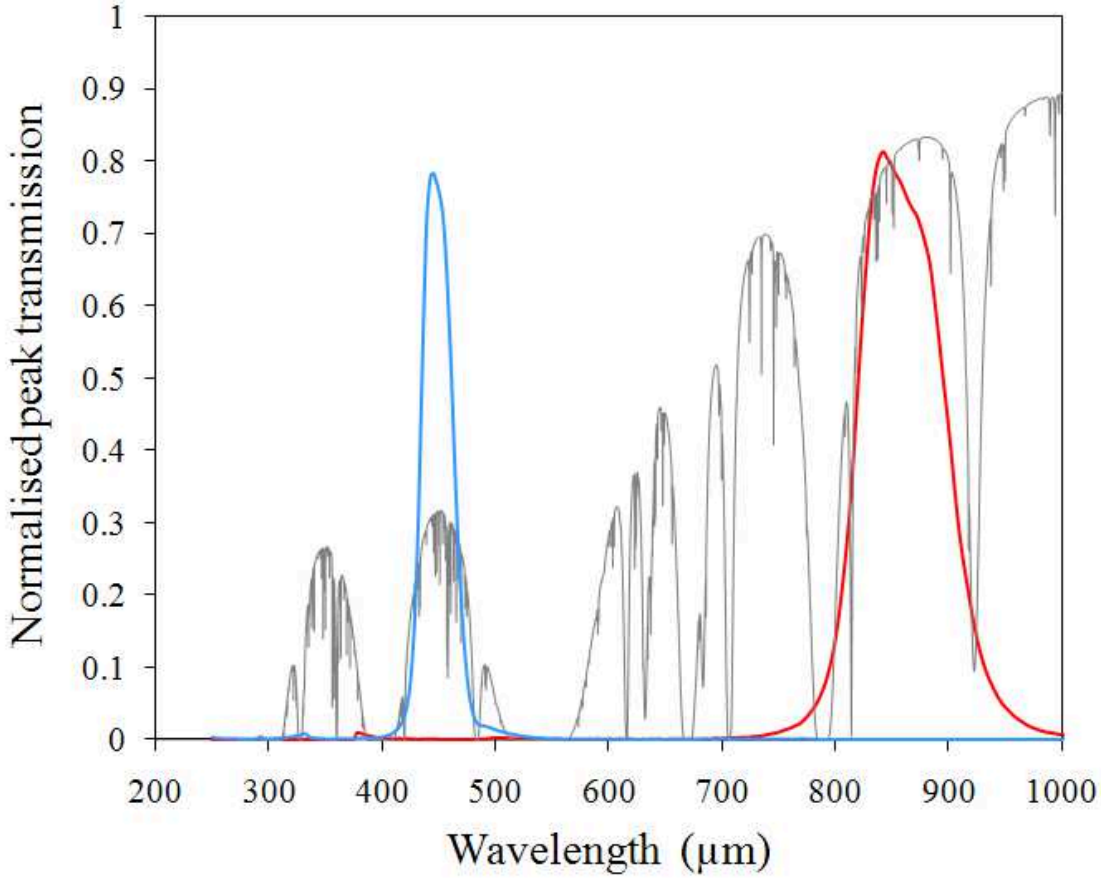

Figure 2.2: Figure reproduced from Holland et al. (2013). SCUBA-2 filter profiles at 450 μm (blue) and 850 μm (red), superimposed over the atmospheric transmission curve at Mauna Kea for PWV = 1 mm (provided by CSO). PWV = 1 mm corresponds to $\tau_{225} = 0.057$ – good band 2 conditions.

(Dempsey et al. 2013) are as follows:

$$\mathrm{FCF}[850]_{\mathrm{arcsec}} = 2.34 \pm 0.08 \text{ Jy pW}^{-1}\text{arcsec}^{-2}, \tag{2.1}$$

$$\mathrm{FCF}[450]_{\mathrm{arcsec}} = 4.71 \pm 0.5 \text{ Jy pW}^{-1}\text{arcsec}^{-2}, \tag{2.2}$$

$$\mathrm{FCF}[850]_{\mathrm{peak}} = 537 \pm 26 \text{ Jy pW}^{-1}, \tag{2.3}$$

$$\mathrm{FCF}[450]_{\mathrm{peak}} = 491 \pm 67 \text{ Jy pW}^{-1}, \tag{2.4}$$

Observations can probe extended structure down to the scale of the JCMT effective beam size, approximately 9.6″ at 450 μm and 14.1″ at 850 μm (Dempsey et al. 2013). The JCMT beam can be described as a superposition of both a main-beam Gaussian and an error-beam Gaussian. The secondary error beam is larger than the effective size of the

main beam, 48″ and 25″ at 850 and 450 µm, respectively, compared to 7.9″ and 13.0″, respectively. The 'beam' describes the response of the telescope to astronomical signal. Its size is strongly related to the diffraction-limited resolution of the telescope (θ), described by $sin\theta = 1.22\lambda/D$, where λ is the wavelength of radiation and D is the diameter of the telescope. However, the final effective beam shape is also affected by factors such as the pixel size used, the emission in the secondary beam (rather than main beam) and the diffraction pattern of the aperture.

2.2 The Data Reduction Process

Once the individual observations of a given cloud have been obtained, the next step is to reduce the data into a single map at each wavelength. Reduction of SCUBA-2 data, along with data analysis itself, uses the Starlink software package[1] (Currie et al. 2014). Starlink was developed to facilitate astronomical data processing, and is particularly used for observations taken by the JCMT.

SCUBA-2 Data reduction is implemented with MAKEMAP, an iterative map-maker which is part of the Submillimetre User Reduction Facility (SMURF[2], Chapin et al. 2013). When a set of data reduction parameters has been finalised, they are used across all regions observed as part of the JCMT GBS. The first set of maps produced this way was referred to as the GBS Legacy Release 1 data set. This data set used a two-stage data reduction process to produce the final SCUBA-2 maps at 450 and 850 m.

The first stage implemented is the automask reduction. This uses high Signal-to-Noise-Ratio (SNR) values in the SCUBA-2 time-stream to identify real sources of emission. The automask reduction is used on each individual observation in turn. The second 'external mask' reduction uses a combination of stacked automask reductions and other available information to constrain areas of real source emission for the reduction. The extra information can take the form of a mask file, in which certain areas of the map are covered. This helps exclude areas of the map that are not expected to contain real signal.

1. Available from the Astrophysics Source Code Library, record ascl:110.012
2. Available from the Astrophysics Source Code Library, record ascl:1310.007

A mask may be produced by retaining only pixels with an SNR greater than a specified value (for example, SNR = 3). An example mask is shown in Section 2.3. In both rounds of reduction, models of the various modes of emission (including common mode subtraction, high pass filtering and real astronomical signal, Chapin et al. 2013) are iterated upon until the average change of the pixels in the map between iterations is reduced to < 0.1 per cent of the map rms.

Individual automask-reduced maps for each field are then co-added into mosaics using the PICARD recipe MOSAIC_JCMT_IMAGES, (Gibb, Jenness, and Economou 2013). Adding multiple observations of the same region together improves the SNR for areas of emission, and also helps to reduce the impact of data artefacts that may be present in individual scans. When adding N maps together, the final signal will increase by N times. In contrast, the noise will increase by $\sqrt{N}$. Therefore, a larger number of observations means an improved SNR.

The data reductions used a spatial filter of 10′, meaning that sources with a Gaussian FWHM size of $< 2.5'$ are robustly detected. Sources with $2.5' <$ FWHM $< 7.5'$ will be detected, but with both flux and size underestimated. Any sources larger than this will depend on the mask being used in the data reduction, or they will be suppressed (Chapin et al. 2013). The tests of Mairs et al. (2015) show that extended structure is suppressed during the data reduction when located outside an external mask. Small-scale structures do not suffer from being located outside the mask to nearly the same extent.

All GBS data are calibrated to units of mJy/arcsec^2 using flux conversion factors in the data reductions. The FCF values from Equation 2.1 and Equation 2.2 are used for 850 and 450 µm data, respectively. Due to the chosen pixel sizes of 3 and 2″ at 850 and 450 µm, respectively, these FCFs are scaled to values of 21.06 ± 0.72 and 18.84 ± 2.00 Jy pW^{-1} pixel^{-1} at 850 µm and 450 µm, respectively.

Table 2.1: Full catalogue of JCMT MJLSG34 observations of Lupus I. τ_{225} is the opacity of the atmosphere at 225 GHz when each observation was undertaken.

	North-West			East			South-West		
	$15^h42^m45^s$ $-34°04'31''$			$15^h45^m22^s$ $-34°21'33''$			$15^h39^m33^s$ $-34°41'31''$		
Scan #	Date	Obs #	τ_{225}	Date	Obs #	τ_{225}	Date	Obs #	τ_{225}
1	15/08/14	00011	0.08	17/01/15	00068	0.07	22/01/15	00079	0.07
2	21/08/14	00024	0.06	17/01/15	00072	0.09	22/01/15	00087	0.06
3	22/08/14	00013	0.05	17/01/15	00078	0.07	24/01/15	00061	0.08
4	13/01/15	00067	0.06	20/01/15	00062	0.06	24/01/15	00066	0.07
5	13/01/15	00068	0.05	20/01/15	00066	0.06	26/01/15	00040	0.10
6	15/01/15	00080	0.06	20/01/15	00071	0.05	26/01/15	00042	0.07
7	...	...	...	...	...	...	26/01/15	00046	0.13

2.3 Data Reduction of Lupus I Observations

2.3.1 The Observations

Three separate fields in the Lupus I molecular cloud were observed with SCUBA-2 (Holland et al. 2013) as part of the JCMT Gould Belt Survey (Ward-Thompson et al. 2007). These fields are designated as NW, E, and SW. Three scans of the NW field were taken in August 2014, with the rest of the scans of Lupus I taken in January 2015. The sky co-ordinates (J2000) on which the NW, E and SW fields are centred, along with other details of the observations, are given in Table 2.1. All of these observations are saved using the Starlink NDF format (Economou et al. 2014).

Most of these observations were completed in dry band 2 weather, with 225 GHz opacity $0.05 < \tau_{225} < 0.08$. Observation 72 of the E field on January 17, as well as observation 40 of the SW field on January 26, were made in band 3 weather, where $0.08 < \tau_{225} < 0.12$. Finally, observation 46 of the SW field on January 26 was in poorer band 4 weather, with $\tau_{225} = 0.13$. The band 3 and band 4 observations had a detrimental effect on the quality of the 450 µm observations in particular, due to low atmospheric transmission at this wavelength (see Section 2.1).

2.3.2 Data Reduction

An initial data reduction of the Lupus I observations had already been produced using default parameters of the Legacy Release 1. In much of Lupus I, emission was faint and signal was low. On investigating I noticed that individual observations seemed to show greater amounts of emission that had seemingly been suppressed during the data reduction process. Therefore, I sought to test out new parameters to use for reducing the Lupus I data. The aim was to improve recovery of the faint submillimetre emission seen from this molecular cloud. The custom data reduction for this analysis is largely consistent with the GBS Legacy Release 1, including gridding data to 3″ pixels at 850 µm and 2″ pixels at 450 µm. However, there are a few differences which will now be highlighted.

To improve the recovery of faint emission, I altered the parameters for the automask reductions for Lupus I compared to the Legacy Release 1. Consistent with tests by Mairs et al. (2015), I allowed lower SNR pixels to be considered as potential source emission by changing the value of the ast.zero_snr parameter from 5 to 3. Additionally, zones of probable source emission were extended from none below a 5 σ floor to include 2 σ pixels around a 3 σ peak, by changing the ast.zero_snrlo parameter from 0 to 2. Here σ means the local noise level in the map, calculated using instrument and atmospheric noise. Essentially this means that any pixel with SNR = 2 can be considered to contain true emission provided it is associated with a peak pixel with SNR = 3. Previously, all pixels were required to have SNR = 5. A similar procedure will be used in the next official GBS data release (currently known as GBS Internal Release 4; IR4). Other values of the ast.zero_snr and ast.zero_snrlo parameters were tested, including 2 and 1, 3 and 1, 4 and 2, and 4 and 3. Ultimately, they were rejected due to either producing too much noise or failing to recover sufficient levels of faint emission compared to the 3 and 2 case.

Individual automask-reduced maps for each field were then co-added into mosaics using MOSAIC_JCMT_IMAGES. The presence of noisy data artefacts in the August 15 scan of the NW field resulted in this scan being excluded from this process, which increased the overall noise of the NW field automask mosaic. This individual scan is included as Figure 2.3. The decrease in SNR due to this was not a major concern, as this step is not the

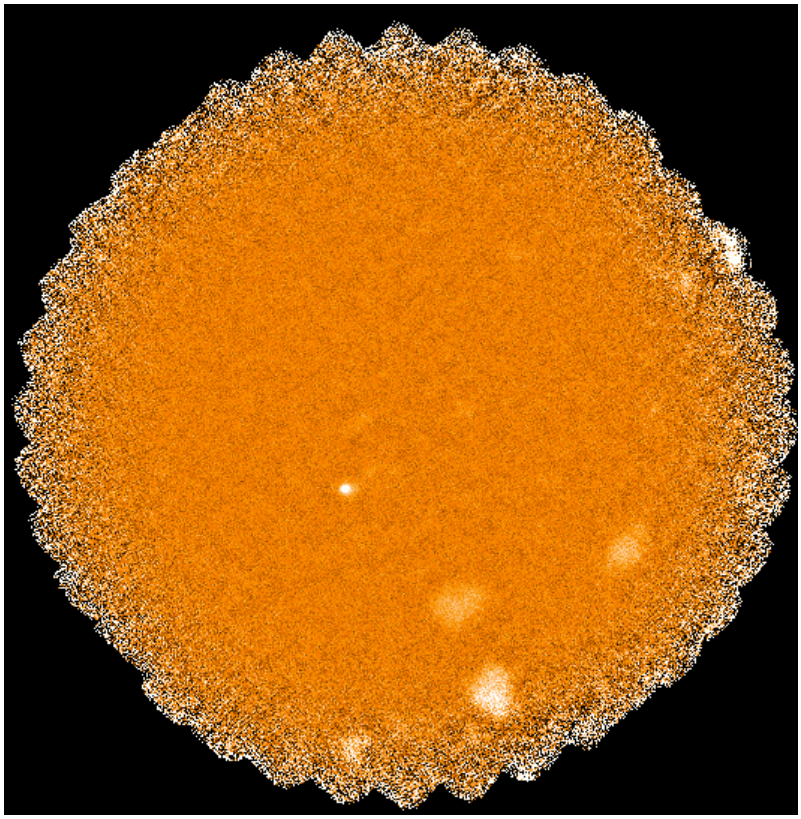

Figure 2.3: SCUBA-2 850 µm PONG scan of the NW field of Lupus I, taken on 15/08/2014. The small, bright object in the centre is real emission, but the larger 'blobs' are not. These are data artefacts produced due to noise spikes during the observation.

final stage of the data reduction.

The 850 µm mosaics were used to identify probable emission structure in order to create masks for use in the extmask reduction stage. Every individual pixel in the SCUBA-2 maps with a signal-to-noise ratio of at least one was included in the masks produced. While this criterion inevitably included fake as well as real emission, masked 'fake' pixels are non-contiguous. Hence, they are not reproduced in the external mask reduction stage.

At 850 µm, I combined the SCUBA-2 masking for the SW field with the *Herschel* (Rygl et al. 2013) 500 µm continuum map, masking off emission below a 1 Jy beam^{-1} threshold. Additionally, circular masks of 1' diameter centred around *Spitzer*-identified sources from Merín et al. (2008) were used. All pixels within these masks could therefore be considered as potential emission structure. The extra masking was used due to the faint emission in the field. Pixels below the SNR of 3 required to be treated as a zone of emission in the automask reduction stage could nonetheless visibly correspond to areas of real emission

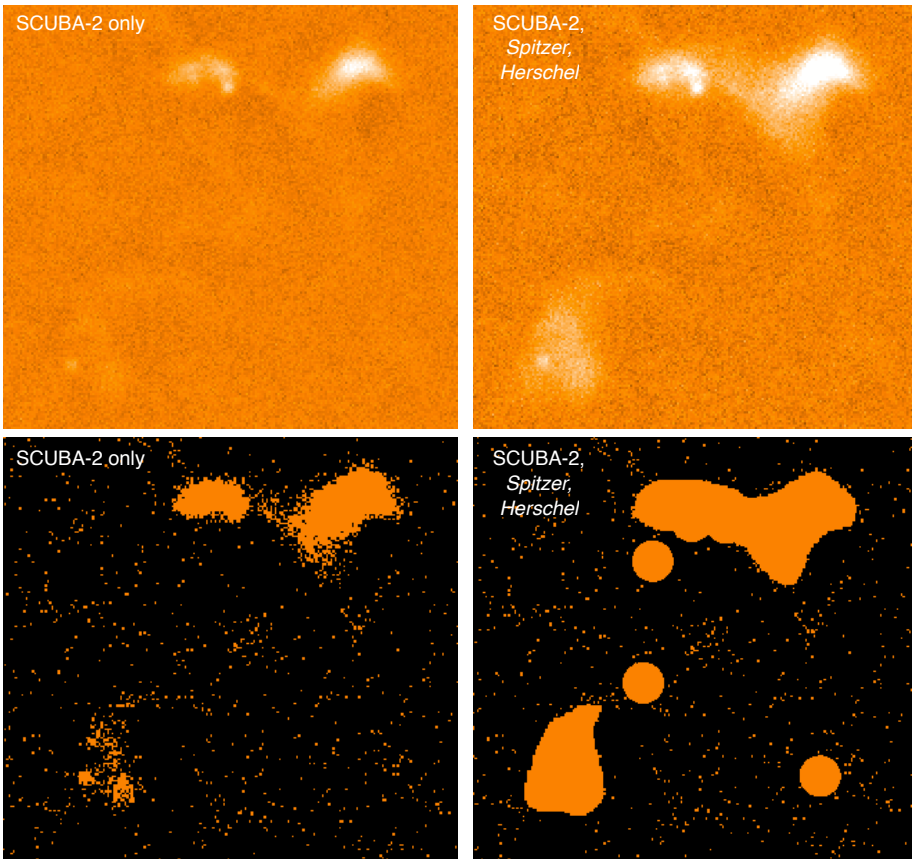

Figure 2.4: SCUBA-2 maps of the Lupus I East field produced using two different masking contours. The reduced images are on the top, while the masks are on the bottom. The left panels contain the image produced using only SCUBA-2 masking contours, with the corresponding mask shown below it. On the right, the image was produced using *Herschel* and *Spitzer* data masking in addition to that from SCUBA-2. The corresponding mask is shown bottom right. *Herschel* and SCUBA-2 contours were produced at the 2 σ level, while *Spitzer* contours used 20″ diameter apertures centred on the positions of known YSOs from Merín et al. (2008).

seen in the *Herschel* map.

As the emission in the NW and E fields is not as faint as it is in the SW field, I did not use additional masking contours beyond those from SCUBA-2 emission. To do so caused unreliable signal to propagate through to the final maps. This is shown in Figure 2.4, where two SCUBA-2 mosaics are shown. One was produced using only SCUBA-2 masking contours, while the other reduction also used contours from *Herschel* and *Spitzer*. The latter produces more permissive masking which covers a larger area. In the East field, this created a pedestal of emission, on which the 'real' SCUBA-2 emission sat.

The 450 µm masks were generally the same as at 850 µm. However, for the SW field only SCUBA-2 850 µm contours were used, simply because the quality of the observations was so low that no form of masking would be able to extract true signal from the noise.

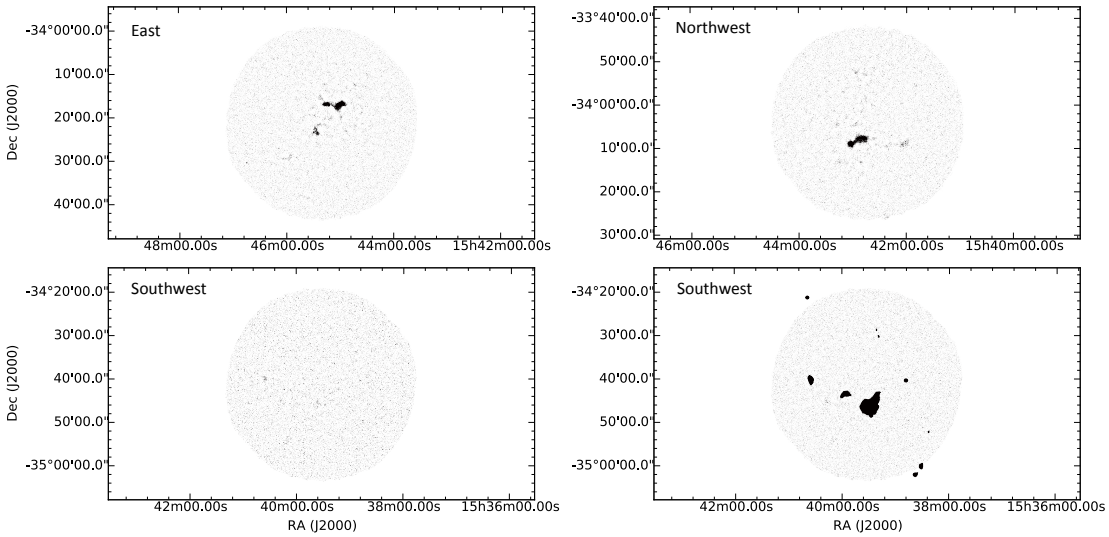

Figure 2.5: SCUBA-2 data reduction masks produced for each field of Lupus I at both 450 and 850 µm. The top left and top right images show the masks used for the East and Northwest fields, respectively. These were identical at both wavelengths. The bottom right mask was used for the 850 µm observations of the SW field (further details are provided in the text). The bottom left panel contains the 450 µm mask for the SW field.

This situation is detailed further in Section 2.4. Figure 2.5 shows the masks used for each field of the Lupus I observations.

Once produced, the masks were then used in the external mask reduction stage. The iterative map-maker was re-run using these masks. The process is otherwise very similar to the automask reduction stage, i.e., the raw observations of each field are used to produce 'extmask' reductions of each observation. The resulting extmask images are shown for each field of Lupus I in Figure 2.6. The changes have allowed more of the faint emission to propagate through the reduction stages. The before image of the SW field contains very little obvious emission. Emission continues to be faint in the after field, but the reduction has allowed YSOs and extended clumps of emission to become visible. Although the changes have increased the noisy appearance of the background in the after images, this does not cause a problem as this faint signal lies below the 3 σ threshold used for source-finding.

The changes made to JCMT GBS SCUBA-2 data reduction in this chapter are similar to those adopted for more recent GBS-wide data reductions (Data Release 3, also known as Internal Release 4, Kirk et al. 2018, in prep.). This is an updated data release compared to that used in most previous GBS publications. Updates to the automask stage of the

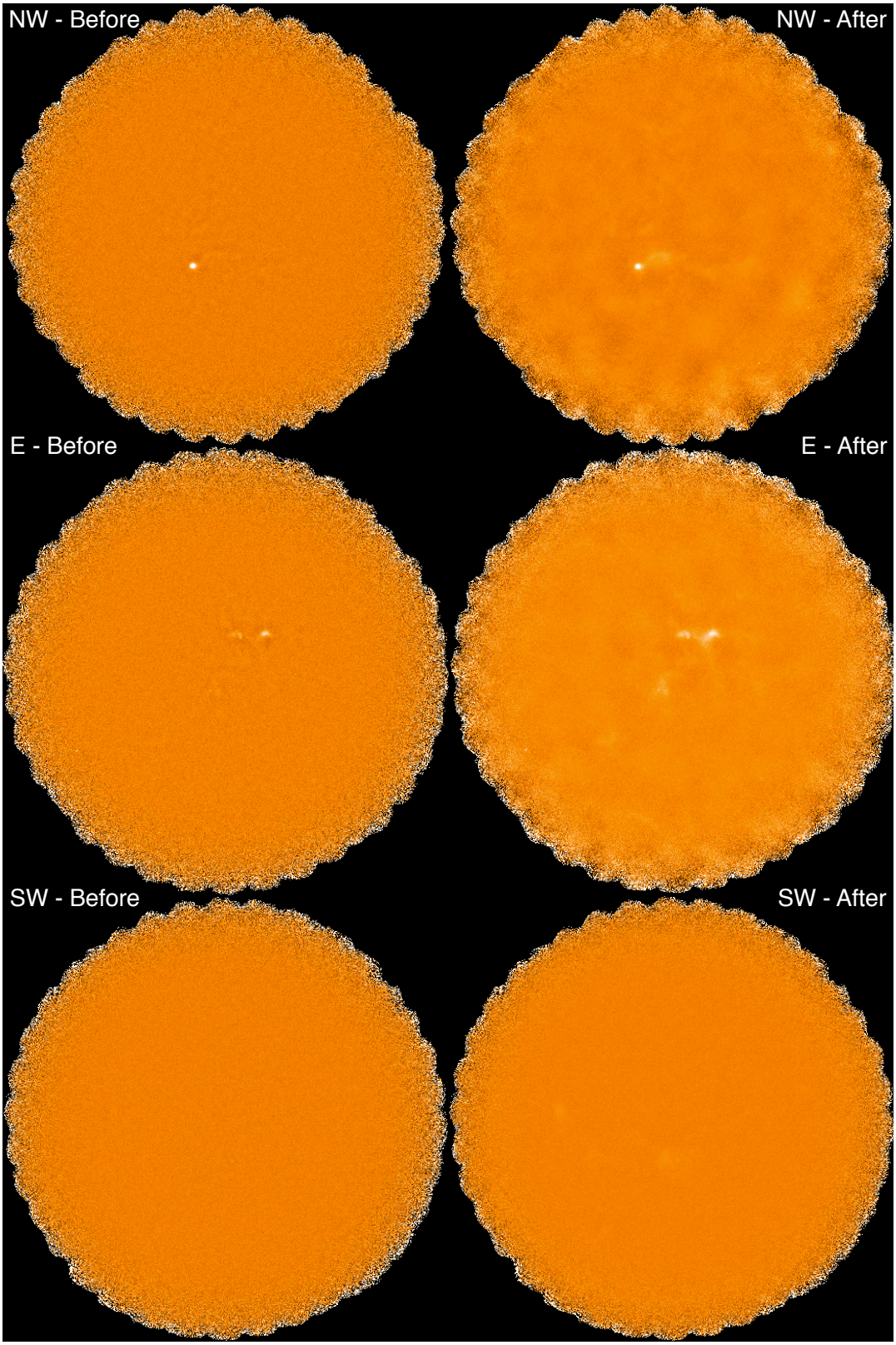

Figure 2.6: Lupus I SCUBA-2 NW, E, and SW fields at 850 µm shown before and after the data reduction changes. Before images are shown on the left, with after images on the right. From top to bottom are the NW, E, and SW fields.

data reduction included considering lower SNR pixels as potential source emission by changing the value of the ast.zero_snr parameter from 5 to 3. Additionally, zones of probable source emission were extended from none below a five sigma floor to include two sigma pixels around a three sigma peak (where 1 σ represents an SNR of 1). This was effected by changing the ast.zero_snrlo parameter from 0 to 2. In addition to the changes to the 'ast' parameters suppression of large scale structure was reduced, by eliminating the flt.filt_largescale_last parameter. We use these newly reduced GBS maps for the work in Chapter 5 and Chapter 6.

2.4 SCUBA-2 maps

Finally, all extmask fields were then mosaiced together to produce maps of the Lupus I molecular cloud at both 850 µm and 450 µm. The noisy edges of the maps were then removed using the KAPPA command ERRCLIP, part of the Starlink package. This removed edge areas with incomplete PONG coverage (with a local noise level of greater than 0.1 mJy/arcsec^2). These maps are provided, as Figure 2.7 and Figure 2.8, respectively. All scans were used to produce the final maps, in order to obtain the best SNR for areas of real emission. However, this approach does allow the possibility of data artefacts in individual scans propagating through to the final map, albeit at reduced levels of significance. Such artefacts are present in one scan of the NW field at 850 µm, though they are not as clear as they appear in Figure 2.3. The presence of data artefacts and speckles of noise is a common difficulty with SCUBA-2 data reduction (Mairs et al. 2015).

The typical pixel-to-pixel RMS noise level at 850 µm is 0.06 mJy/arcsec^2. Noise is larger and more variable at 450 µm, with values of 1.7, 2.8 and 5.1 mJy/arcsec^2 for the NW, E and SW fields respectively. Due to the widely varying noise levels in the 450 µm map, the use of ERRCLIP resulted in more clipping of the noisier fields, SW in particular. Full SCUBA-2 error maps of the region are presented as Figure 2.9.

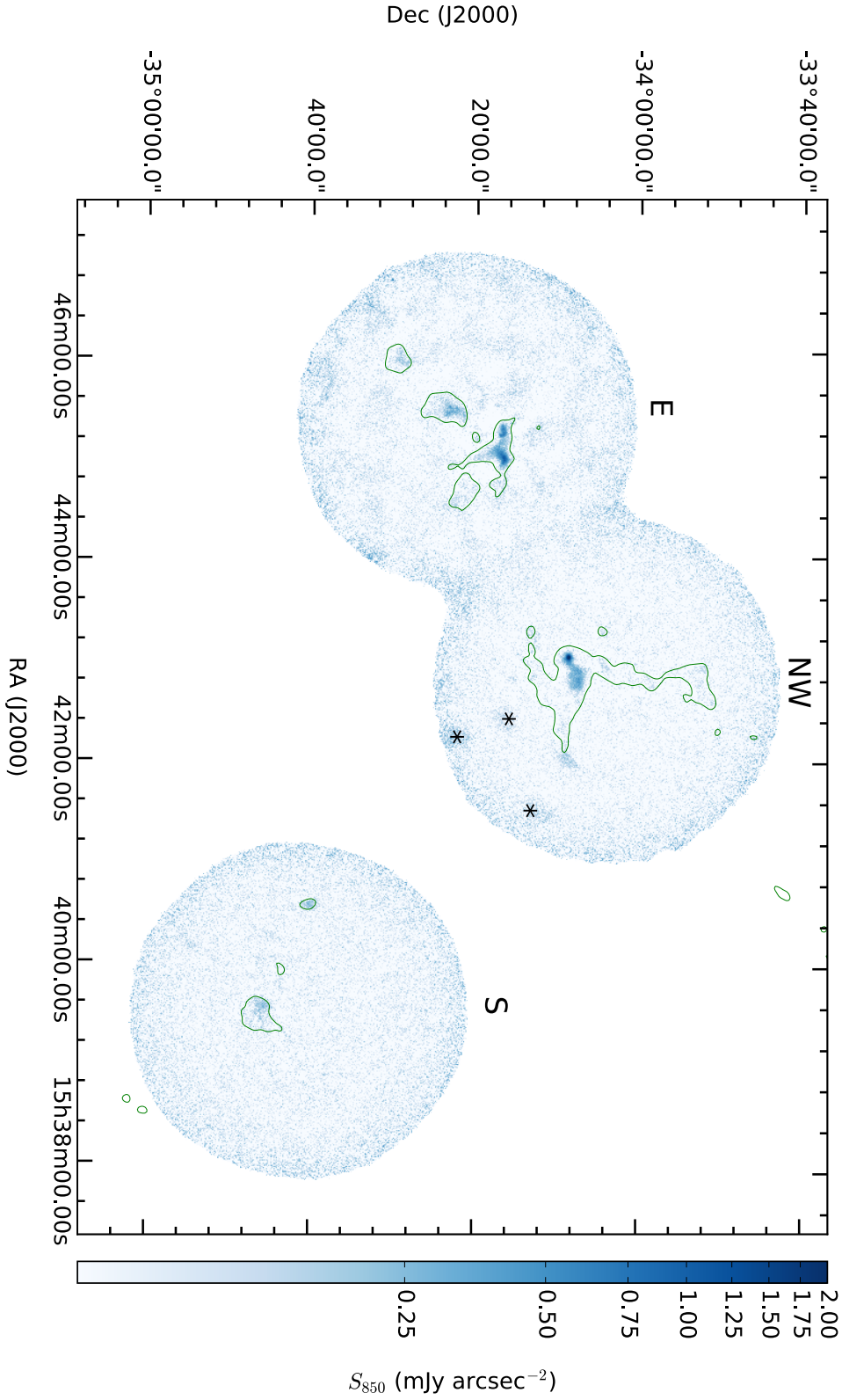

Figure 2.7: SCUBA-2 850 µm dust continuum map of the Lupus I molecular cloud. Noisy edges of the three fields have been largely removed from the map. Artifacts in the data from the August 15 scan of the NW field, in the bottom right of the field, are marked with asterisks. *Herschel* 500 µm emission (Rygl et al. 2013) is shown with green contours, at a level of 30 MJy sterad^{-1}.

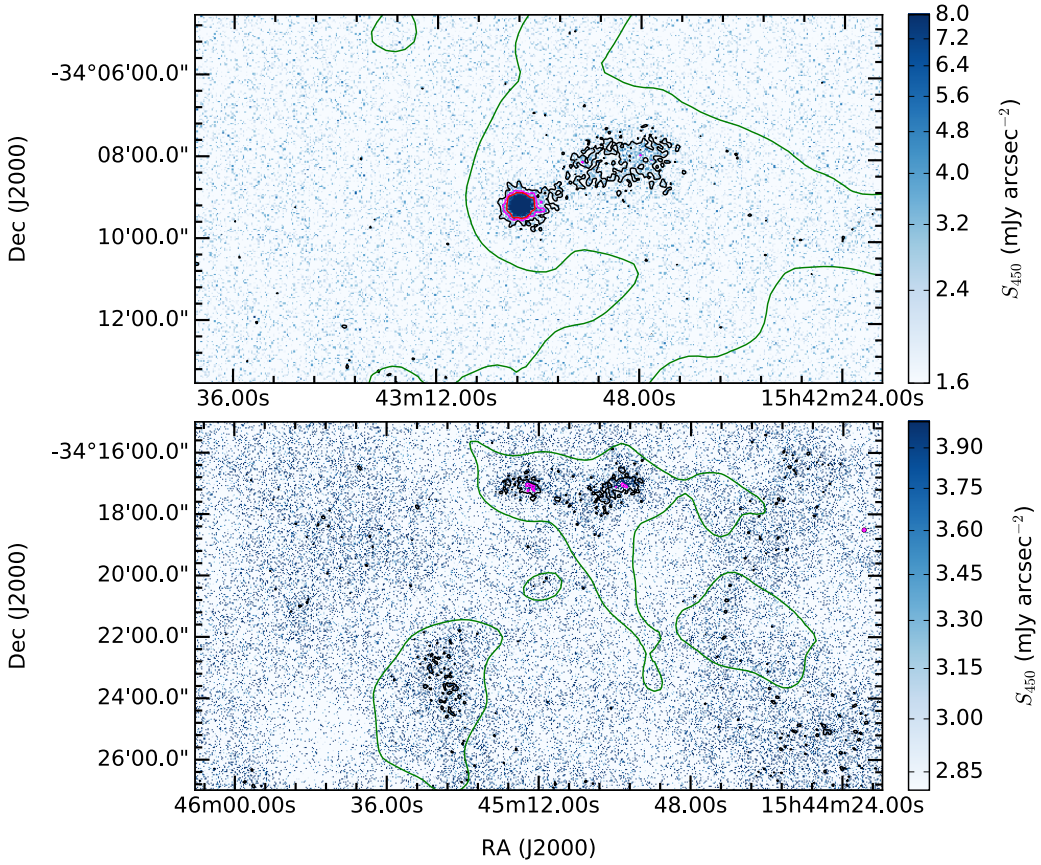

Figure 2.8: SCUBA-2 450 µm dust continuum maps of the Lupus I molecular cloud NW (top) and E (bottom) fields. Only regions containing significant detections are shown. Contours signify emission at 1 σ, 2 σ and 3 σ (black, magenta and red, respectively). *Herschel* 500 µm emission (Rygl et al. 2013) is shown with large-scale, smoothed green contours at a level of 30 MJy sterad^{-1}.

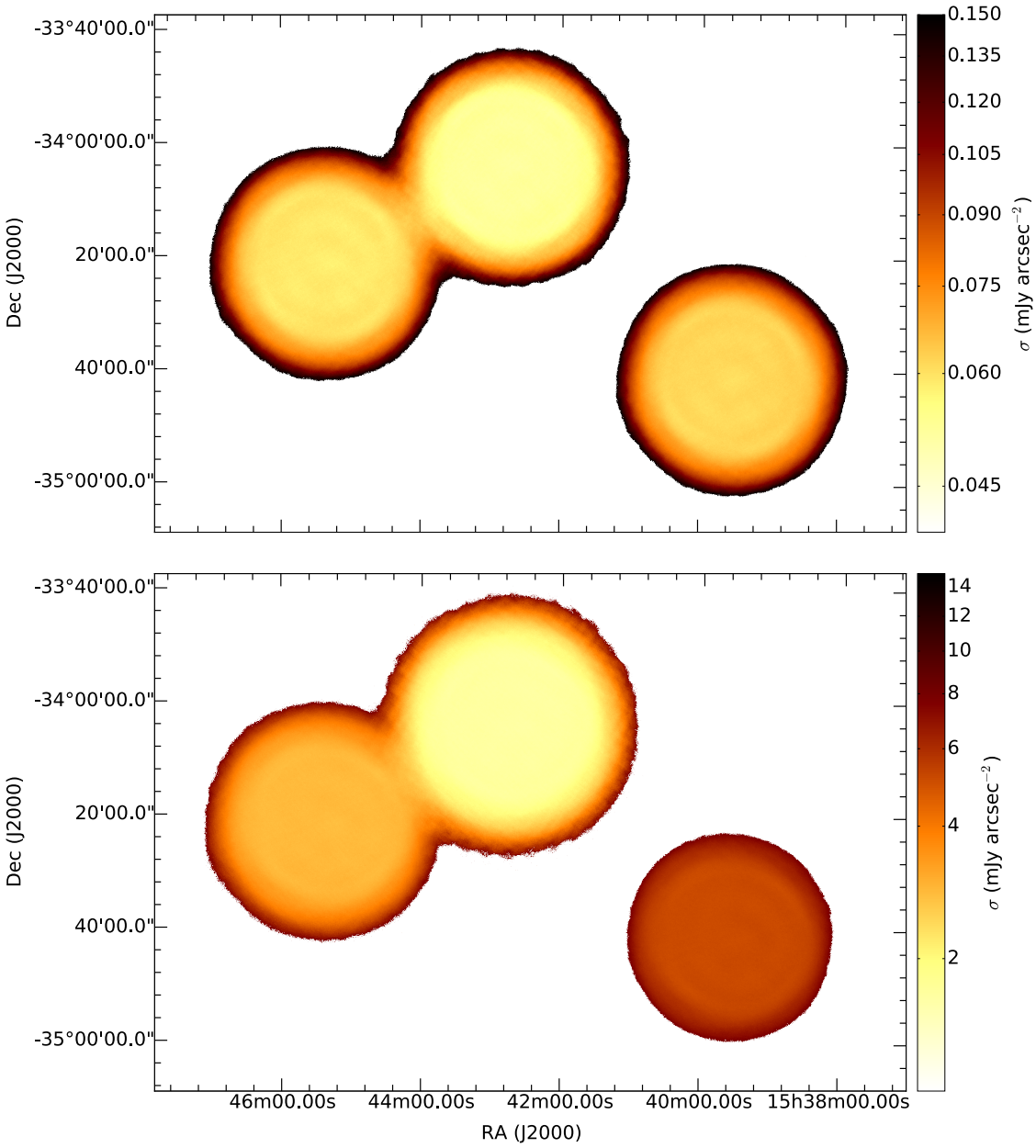

Figure 2.9: SCUBA-2 450 and 850 µm error maps of the Lupus I molecular cloud. The 850 µm error map is on top, with the 450 µm map below. Noise is consistent across all fields at 850 µm, but varies field-to-field at 450 µm.

Chapter 3

Lupus I - A First Look With SCUBA-2

"Ever since the beginning of time, man has yearned to destroy the sun. I shall do the next best thing: block it out."

— C.M.Burns

In this chapter I present the results of my analysis of the JCMT GBS SCUBA-2 maps of Lupus I. This work has been published as Mowat et al. (2017). This work uses the SCUBA-2 continuum maps of Lupus I to study the population of Young Stellar Objects (YSOs) - largely identified from *Spitzer* Space Telescope observations (Merín et al. 2008) - as well as dense cores and their stability against collapse.

The structure of this chapter is as follows. Section 3.1 discusses the structure in the SCUBA-2 maps of Lupus I first presented as Figure 2.7 and Figure 2.8 in Chapter 2. Section 3.2 focuses on the YSOs found in Lupus I. Disk properties are explored, and Spectral Energy Distributions (SEDs) of the known YSOs in the region are produced by combining SCUBA-2 data with data from a variety of other surveys. Extended structures, treated as protostellar, pre-stellar, and starless cores, are examined in Section 3.3. The size and stability of these cores is evaulated. In Section 3.4, the conclusions of this chapter are summarised. Refer to Chapter 2 for a discussion of the observations and reduction process used for the Lupus I data analysed here.

3.1 Structure in the SCUBA-2 Maps

The 850 µm map (Figure 2.7) shows evidence for both compact sources and more extended structures. The chief area of emission is seen in a line from the south-east to north-west corners of the E field, corresponding with the areas of extended filamentary structure seen in the *Herschel* maps of the region (Rygl et al. 2013). Additionally, the strong emission seen in the NW field is associated with the protostar IRAS 15398-3359 (Heyer and Graham 1989; Oya et al. 2014). Both emission from the envelope of the star itself and an associated filamentary-like structure can be seen. Areas of faint, extended emission can also be seen in the SW field. The SW field contains evidence of a faint protostellar envelope. This envelope is only detected at a 2 σ level, however it corresponds to the position of a known protostar and so is included in the analysis (see Section 3.2.1.1). The NW field is affected by the data artefacts in the 15/08/2014 scan. These are denoted with asterisks in Figure 2.7 and shown explicitly in Figure 2.3. Despite the artefacts, the inclusion of this scan in the final data reduction stage maximises the signal-to-noise ratio for true emission in the field. Data artefacts and speckles of noise can be seen elsewhere in the 850 µm maps.

The 450 µm maps (Figure 2.8) exhibit greatly increased levels of noise compared to those at 850 µm (see Section 2.4). The entire SW field, which is seen to contain only faint detections in the 850 µm map, as well as much of the E field, has a majority of pixels with a very low signal to noise ratio. This has left some of the areas of compact and extended emission entirely undetected at 450 µm. The protostar in the NW field (IRAS 15398-3359) is detected - at a signal to noise ratio of ~ 20 - as well as nearby extended structure. Also visible is the cluster of emission found in the centre of the E field, with a maximum SNR or ~ 5, though there are many noisy pixels.

Some of the compact sources (assumed to be point sources) found in the 850 µm map are isolated, for example at the southeast corner of the E field. The positions of many, however, are found within the areas of extended emission. Compact sources can be seen within the cluster of emission in the E field, and also in the centre of the SW field. These compact sources are expected to correspond to circumstellar disks around young stars, because SCUBA-2 does not have the required resolution to resolve disks. Taking

the distance to Lupus I to be 182^{+7}_{-6} pc (Galli et al. 2013), the 850 µm beam size (14.1″) corresponds to a spatial scale of ~ 2500 AU, and the 450 µm beam size to ~ 1750 AU. This large extent means that the spatial scales of circumstellar disks, usually < 1000 AU (McKee and Ostriker 2007) and averaging ~ 200 AU (Andrews and Williams 2007) fall well within the JCMT beam sizes. Hence, they are simply observed as unresolved point sources.

Overall, the amount of structure visible with SCUBA-2 in Lupus I is low. Compared to other regions observed with SCUBA-2, e.g., Ophiuchus (Pattle et al. 2015), Orion A (Salji et al. 2015a; Mairs et al. 2016), Orion B (Kirk et al. 2016) and Perseus (Chen et al. 2016), the maps show many fewer bright, compact objects and clustered structures. Lupus I's appearance is more in line with the relatively quiescent Auriga-California Nebula (Broekhoven-Fiene et al. 2017), although even Auriga-California contains more structure than Lupus I. Nevertheless, Lupus I contains several YSOs (see Section 3.2) and dense cores (see Section 3.3). Detections in the submillimetre enable the amount of cold material to be estimated. Hence, masses of circumstellar disks for more evolved sources (e.g., Buckle et al. 2015; Dodds et al. 2015) or circumstellar envelopes for more embedded sources (e.g., Rumble et al. 2015) can be determined.

3.2 Young Stellar Objects

3.2.1 YSO Fluxes and Previous Observations

3.2.1.1 SCUBA-2 Fluxes

The Lupus I molecular cloud was observed as part of the *Spitzer* c2d project ('From Molecular Cores to Planet-Forming Disks', Evans et al. 2003; Evans et al. 2009), using the *Spitzer* Space Telescope (Werner et al. 2004). Observations of Lupus I with *Spitzer* were presented in Merín et al. (2008), and the positions of 13 YSOs are used to guide photometry within the area of Lupus I observed by SCUBA-2. An additional four YSOs present in Merín et al. (2008) are outside the SCUBA-2 field of view. Source positions and the *Spitzer* area of coverage are presented, overlaid on the SCUBA-2 850 µm map, in Figure 3.1. Zoomed-in

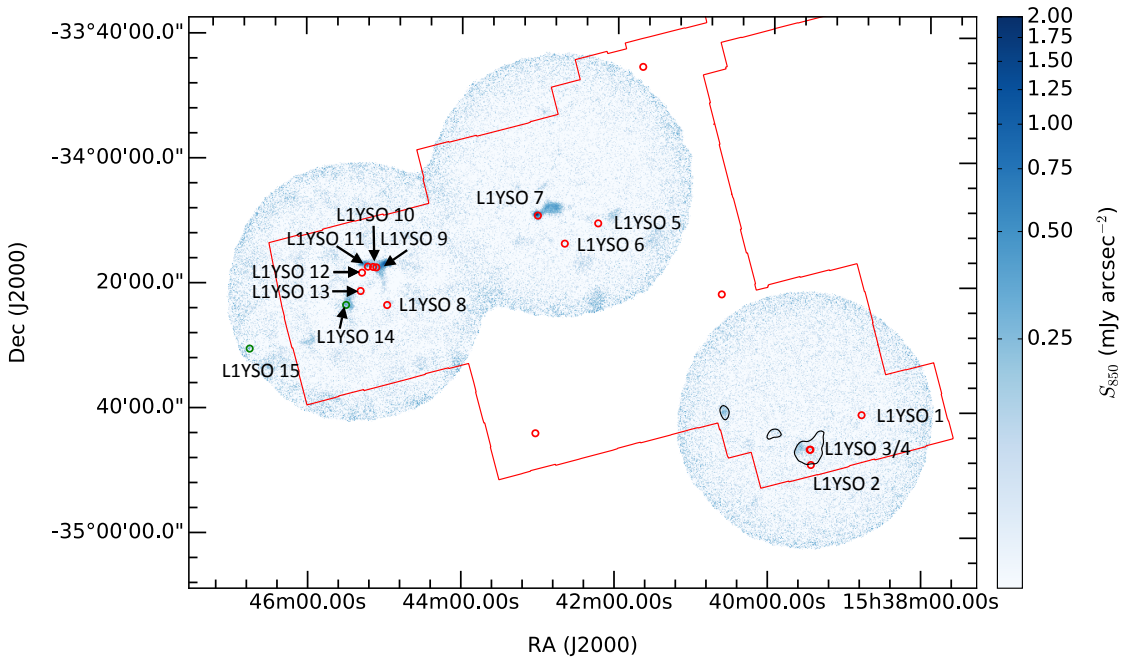

Figure 3.1: SCUBA-2 dust continuum map of the Lupus I molecular cloud at 850 µm. Additional masking contours produced from the Herschel 500 µm Lupus map (Rygl et al. 2013) are shown, and *Spitzer* YSO positions are overlaid. *Herschel* masking contours are black at the threshold used in the data reduction stage of 1 Jy. Red circles on the 850 µm map denote the position of YSOs detected by *Spitzer* (Merín et al. 2008), as detailed in Table 3.1. Green circles correspond to those disk sources not in the *Spitzer* paper that were detected by IRAS (labelled as L1YSO 14 and L1YSO 15). The straight red contours outline the field of view of IRAC in Lupus I.

850 µm images of each of the YSOs are shown in Figure 3.2.

Photometry was also carried out for two additional sources. The source IRAS 15422-3414 (L1YSO 14) is visibly present in the IRAC / MIPS observations of the region, but was excluded from Chapman et al. (2007) and Merín et al. (2008) due to being missed by the automated YSO detection criteria. Outside of the *Spitzer* coverage region, a detection was obtained of the T-Tauri star GW Lup (e.g., Kukarkin et al. 1971, Cutri et al. 2003) at 850 µm (L1YSO 15). This source was not within the 450 µm field of view due to the noisy edge clipping discussed in Chapter 2. Note that all YSOs examined in this work have been previously observed; no new YSOs are found.

Source fluxes were extracted using the Starlink *GAIA* image display and analysis tool (Draper et al. 2009). Aperture photometry was used to obtain fluxes at specified positions. Aperture photometry uses a circular region of the map (aperture) and sums the total flux found within this area. A background annulus can also be specified, defining a ring-like region around the aperture. The pixels can again be summed in this area to approximate a

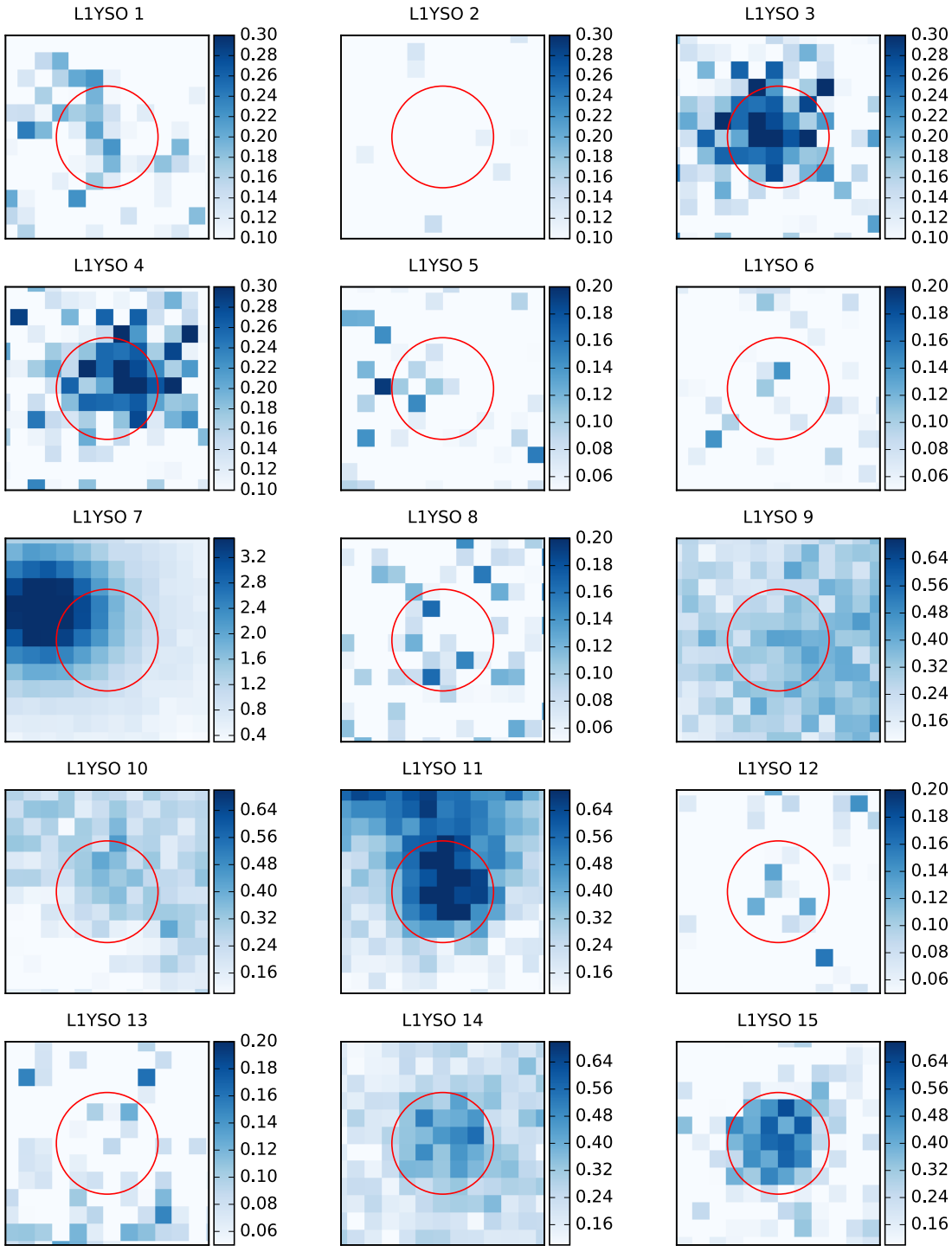

Figure 3.2: Individual images of 15 YSOs in Lupus I at 850 µm. Images are 36″ across. Published YSO positions are shown with red circles. Each colour scale has units of mJy/arcsec^2.

background, which can then be subtracted from the count inside the aperture. Typically, there will be a gap between the outer edge of the aperture and the inner radius of the annulus.

To provide fluxes for the YSOs in Lupus I, apertures were centred on the literature positions of these sources. At 450 µm, apertures with a diameter of 20″ were used for all sources. The total flux within the apertures was extracted and annuli with inner radii at 1.5 times the aperture radius and outer radii at 2.0 times the aperture radius were used to estimate a background flux - that was then subtracted.

At 850 µm, 20″ diameter apertures were used for most sources following Buckle et al. (2015). This size ensures the apertures fully encompass the SCUBA-2 primary beam. For the binary of IK Lup / Sz 65 (L1YSO 3) and Sz 66 (L1YSO 4), which is unresolved in the SCUBA-2 map, as well as L1YSO 10, 30″ diameter apertures were used instead. These sources visibly extend beyond a 20″ aperture in the 850 µm map. As they are not separately resolved, flux values for each of the sources in the binary are detected as one combined value by SCUBA-2 (as well as AKARI, IRAS and SEST). To plot SEDs for the L1YSO 3/4 binary, observed fluxes were divided according to the average ratio between IRAC and MIPS fluxes, as given in Table 3.2. Since the SCUBA-2 detection itself was of the sources combined, however, the same single flux is given for both sources in Table 3.1. The splitting of the fluxes assumes that both sources are equally evolved. This assumption is supported by the similarity between the values of the mid-infrared spectral indices (at -0.86 and -0.78) for each source (see Section 3.2.3), as well as the consistency between each individual flux ratio (2.8 ± 0.1).

A further exception to the 850 µm 20″ aperture sizes is given by the bright source in the NW field (L1YSO 7). Though this protostar was detected by *Spitzer* (as SSTc2d_J154301.3-340915), it clearly does not share the compact characteristics of the rest of the sources in this region. Therefore, an aperture of diameter 80″ was used for this source, with a background flux annulus between 120″ and 160″. The emission from this protostar extends far outside a 20″ aperture, so the use of such a small aperture would have produced an inaccurate flux measurement.

The JCMT beam itself extends out beyond 20″, so apertures of this size will not pick up all flux associated with an unresolved source. Therefore, fluxes were multiplied by aperture correction factors depending on the size of the aperture used. These factors can be found in Table 3 of Dempsey et al. (2013). This correction is done under the assumption that sources are point-like, so it would not be valid for an extended source (like L1YSO 7).

Photometry for all 15 sources, both detected and undetected, is given in Table 3.1. Some sources are listed in this table as detections, while not being clearly defined in Figure 3.2. This is because detections were simply defined based on $SNR \geq 3$ within the aperture centred at the position of the known YSO. The apparent offset of L1YSO 7 is likely due to the confusion of two sources in the original paper of Merín et al. (2008). However, these sources - lying in similar spatial locations - are not separately listed by Merín et al. (2008), nor are they distinguished in the SCUBA-2 maps at either 450 or 850 μm. Figure 5.2 shows that the offset seen would not be atypical for SCUBA-2 sources.

Where fluxes from SCUBA-2 were not available, upper limits were instead used. To calculate an upper limit for the flux of a source, each was modelled as a spherically symmetric Gaussian distribution of flux, $S(r) = S_0 e^{-r^2/2\alpha^2}$, where $\alpha = \mathrm{FWHM}/\sqrt{8\ln 2}$. The central peak flux values S_0 were set based on the noise levels in the map (σ = 0.05 mJy/arcsec^2 for the NW field and 0.06 mJy/arcsec^2 for the E and SW fields at 850 μm, σ = 1.7, 2.8 and 5.1 mJy/arcsec^2 for the NW, E and SW fields, respectively, at 450 μm). The noise level at the position of L1YSO 15, due to its proximity to the edge of the map, was higher than elsewhere with a value of 0.12 mJy/arcsec^2 at 850 μm. The full width at half maximum (FWHM) of the Gaussian was set based on the size of the aperture used (20″ in all cases where the source was not detected). To calculate the threshold for a 3 σ detection the peak value was specified to this level. Total flux values were then calculated as the integral under the Gaussian within the aperture, modified by the aperture correction factors.

Where fluxes for YSOs were available at both 450 μm and 850 μm, a consistency check between the fluxes at each wavelength (assuming a fixed temperature) was performed

Table 3.1: SCUBA-2 450 and 850 µm fluxes for YSOs identified by *Spitzer* (Merín et al. 2008), with additional IRAS sources (Beichman et al. 1988). Aperture diameters used to extract flux at 850 µm are provided.

SCUBA-2 ID	SSTc2d / IRAS ID	S_{450} (mJy)	S_{850} (mJy)	850 µm Aperture (″)
L1YSO 1	J153848.2-344041	≤ 308.97	38.22 ± 5.61	20
L1YSO 2	J153927.3-344844	≤ 308.97	≤ 8.46	20
L1YSO 3	J153927.8-344617	≤ 308.97	80.89 ± 8.24	30
L1YSO 4	J153928.3-344618	≤ 308.97	80.89 ± 8.24	30
L1YSO 5	J154214.6-341026	≤ 99.18	≤ 7.05	20
L1YSO 6	J154240.3-341343	≤ 99.18	≤ 7.05	20
L1YSO 7	J154301.3-340915	18266.00 ± 2499.38	3508.56 ± 150.81	80
L1YSO 8	J154457.9-342340	≤ 170.72	12.93 ± 3.84	20
L1YSO 9	J154506.3-341738	≤ 170.72	24.62 ± 6.83	20
L1YSO 10	J154508.9-341734	580.17 ± 191.32	56.78 ± 9.49	30
L1YSO 11	J154512.9-341731	609.78 ± 227.60	187.49 ± 62.03	20
L1YSO 12	J154517.4-341829	≤ 170.72	19.38 ± 5.29	20
L1YSO 13	J154518.5-342125	≤ 170.72	≤ 8.46	20
L1YSO 14	IRAS 15422-3414	327.42 ± 155.32	67.96 ± 7.61	20
L1YSO 15	IRAS 15435-3421	...[1]	133.09 ± 24.96	20

[1] No value is given here as the source is outside the error-clipped 450 µm SCUBA-2 map.
Note: Aperture sizes at 450 µm are all 20″ in diameter.

using the relation

$$\frac{F_{450}}{F_{850}} = \left(\frac{\nu_{450}}{\nu_{850}}\right)^{\alpha} \tag{3.1}$$

where F denotes flux, ν denotes frequency and $\alpha = 2.8$ is an appropriate spectral index for disks (Buckle et al. 2015). For the three point-like sources detected at 450 µm (L1YSO 10, L1YSO 11 and L1YSO 14), the flux at 450 µm was predicted according to Equation 3.1 using the flux obtained at 850 µm. Flux values were found to be consistent within 2 σ.

In addition to the SCUBA-2 fluxes at 850 µm and 450 µm, flux measurements from the optical B band to the millimetre regime at 1300 µm were compiled to construct SEDs for all YSOs (within the field of view of SCUBA-2) where data are available.

3.2.1.2 *Spitzer* Space Telescope

The first additional data set used is that of the *Spitzer* observations used to set the positions of the YSOs. The observations carried out at 24, 70 and 160 µm with MIPS are presented by Chapman et al. (2007). Additionally, observations at 3.6, 4.5, 5.8 and 8.0 µm with IRAC,

Table 3.2: *Spitzer* photometry for YSOs in Lupus I, identified with IRAC and MIPS, from Merín et al. (2008). The source IRAS 15422-3414 (L1YSO 14) is also included, with IRAC and MIPS flux values as given in the original YSO candidate catalogue.

ID	$S_{3.6}$ (mJy)	$S_{4.5}$ (mJy)	$S_{5.8}$ (mJy)	$S_{8.0}$ (mJy)	S_{24} (mJy)	S_{70} (mJy)	S_{160} (mJy)
L1YSO 1	3.95 ± 0.40	2.76 ± 0.40	9.58 ± 0.75	42.70 ± 3.11	114.00 ± 11.20	2920.0 ± 279.0	...
L1YSO 2	0.49 ± 0.03	0.37 ± 0.03	0.35 ± 0.04	0.25 ± 0.06	0.41 ± 0.46	≤ 50.0	...
L1YSO 3	255.00 ± 14.30	225.00 ± 14.30	231.00 ± 12.50	284.00 ± 14.00	483.00 ± 44.60	468.00 ± 47.3	...
L1YSO 4	95.80 ± 4.98	81.50 ± 4.98	82.50 ± 3.99	100.00 ± 4.84	167.00 ± 15.50	≤ 50.0	...
L1YSO 5	2.18 ± 0.14	1.78 ± 0.14	3.52 ± 0.23	16.40 ± 0.92	56.10 ± 5.20	593.0 ± 56.2	...
L1YSO 6	178.00 ± 11.00	120.00 ± 11.00	99.80 ± 5.06	68.80 ± 3.28	13.00 ± 1.22	≤ 50.0	...
L1YSO 7	...	25.20 ± 2.00	35.80 ± 3.00	118.00 ± 18.00	991000.00 ± 99.00[1]	15400.0 ± 1540.0	57.2 ± 11.4[1]
L1YSO 8	5.48 ± 0.27	4.06 ± 0.27	3.29 ± 0.16	3.73 ± 0.18	3.44 ± 0.38	≤ 50.0	...
L1YSO 9	14.10 ± 0.68	15.40 ± 0.68	16.20 ± 0.77	19.10 ± 0.90	69.90 ± 6.46	204.0 ± 23.2	...
L1YSO 10	101.00 ± 5.12	104.00 ± 5.12	100.00 ± 4.73	94.30 ± 4.66	137.00 ± 12.70	702.0 ± 67.8	...
L1YSO 11	1580.00 ± 132.00	1420.00 ± 132.00	1690.00 ± 97.90	2170.00 ± 130.00	286.00 ± 270.00	4900.0 ± 459.0	52000.0 ± 10400.0
L1YSO 12	111.00 ± 5.84	120.00 ± 5.84	94.60 ± 4.59	83.00 ± 4.12	100.00 ± 9.72	154.0 ± 20.1	...
L1YSO 13	37.70 ± 1.89	37.90 ± 1.89	35.80 ± 1.71	40.30 ± 1.91	38.50 ± 3.56	≤ 50.0	...
L1YSO 14	333.70 ± 26.30	323.0 ± 18.3	311.00 ± 17.10	255.3 ± 46.6	282.00 ± 26.20	296.00 ± 36.00	...
L1YSO 15	...	...	...	...	...	...	...

[1] These values are deemed unreliable in this analysis and hence are not used to produce the SEDs of this study.
Note: The full *Spitzer* YSO catalogue, including YSO classifications and fluxes / magnitudes from other surveys used, can be found in the online catalogue of Merín et al. (2008).

and comparisons with the MIPS data, were carried out by Merín et al. (2008). A total area of 1.39 deg^2 in Lupus I was observed by IRAC in each band, at angular resolutions of $< 2''$ (Fazio et al. 2004).

A total of 17 candidate YSOs were identified by *Spitzer*, 13 of which are within the SCUBA-2 field of view. The full catalogue of YSOs can be found in the online data of Merín et al. (2008), with these data also being carried through to the compilation of Dunham et al. (2015). The *Spitzer* sources within the field of view of the SCUBA-2 maps in this publication are listed in Table 3.2.

3.2.1.3 *Herschel*

Bustamante et al. (2015) measure *Herschel* fluxes for four YSOs in Lupus I (L1YSOs 3, 4, 11 and 12). SPIRE fluxes at 250, 350 and 500 µm are of particular interest for this analysis. Fluxes at these wavelengths would help fill the sparse submillimetre regime of the SEDs. However the *Herschel* beam sizes, particularly at 500 µm, can be much larger than SCUBA-2's at 850 µm. Aperture sizes used in source photometry are also correspondingly larger (42″ at 500 µm). These large apertures mean that there is significant contamination present in the *Herschel* fluxes from other structures near the YSOs. This effect is most pronounced for L1YSO 11, as the *Herschel* apertures encompass much of the structure identified as the

cores L1S2s 3, 4 and 5 later in this chapter. Hence, there is roughly an order of magnitude difference between the fluxes from *Herschel* at 500 µm and SCUBA-2 at 450 µm, respectively. This discrepancy means that a correction of the *Herschel* fluxes would be required for future analysis, when a complete census for all *Herschel* sources in Lupus I is published. *Herschel* fluxes are thus not used by us.

3.2.1.4 IRAS

Two additional sources were detected by the InfraRed Astronomical Satellite (IRAS, Neugebauer et al. 1984). The first of these sources, IRAS 15422-3414, was detected by *Spitzer* (and hence fluxes were available for use in this study) but was not presented in Merín et al. (2008). The second, IRAS 15435-3421, was outside the *Spitzer* field of view. IRAS fluxes from the point source catalogue, at 12, 25, 60 and 100 µm (Beichman et al. 1988) were used for these sources and others where available. The effective resolution of these IRAS bands is between 2 and 5′.

3.2.1.5 AKARI

Data from the AKARI mid-infrared all-sky survey (Murakami et al. 2007) are used where possible. AKARI observed with the InfraRed Camera (IRC, Onaka et al. 2007) in 9 and 18 µm bands, with a resolution of approximately 9″, and with the Far-Infrared Surveyor (FIS, Kawada et al. 2007) in four bands at 65, 90, 140 and 160 µm, with an effective resolution of between 0.6 and 0.9′. IRC fluxes for sources in Lupus I can be found in Ishihara et al. (2010) and FIS fluxes are from Yamamura et al. (2010).

Table 3.3 lists the nine sources for which AKARI fluxes are available, along with the relevant identifiers. Source positions often differ slightly from those given in the *Spitzer* catalogues. Therefore, sources were matched by ensuring the given positions differed by less than the given accuracy of 2″ (Ishihara et al. 2010) and that flux values appeared consistent with other surveys.

Table 3.3: AKARI all-sky survey fluxes from Ishihara et al. (2010) and Yamamura et al. (2010) for YSOs within the SCUBA-2 field of view in Lupus I.

ID	MIR ID[1]	S_9 (mJy)	S_{18} (mJy)	FIS ID[1]	S_{65} (mJy)	S_{90} (mJy)	S_{140} (mJy)	S_{160} (mJy)
L1YSO 1	1538484-344036	160.6 ± 31.6	...	1538486-344033	3261 ± 505	4603 ± 104	5360 ± 1720	≤ 4334
L1YSO 3	1539278-344617	441.1 ± 28.6	521.5 ± 49.1	1539278-344616	≤ 854.3	602.7 ± 51.4	≤ 1164	≤ 5274
L1YSO 5	...	...	...	1542148-341020	≤ 933.9	986.8 ± 130	≤ 3701	≤ 492.3
L1YSO 7	1543022-340907	110.5 ± 18.9	491.1 ± 37.1	1543019-340906	13440 ± 642	26260 ± 943	46280 ± 6260	78380 ± 3110
L1YSO 10	1545088-341734	125.4 ± 25.4	...	...	...	...	...	...
L1YSO 11	1545128-341730	2008 ± 14.2	2967 ± 26.7	1545123-341721	5554 ± 291	11910 ± 176	30280 ± 6780	54130 ± 967
L1YSO 12	1545174-341826	96.44 ± 2.79	...	...	...	...	...	...
L1YSO 14	1545297-342339	256.7 ± 17.6	317.7 ± 13.6	...	...	...	...	...
L1YSO 15	1546447-343035	176.9 ± 42.5	...	...	...	...	...	...

[1] Multiple IDs are given to ensure clarity, including the separate IDs for AKARI mid-infrared (MIR) and far-infrared and submillimetre (FIS).
Note: As with other surveys, fluxes for L1YSOs 3 and 4 are unresolved. They are listed in this table as given in the AKARI catalogues, under the ID of the brighter of the two sources. However, for the SED analysis all were split according to the average flux ratio between the two sources for all IRAC and the MIPS 1 band.

3.2.1.6 WISE

Magnitudes obtained from the WISE All-Sky Survey (Wright et al. 2010) were used for all 15 sources. WISE mapped the whole sky in four infrared bands. These bands (W1, W2, W3 and W4) have effective wavelengths of 3.4, 4.6, 12 and 22 µm respectively. The effective resolutions of these bands are 6.1, 6.4, 6.5, and 12″, respectively. The magnitudes for all objects, including those in Lupus I, are listed in the WISE All-Sky Data Release (Cutri et al. 2012). WISE data were available across all bands for every one of these YSOs, further enhancing the level of sampling in the mid-infrared regime.

Table 3.4 cross-matches all *Spitzer* sources, as well as the additional IRAS sources, with sources from the WISE All-Sky Data Release (Cutri et al. 2012). Source positions are again not identical to those in the *Spitzer* catalogues, but they are usually well within the angular resolution of IRAC I (which has the highest diffraction-limited resolution value across both telescopes of 1.5″; Rieke et al. 2004). Noticeably, they do not match within 1.5″ for the source IRAS 15398-3359. In Merín et al. (2008), the J2000 position of the bright, extended protostar (15:43:02.2 -34:09:09) appears to have been confused with that of a nearby much fainter compact object (15:43:01.3 -34:09:15). This object cannot be separately resolved from the protostar with, e.g., SCUBA-2, but is visible in the IRAC 1 map.

Table 3.4: WISE magnitudes for each YSO, in the four WISE bands (3.4, 4.6, 12 and 22 µm), taken from the WISE All-Sky Data Release (Cutri et al. 2012).

ID	WISE ID	W1 (mag)	W2 (mag)	W3 (mag)	W4 (mag)
L1YSO 1	J153848.37-344038.0	10.446 ± 0.022	10.111 ± 0.018	6.018 ± 0.014	4.044 ± 0.020
L1YSO 2	J153927.25-344844.2	14.811 ± 0.045	14.194 ± 0.059	11.509 ± 0.186	8.679 ± 0.338
L1YSO 3	J153927.75-344617.2	7.626 ± 0.028	7.178 ± 0.022	5.146 ± 0.015	3.193 ± 0.024
L1YSO 4	J153928.25-344618.1	8.579 ± 0.039	8.029 ± 0.034	6.312 ± 0.033	4.383 ± 0.066
L1YSO 5	J154214.56-341025.5	12.452 ± 0.023	11.998 ± 0.023	8.012 ± 0.023	5.302 ± 0.035
L1YSO 6	J154240.30-341342.8	8.006 ± 0.023	7.869 ± 0.020	7.385 ± 0.018	6.960 ± 0.096
L1YSO 7	J154302.21-340907.7	12.685 ± 0.023	8.872 ± 0.017	6.699 ± 0.018	2.371 ± 0.013
L1YSO 8	J154457.88-342339.4	11.891 ± 0.023	11.580 ± 0.022	9.798 ± 0.043	7.591 ± 0.128
L1YSO 9	J154506.33-341738.0	11.224 ± 0.023	10.233 ± 0.021	7.996 ± 0.020	5.126 ± 0.031
L1YSO 10	J154508.87-341733.6	8.864 ± 0.022	8.020 ± 0.020	6.339 ± 0.015	4.053 ± 0.022
L1YSO 11	J154512.84-341730.6	5.723 ± 0.054	4.973 ± 0.032	2.891 ± 0.010	0.856 ± 0.016
L1YSO 12	J154517.40-341828.4	8.440 ± 0.022	7.830 ± 0.018	6.510 ± 0.016	4.382 ± 0.023
L1YSO 13	J154518.51-342124.6	10.119 ± 0.022	9.464 ± 0.019	7.526 ± 0.018	5.738 ± 0.038
L1YSO 14	J154529.76-342338.9	7.769 ± 0.024	6.926 ± 0.019	5.429 ± 0.015	3.532 ± 0.019
L1YSO 15	J154644.72-343035.8	8.475 ± 0.023	8.046 ± 0.023	5.723 ± 0.015	3.680 ± 0.024

3.2.1.7 Optical and Near-Infrared Magnitudes

Optical and near-infrared magnitudes are also used in the production of the YSO SEDs. The Two Micron All Sky Survey (2MASS, Skrutskie et al. 2006) observed simultaneously in the J, H and K bands. Magnitudes for the sources in Lupus I are taken from Cutri et al. (2003). Comerón, Spezzi, and López Martı (2009) presented imaging of Lupus I, III and IV undertaken with the Wide Field Imager (WFI) at the MPI-ESO 2.2 m telescope (Baade et al. 1999). Magnitudes in 3 bands (R_c, I_c and z_{wfi}) corresponding to 0.64, 0.79 and 0.96 µm respectively were obtained. B and V magnitudes used in this work, corresponding to wavelengths centred around 0.44 and 0.55 µm respectively, are taken from the NOMAD catalogue (Zacharias et al. 2005).

3.2.1.8 SEST

Fluxes at 1300 µm, observed with the Swedish-ESO Submillimetre Telescope (SEST, Booth et al. 1989), are taken from the independent observations of either Reipurth et al. (1993) or Nuernberger, Chini, and Zinnecker (1997) when available. The effective resolution at 1300 µm is approximately 23″.

Table 3.5: B, V, R_c, I_c, z_c, J, H and K bands, as well as WISE 1-4, shown with their corresponding central wavelengths and zero-magnitude reference fluxes.

Band	Wavelength (μm)	Zero-mag Reference Flux (Jy)
B[1]	0.44	4130
V[1]	0.55	3781
R_c[1]	0.64	3080
I_c[1]	0.79	2550
z_{wfi}[2]	0.96	2450
J[3]	1.23	1594
H[3]	1.66	1024
K[3]	2.16	666.7
W1[4]	3.35	309.5
W2[4]	4.60	171.8
W3[4]	11.6	31.67
W4[4]	22.1	8.363

[1] Zero-magnitude reference fluxes from Bessell (1979).
[2] Waveband and zero-magnitude reference flux from Comerón, Spezzi, and López Martı (2009).
[3] 2MASS calibration from Cohen, Wheaton, and Megeath (2003).
[4] WISE zero-magnitude reference fluxes from Jarrett et al. (2011).

3.2.1.9 Comparison between *Spitzer* and WISE fluxes

As the IRAC 1, 2 and MIPS 1 detectors of *Spitzer* match closely in wavelength with WISE bands 1, 2 and 4 respectively (Werner et al. 2004; Wright et al. 2010), a comparison between the fluxes of *Spitzer* and the magnitudes of WISE enables an investigation of the consistency between these two surveys. To compare fluxes properly, *Spitzer* fluxes from IRAC 1, IRAC 2, IRAC 4 and MIPS 1 first had to be converted to magnitudes using Equation 3.2. *Spitzer* zero-point reference fluxes for IRAC 1, 2 and 4 are 280.9 ± 4.1, 179.7 ± 2.6 and 64.13 ± 0.94 Jy respectively (Reach et al. 2005). The zero-point flux for MIPS 1 is 7.17 ± 0.11 Jy (Rieke et al. 2008).

Once *Spitzer* fluxes were converted to magnitudes, the values needed to be modified to take into account differences, including in effective wavelengths, between the *Spitzer* and WISE filters. By interpolating between *Spitzer* bands, and providing corrective magnitude

shifts, Antoniucci et al. (2014) produce relations to calculate effective *Spitzer* magnitudes at 3.4, 4.6 and 22 µm, i.e., corresponding to the effective wavelengths of the WISE 1, 2 and 4 bands.

IRAC 1 and MIPS 1 fluxes were not available for L1YSO 7, so the *Spitzer*-WISE comparison could not be made. Additionally, L1YSO 15 could not be compared as it was not observed by *Spitzer*. Thus, only 13 sources had their magnitudes compared.

Effective *Spitzer* magnitudes for W1 and W2 for L1YSO 1 differ from the WISE magnitudes by approximately 6 σ. Antoniucci et al. (2014) perform a search for candidate eruptive variable protostars based on there being at least a 5 σ difference. This difference would be significant as *Spitzer* and WISE observations were undertaken during different epochs, and variable stars observed this way would be expected to show a difference in brightness. In order to perform the comparisons, however, Antoniucci et al. (2014) specify that a source must not be flagged as extended in the WISE catalogue (Cutri et al. 2012). Since L1YSO 1 is flagged as extended, this analysis may not be valid for this YSO.

Another YSO, L1YSO 3, demonstrates a 5 σ difference between magnitudes in the W4 band. Across the rest of the sources average differences are much lower (less than 2σ) and no other individual band has a difference approaching 5σ. Therefore, values appear to be more consistent between *Spitzer* and WISE for most point-like, more evolved sources.

3.2.2 Spectral Energy Distributions

SEDs have been produced for each of the 15 YSOs in Lupus I, including all available literature fluxes for each source. The collation of these data allows for the fitting of model SEDs to each YSO. Also enabled for each source are the calculations of a mid-infrared spectral index, bolometric luminosity, and bolometric temperature. SEDs for all sources, using observed fluxes (i.e., not extinction-corrected) are presented in Figure 3.3.

In order to be plotted, data values originally given as magnitudes were converted to

fluxes using the Pogson relation (Pogson 1856)

$$\frac{F_1}{F_2} = 2.512^{-(m_1 - m_2)} \tag{3.2}$$

where F_1 is the desired flux to be derived from the observed magnitude m_1. F_2 is the zero-magnitude reference flux for the particular band, and hence m_2 is by definition zero. Reference flux values used are given in Table 3.5. Table 3.5 also includes the custom z band as defined in Comerón, Spezzi, and López Martı (2009).

Where values from previous surveys were not available, the wavelength was simply not included in the SED. Upper limits for all sources in the c2d paper were also plotted as listed in Merín et al. (2008). For the two sources L1YSO 14 and L1YSO 15 which are not in the c2d paper, upper limits for IRAS fluxes are plotted as given in the IRAS point source catalogue (Beichman et al. 1988).

Similarly to *Herschel* (Section 3.2.1.3), IRAS and AKARI also have large beam sizes, and hence aperture photometry will suffer contamination from nearby structure if present, as it is with L1YSO 11. In particular, this aperture contamination provides an explanation for the strange shape of the SED for this YSO (seen in Figure 3.3).

Where the beam at a certain wavelength large, it is also possible for multiple sources to fall within it. Therefore, certain fluxes may actually correspond to more than one YSO, resulting in a change in the shape of some SEDs. L1YSOs 3 and 4 are not resolved by SCUBA-2, while L1YSOs 9, 10, and 11 are in close proximity to each other, so their SEDs may be contaminated.

For L1YSO 7, MIPS 1 and MIPS 3 fluxes given in Merín et al. (2008) are inconsistent with all other fluxes from this source observed across multiple surveys. The MIPS 1 flux is almost two orders of magnitude greater than the MIPS 2 flux, while the MIPS 3 flux is over two orders of magnitude lower than the MIPS 2 flux. Hence, they have been excluded entirely from our SED analysis. The IRAS flux at 25 µm, the WISE magnitude at 22 µm, and the AKARI flux at 160 µm for this source mean that these areas of the spectrum are still reasonably well represented in the SED.

Spitzer data for the source L1YSO 14 is in fact available from the original YSO candidate catalogue. Though this source is still referred to by its IRAS name (and not by a preliminary *Spitzer* designation), these fluxes are used to help produce the SED for this YSO. These *Spitzer* fluxes appear to be consistent with those from IRAS and AKARI.

3.2.3 Spectral Index

Once the datasets for each of the YSOs were collated, their evolutionary stages were estimated using the mid-infrared spectral index. This was calculated for each source using Equation 1.23 with a linear least-squares fit to all available data between 2.2 µm (K band) and 25 µm (IRAS 2). These values can be found in Table 3.6. Values for α of > 0.3 were used to classify a YSO as a Class I protostar and values of -0.3 ≥ α ≥ -1.6 resulted in a Class II classification, leaving values of 0.3 ≥ α ≥ -0.3 to indicate a Flat-spectrum YSO (hereafter referred to as Class F). Any YSO with an α value of ≤ -1.6 was considered as Class III.

Spectral indices were calculated both for observed and extinction-corrected flux values. Fluxes were corrected using the extinction law of Robitaille et al. (2007) - see also references therein. This extinction law was chosen to be consistent with the model fitting in Section 3.2.6.3. It does not differ substantially from the law of Weingartner and Draine (2001a) used by Dunham et al. (2013) to calculate luminosities of *Spitzer* c2d-identified YSOs.

To perform these extinction corrections, a value for A_V was required for each YSO. Values found from the model fitting in Section 3.2.6.3 were preferred when that source was 'well-fit' by the models (values given in Table 3.10). Where a YSO was not 'well-fit,' A_V was assigned the same value as was used in Dunham et al. (2013). In the case where neither of these options was possible, the value obtained from the best-fitting model (directly output from the SED fitter) to each YSO was used (Section 3.2.6.3, Table 3.9). A best-fitting model was always available, but was not necessarily a good fit to the data (i.e., well-fitting).

Of the 15 sources, three are Class 0/I, two are Class F/II (borderline), one is class III and the remaining nine are Class II sources. SCUBA-2 detected 11 of the 15 YSOs within

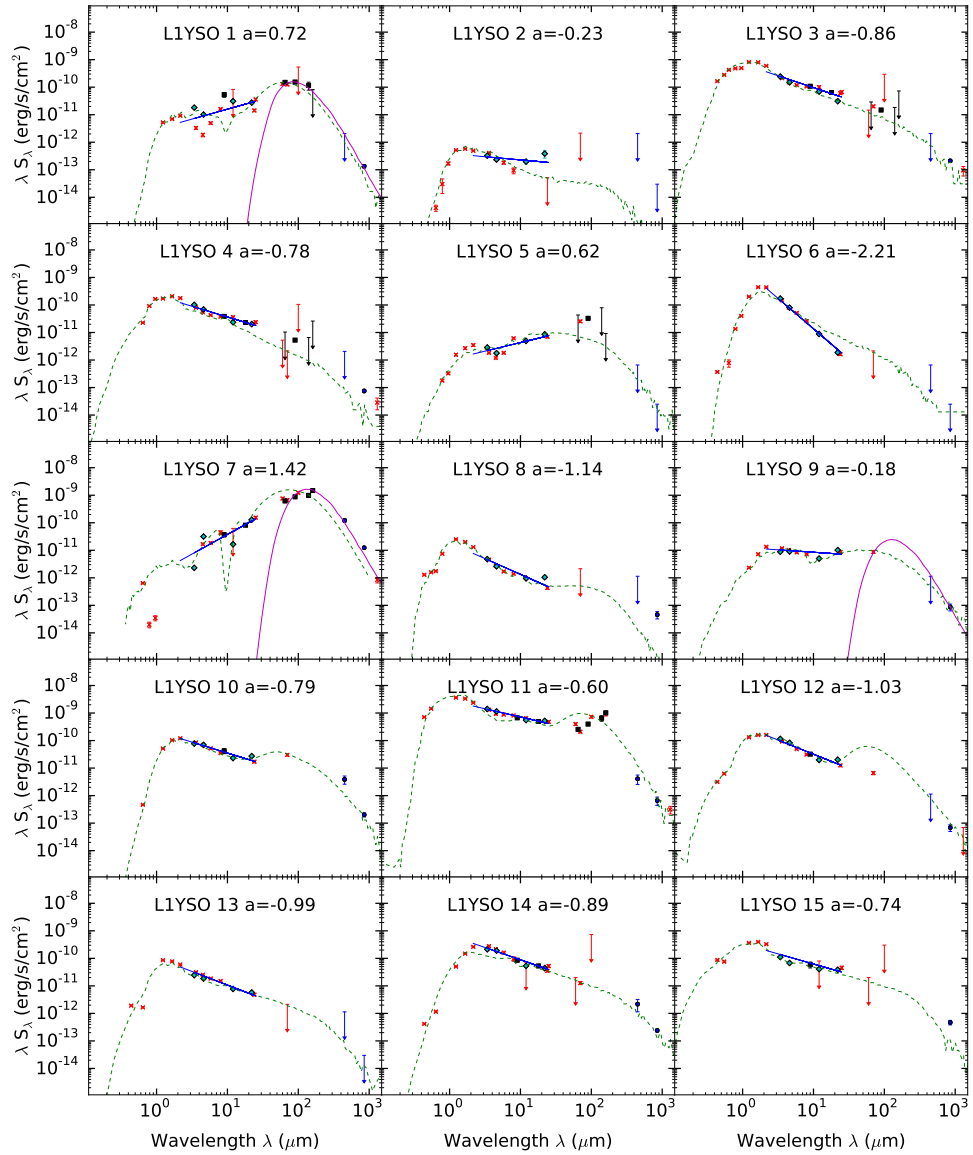

Figure 3.3: SEDs of all YSOs within the SCUBA-2 field of view (see Table 3.1) are presented here. Fits obtained using SED models in Section 3.2.6.3 are plotted as green dashed lines. Additionally, single temperature modified blackbody fits (Section 3.2.5) for protostellar envelopes are plotted as solid pink lines. SCUBA-2 data are plotted as solid blue circles, to distinguish them from the previously available data plotted as red crosses. Data from the AKARI mission (Ishihara et al. 2010; Yamamura et al. 2010), which were also not available for analysis by Merín et al. (2008), are plotted as black squares. The blue diamonds represent WISE fluxes (Cutri et al. 2012). Upper limits to fluxes are shown in the colours of their respective data sets. Values for the mid-infrared spectral index (a) are provided, and the slopes themselves are plotted as blue lines.

the field of view at 850 µm, with the spectral indices determine that two are Class 0/I, one is Class F, and eight are Class II. Non-detections were not confined to more evolved YSOs, as missing YSOs encompass all spectral classes.

Of the 13 sources present in both Merín et al. (2008) and this work, eleven have the same classification in both. Note that the source L1YSO 2 is classified as Class F/II by us, and yet as Class III by Merín et al. (2008). New WISE data for L1YSO 2 have demonstrated increased emission at longer wavelengths (beyond 8 µm) and hence caused the source to be reclassified from Class III to an earlier type. Due to the lack of available long-wavelength fluxes, however, the evolutionary stage of this low-luminosity object is not certain. The other source, the Class 0 L1YSO 7, was classified as a flat-spectrum source in the *Spitzer* paper, which seems unreliable given the steeply rising SED in the mid-infrared regime. The only other Class III YSO identified by *Spitzer* (L1YSO 6) was not detected by SCUBA-2.

These numbers are similar, both in ratio and overall quantity, to those seen in the Ophiuchus North region. That cloud is near the Upper Scorpius region of the Sco-Cen OB association just as Lupus I is near Upper Centaurus-Lupus. In Ophiuchus N, Hatchell et al. (2012) find three Class 0, one Class F, seven Class II and one Class III sources, giving a total of twelve YSO candidates in the region, as part of a *Spitzer* c2d survey. The fraction of Class 0/I sources in both of these regions is much greater than for Lupus III, which has five Class I sources and 56 that are Class II. Additionally Lupus III has approximately the same number of Class III as Class II objects (Merín et al. 2008). This difference suggests that Lupus I is a region with low-efficiency, ongoing star formation akin to Ophiuchus N, and in contrast to Lupus III (although the YSO sample sizes in Lupus I and Ophiuchus N are admittedly small).

The protostellar fraction for Lupus I (including Class 0, I, and F) are also similar to those seen in the main Ophiuchus clouds, as well as Serpens (Dunham et al. 2015), although the total number of YSOs in these clouds is much higher. However, including the four additional YSOs in Merín et al. (2008) (one Class F, one Class II, and two Class IIIs), compared to the entire Dunham et al. (2015) catalogue of YSOs in the Gould Belt, the fraction of Class 0 / I sources is proportionally higher (16 per cent vs. 11 per cent) in Lupus I. Note that while this fraction is higher, the difference is not statistically significant. The

fraction of Class II sources is lower, and with three Class III sources, giving a percentage of 16 per cent (compared to 40 per cent in the whole Gould Belt) the proportion of these more evolved YSOs is much lower (though again, due to low numbers, not statistically significant). The ambiguity of L1YSO 2 means that it is difficult to say whether the number of Class F sources in Lupus I is typical or not.

The higher number of Class 0 / I sources in Lupus I, and lower number of Class III YSOs, suggest that Lupus I is young. The ratio of Class 0 / I to Class III sources in the SCUBA-2 map of Lupus I is 1:1, compared to 0.275 in the Dunham et al. (2015) catalogue. The apparent recent trigger for star formation is consistent with the hypothesis of Gaczkowski et al. (2015) that expanding shells from the Sco-Cen OB association have recently shocked Lupus I into a star-forming event. The number of YSOs in Lupus I (19) is low, so caution should be exercised with this result.

3.2.4 L_{bol} and T_{bol}.

The complete SEDs also allow for calculations of a bolometric luminosity (L_{bol}) and bolometric temperature (T_{bol}) for each source. To calculate the integrals in Equations 1.26 and 1.25, the trapezoidal rule was used to estimate the area under the SED, following Dunham et al. (2013). The trapezoidal rule was only used within the range of the data points, with no extrapolation outside these areas. Table 3.6 lists L_{bol} and T_{bol} for each of the YSOs in Lupus I. Values are calculated both from the observed fluxes of these YSOs, and using the extinction correction detailed in Section 3.2.3. Extinction values used are through the cloud, rather than within the individual sources.

T_{bol} was used to estimate the evolutionary classifications of the YSOs in Lupus I (Section 1.3.4). Classifications for the 15 sources, based on T_{bol} values, largely agree with those derived from spectral indices. An exception is L1YSO 2, which is classed as a flat-spectrum object (instead of Class I). Spectral index values do not distinguish between Class 0 and Class I sources, but T_{bol} can. Therefore, T_{bol} is used to classify L1YSO 7 as a Class 0 protostar, and this is the Class given in Table 3.6. A plot of α against T_{bol}, for both observed and extinction corrected fluxes, can be seen in Figure 3.4.

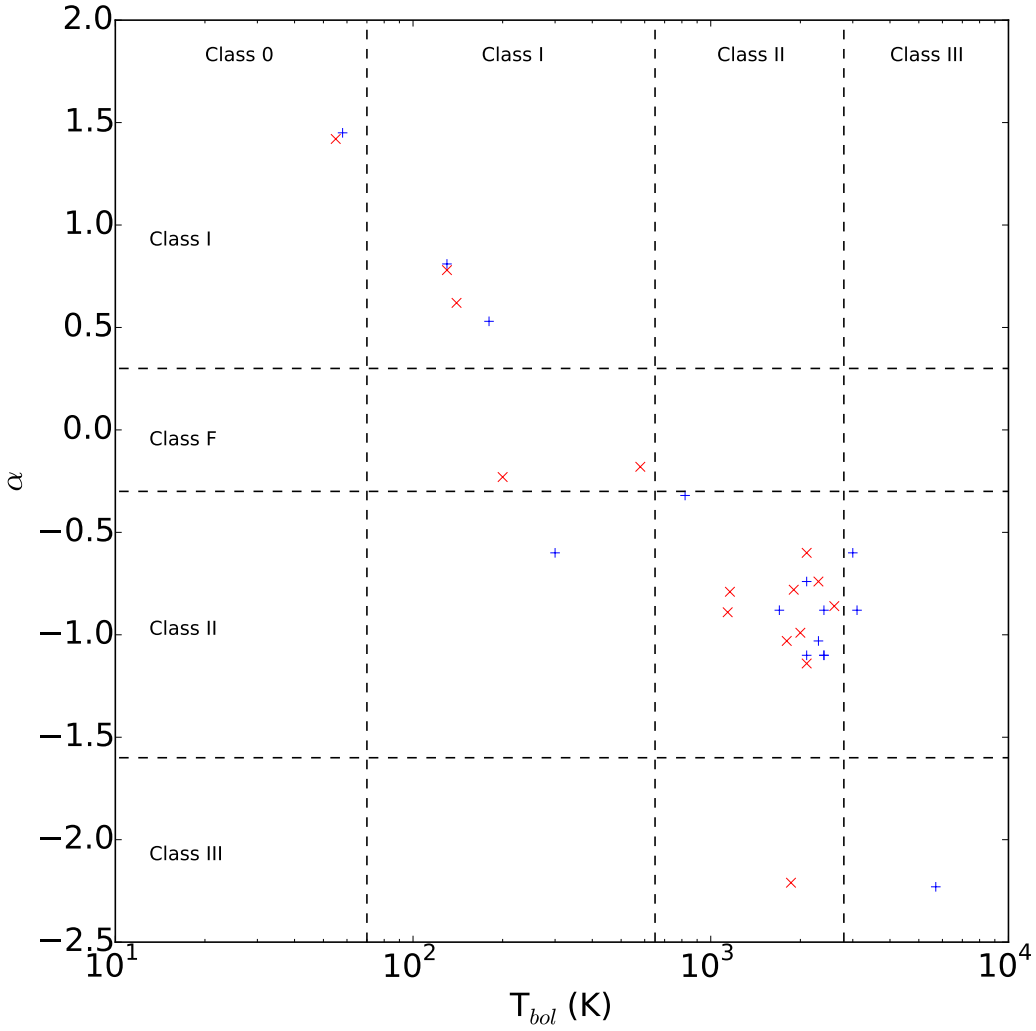

Figure 3.4: Spectral index plotted against bolometric temperature for both observed and extinction corrected fluxes for the 15 YSOs in the SCUBA-2 field of view. Red crosses represent observed fluxes, with blue plus symbols being used for extinction corrected calculations.

Ten of the YSOs in this work are analysed by Dunham et al. (2015); L1YSOs 2, 7, 11, 14 and 15 were not. While it would at first appear that L1YSO 7 was analysed, the YSO at the relevant position has a very low luminosity, and a negative spectral index (-0.21). Therefore, it clearly does not correspond to the relatively bright Class 0 protostar, L1YSO 7. If there is indeed a smaller, more evolved source in close proximity to L1YSO 7, it may have provided a significant contribution towards the short-wavelength fluxes in the SED of this source.

Where the bolometric luminosities in this chapter are not consistent with the Dunham et al. (2015) values, they are generally slightly higher. Similarly, the bolometric temperature values are often slightly lower. These differences are largely due to the inclusion of upper

Table 3.6: Calculated values of both observed and extinction corrected bolometric temperatures and luminosities for YSOs in Lupus I, along with spectral index a values. Evolutionary Classes are specified, and values of extinction used in the corrections are provided.

SSTc2d ID	A_V	Observed			Corrected			YSO Class
		L_{bol} ($L_\odot$)	T_{bol} (K)	a	L_{bol} ($L_\odot$)	T_{bol} (K)	a	
L1YSO 1	0.05	0.42	130	0.78	0.42	130	0.81	I
L1YSO 2	2.8	0.01	200	-0.23	0.01	300	-0.60	F/II
L1YSO 3	1.0	1.4	2600	-0.86	2.0	3100	-0.88	II
L1YSO 4	2.0	0.37	1900	-0.78	0.58	2400	-0.88	II
L1YSO 5	2.9	0.10	140	0.62	0.11	180	0.53	I
L1YSO 6	9.0	0.48	1860	-2.21	6.0	5700	-2.23	III
L1YSO 7	2.9	2.3	55	1.42	2.4	58	1.45	0[1]
L1YSO 8	0.0	0.04	2100	-1.14	0.04	2100	-1.10	II
L1YSO 9	5.7	0.05	580	-0.18	0.06	820	-0.32	F/II
L1YSO 10	5.0	0.27	1160	-0.79	0.48	1700	-0.88	II
L1YSO 11	1.4	8.6	2100	-0.60	12.4	3000	-0.60	II
L1YSO 12	2.5	0.34	1800	-1.03	0.54	2400	-1.10	II
L1YSO 13	2.3	0.14	2000	-0.99	0.22	2400	-1.10	II
L1YSO 14	6.8	0.51	1140[2]	-0.89	1.8	2300	-1.03	II
L1YSO 15	0.8	0.75	2300[2]	-0.74	1.1	2100	-0.74	II

[1] The evolutionary Class for L1YSO 7 was clarified using T_{bol}.
[2] The large IRAS 100 µm upper limit would have served to artificially lower T_{bol}. Therefore, it was removed for these sources.
Note: The presence of upper limits in the far-infrared and submillimetre regimes will serve to artificially lower T_{bol} and similarly raise L_{bol}.

limits to fluxes in these calculations. For sources with several upper limits in the submillimetre regime, the true value will likely lie within the range between the calculations of this work and those of Dunham et al. (2015).

Uncertainties in the calculations of L_{bol} and T_{bol} can be very large, potentially over 50 per cent if there is no available data from MIPS 3 or AKARI at 160 µm (Enoch et al. 2009). Furthermore, Dunham et al. (2013) show that sources lacking far-infrared and submillimetre detections will have L_{bol} underestimated by an average of a factor of 2.5. Sources with such a gap in wavelength coverage include L1YSO 2 and L1YSO 15. Additionally, when upper limits are used, L_{bol} may be calculated as being much higher than in reality, and T_{bol} will be correspondingly too low. IRAS 100 µm upper limit values were not included in the calculations for L1YSOs 14 and 15 because the limits are very large, and would have had an unacceptable effect on the derived values of L_{bol} and T_{bol}.

Using the criterion of Di Francesco et al. (2007), that internal luminosity $L_{\rm int} < 0.1$ $L_\odot$, embedded (i.e. Class 0 / I and potentially Class F) sources with $L_{\rm bol}$ below this value (where $L_{\rm bol} = L_{\rm int} + L_{\rm ext}$) must be Very Low Luminosity Objects (VeLLOs, see also Dunham and Vorobyov 2012). Two of the observed YSOs (2 and 9) are in this group, with another (L1YSO 5) at the border of the classification, having $L_{\rm bol} = 0.11$ $L_\odot$. L1YSOs 2 and 5 were among the four sources in total not detected by SCUBA-2 at either 450 or 850 µm (also including L1YSO 6 and L1YSO 13). Figure 3.2 shows very little emission in the vicinity of these YSOs.

Protostellar sources may still be VeLLOs if $L_{\rm bol} > 0.1$ $L_\odot$ when their luminosities are dominated by the external component. This situation may arise, for example, due to heating by the interstellar radiation field (Dunham et al. 2008). Indeed, the high temperature derived in Section 3.2.5 (below) for L1YSO 1 indicates that it may also be a VeLLO. If so, then up to four Class 0, I and F YSOs in Lupus I would be VeLLOs, a much larger fraction than the 30 per cent found by Dunham et al. (2008). However, due to the low numbers involved, this difference would not be statistically significant. Beyond VeLLOs, six sources have $L_{\rm bol} > L_\odot$ (once corrected for extinction). L1YSO 8 has a luminosity below 0.1 $L_\odot$, but as a Class II (non-embedded) source it cannot be considered as a VeLLO.

L1YSO 11 (HT Lup) is the most luminous YSO, with $L_{\rm bol} = 12.4$ $L_\odot$. This is consistent with the value of $14.49^{+17.44}_{-6.23}$ $L_\odot$ from Prato, Greene, and Simon (2003). Luminosities of the five YSOs (L1YSOs 3, 4, 11, 12, and 15) also analysed in Hughes et al. (1994) often differ between their study and ours. The luminosity estimates of our study should be more accurate, because they were made using a greater number of fluxes. For example, for L1YSO 15, the SCUBA-2 850 µm flux value is the first point on the SED of this source beyond 25 µm.

L1YSOs 7, 10 and 11 do not have any upper limits in the submillimetre regime; all available fluxes are actual detections. Hence luminosity and temperature calculations for these sources will not be affected by this 'upper limit problem'.

3.2.5 Opacity-modified blackbody SED envelope fitting

The main source of submillimetre emission for an early-type YSO (Class 0 / I) is the dust envelope in which it is embedded (Adams, Lada, and Shu 1987), with envelope contribution also likely to be significant for Class F sources. The spectral index calculations in Section 3.2.3 suggest a total of five YSOs in Lupus I are either Class 0, I or F, with only three of these detected by SCUBA-2.

For these three sources, L1YSOs 1, 7, and 9, a modified blackbody fit for the YSO envelope (at long wavelengths) was performed. Such a fit allows estimates of the temperatures and masses of cold protostellar envelopes. A closer view of the envelopes of these YSOs is shown in Figure 3.2.

Single temperature modified blackbody SEDs for each of the sources were produced by iterating over a grid of possible temperatures and masses. Each model was produced using the following relation:

$$S_\nu = \kappa_\nu \cdot \left(\frac{M}{d^2}\right) \cdot B_\nu(T, \nu). \tag{3.3}$$

M/d^2 is treated as a scaling factor (N), with M corresponding to envelope mass and d being the distance to Lupus I (182 pc). $B_\nu(T, \nu)$is the Planck function

$$B_\nu(T, \nu) = \frac{2h\nu^3}{c^2} \frac{1}{e^{\frac{h\nu}{k_B T}} - 1} \tag{3.4}$$

with $B_\nu(T, \nu)$ the specific intensity of light at frequency ν and temperature T. κ_ν is the opacity. Model 5 (thin ice mantles, gas density of 10^6 cm^{-3}) from Ossenkopf and Henning (1994) was used to provide opacity values via linear interpolation. For each YSO, $B_\nu(T, \nu)$, κ_ν, and consequently model flux, were evaluated at every wavelength corresponding to a data point longward of 60 µm. Where only upper limits to the flux were available, the data point was ignored for the purpose of fitting.

A probability was then calculated for each modified blackbody model. To calculate a likelihood for each model, χ^2 was evaluated based on each data point and corresponding

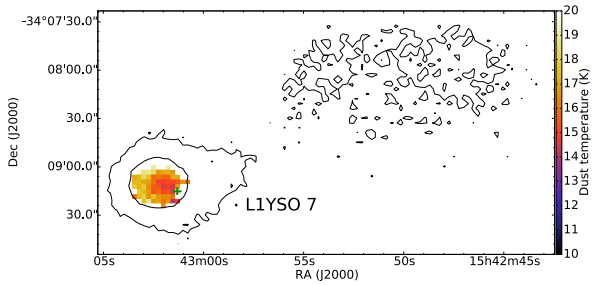

Figure 3.5: SCUBA-2 dust temperature map of the Lupus I molecular cloud NW field. The position of the Class 0 protostar L1YSO 7 is marked with a cross. SCUBA-2 850 µm contours are marked at the 5 and 15 σ level.

model flux. These likelihoods were then combined with simple priors on temperature and mass to produce final probability values.

The prior on mass was the same for all YSOs. Probability was zero outside the interval of 1×10^{-4} to 50 $M_{\odot}$. Within this interval, P(log(M)) was set to be flat, meaning that lower masses would be favoured over higher ones.

For L1YSOs 1 and 9, the temperature prior was set to be flat within the interval of 1 to 50 K, meaning that any temperatures within this range were considered to be equally probable.

A temperature for L1YSO 7 was calculated from the ratio of SCUBA-2 fluxes, assuming a full, opacity-modified Planck function (Reid and Wilson 2005) and a constant dust opacity spectral index, $\beta = 1.8$ (Hatchell et al. 2013). Following the method of Aniano et al. (2011), Pattle et al. (2015) and Rumble et al. (2016), a model beam convolution kernel was used to produce a map of dust temperature for the Class 0 protostar L1YSO 7, shown in Figure 3.5. A mean dust temperature for L1YSO 7 was calculated to be 17±2 K. This mean dust temperature was then used to provide a temperature prior for the model fitting, with probability (within the same temperature interval as the other YSOs) described by a Gaussian distribution. This function was centred at a temperature of 17 K, with a FWHM of 2 K.

Once probabilities were calculated for every model in the grid, mass and temperature were separately marginalised out to produce 1D probability distributions for temperature and mass, respectively. The temperature and mass distributions for the three YSOs are

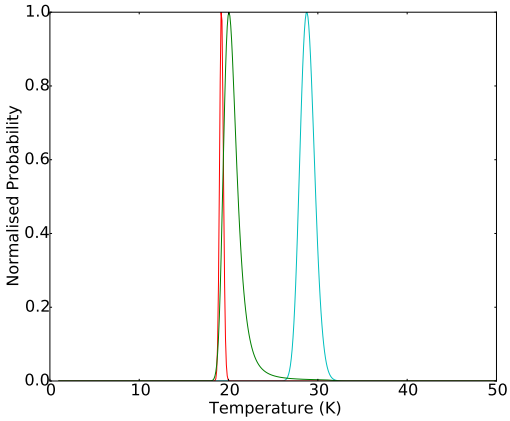

Figure 3.6: Modified blackbody envelope temperature probability distributions for L1YSOs 1 (blue), 7 (red) and 9 (green).

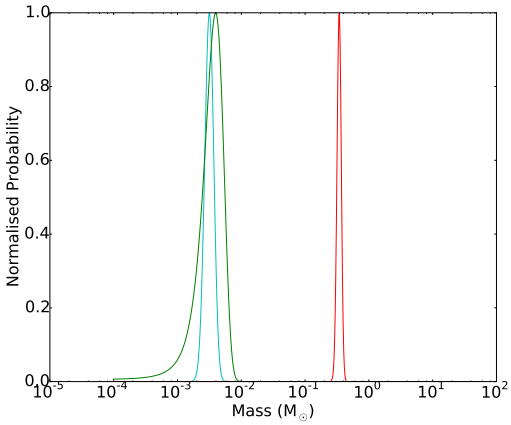

Figure 3.7: Modified blackbody envelope mass probability distributions for L1YSOs 1 (blue), 7 (red) and 9 (green).

plotted in Figure 3.6 and Figure 3.7, respectively. Final temperature and mass values are taken to be the most probable values (following the marginalisation), with uncertainties given as 95 per cent (2 σ) confidence intervals. These values can be found in Table 3.7. Within the specified confidence limits, temperature and mass values are anti-correlated. The modified-blackbody-derived temperature for L1YSO 7 of $19.2^{+0.6}_{-0.3}$ K is consistent with the value of 17 ± 2 K obtained from the dust temperature map. Modified blackbody SEDs corresponding to the most probable temperatures and masses for each YSO are plotted with the relevant SEDs in Figure 3.3, and shown separately as Figure 3.8.

The envelope temperatures derived here, especially for L1YSO 1, are warmer (between ~ 19 and 29 K) than might normally be expected. For example, Kirk, Johnstone,

Table 3.7: YSOs on which modified blackbody SED fits for the envelope were performed, and the values obtained for the temperatures and masses of the envelopes. Uncertainties are the 95 % confidence intervals.

ID	$T_{\rm env}$ (K)	$M_{\rm env}$ 10^{-3} ($M_\odot$)
L1YSO 1	$28.8^{+1.9}_{-1.5}$	$3.2^{+1.1}_{-0.9}$
L1YSO 7	$19.2^{+0.6}_{-0.3}$	350 ± 60
L1YSO 9	$20.1^{+4.4}_{-1.0}$	$4.0^{+2.4}_{-3.3}$

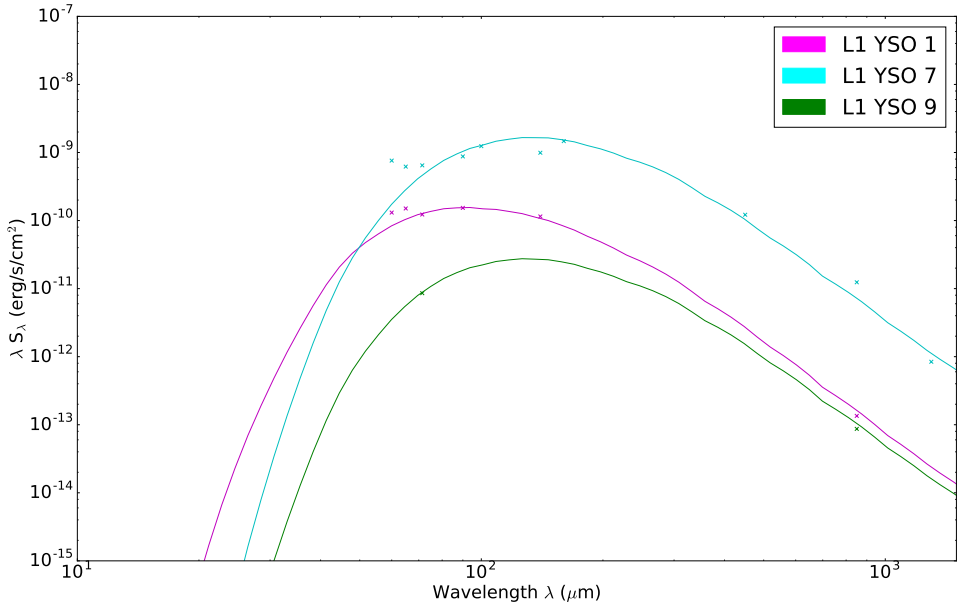

Figure 3.8: Modified blackbody envelope SEDs for L1YSOs 1 (magenta), 7 (cyan) and 9 (green).

and Di Francesco (2006) find that most submillimetre cores in the Perseus molecular cloud are fit by Bonner-Ebert spheres with temperatures of between 10 and 19 K. In addition, Rumble et al. (2015) calculate a mean temperature of ~ 15 K for YSOs in the Serpens MWC 297 region, also consistent with observations of the W40 complex (Rumble et al. 2016).

These higher temperatures, particularly for L1YSO 1, could be caused by the influence of the nearby Sco-Cen OB association, although Pattle et al. (2015) do not find such high temperatures in the nearby region of Ophiuchus. Gaczkowski et al. (2015) argue that Lupus I is affected by the interaction between an HI shell from Upper Scorpius (de Geus 1992) and a wind bubble from Upper Centaurus-Lupus. Such an interaction would have the potential to send shocks through the Lupus I molecular cloud .

The modified blackbody SED peak for L1YSO 1 lies at a shorter wavelength than seen with L1YSO 7, and this has led to the greater envelope temperature calculated by the fitting process. Further submillimetre data points (e.g., from *Herschel*) would clarify whether this 'early' peak is real. Similarly, L1YSO 9 has only two data points in the wavelength regime of the modified blackbody fitting process. Without more data points to fit, there is an increased range of temperatures and masses that produce a good fit to the data. Any future submillimetre observations of this YSO would improve the constraints provided by this fitting process.

At just a few Jupiter masses, the envelopes for L1YSOs 1 and 9 are not large. Given that L1YSO 9 is a Class F source, it would be expected that much of the protostellar envelope has already been accreted and / or dispersed. Therefore, a low envelope mass for this YSO is not surprising. It is possible that what is being seen here as an 'envelope' is actually partially or even wholly a circumstellar disk. The modified blackbody fits here are not able to distinguish between the two, but the models in Section 3.2.6.3 (below) are. The low envelope mass of L1YSO 1 is consistent with detection only being at a signal-to-noise ratio of 2 at 850 µm, as a weak detection indicates a low amount of emitting dust particles. The mass for this YSO envelope is far below the brown dwarf limit, and may even be low enough for a sub-brown dwarf to be forming.

The envelope for L1YSO 7 is much more massive, at 0.35 ± 0.06 $M_{\odot}$. At a typical core to star efficiency of up to 40 per cent (André et al. 2010), this envelope mass suggests that this protostar may go on to form a low mass star with a mass of approximately 0.15 $M_{\odot}$, or perhaps a multiple system with this total mass. Kristensen et al. (2012) used radiative transfer modelling in combination with observed submillimetre fluxes to find a mass for L1YSO 7 of 0.5 $M_{\odot}$, consistent to well within a factor of two.

3.2.6 YSO Properties

3.2.6.1 Protostellar Envelope Masses

For the three sources which had modified blackbody fits performed, the masses as estimated from fitting (listed in Table 3.7) were preferred to those calculated from a single submillimetre flux. Therefore, these are the masses provided in Table 3.8. For the remaining two Class I / F YSOs (2 and 5), which were not detected by SCUBA-2, an upper limit to mass was calculated based on the upper limit to the flux at 850 µm (Table 3.2) using the relation

$$M = \frac{S_{850\mu m} d^2}{\kappa_{\nu(850\mu m)} B_{\nu(850\mu m)}(T)}, \tag{3.5}$$

adapted from Hildebrand (1983). Here, $S_{850\mu m}$ is the total flux density at 850 µm, d is the distance to Lupus I (182^{+7}_{-6} pc) and $B_{\nu(850\mu m)}(T)$ is the Planck function. $\kappa_{\nu(850\mu m)}$ is the dust opacity at 850 µm of 0.012 $cm^2 g^{-1}$, consistent with both model 5 from Ossenkopf and Henning (1994) and the relation of Beckwith et al. (1990) ($\kappa_\nu = 0.1(\nu/10^{12}\text{Hz})^\beta cm^2 g^{-1}$) when dust spectral index $\beta = 2.0$. Note that a decrease in the value of β would lead to smaller masses being calculated.

To calculate the value of the Planck function, a temperature of 15 ± 2 K, consistent with the YSO temperatures from Rumble et al. (2015), was assigned. Note that the assumption of larger temperatures leads to the determination of smaller masses, and vice-versa. The calculated envelope mass limits for L1YSOs 2 and 5 are given in Table 3.8.

While the masses given in Table 3.8 for L1YSOs 1, 7 and 9 were estimated using modified blackbody fitting, the submillimetre (850 µm only) masses were also calculated. The same assumptions, given previously, were used as with the upper limits for L1YSOs 2 and 5. These values are provided, in parentheses, next to the modified-blackbody-derived masses in Table 3.8. The 850 µm masses are larger than the modified blackbody masses, largely because the temperature assumed (15 K) is lower than that found by the fitting.

3.2.6.2 Disk Masses

Typically, circumstellar disks will begin to be the main source of submillimetre continuum emission from YSOs once they reach later stages of evolution and become spectral Class II or Class III objects (Wilking, Lada, and Young 1989). As previously mentioned, Class F YSOs are also likely to have a significant contribution to their submillimetre emission coming from a circumstellar disk. Spectral index values classify twelve YSOs in Lupus I as either Class F, II, or III; nine of these disk sources are detected by SCUBA-2. Of these nine sources, there are eight distinct detections; the L1YSO 3/4 binary is unresolved by SCUBA-2.

The submillimetre continuum flux for point-like sources, with a size less than the effective JCMT beam size of 14.1″ at 850 µm (Dempsey et al. 2013), traces emission from the disks of material around these protostellar objects. At 850 µm, emission from the disk is assumed to be optically thin, meaning that the whole of the disk is probed. Thus, whole-disk masses can be calculated from submillimetre flux (Hildebrand 1983).

The treatment of some YSOs as disk sources contrasts with the methodology of Chapter 5 and Chapter 6, where all objects are treated as though they are protostars with the characteristics of Bonnor-Ebert spheres. To ensure that there is no contadiction in the way that sources are treated, the YSOs these later chapters all have specific indications that they may be protostellar, with objects with no such characteristics being excluded from the analysis. The types of YSOs with no protostellar characteristics (from either spectral index or T_{bol}) are the types being analysed here as disk sources.

The flux values obtained from the 850 µm data, given in Table 3.2, were used to calculate submillimetre continuum disk masses for these sources using Equation 3.5. In this case, T is assumed to be 20 K, in line with the work of Buckle et al. (2015) on the calculation of disk masses. The envelope temperatures calculated in Section 3.2.5 suggest that this dust disk temperature assumption may be too low, however. In general, more compact sources such as disks will be warmer than prestellar cores and protostars. Nevertheless, with the absence of hard evidence of higher disk temperatures, the standard value of $T = 20$ K was maintained. Should the temperature of these disks be higher in reality, this would lead to

a reduction in the calculated disk masses. Moreover disk temperature values will vary radially within the disk (e.g., Andrews and Williams 2005). Thus, disk masses calculated assuming a uniform temperature distribution should be treated as estimates.

Opacity is this time calculated assuming a β value of 1.0 to account for more-evolved dust around these YSOs (Beckwith and Sargent 1991). The evolution of dust from diffuse ISM to protostellar disks can alter grain properties. As β is an optical property of dust grains, it can be expected to decrease with increasing grain growth (see Chen et al. 2016 and references therein). The effect of this change is a reduction in the calculated dust mass for compact sources as compared to more extended envelope structure. The calculated disk masses are listed in Table 3.8. When a source was not detected, an upper limit to the mass was instead calculated, based on the flux upper limits given in Table 3.1.

The distance used in this work of 182^{+7}_{-6} pc is larger than some previous estimates of distance to the region (e.g., 155 ± 8 pc, Lombardi, Lada, and Alves 2008). Masses derived using a distance of 182 pc will be approximately 1.4 times greater than if a distance of 155 pc had been used.

Overall the mean disk mass for the nine Class F and II YSOs detected by SCUBA-2 (the only Class III is not detected) is 5.9 $\times 10^{-3}$ $M_{\odot}$, with values ranging over 1 – 17 $\times 10^{-3}$ $M_{\odot}$. This is within a factor of two of the value of 4.5 $\times 10^{-3}$ $M_{\odot}$ found by Buckle et al. (2015) in L 1495. Mean disk mass calculations will be skewed by the larger disks in the sample. However, they allow us to compare our results to those of Buckle et al. (2015), and they provide a sense of the overall mass in disks in Lupus I relative to the number of objects.

The source L1YSO 11 (with a disk mass of 17 ± 6 $\times 10^{-3}$ $M_{\odot}$) has a disk mass greater than the minimum mass Solar nebula (MMSN). This disk mass is consistent with the value of 15.5 $\times$ 10^{-3}. derived from 1300 µm flux by Nuernberger, Chini, and Zinnecker (1997). This YSO is also the most luminous of the sample, with a bolometric luminosity of 12.4 $L_{\odot}$ (Table 3.6). The bright emission is visible in Figure 3.2. This star is the Herbig Ae/Be star HT Lup (e.g., Kukarkin et al. 1971; Cutri et al. 2003), and demonstrates that one of the most massive and luminous stars in this low-mass region also has a potentially planet-forming disk of comparable mass to that of the young Solar System.

Table 3.8: Envelope and / or disk masses for the YSOs in Lupus I, calculated from 850 µm flux or modified blackbody fitting (where specified).

SSTc2d ID	Envelope Mass 10^{-3} $M_\odot$	Disk Mass 10^{-3} $M_\odot$
L1YSO 1[1]	$3.2^{+1.1}_{-0.9}$ (16 ± 3)	...
L1YSO 2	≤ 3.6	≤ 0.9
L1YSO 3	...	7.5 ± 0.8[2]
L1YSO 4	...	7.5 ± 0.8[2]
L1YSO 5	≤ 2.9	...
L1YSO 6	...	≤ 0.8
L1YSO 7[1]	350 ± 60 (1500 ± 200)	...
L1YSO 8	...	1.2 ± 0.4
L1YSO 9[1]	$4.0^{+2.4}_{-3.3}$ (11 ± 3)	2.3 ± 0.6
L1YSO 10	...	5.3 ± 0.9
L1YSO 11	...	17 ± 6
L1YSO 12	...	1.8 ± 0.5
L1YSO 13	...	≤ 0.9
L1YSO 14	...	6.3 ± 0.7
L1YSO 15	...	12 ± 2

[2] These sources are not separately resolved by SCUBA-2, so the mass listed for both is the combined mass of the system.
[1] The envelope masses provided for these sources were calculated in Section 3.2.5. Values in parentheses were calculated from 850 µm flux.
Note: Envelope masses are provided for Class 0, I and F YSOs, with disk masses being calculated for Class F, II and III YSOs. In reality the masses for a Class F YSO would be expected to be a combination of the two values.

This single detection of a MMSN disk in Lupus I is consistent with the L1495 region of Taurus observed by Buckle et al. (2015). There, 20 YSOs were detected by SCUBA-2, and of these two have disk masses (at T = 20 K) greater than the MMSN.

Additionally, L1YSO 15 has a disk mass of 12 ± 2 $\times 10^{-3}$ $M_\odot$. This matches the 1300 µm value of 12.2 $\times 10^{-3}$ $M_\odot$ from Nuernberger, Chini, and Zinnecker (1997) and means that this YSO also has a disk with a mass of approximately the MMSN. The binary of L1YSOs 3 and 4 is found to have a total disk mass of 7.5 ± 0.8 $\times 10^{-3}$ $M_\odot$, similar to the value of 6.4 $\times 10^{-3}$ $M_\odot$ found by Nuernberger, Chini, and Zinnecker (1997). This disk mass should be taken as an estimate for the combined disk mass of the system, acting as an upper bound for each individual YSO. As with its envelope mass in Section 3.2.6.1, the

disk mass for the Flat-spectrum L1YSO 9 should be treated as an upper limit. This YSO could be either a true protostar, or a disk obscured behind other extended material.

Following Buckle et al. (2015), disk masses were calculated from fluxes extracted at the literature positions of YSOs. Therefore, it is possible for smaller-scale cloud structure to be misidentified as disk emission at known YSO locations. Positive emission is found near the position of L1YSO 8, but away from any YSO or core structure identified by SCUBA-2. Additionally, there is no obvious visual sign of a disk at this position in the SCUBA-2 maps. This means that the possibility of cloud structure contaminating disk signal for L1YSO 8 cannot be discounted. The detection of L1YSO 12 appears consistent with being faint disk emission, but again the potential contribution of ambient cloud signal is not entirely ruled out. It should be remembered, however, that the aperture photometry at these positions included a background subtraction (using an annulus) with the express purpose of removing ambient signal from the detection.

3.2.6.3 Model SEDs

Robitaille et al. (2006) presented a grid of over 200,000 model SEDs computed via radiative transfer, which cover a wide range of disk and envelope masses as well as stages of evolution. A Python fitting tool[1], outlined in Robitaille et al. (2007), was used to fit models from the grid to the SED of each of the *Spitzer*-identified YSOs. The disk and envelope masses of well-fitting models were compared to those derived from the SCUBA-2 data (presented in Table 3.8), and constraints on interstellar extinction values for each YSO were sought. Furthermore, the fitting process revealed 'gaps' in the model grid, by finding SEDs that were not well-fit by any models.

These models have been widely used to fit data in the mid-infrared regime (e.g., Simpson et al. 2012; Azimlu, Martínez-Galarza, and Muench 2015) but fits involving submillimetre data have tended to focus on more distant, massive YSOs (e.g., Mottram et al. 2011; Faimali et al. 2012). Buckle et al. (2015) fit these models to data including SCUBA-2 fluxes but this is only performed on two YSOs. Moreover, for one of the YSOs, the model

1. url: http://sedfitter.readthedocs.org/en/stable/

is a poor fit in the region of the SCUBA-2 data.

Convolved model fluxes were produced for each wavelength filter for which observed data were available. Many of these model fluxes were already available within the fitting tool, including *Spitzer*, 2MASS and IRAS. However, model fluxes had to be computed for the WISE, AKARI and SCUBA-2 filters. WISE filter profiles (Wright et al. 2010) are available online[2], with wavelength and relative system response (RSR) provided. AKARI IRC filter profiles are shown in Onaka et al. (2007), with FIS profiles given in Kawada et al. (2007); RSRs for all filters are also available online[3]. SCUBA-2 filter profiles were available from the JCMT staff. It should be noted that in order to produce convolved flux files with the fitting tool, wavelengths in the input files must be in ascending order. This is not specified in the SED fitter documentation.

Data values, including uncertainties, were read in as fluxes, magnitudes or limits. Where a limit was used a confidence interval was specified, which for the fitting of these models was set to 3 σ (99.7 per cent). This can allow an SED to have a greater flux value than the upper limit at a certain wavelength, if doing so produces the best fit to the data. However, this is not likely to happen and is indeed not seen with any of the best-fit models in this analysis.

Extinction was also included in the fitting process, with a range of $0 \leq A_{\mathrm{v}} \leq 7.39$. This range was chosen based on possible extinction values of up to the maximum value for Lupus I given in Cambrésy (1999). The range of possible distances was 182^{+7}_{-6} pc, consistent with the other analyses in this study.

A selection of best-fitting models was initially found by minimising χ^2. For each YSO, every model with a χ^2 per point value of less than 100 was initially selected. If no model fulfilled this criterion, then the overall best-fitting model for the YSO was still chosen, though parameters were not considered reliable. The best-fit model SEDs for each source, according to the least-squares fitting process, are shown over-plotted on the SEDs in Figure 3.3. The exact model numbers for each source can be found in Table 3.9.

2. url: http://wise2.ipac.caltech.edu/docs/release/prelim/expsup/
3. url: http://svo2.cab.inta-csic.es/svo/theory/fps3/

Once a selection of models satisfying the χ^2 criterion was obtained, further statistical tests were run on them to exclude models that were not good fits, despite their (relatively) low χ^2 value.

First, a Kolmogorov-Smirnov (KS) test was run on the residuals between the data and model fluxes at each filter's central wavelength. The KS test compares a sample with a reference probability distribution, with the null hypothesis being that the sample was drawn from the reference distribution. If the probability of the sample being drawn from the reference distribution is below a specified confidence interval, the null hypothesis is rejected.

To calculate residuals, convolved filter fluxes for each model were interpolated to correspond to the correct wavelength, and had distance and extinction corrections applied according to the values found in the fitting procedure. Residuals were fractional, with $R_\lambda = (S_{\rm data} - S_{\rm model})/S_{\rm model}$. These fractional residuals were then normalised as $R_\lambda/R_{\rm rms}$, where $R_{\rm rms}$ is the rms of all residual values.

The distribution of normalised residuals was tested against a normal distribution with a mean of 0 and standard deviation of 1. For a model to be a good fit, any deviations between it and the data should be due to random fluctuations. Therefore, a failure to be consistent with a normal distribution is a mark of a poor fit. Consequently, a model was rejected if the distribution of normalised residuals failed a K-S test at the 10 % level. A level of 10 % is more permissive than is used in later chapters (e.g., Chapter 6 uses a level of 3σ / 99.7 % in significance tests.). This allows for a wider range of models to be examined, while still excluding those models that fit the data very poorly. Passing this threshold is not automatically taken to mean that the model accurately describes the observed YSO. In contrast, a 3σ threshold in Chapter 6 is directly used to determine whether the differences between distributions of objects are statistically significant.

An example of the utility of the K-S test can be seen in the 'best-fit' model of L1YSO 8, seen in Figure 3.3. The χ^2 per point value for this model's fit to the data is low, so it is not rejected initially. However, the model is substantially underestimating flux in the sub-mm regime (by more than an order of magnitude compared to the data at 850 μm).

The strength of this deviation means that the model fluxes are very unlikely to have come from the same distribution as the data, therefore the K-S test enables this model, and others like it, to be rejected.

The second test was a Wald-Wolfowitz runs test. This tests explores whether a model can be rejected due to having too many model points above or below the data in sequence (a run). If a model is a good fit, the scatter of data points above and below the model values should be random. A very low number of runs is inconsistent with random scatter, and indicates that a model is not a good fit. Specifically, a model was considered to have failed the runs test if there was less than a 10 per cent chance of the observed number of runs being consistent with being drawn from a normal distribution about the expected number of runs.

After running these tests, a final set of well-fitting models was available for analysis (shown in Table 3.10). Overall, seven YSOs have at least one well-fitting model, and the remaining eight do not. Of the YSOs fit by well-fitting models, L1YSOs 1 and 11 are only well-fit by one model. The remaining five YSOs (9, 10, 12, 13, and 15) are fit by more than one model, with L1YSO 10 fit by 276 models in total. The best-fitting SEDs for all YSOs are plotted in Figure 3.3.

For YSOs with multiple well-fitting models, constraints on disk mass, envelope mass, and extinction were sought. Extinction was constrained for all five of these YSOs, with the lowest extinction being found for L1YSO 15 ($A_V = 0.8 \pm 0.1$). Values for the other six YSOs, also detailed in Table 3.10, range between $A_V = 2.3$ and $A_V = 5.7$. Uncertainties in A_V, given in Table 3.10, are the standard deviation of extinction values from the mean for all well-fitting models divided by the number of models. Uncertainties are only given when standard deviations are less than the mean value. The lower extinction for L1YSO 15 coincides with the relatively off-cloud location of this source; the other four YSOs lie on areas of extended emission visible on the 850 μm map.

Extinction values for the four well-fit Class II sources (L1YSOs 10, 11, 12, and 13) are also provided by Merín et al. (2008). The extinction values derived from the model fitting are consistent with these values for YSOs 11, 12, and 13. This is particularly the case

for L1YSO 11, with values of A_v = 1.5 and A_v = 1.4 respectively. Additionally, Hughes et al. (1994) also derive an extinction for this YSO of A_v = 1.45. The value calculated for L1YSO 10 is higher than that derived from the model fitting, at A_v = 10.0. However, the model fitting did not produce a higher extinction value for L1YSO 10 even when values of up to A_v = 10.0 were allowed.

Disk and envelope masses for the well-fitting models are also given in Table 3.10. Disk masses are constrained for L1YSOs 13 and 15, with values of 2.21 ± 0.43 and 9.56 ± 0.96 M_{Jup}, respectively. Compared to these YSOs, L1YSOs 9, 10, and 12 have many more corresponding fits. The groups of models for these three YSOs gives disk mass ranges of < 0.01–45, 0.01–70 and 0.36–33 $\times 10^{-3} M_\odot$, respectively.

Some disk masses are consistent with those calculated from the 850 µm data in Section 3.2.6.2, while others are not. Two Class II YSOs (13 and 15) do have constrained mass ranges from models. For L1YSO 13 the mean model disk mass is too large to be consistent with the model being a non-detection at 850 µm. For L1YSO 15, the range of 9.6 ± 1.0 $\times 10^{-3}$ $M_\odot$ is consistent with the value of 12 ± 2 $\times 10^{-3}$ $M_\odot$ derived from the SCUBA-2 data.

Envelope mass constraints for the Class II L1YSOs 13 and 15 indicate that if there is any envelope left, it should be very small ($\ll$ 1 Jupiter mass). For L1YSOs 9 (Class F), 10 (Class II) and 12 (Class II), there is again a spread of possible values from models, with envelope masses ranging between < 0.01–0.14, < 0.01–0.41 and < 0.01 $M_\odot$, respectively. YSO 9 is classified as Class F, and could therefore still have a significant protostellar envelope. However, L1YSO 10 (Class II) apparently has the largest model envelope mass. This result suggests that, while there are many well-fitting models for L1YSO 10, the fitting process is still unable to constrain the origin of fluxes in the submillimetre wavelength regime. It is unsurprising that uncertainties are large for these remnant envelopes, as they fall around or below the SCUBA-2 mass sensitivity limit of approximately 3.7×10^{-3} $M_\odot$ at 182 pc (Holland et al. 2013).

A lack of constraint across both disk and envelope masses demonstrates that even for a single source, there can be significant variations in the properties of models that provide

a 'good' fit to the data. It is therefore very difficult to derive reliable dust mass estimates from this SED fitting method alone. Spatial information on specific sources could help rule out some models. For example, a YSO observed as being a point source in Lupus I (at 182 pc) is unlikely to have a massive circumstellar envelope.

Furthermore, the envelope geometry of the models in the grid is dominated by free-fall rotational collapse. The resulting envelope structure may be less applicable to the outer regions of envelopes, where turbulence, magnetism, and other conditions may be more important and which would be expected to show strong emission in the sub-mm regime. Also, the envelope models could be missing the colder, outer regions because of the way the outer radius is defined. In the models, the outer envelope radius can be at an absolute maximum four times the radius at which the optically thin radiative equilibrium temperature falls to 30 K. Often, however, it will be substantially less than this, being sampled from within the range of $4R_0$ to $R_0/4$.

Although the model grid contains over 20,000 modelled YSOs (each at 10 inclinations), the observed SEDs for some sources are not realised in the grid. All but one model in the fitting of L1YSO 2 was unable to fit the data at all, suggesting gaps in the available models at this low-mass, low-luminosity extreme. Additionally, no model was able to fit the shorter wavelength fluxes of L1YSO 8 while still having a massive enough disk to produce the signal observed by SCUBA-2 at 850 µm. Such discrepancies are not exclusive to these two YSOs; rather, they provide effective examples.

A lack of models consistent with the SEDs of certain YSOs could also be caused by contamination in some of the larger-beam fluxes (e.g., IRAS). In such a case, fluxes could contain signal not corresponding to the specific YSO in question. This would move the shape of the SED away from that of an isolated YSO, and therefore away from the SEDs in the model grid.

It is possible that L1YSO 8 is being fit very well. As mentioned in Section 3.2.6.2, 850 µm flux for L1YSO 8 may be being confused with or contaminated by ambient cloud emission. This would have the effect of increasing the sub-mm signal beyond that truly emitted by the underlying YSO.

In many cases, only one or two fluxes were available in the sub-mm regime for the YSOs in this work, while coverage in the mid-infrared regime is far more comprehensive. Since the model fitting is done via a least-squares method, short wavelength fluxes may be constraining fits too much, with long-wavelength accuracy sacrificed as a result.

There is also the possibility that some excess at long wavelengths in the SED of L1YSO 11 is being caused by a nearby companion object. HT Lup is a triple-star system (Ghez et al. 1997) consisting of two close stars separated by 0.126″, with an A:B flux ratio of 0.16, and a third star 2.808″ away with an A:C flux ratio of 0.07. (Correia et al. 2006). Prato, Greene, and Simon (2003) find masses of the A, B and C components to be 2.5, 1.1 and 0.1 $M_{\odot}$ respectively.

HT Lup A and B are too close to resolve even in the mid-infrared, being much closer than the diffraction-limited resolution of IRAC. However the separation of A and C is great enough so as to be resolvable with *Spitzer* (with angular resolution < 2″) but not by longer-wavelength surveys (e.g., SCUBA-2 with a 9″ beam size at 450 µm. Therefore this companion object could be contributing some flux to the overall observed values for HT Lup at longer wavelengths. Given the contrast in luminosity between A + B and C, this companion would have to be younger than the main binary in order to produce sufficient long-wavelength flux.

Among the simply 'best-fitting' models for the YSOs, disk masses from the models are usually higher than those from single temperature fits. The models are able to characterise disks at multiple temperatures, which allows mass to be added at higher temperatures without significantly affecting the emission seen at 850 µm. It is also possible that variations in the dust model chosen (the SED models use a combination of Kim, Martin, and Hendry 1994 and Whitney et al. 2003) and the value of the opacity spectral index β have caused these discrepancies.

The exception to this is L1YSO 8. As previously discussed, the model fitting underestimates flux at long wavelengths for this source, leading to a corresponding decrease in dust mass. However, it should be noted that attempts to derive YSO dust masses from individual models are not the intended use of the SED fitter. In addition, the models were

Table 3.9: *Spitzer*-identified YSOs, along with the additional IRAS sources, and their corresponding best-fit models from Robitaille et al. (2006) and Robitaille et al. (2007). Where possible, a best-fitting model is one that passed all tests and has the lowest χ^2 value. Where no models for a particular YSO passed all tests, the best-fit models from χ^2 only are given. Values are given for the masses (from these models) of the YSO disks and envelopes.

ID	Best-fit Model #	χ^{2a}	$M_{\rm disk}{}^{b}$ ($10^{-3}M_\odot$)	$M_{\rm env}{}^{b}$ ($10^{-3}M_\odot$)	A_V
L1YSO 1	3015615_6	94.3	0.79	30	0.1
L1YSO 2	3010945_1[c]	19	0.82	0.19	2.8
L1YSO 3	3013816_7[c]	21	5.2	...	2.1
L1YSO 4	3009154_5[c]	65	5.0	...	1.3
L1YSO 5	3006636_2[c]	71	1.9	...	2.7
L1YSO 6	3014557_2[c]	450	5.7	...	6.1
L1YSO 7	3010808_9[c]	300	0.35	740	0.0
L1YSO 8	3006431_4[c]	62	0.64	...	0.2
L1YSO 9	3017650_2	27	11	0.42	2.1
L1YSO 10	3007290_5	13	11	0.31	7.2
L1YSO 11	3011911_9	290	84	84	1.4
L1YSO 12	3010550_3	30	7.9	1.8	0.1
L1YSO 13	3002284_10	93	2.2	...	2.3
L1YSO 14	3011667_5[c]	220	21	...	6.8
L1YSO 15	3015916_10	81	7.8	0.31	0.6

[a] χ^2 values are given per data point.
[b] Values are left blank if less than 0.01 Jupiter masses.
[c] Parameters should be considered unreliable, as these best-fitting models were not considered 'good' fits .

Table 3.10: Parameters for the YSOs for which at least one model was well-fitting, along with the total number of these models. Parameters are given as the mean values across all well-fitting models.

ID	N_{models}	$M_{\rm disk}$ ($10^{-3}M_\odot$)	$M_{\rm env}$ ($10^{-3}M_\odot$)	A_V
L1YSO 1	1	0.79	30	0.05
L1YSO 9	20	6.0 (0.01-45)	4.8 (0.01-14.2)	5.7 ± 0.6
L1YSO 10	276	3.6 (0.01-70)	36 (0.01-405)	5.0 ± 0.1
L1YSO 11	1	84	84	1.4
L1YSO 12	53	6.8 (0.36-33)	1.3 (0.01-10.6)	2.5 ± 0.2
L1YSO 13	5	2.2 (1.29-3.24)	0.02 (0.01-0.04)	2.3 ± 0.2
L1YSO 15	2	9.6 (8.20-10.92)	< 0.01	0.8 ± 0.1

Note: Uncertainties are only provided for extinction values, otherwise parameter ranges are shown in parentheses.

primarily created to constrain shorter wavelength data, with a reduced capacity to fit to submillimetre data.

The envelope mass of the best-fit model to L1YSO 7 of 0.74 $M_\odot$ (as given in Table 3.9) is greater than the value of 0.35 ± 0.06 $M_\odot$ calculated from the modified blackbody SED fitting, but is still consistent within a factor of two. L1YSO 9 was well-fit by more than one model, with a mean envelope mass across all well-fitting models (Table 3.10) of 4.8 $\times 10^{-3}$ $M_\odot$. Though this appears to be consistent with the 850 µm mass, the model envelope masses were spread over several orders or magnitude, so the mean is not a well-constrained quantity.

The envelope mass of the single well-fitting model for L1YSO 1 is, at 30 $\times 10^{-3}$ $M_\odot$, too large to be consistent with the modified blackbody SED mass. The temperature of this source derived from the modified blackbody fitting is high (~ 29 K, Table 3.7). A decrease in this temperature (possible if, e.g., the AKARI fluxes are unreliable) could increase the calculated mass value by enough to allow for consistency with the well-fitting model. Additionally, the main constraint on the envelope masses for L1YSO 1 is the SCUBA-2 850 µm flux, which is close to the detection limit and hence has correspondingly high uncertainties.

Forbrich et al. (2010) use the Robitaille et al. (2006) models to constrain protostellar evolutionary stages in the NGC 2264 and IC 348 clusters. Sources able to be fit by models with an envelope mass of less than 10^{-3} $M_\odot$ are considered to be Class II sources, rather than protostellar. Looking at the best-fit models for the Lupus I YSOs in Table 3.9, the envelope mass of L1YSO 9 (0.42 $\times 10^{-3}$ $M_\odot$) lies below this threshold. However, there is a degeneracy between models which fit the SED. The average mass across all well-fitting models for this YSO is large enough for this source to be considered protostellar. Moreover, an envelope mass of 0.084 $M_\odot$ is predicted for the Class II source L1YSO 11. This may be an effect of the aperture contamination from nearby extended emission discussed in Section 3.2.2. All envelope sources are small enough that they will not be affected by spatial filtering in the SCUBA-2 data reduction, as none are larger than 2.5′.

Following on from the SED comparison, when the models underestimate intensity

as compared to SCUBA-2 in the submillimetre regime this has the effect of modelling the envelope as less massive than it actually is. This helps explain why the model masses for IRAS 15398-3359 and J154457.9-342340 are too low. Moreover, the other source with underestimated model mass (J154517.4-341829) is seen in the SCUBA-2 maps to be embedded within a region of non-uniform extended emission. This would lead to an increased photometric intensity manifesting itself as a larger mass value.

The model for the source J153848.2-344041 has a mass far larger than is derived from SCUBA-2. It is also (going by spectral index) the next-least evolved source. It would be expected for such a source that envelope emission would dominate (Wilking, Lada, and Young 1989). Thus, treating largely cold envelope emission as relatively warmer emission (for calculating a SCUBA-2 mass) would more significantly underestimate mass for this source than with more evolved ones. As the model from Robitaille et al. (2006) treats most mass as contained in a protostellar envelope, the discrepancy here would be expected to be larger than for other, more evolved YSOs observed as point sources.

Another large variation comes for IRAS 15422-3414 which, as mentioned previously, had its envelope signal overestimated by the model. Thus it would also be expected that the model envelope mass would be significantly larger than the SCUBA-2 mass. At approximately 6.5 times greater, that is indeed the case. Additionally, the source J154506.3-341738 is a relatively young, flat spectrum source. This would be expected to have more envelope contribution than a typical Class II source, leading to a larger mass ratio between model and SCUBA-2. Again, this is observed to be the case (with a value of 5.5).

Across the rest of the range of Class II sources detected by SCUBA-2, values for the ratio between the model mass to SCUBA-2 mass vary between $\sim$ 1.65 to 3.5. This would seem to be indicative of a systematic discrepancy between the models of Robitaille et al. 2006 and submillimetre continuum observations of approximately a factor of 2 (in favour of the models). This is the discrepancy even when the treatment of submillimetre emission as disk-like should be correct (i.e. for more evolved Class II sources). This may be because the assumed temperature for disks used to calculate continuum mass (20 K) is too low. Indeed, the fits to protostellar envelopes (Section 3.2.5) show that this temperature is appropriate for less evolved and presumably cooler YSOs.

3.2.7 Star Formation Rate

A previous estimate of the star formation rate (SFR) in Lupus I was 3.25 ± 1.8 $M_\odot$ Myr^{-1} (Heiderman et al. 2010). This SFR has been updated based on a revised YSO count and recent mass and lifetime estimates. For example, Gaczkowski et al. (2015) derive masses specifically for B228 (the main filamentary ridge of Lupus I) from *Planck*, *Herschel* and LABOCA (Siringo et al. 2009) observations of ∼ 170 $M_\odot$. This mass is modified to 250 ± 20 $M_\odot$ due to the assumed distance in this work of 182 pc.

Galli et al. (2015) find an average disk lifetime in Lupus (specifically for Classical T-Tauri Stars, CTTS, before they transition to Weak-line T-Tauri Stars) of $3\times10^6(M_\star/M_\odot)^{0.55\pm0.1}$ years. Assuming an average stellar mass of 0.5 ± 0.1 $M_\odot$ as used by Heiderman et al. (2010) (consistent with the initial mass function of Chabrier 2003 and constrained by the mass distribution of YSOs observed by *Spitzer* in Spezzi et al. 2008), an average lifetime of 2.1 ± 0.3 Myr is expected.

A total of 11 *Spitzer* YSOs lie within the LABOCA field of view (B228). Adding L1YSOs 14 and 15 to this number means that there are a total of 13 known YSOs on the ridge. Of these YSOs, 11 are Class II (CTTS) or Class F. Therefore the star formation rate for B228, using these updated quantities, is 2.6 ± 0.6 $M_\odot Myr^{-1}$.

Compared to the SFRs in Heiderman et al. (2010), this represents a lower SFR than is seen in Lupus III, V, and VI, but it is similar to the SFR of Lupus IV. Chamaeleon I is similarly massive to Lupus I, but has a higher star formation rate (22.2 ± 12 $M_\odot$ Myr^{-1}).

More massive regions such as Ophiuchus (72.5 ± 39 $M_\odot$ Myr^{-1}), and Perseus (96.2 ± 52 $M_\odot$ Myr^{-1}), have much higher star formation rates. However, Chamaeleon III, which is more massive than Lupus I, has a lower SFR of 1.00 ± 0.54 $M_\odot$ Myr^{-1}.

Overall, this indicates that, while the SFR of Lupus I is fairly low compared to other Gould Belt clouds, it is not low enough so as to be unusual.

Using the age of the oldest YSO in B228 for which an age has been calculated (3.16 ± 1.09×10^6 years for L1YSO 15, Hughes et al. 1994) as an approximation of cloud lifetime,

this then gives a star formation efficiency of 3.3 ± 1.4 per cent. Note that this is the efficiency of the main ridge of Lupus I, and not the entire cloud.

3.3 Cores

So far this work has focused on the YSOs of Lupus I. The extended submillimetre structures in the cloud, including starless, prestellar, and protostellar cores, are examined in the following analyses.

3.3.1 Identification and Masses

3.3.1.1 Core extraction

Protostars and prestellar cores do not have sharply defined boundaries, but rather will tend to decrease in density from central areas of peak emission until they merge with their natal cloud. Thus, a method is required which can delineate effective boundaries for individual starless and star-forming cores.

The Starlink CUPID package[3] (Berry et al. 2013) allows for the identification of extended cores in SCUBA-2 dust continuum emission maps. In order to identify the bounds of extended objects within the Lupus I map, the FellWalker algorithm (Berry 2015) was used. This method treats cores as individual areas of emission which share a common significant peak. For a separate core to be identified, it must contain emission at a minimum specified value, which can act as the peak. The FellWalker algorithm has been used previously, by Rumble et al. (2015) for the identification and characterisation of cores in the Serpens MWC 297 region, and Kirk et al. (2016) in Orion B.

FellWalker is a gradient-tracing algorithm; it proceeds iteratively from a low value in the map up to a peak data value. FellWalker attempts to associate each pixel above a specified threshold with a nearby significant peak by moving to an adjacent pixel with a higher value. For the identification of cores in the 850 µm map of Lupus I, the low value

3. Available from the Astrophysics Source Code Library, record ascl:1311.017

was specified to be a pixel (9 arcsec^2) at a level of at least 0.12 mJy/arcsec^2 (2 σ RMS in the E and SW field and 2.4 σ in the NW field). Peaks had to have a minimum value of 0.3 mJy/arcsec^2 (i.e., a 5 σ detection in the SW and E fields and 6 σ in the NW field) for them to be considered as the central point of a core. Any emission at a level lower than 0.12 mJy/arcsec^2 was not considered as part of a core, and was ignored. Unlike in Chapter 5, the source extraction was not implemented on SNR maps, though the end result here is the same. As Lupus I is a single region, specific noise levels from the map were able to be used, as the source finding did not also have to work on other regions with different noise levels.

Additionally, for pixels to be considered as part of a core, it was specified that they must be within 4 pixels of a pixel already included in a core-like structure. To avoid noisy pixels and prevent undesired levels of fragmentation, a minimum core size of 15 pixels was enforced, corresponding to a size of 135 arcsec^2. Overall, the non-default parameters used were: 'MaxJump=4', 'MinDip=0.12', 'Minheight=0.3', 'MinPix=15', 'FwhmBeam=2' and 'MaxBad=0.5'.

All pixels considered as part of the same core were assigned the same index value within a data mask, starting at one for the first area identified by the algorithm. Candidates located in the PONG edge regions of the map, where local noise is higher than the global noise used in FellWalker, were rejected by visual inspection. This strategy left a total of 14 separate objects corresponding to true signal. Some of these, identified in relative isolation, are disk detections corresponding with the aperture photometry measurements already taken. Therefore, two objects were excluded on the basis that they had already been identified, characterised and analysed as disk-like sources (The unresolved binary of L1YSOs 3 & 4, and L1YSO 15). Both are isolated point sources, with no extended structure evident.

To extract flux for the twelve identified cores at 450 µm, the core boundaries calculated for the 850 µm map were transposed over to the 450 µm map, and the flux within the boundaries of each identified core was measured. The position of the peak at 850 µm was used as the sky position of the core. The total flux of the core was then the sum of the flux at each pixel marked as part of the core footprint. Uncertainties were calculated

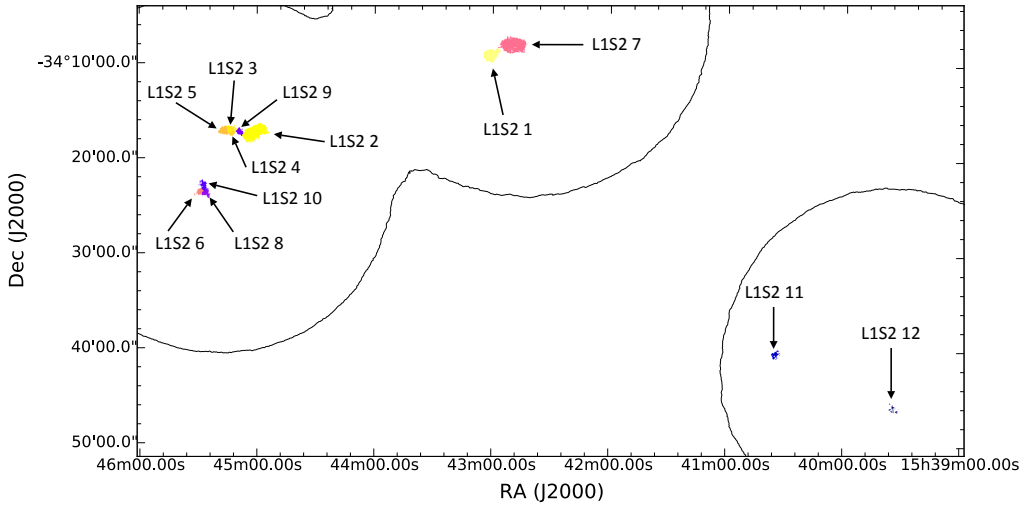

Figure 3.9: Protostars and prestellar cores (see Table 3.12) identified from the SCUBA-2 850 µm map of Lupus I using FellWalker (Berry 2015). Black contours show the edge of the SCUBA-2 coverage.

assuming an error of 1 $\sigma_{\rm rms}$ per pixel. Consistency between the 450 µm and 850 µm fluxes (see Table 3.12) was checked using the relation

$$\frac{S_{450}}{S_{850}} = \frac{B_{450}(T)}{B_{850}(T)} \left(\frac{850}{450}\right)^{\beta}, \tag{3.6}$$

where the temperatures used are detailed in Section 3.3.1.2, and can be found in Table 3.11. All fluxes were found to be consistent (within uncertainties), provided that the cores L1S2 3, L1S2 4 and L1S2 5 are treated as a single agglomeration.

The twelve cores are presented in Table 3.12, with Figure 3.9 showing the positions of each of these sources. 3 σ upper limits for L1S2 11 and L1S2 12 were calculated at 450 µm using the same method used for point sources in Section 3.2.1.1. Sources were treated as Gaussian distributions of flux, with a peak emission at 5 σ. The FWHM assumed for each core was set to twice the core radius. Core radii were calculated from the number of pixels comprising the core area, and were not deconvolved.

The assumption of cores as spherical (in order to calculate radii and volumes) provides consistency with the work of Rumble et al. (2015), which also used FellWalker. Cores can, however, be elongated rather than spherical (seen with L1S2 2 and L1S2 7). In this case, the effective radius of a core will be a lower limit if the third dimension is elongated, and an upper limit if the third dimension is shortened.

3.3.1.2 Core Masses

The submillimetre continuum derived masses for these cores were calculated using Equation 3.5 and the extracted submillimetre flux at 850 µm. The same value for the dust opacity of 0.012 cm^2g^{-1} was used for these cores as was used for the protostellar envelope calculations in Section 3.2.6.1. This is again consistent with both model 5 of Ossenkopf and Henning (1994) and the relation of Beckwith et al. (1990) when $\beta = 2.0$.

The observations of Gaczkowski et al. (2015) identified a total of 15 prestellar, protostellar and starless cores, in the main ridge of Lupus I, with LABOCA. They also derive temperatures for each of these cores by using *Herschel* SPIRE (Griffin et al. 2010) observations to create temperature maps. The correspondence between SCUBA-2 and LABOCA cores is shown in Table 3.11.

Where there is a match in position between LABOCA and SCUBA-2 cores, these derived temperatures are used in Equation 3.5 in order to calculate the value of the Planck function. In the cases where a SCUBA-2 core corresponds to multiple LABOCA cores, the temperature used is the mean value across all relevant LABOCA cores. Moreover, where a SCUBA-2 core has no corresponding LABOCA object, the mean temperature value across all LABOCA cores (within the SCUBA-2 field of view) of 14 ± 3 K is used as an estimate.

The core L1S2 1 corresponds to the YSO L1YSO 7. Therefore, two temperatures were available to use for this source (from *Herschel* and SCUBA-2 in Section 3.2.5). The SCUBA-2-derived temperature value applies to a smaller scale (i.e., has better resolution) than the *Herschel* temperature, because the longest-wavelength SCUBA-2 resolution is superior to the longest-wavelength *Herschel* resolution. The identified FellWalker core has a higher flux value than was extracted for L1YSO 7 from aperture photometry as it covers a wider area of extended emission. Therefore, the temperature used to calculate the mass for L1S2 1 is the mean of the *Herschel* and SCUBA-2 values (14.0 K and 17 K, respectively).

The mass-size relationship for these cores is plotted in Figure 3.10. The cores with the largest radii are also the most massive. Core mass can be modelled simply as $M = 2\pi\Sigma_m r^2$, with Σ_m the mean mass per unit surface area. Therefore, a core with a larger radius will

be more massive provided $\Sigma_m \sim r^{-\gamma}$ where $\gamma < 2$. For these cores, Σ is uncorrelated with the mean core radius, meaning that $\gamma \sim 0$ and the largest cores will indeed be the most massive. Also visible in this Figure is the cluster of cores at similar sizes / radii. The majority of the cores identified range between 0.1 to 0.4 $M_\odot$ in mass, and approximately 3000 to 5000 AU in size (corresponding to approximately 1 – 2 beam FWHM at 850 µm).

One core (L1S2 12) has a low mass for its size, below the 3σ detection limit. This is because it is seen as a several small, related areas of high signal-to-noise ratio emission rather than one solid shape (see Figure 3.9). This does not mean that there is no material in the areas in between, but rather than these areas contain signal below the 2σ threshold required for FellWalker to consider them as part of the core. The MaxJump parameter allows non-adjacent pixels to be grouped in the same 'clump' provided they do not correspond to different peaks.

Of the twelve extended sources, three have $M > 1.0$ $M_\odot$, eight have masses between 0.1 and 1.0 $M_\odot$, and one has a mass below 0.1 $M_\odot$. The total mass of all cores is 8.7 $M_\odot$, with a mean mass of the cores seen with SCUBA-2 of 0.73 $M_\odot$. Assuming a typical core-to-star mass efficiency of 40 per cent, star formation possibilities include low-mass stars (a maximum of ~ 1 $M_\odot$ from L1S2 2) and brown dwarfs, assuming core collapse proceeds in the first place.

As discussed previously, single temperature assumptions may not provide a wholly accurate mass. If the value assumed is too low, then core masses will be overestimated and vice versa. Similarly, decreasing the value used for β will decrease calculated masses, and vice versa.

3.3.1.3 Comparison with LABOCA 870 µm observations

The most clustered region in Lupus I is at the south-east part of the ridge, known here as the E field. In this region, eight cores were identified by SCUBA-2 and six by LABOCA. In addition, two cores were identified by SCUBA-2 in the area of the N field. In contrast, LABOCA identified eight cores in this region. Cores identified by LABOCA and other studies are shown in Figure 3.11. Further cores were identified in both analyses, but these

were not in areas with shared coverage. SCUBA-2 cores were identified by FellWalker, and LABOCA cores were identified using CLUMPFIND (Williams, de Geus, and Blitz 1994).

Of the seven SCUBA-2 identified cores for which there is a corresponding LABOCA core, the continuum masses are consistent between all but one of them, once uncertainties are taken into account. The mass of L1S2 8 is significantly lower than the corresponding LABOCA core (0.21 vs. 0.53 $M_{\odot}$). Both SCUBA-2 and LABOCA masses for corresponding cores are given in Table 3.11.

The LABOCA cores all have larger given sizes than the SCUBA-2 cores, and fluxes are also larger, with the exception of Core 1 (L1S2 1). The LABOCA beam size (21.2″) is larger than the SCUBA-2 beam size (14.1″). Additionally, the LABOCA observations exhibit superior recovery of faint, large-scale emission found in the regions around cores. This enables LABOCA cores to have a larger extent, and consequently produce a greater flux detection, than the SCUBA-2 cores. L1S2 7 also has an extent greater than 2.5′ along one axis, meaning that it may be affected by the spatial filtering in the SCUBA-2 data reduction. The effect of this would be an underestimation of both the flux, and size, of the core.

The presence of YSOs near or within certain cores (e.g., L1YSO 11 is coincident with L1S2 4) means that T and β will likely not be uniform across all of these structures. Treating all emission as extended (with $\beta = 2.0$ and $T < 20$ K) is therefore likely to lead to an overestimation of masses in these cores.

CLUMPFIND uses contours in the data to identify clumps of emission, but noise spikes in the data (corresponding to a single 'real' core) can lead to several separate clumps being identified (see Berry 2015 and references therein). FellWalker would be expected to avoid this problem, thus providing a possible explanation for the identification of L1S2 7 as five separate LABOCA cores (6, 7, 8, 9, 10). There is no clear visual indication in the SCUBA-2 map of significant substructure in L1S2 7 corresponding to the locations of the LABOCA cores. If, however, L1S2 7 does in fact consist of five separate cores, then there will be a greater number of cores in Lupus I, with a lower mean mass.

Table 3.11: Correspondences between cores identified by SCUBA-2 (this work) and LABOCA (Gaczkowski et al. 2015). The 870 µm masses are provided, as well as the temperatures used in calculating core masses from SCUBA-2 fluxes (discussion in text).

Core ID SCUBA-2	Core ID LABOCA	M_{870} $M_\odot$	M_{850} $M_\odot$	T (K)	Field
L1S2 1	1	1.71	1.69 ± 0.40	15.5 ± 3.6[a]	NW
L1S2 2	2, 5	2.05	2.99 ± 0.85	12.8 ± 3.6	E
L1S2 3, 4, 5	3, 4	0.67	0.90 ± 0.15	15.0 ± 3.0	E
L1S2 6	...	...	0.18 ± 0.05	14.0 ± 3.0[b]	E
L1S2 7	6, 7, 8, 9, 10	2.61	2.11 ± 0.44	13.0 ± 2.6	NW
L1S2 8	11	0.53	0.21 ± 0.05	13.5 ± 2.7	E
L1S2 9	...	...	0.17 ± 0.05	14.0 ± 3.0[b]	E
L1S2 10	...	...	0.25 ± 0.06	14.0 ± 3.0[b]	E
L1S2 11	...	...	0.16 ± 0.04	14.0 ± 3.0[b]	SW
L1S2 12	...	...	0.07 ± 0.02	14.0 ± 3.0[b]	SW

[a] Mean of both SCUBA-2 and *Herschel* temperatures.
[b] Temperatures are the mean of LABOCA core temperatures within the SCUBA-2 field of view.
Note: Uncertainties on LABOCA masses are conservatively 20 per cent per core.

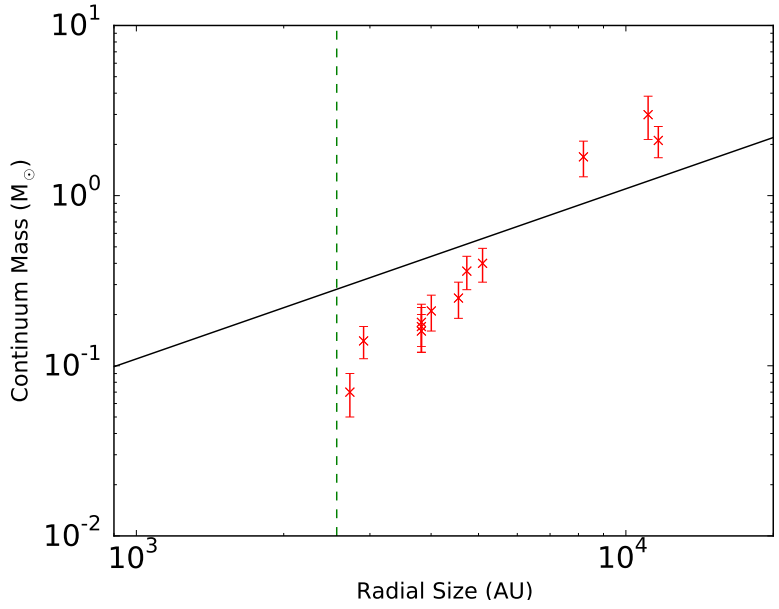

Figure 3.10: Masses of protostars and prestellar cores in Lupus I identified with the FellWalker algorithm (Berry 2015) and their radii. The solid black line represents the Jeans mass for given sizes, assuming a temperature of 14 K, and a β value of 1.8). The green dashed line represents the JCMT beam size (14.1″ at 850 µm).

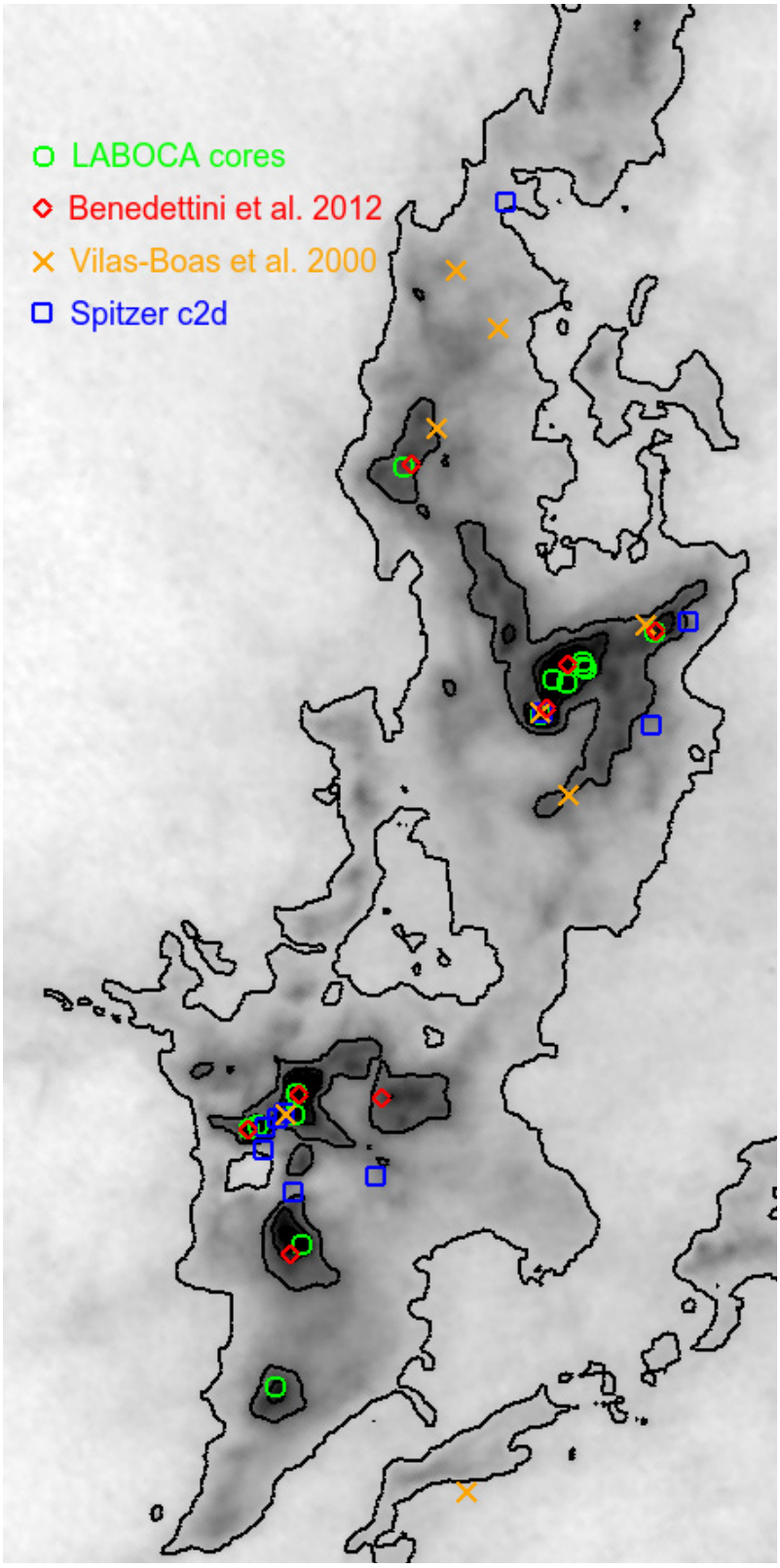

Figure 3.11: Figure reproduced from Gaczkowski et al. (2015). Cores in Lupus I identified using previous studies, plotted over a *Herschel* column density map of the region of Lupus I corresponding to the NW and E fields. Contours are at levels of 1.1, 4, 7 and 10 $\times 10^{21}$ cm^{-2}. Cores identified by LABOCA and MOPRA (Benedettini et al. 2012), CO cores identified by Vilas-Boas, Myers, and Fuller (2000), and *Spitzer* c2d YSOs are shown.

3.3.1.4 Comparison to Cores Identified by Mopra

Benedettini et al. (2012) used molecular line data obtained with the Mopra telescope to map the Lupus I, III, and IV molecular clouds. In Lupus I, the observations cover the main ridge (B228). They identify eight cores in this region, with five corresponding to ones identified by SCUBA-2 (Lup1_C3, 4, 6, 7 and 8 corresponding to L1S2 7, 1, 2, 5 and 6 respectively). The positions of these cores are also plotted in Figure 3.11. Emission lines from several molecular tracers were observed by Mopra, including NH_3, N_2H^+, HC_3N, CS, and CH_3OH. Cores were then identified using whichever tracer best-defined the clump. The five matching cores are listed with CS (2–1) transition linewidth information in Table 3.13.

SCUBA-2 identifies cores not seen with Mopra, and the reverse is also true (although the three most massive cores identified by SCUBA-2 are also seen with Mopra). SCUBA-2 has identified up to seven cores that Mopra did not detect, including two in the SW field not observed with Mopra. Some will likely be due to the clustered sources in the E field being detected as single objects by the larger Mopra beam, which at 3 mm is 35″. This low resolution means that, particularly in the vicinity of L1S2 5, Mopra may also have picked up emission from the nearby cores identified by SCUBA-2 (3 and 4). Additionally, L1S2 6 lies near L1S2 8 and L1S2 10, meaning that these could also be effectively merged into the single Mopra core Lup1_C8.

Three cores were identified with Mopra that SCUBA-2 did not detect. All three of these cores (C1, C2, and C5) were detected weakly, or not at all, in NH_3 and N_2H^+. These species effectively trace the denser, inner regions of cores (Di Francesco et al. 2007), and an abundance of these molecules is indicative of a more evolved core (prestellar or protostellar). This, therefore, suggests that these three cores are starless, and represent relatively low-density extended emission. The SCUBA-2 data reduction process suppresses large scale areas of emission without strong central peaks of emission (Mairs et al. 2015). This suppression happens to a greater extent than with, for example, the *Herschel* 500 µm observations of Lupus I (Rygl et al. 2013). Therefore extended cores without strong emission peaks, such as these three, can fail to appear in the SCUBA-2 map while still being identified

Table 3.12: Protostar and prestellar core properties derived from SCUBA-2 continuum data (discussion in text).

ID	JCMTLSG Name	S_{450} (mJy)	S_{850} (mJy)	M_{850} ($M_\odot$)	Radius (arcsec)	$M_{\rm Jeans}$[1] ($M_\odot$)	$M_{850}/M_{\rm Jeans}$	$M_{\rm Virial}$ ($M_\odot$)	$\alpha_{\rm vir}$
L1S2 1	J154301.6-340909	24400 ± 200	4176 ± 9	1.69 ± 0.40	45	1.0 ± 0.2	1.7 ± 0.6	4.3 ± 0.6	2.6 ± 0.7
L1S2 2	J154500.6-341718	23800 ± 300	5302 ± 9	2.99 ± 0.85	61	1.1 ± 0.3	2.7 ± 1.1	3.3 ± 0.6	1.1 ± 0.4
L1S2 3	J154513.4-341702	5890 ± 200	833 ± 6	0.36 ± 0.08	26	0.6 ± 0.1	0.6 ± 0.2	...	...
L1S2 4	J154512.7-341727	1220 ± 160	317 ± 5	0.14 ± 0.03	16	0.3 ± 0.1	0.4 ± 0.1	...	...
L1S2 5	J154516.8-341710	4470 ± 210	932 ± 7	0.40 ± 0.09	28	0.6 ± 0.1	0.7 ± 0.2	3.9 ± 0.4	9.8 ± 2.4
L1S2 6	J154529.2-342335	2250 ± 170	365 ± 5	0.18 ± 0.05	21	0.4 ± 0.1	0.4 ± 0.1	1.5 ± 0.2	8.4 ± 2.6
L1S2 7	J154249.8-340805	18300 ± 200	3856 ± 10	2.11 ± 0.44	64	1.2 ± 0.3	1.8 ± 0.5	11.6 ± 1.4	5.5 ± 1.3
L1S2 8	J154525.8-342346	3220 ± 170	408 ± 5	0.21 ± 0.05	22	0.4 ± 0.1	0.5 ± 0.2	...	...
L1S2 9	J154508.7-341718	1930 ± 170	358 ± 5	0.17 ± 0.05	21	0.4 ± 0.1	0.4 ± 0.1	...	...
L1S2 10	J154527.1-342256	3860 ± 180	514 ± 6	0.25 ± 0.06	25	0.5 ± 0.1	0.5 ± 0.2	...	...
L1S2 11	J154035.0-344022	≤ 430	328 ± 5	0.16 ± 0.04	21	0.4 ± 0.1	0.4 ± 0.1	...	...
L1S2 12	J153934.5-344556	≤ 320	153 ± 3	0.07 ± 0.02	15	0.3 ± 0.1	0.2 ± 0.1	...	...

[1] Although not quantified, volumes being treated as spherical will lead to additional uncertainties in the Jeans mass.
Note: Uncertainties from flux calibration, not included in the table, are 8 per cent and 12 per cent at 850 µm and 450 µm, respectively (Dempsey et al. 2013).
Note: Core radii are not deconvolved.

by other instruments (Ward-Thompson et al. 2016).

3.3.2 Stability Analysis

The simplest form of stability analysis performed was the consideration of the Jeans instability (Jeans 1902), which treats stability as the balance between thermal support and gravitational contraction. The Jeans mass is the critical mass at which a dense core, at a given temperature and density, will become unstable to perturbations. The Jeans mass for each of the cores was estimated using Equation 1.4. Jeans masses for all cores are provided in Table 3.12.

The average number density of molecules is given by $\langle n_0 \rangle = M/\mu m_p V$, where M is the mass of the core calculated using the submillimetre continuum flux, μ is the assumed mean molecular mass (for the combination of H_2 and He) of 2.38 (Kauffmann et al. 2008). and m_p is the mass of a proton. V is the ellipsoidal volume of the source, calculated from the core radius given in Table 3.12. The same temperatures were used to calculate the Jeans mass for each core as were used in calculating the core masses (see Table 3.11).

Less massive cores, for which the calculated submillimetre continuum mass is below the estimated Jeans mass, are sufficiently supported against gravitational collapse by thermal motions alone. For some, this state implies they will not collapse to form YSOs

in the first place. Other sub-Jeans cores correspond to areas that have already formed YSOs, such as L1S2 4. This core contains the object L1YSO 11 (HT Lup), and thus has already undergone collapse in the past and will not fragment further. Additional sub-Jeans cores in which class II YSOs can be found are L1S2 6 and L1S2 9 (with L1YSOs 14 and 10 respectively).

Under the assumption that only thermal pressure is available to support against gravitational collapse, the Jeans mass suggests that the three larger, more massive cores in this sample (L1S2 1, L1S2 2 and L1S2 7) should be unstable against gravitational collapse, due to having masses significantly larger than the estimated Jeans mass for a core with similar density and temperature. Smaller cores, for which the calculated submillimetre continuum mass is below the estimated Jeans mass, are sufficiently supported against gravitational collapse by thermal motions alone, and so are gravitationally bound. This could either mean that they will not collapse, or that they have already collapsed and formed protostellar objects. For example, L1S2 1 already contains the protostar L1YSO 7. As such, it would no longer be expected to satisfy the Jeans stability criterion.

An additional mechanism for preventing the gravitational collapse of a core is provided by the virial theorem (Collins 1978). The total kinetic energy term not only takes into account thermal support (as with Jeans stability) but also non-thermal support via turbulent motions in the cloud. The virial mass of a core describes the critical mass at which a core supported by thermal and non-thermal motions will become unstable to gravitational collapse. The virial mass can be calculated using Equation 1.11.

Different gas molecules will trace different regions within a dense core. Observation of NH_3 or N_2H^+ will probe the more dense inner regions of these cores, whereas species such as CO and CS will trace the less dense external shells of such cores. This is partly due to carbon depletion at densities greater than $\sim 10^5$ cm^{-3} (Di Francesco et al. 2007). Hence, as the CS cores size better matches the dust core size than the other available species, this analysis uses the observations of the CS (2–1) transition in Lupus I made by Benedettini et al. 2012 to calculate the virial mass for submillimetre identified cores in Lupus I. The one-dimensional velocity dispersions are provided in Table 3.13).

In characterising the stability of a dense core, the Virial mass can be divided by the mass of the core in order to obtain the Virial parameter $\alpha_{\rm vir}$ (Bertoldi and McKee 1992). The virial parameter $\alpha_{\rm vir}$ (Bertoldi and McKee 1992) was calculated for each core with an available linewidth, with $\alpha = M_{\rm vir}/M_{850}$. In the simplest case of treating a core as a constant density sphere, $\alpha_{\rm vir} < 1$ would indicate that the core is supercritical. When the core is instead treated as a Bonnor-Ebert sphere (Ebert 1955; Bonnor 1956) or is elongated (Bertoldi and McKee 1992) supercriticality is found with cores where $\alpha_{\rm vir} < 2$ (Kauffmann, Pillai, and Goldsmith 2013). When the mass of a core is supercritical, the core will be gravitationally bound and potentially undergoing collapse.

A total of five cores identified by Benedettini et al. (2012) with available CS (2–1) transition data (Lup1_C3, Lup1_C4, Lup1_C6, Lup1_C7, and Lup1_C8) were also observed by SCUBA-2. Observations of the CS (2–1) transition were used to calculate the virial mass as CS provides a better match to dust core size than the other available species (Di Francesco et al. 2007). The one-dimensional line widths $(\Delta v_{\rm 1D})^2$ were converted to three-dimensional velocity dispersions $\sigma_{\rm 3D})^2$ using the relation

$$(\sigma_{\rm 3D})^2 = \frac{3(\Delta v_{\rm 1D})^2}{8{\rm ln}2}. \tag{3.7}$$

These line widths, listed in Table 3.13, were used in calculating the critical virial mass for five of the identified dense cores in Lupus I (see Table 3.12).

Once non-thermal turbulent support is taken into account, these calculations show that four of the five cores (L1S2 1, 5, 6 and 7) are virially stable. The core L1S2 1 contains the known protostar IRAS 15398-3359 (Heyer and Graham 1989), identified as SSTc2d J154301.3-340915 by *Spitzer* (Chapman et al. 2007; Merín et al. 2008) and as L1YSO 7 in our work. The presence of a protostar in this core indicates that it has already undergone gravitational collapse. Indeed, indications of infall towards this source in *Herschel* water spectra were observed by Mottram et al. (2013). The calculation of virial masses using Equation 1.11 assumes that the CS (2–1) linewidth is produced by turbulent motions, which are able to support against collapse. This would not be the case if the linewidths were a result of outflowing / infalling material from a central object, as may be the case with L1S2

1 / L1YSO 7.

L1S2 7 has a mass greater than its associated Jeans mass, but the virial parameter for this core is 5.5. This difference may be an indication that turbulent support in L1S2 7 is more important than thermal support. The proximity of L1S2 7 to L1S2 1, which contains L1YSO 7, could mean that turbulent activity has been induced by this nearby star formation. However, the CS (2–1) linewidths are all supersonic. This suggests that the cores are being supported by an additional support mechanism, perhaps pressure confinement (Pattle et al. 2015), which is preventing the turbulent pressure from breaking them apart.

The final core of the five, L1S2 2, has a virial parameter of 1.1 ± 0.4. This indicates that the core may be virially unstable and about to undergo gravitational collapse. The potential instability of L1S2 2 is notable given that there are no known YSOs within this core (with the nearest being L1YSO 9 at the edge), though the close proximity of L1YSOs 9, 10, and 11 shows a history of star formation in the vicinity of L1S2 2. With a mass of 2.99 $M_\odot$ it could be in the very earliest stages of birthing new stars. If there are deeply embedded YSOs in this core, then they would be expected to produce outflows of material.

The virial analysis here has shown L1S2 7 to be virially stable, and L1S2 2 to be potentially unstable. This difference indicates that starless, super-Jeans cores may be reaching the pre-stellar stage, or they may actually be subcritical thanks to additional support over thermal motions. Sadavoy, Di Francesco, and Johnstone (2010) examine 17 cores with masses greater than their Jeans mass, previously classified as starless. They find three are genuinely starless, similar to L1S2 2 and L1S2 7. These cores may be supported by non-thermal motions, or they may also be virially unstable precursors to star formation. Pattle et al. (2015) find one of these starless cores, in Ophiuchus, to have a lower mass than calculated in Sadavoy, Di Francesco, and Johnstone (2010). These newer observations with SCUBA-2 indicate that this core may not be super-Jeans at all.

Mairs et al. (2016) find two seemingly gravitationally unstable objects in Southern Orion A that contain no known YSOs. The contrast in virial stability between L1S2 2 and L1S2 7 indicates that such objects may or may not be prestellar. This is also seen by Pattle et al. (2015); of the four cores in Ophiuchus (out of 23) that are clearly gravitationally bound,

Table 3.13: List of cores with their corresponding Mopra IDs and CS (2–1) linewidths from Benedettini et al. (2012)

SCUBA-2 ID	Mopra ID	Δv (km s^{-1})
L1S2 1	Lup1_C4	0.72 ± 0.07
L1S2 2	Lup1_C6	0.54 ± 0.07
L1S2 5	Lup1_C7	0.87 ± 0.06
L1S2 6	Lup1_C8	0.62 ± 0.07
L1S2 7	Lup1_C3	0.99 ± 0.08

three are virially bound (so prestellar) and one is not (though uncertainties mean that this is not definitive). Overall, it seems that the incidence of a low number of both starless and prestellar super-Jeans cores is typical in Gould Belt clouds. Southern Orion A is, however, a much more massive cloud than Lupus I, with an extinction-derived mass within the SCUBA-2 footprint of 9.5 $\times 10^4$ $M_\odot$, compared to the distance-adjusted value for Lupus I of approximately 250 $M_\odot$. Additionally, the total mass of the islands observed by SCUBA-2 is 1.3 $\times 10^3$ $M_\odot$ in Southern Orion A, and only 8.7 $M_\odot$ in Lupus I. This seems to suggest that Lupus I shows a larger incidence of super-Jeans cores, but caution should be exercised with this assessment, as the total number of cores in Lupus I (twelve) is small.

3.4 Summary and Conclusions

In this study, both point-like sources (assumed to be YSOs) and extended emission (assumed to be protostellar, pre-stellar or starless cores) were extracted from the JCMT GBS SCUBA-2 maps of the Lupus I molecular cloud. YSOs were extracted using aperture photometry while extended objects were identified using the FellWalker source extraction algorithm. These observations have provided evidence for both ongoing and potential future star formation within Lupus I.

Eleven previously-identified YSOs were detected by SCUBA-2 at 850 µm. Of these, four were also detected at 450 µm. One of the eleven sources is Class 0, one is Class I, one is a Class F, and the rest are Class II; no Class III sources were detected by SCUBA-2. This distribution of Classes and evidence of ongoing star formation is similar to that found in

the Ophiuchus North region, also in Sco-Cen (Hatchell et al. 2012), and contrasts with the low number of Class I and high number of Class III sources in Lupus III (Merín et al. 2008).

The overall fraction of YSOs in Lupus I that are protostellar (Including Class F) is consistent with that seen in other Gould Belt regions, such as Ophiuchus and Serpens (Dunham et al. 2015). The fraction of Class 0 / I YSOs is greater in Lupus I (16 per cent vs. 11 per cent), while the Class III fraction is low (16 per cent vs. 40 per cent). This may suggest that it is younger than many other Gould Belt clouds, but the differences here are not statistically significant. Four additional YSOs detected by *Spitzer* were too faint to be detected by SCUBA-2, leading to a total of 15 YSOs being analysed further here.

For the ten more evolved Class II and III sources, as well as two Class F sources, calculations of disk mass from submillimetre continuum emission (assuming T = 20 K and β = 1) reveal only one source has a disk mass of over the minimum mass Solar nebula (MMSN). This single occurrence is consistent with 2/20 YSOs detected by SCUBA-2 in Taurus L1495 having disk masses greater than the MMSN (Buckle et al. 2015). Among the nine Class F and II sources, the mean circumstellar disk mass is 5.9×10^{-3} $M_{\odot}$.

For the three less-evolved Class 0 and I YSOs, as well as the two Class F YSOs, protostellar envelope masses, and temperatures, were estimated using opacity-modified blackbody SED envelope fits for the three sources which were detected by SCUBA-2. When a less-evolved source was not detected by SCUBA-2, an upper limit to envelope mass was instead calculated. All of these envelope masses are low enough that any YSOs produced would be low-mass stars, brown dwarfs or even sub-brown dwarfs. Temperatures were found to be greater than the typical value of 14 K, particularly for L1YSO 1 (T = 28.8 K), which is located off the main ridge in the SW field.

Bolometric temperatures and luminosities were calculated for all 15 YSOs. Classifications based on $T_{\rm bol}$ largely match those based on spectral index. Three have $L_{\rm bol} < 0.1$ $L_{\odot}$ and another three have $L_{\rm bol} > 1$ $L_{\odot}$, with the rest lying within this range. The embedded YSOs with $L_{\rm bol} \leq 0.1$ $L_{\odot}$, L1YSO 2 and L1YSO 9, are therefore Very Low Luminosity Objects (VeLLOs). A third source with $L_{\star} \sim 0.1$ $L_{\odot}$, L1YSO 5, is also consistent with being a VeLLO, due to a large uncertainty on $L_{\rm bol}$. Furthermore, a fourth source, L1YSO 1, may be an

example of a protostellar VeLLO being heated to a higher bolometric luminosity by the interstellar radiation field. This number of VeLLOs represents a larger fraction of VeLLOs than was found by Dunham et al. (2008) across the *Spitzer* c2d survey regions, though the difference is not statistically significant due to the low numbers involved.

Spectral energy distributions for all 15 YSOs within the field-of-view of SCUBA-2 in Lupus I were produced. The model SEDs of Robitaille et al. (2006) were fit to the observed fluxes for each YSO. Statistical tests were used to separate well-fit SEDs from poorly-fit ones. Where multiple models provided good fits to the SED of a particular YSO, the ranges of disk masses, envelope masses, and interstellar extinction values were found. In general, the parameter most effectively constrained by these models was the interstellar extinction, with large degeneracies being found in disk and envelope masses. The upcoming *Herschel* point source catalogue for Lupus I will provide further data in the submillimetre regime, which should facilitate improved models.

An updated star formation rate (SFR) for Lupus I, of 2.6 ± 0.6 $M_\odot$ Myr^{-1}, was calculated. Whilst this is low compared to many other Gould Belt regions, the low mass of Lupus I means that it is not unusual.

Next, twelve areas of extended emission, corresponding to starless, pre-stellar, or protostellar cores were found in the SCUBA-2 850 µm map. Across all twelve, the mean mass is 0.73 $M_\odot$, and the total mass is 8.7 $M_\odot$, approximately 1/20 of the total mass in the main part of the cloud.

Values for the thermal Jeans mass are estimated for each of these cores, with values between 0.3 and 1.1 $M_\odot$. The three largest cores are not Jeans stable. One of these cores, however, contains a known protostar, therefore two starless super-Jeans cores are detected in Lupus I. This is consistent with observations in Southern Orion A by Mairs et al. (2016), which also contain two starless super-Jeans cores.

Virial stability analysis, including non-thermal linewidths, is thus also performed using CS (2–1) transition data for five sources in Lupus I. Four sources are found to be stable against collapse, including one of the starless super-Jeans cores. The fifth core is virially bound, with a virial parameter of 1.1 ± 0.4. This core, L1S2 2, contains no known

YSO detections, and has a mass of 2.99 $M_{\odot}$. This core may therefore be a prestellar core candidate, meriting further observations.

The presence of a prestellar core candidate, and the high Class 0 / I to Class III YSO ratio of 1:1, provides further evidence that a star formation event in Lupus I has been triggered recently by a shock (Gaczkowski et al. 2015). The shock is a result of being located between two H I shells in the Sco-Cen OB association, which has compressed interstellar material to begin forming young stars.

Chapter 4

First Hydrostatic Core Candidates in Serpens South

> *"Look at them all, through the darkness I am bringing. They're not sad at all. They're actually singing. They sing without juicers. They sing without blenders. They sing without flungers, cabdabblers, and smendlers!"*
>
> — *C.M.Burns*

In this chapter I detail the observational work I undertook as part of a study on First Hydrostatic Core (FHSC) candidates. Whereas Chapter 3, Chapter 5 and Chapter 6 all document work I did as a first author, I was a collaborator for this study. The first author, Alison Young, is another Ph.D student at the University of Exeter. She produced Smoothed-Particle Hydrodynamics (SPH) models of FHSCs which could be fit to multi-wavelength observations of FHSC candidates in the Gould Belt. My responsibility was to measure the fluxes of a set of candidates at far-infrared and submillimetre wavelengths and then use these observations to construct SEDs for these candidates. By fitting the FHSC models to these observed SEDs, the properties of the FHSC candidates could be examined.

The structure of this chapter is as follows: Section 4.1 introduces FHSCs, Section 4.2 details the observations used to find fluxes for FHSC candidates, Section 4.3 describes how candidates were initially identified, Section 4.4 explains how multi-wavelength fluxes were assigned to candidates, and Section 4.5 outlines how these observations were used by the

first author to obtain results that were published as Young et al. (2018).

4.1 Introduction

When a protostar begins to form, it will collapse isothermally. Once a certain density is reached, however, the centre of the collapsing cloud of molecular hydrogen (H_2) becomes opaque enough that heat cannot be radiated away. This causes the temperature to rise enough that the thermal pressure can stop collapse. An object therefore exists that is approximately in hydrostatic equilibrium (Larson 1969). This is known as an FHSC. Material outside this core will continue to collapse, meaning that eventually the temperature of the core will rise to $\sim$ 2000 K. At this point, the H_2 will dissociate to produce atomic hydrogen (HI) and a second collapse will begin.

By their very nature, FHSCs are deeply-embedded and low-luminosity. SEDs produced from models of protostellar evolution (e.g., Young and Evans 2005) peak at wavelengths of between 100 and 500 µm. They have little short-wavelength emission and few, if any, features. Figure 4.1 shows panel one of Figure 8 from Young and Evans (2005). This model shows how the SED of a particular 1 $M_\odot$ FHSC would be expected to look if observed. As an FHSC evolves, the peak of the SED will move to shorter wavelengths (Saigo and Tomisaka 2011). Evolutionary modelling has also been able to demonstrate the effects of FHSC properties such as inclination on their SEDs (Boss and Yorke 1995). Therefore, it should be possible to match models to observed SEDs to determine whether an object may be an FHSC and constrain its properties.

In order to fit an observed candidate with FHSC SED models, such candidates must first be identified. Few FHSC candidates exist in the literature. One reason for this is that *Spitzer* YSO catalogues (Dunham et al. 2015) require sources to be detected at 24 µm. As FHSCs are often very faint at this wavelength, they end up excluded from lists of YSOs and hence overlooked. Nevertheless, five previously-identified literature FHSC candidates were able to be examined by Young et al. (2018). These objects are: B1-bN, B1-bS, Per-Bolo 58 (all in Perseus), Chamaeleon-MMS1, and CB17-MMS.

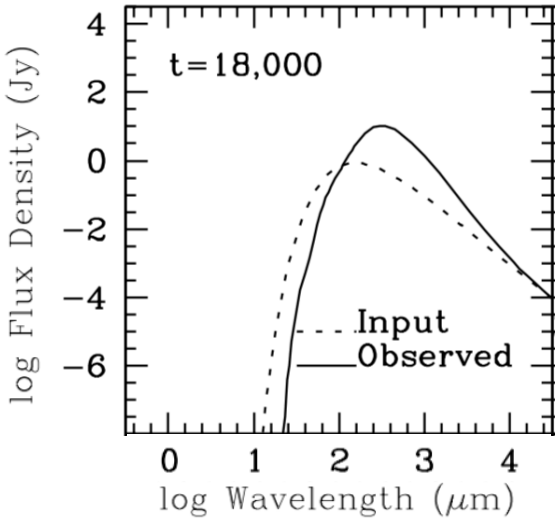

Figure 4.1: Figure reproduced from the first panel of Figure 8, Young and Evans (2005). Model SED of a 1 $M_{\odot}$ FHSC at an age of 18,000 years. The solid line represents the output SED as it would be observed, produced using a radiative transfer code.

In addition to these five sources, new FHSC candidates were searched for in Serpens South (see Section 1.5.2). The high star formation rate and high number of protostars (see Chapter 6) makes Serpens South a promising place to look for FHSC candidates. Because there were no previously published FHSC candidates in Serpens South, possible FHSCs were identified using data from multiple surveys.

4.2 Observations

First Hydrostatic Core Candidates in Serpens South were identified on the basis of their submillimetre, far-infrared, and mid-infrared fluxes. These fluxes were extracted from observations by SCUBA-2, *Herschel* PACS and SPIRE, *Spitzer* MIPS, and WISE.

4.2.1 SCUBA-2

The Aquila region, containing Serpens South, was observed with SCUBA-2 at 450 and 850 µm as part of the JCMT GBS. The observations were first presented in Rumble et al. (2016), though the updated GBS data reduction was used for this work (see Section 2.3.2 for details). Figure 4.2 shows the Serpens South cloud at 850 µm. The FHSC candidates in

Serpens South are labelled. Four of the candidates are situated along the main filament of material, while a fifth is located away from the main cloud.

4.2.2 *Spitzer*

Serpens South was observed using MIPS as part of the *Spitzer* GB Legacy Survey. The MIPS 1 maps containing Serpens South were used to obtain photometry for FHSC candidates at 24 µm. Serpens South appears at the boundary between two separate MIPS map areas. Three candidates are located in one map, with two in the other. These maps were published as part of the *Spitzer* GBS (Gutermuth et al. 2008), PID 30574.

4.2.3 *Herschel*

The *Herschel* Space Observatory was used to observe Serpens South as part of the *Herschel* GBS. The observations were performed with both PACS (Poglitsch et al. 2010) and SPIRE (Griffin et al. 2010). Photometry for FHSC candidates in the Serpens South region was obtained at 70 and 160 µm (observed with PACS), and 250 µm (observed with SPIRE). The *Herschel* Aquila data is available from the GBS website[1].

4.2.4 WISE

The Wide-field Infrared Survey Explorer (WISE) mapped the whole sky in four wavelength bands. Band W4 has an effective wavelength of 22 µm, and so the W4 map in the vicinity of Serpens South was used, in conjunction with the *Spitzer* data, in the identification of FHSC candidates (detailed below, in Section 4.3). WISE maps were downloaded from NASA SkyView[2].

1. http://www.herschel.fr/cea/gouldbelt/en/Phocea/Vie_des_labos/Ast/ast_visu.php?id_ast=66
2. https://skyview.gsfc.nasa.gov

4.3 Identification

The identification of FHSC candidates was implemented by J.Hatchell. A brief summary of the identification procedure follows. FHSC candidates were identified using a five-step procedure. Initially, the FellWalker clump-finding algorithm was used to identify peaks in the SCUBA-2 450 µm emission. Next, centrally-concentrated cores were selected as collapse candidates, with concentration values of $C > 0.3$ accepted, following Johnstone et al. (2001). The concentration parameter, C, is defined as

$$c = 1 - \frac{1.13B^2 S_{850}}{(\pi R_{\rm obs}^2) f_0} \tag{4.1}$$

where B is the beam effective FWHM (14.1″ at 850 µm), S_{850} is the total flux, $R_{\rm obs}$ is the core radius, and f_0 is the peak flux (Jy/beam). A concentration value of ~ 0.3 is the minimum expected for a Bonnor-Ebert sphere (Johnstone et al. 2000).

Infrared-bright cores were then rejected by cross-matching with sources in the WISE catalogue (Cutri et al. 2012), and *Spitzer* YSO catalogue (Dunham et al. 2015). The relevant wavelengths checked were 22 and 24 µm for WISE and *Spitzer*, respectively. Additionally, potential FHSCs were overlaid on the WISE 22 µm and *Spitzer* 24 µm maps. Then, *Herschel* non-detections at 160 µm (based on a preliminary flux extraction) were rejected, as it would be expected for the SED of a cold source such as a FHSC to peak near this wavelength. Finally, FHSC candidate SEDs were compared with FHSC models, and those with the highest 24:450 µm flux ratios were rejected. This procedure found a total of five compact submillimetre infrared-faint sources considered to be FHSC candidates in Serpens South.

Images of these five FHSC candidates are shown in Figure 4.3. Five images per FHSC candidate are shown, at 24 µm (MIPS 1), 70 and 160 µm (*Herschel* PACS), and 450 and 850 µm (SCUBA-2). Pixel sizes are 2.54, 3.0, 3.0, 2.0, and 3.0 arcseconds, at 24, 70, 160, 450, and 850 µm, respectively. Candidate 55 is the only object clearly visible at 24 µm. Candidate 37 is very faint at 24 µm but becomes clearly visible in the next image (at 160 µm). Other candidates are not visible until 250 or even 450 µm, but all are seen at both SCUBA-2 wavelengths.

4.4 Fluxes

4.4.1 24 µm fluxes

Fluxes for each of the five FHSC candidates were extracted from the MIPS 1 maps of Aquila using aperture photometry. Each image was analysed using *GAIA*, as with the YSOs in Chapter 3. Each aperture had a radius r = 3.5″, with background annuli between 1.71 and 2.29 r. This aperture encircles half of the first dark ring of the beam. Uncertainties were extracted from the corresponding error maps, using apertures of the same size, but without annuli. Fluxes from these apertures were corrected using a factor of 2.78, and a 4 % calibration uncertainty was added (Engelbracht et al. 2007). This corrective factor was used to account for the fact that not all of the MIPS point response function (a modified point spread function) lies within the aperture used. The aperture radius of 3.5″ was used as it is the smallest aperture size for which corrections are available. I tested flux extraction with these apertures on known sources in the Dunham et al. (2015) catalogue, and all fluxes were within 10 % of the literature values. These fluxes are given in Table 4.1.

4.4.2 *Herschel* Fluxes

Aperture photometry was also used to find fluxes for each candidate from the 70 and 160 µm maps. Apertures had 15″ radii, with annuli between 1.5 and 2.0 r, giving aperture corrections of 1/0.829 (70 µm) and 1/0.729 (160 µm, Balog et al. 2014). This aperture size was chosen to be consistent with photometry at 850 µm. Photometric uncertainties were then combined with a conservative calibration uncertainty of 15 per cent, following Kelly et al. (2012) and Könyves et al. (2015). The resulting fluxes are provided in Table 4.1.

Fluxes for each of the candidates were also obtained at 250 µm. According to the Recipe for SPIRE Photometry[3], aperture photometry is not recommended for use with SPIRE maps for point sources. Therefore, 250 µm fluxes were found by cross-matching FHSC candidate positions with the source catalogue of Könyves et al. (2015). These fluxes are also given in Table 4.1.

3. Available at herschel.esac.esa.int/hcss-doc-15.0/load/spire_drg/html/ch06s09.html

Table 4.1: Fluxes and upper limits for the five candidate FHSCs in Serpens South. Fluxes are given at 24 µm (*Spitzer* MIPS 1), 70 and 160 µm (*Herschel* PACS), and 450 and 850 µm (SCUBA-2). The positions given are the coordinates of the peak of flux at 450 µm.

ID	Position (J2000)	S_{24} (mJy)	S_{70} (mJy)	S_{160} (mJy)	S_{250} (mJy)	S_{450} (mJy)	S_{850} (mJy)
37	18:29:03.6 -01:39:07	≤ 1.0	1410 ± 220	15700 ± 2400	15400 ± 800	3995 ± 353	1076 ± 42
55	18:30:12.3 -02:06:57	2.3 ± 0.9	403 ± 83	4940 ± 790	6940 ± 450	1923 ± 306	639 ± 39
78	18:30:04.7 -01:59:59	≤ 1.1	≤ 104	2530 ± 440	2450 ± 470	810 ± 271	216 ± 33
131	18:29:00.0 -01:42:47	≤ 0.9	≤ 50	764 ± 155	1370 ± 460	916 ± 358	304 ± 43
230	18:29:41.0 -02:13:43	≤ 1.1	≤ 37	279 ± 125	718 ± 135	581 ± 358	197 ± 43

4.4.3 SCUBA-2 Fluxes

Flux extraction from the SCUBA-2 450 and 850 µm maps of Aquila used 10 and 15″ aperture radii, respectively. In this instance, aperture corrections of 1/0.72 and 1/0.85 were used at the respective wavelengths (Dempsey et al. 2013). Uncertainties were extracted from the error maps at the positions of each candidate, and then combined with SCUBA-2 calibration uncertainties of 5 % and 10 % at 850 and 450 µm, respectively. The use of a 10″ aperture radius for 450 µm photometry differs from the 15″ radius used to extract 70, 160, and 850 µm fluxes. However, this smaller aperture size means overall lower uncertainty on the 450 µm fluxes, and reduced background contamination (visible in Figure 4.3, particularly for candidates 37 and 55). The SCUBA-2 fluxes are given, along with the MIPS and *Herschel* fluxes, in Table 4.1.

4.4.4 Discussion of Fluxes

The candidates have varying levels of brightness, but all are faint at 24 µm, with only candidate 55 detected. Candidates 37 and 55 are the only ones detected at 70 µm, whereas all candidates are detected at both SCUBA-2 wavelengths. To quantify this 'faintness', the ratio of 450 µm flux to 24 µm flux (or upper limit) was calculated and compared to that of a known Class 0 protostar. IRAS 15398-3359 is a known Class 0 protostar in Lupus I (see Section 3.2 and Mowat et al. 2017), and has a 450 µm flux approximately 19 times greater than its flux at 22 µm. The 22 µm flux from WISE (Cutri et al. 2012) was used as the 24 µm MIPS 1 flux from Merín et al. (2008) was deemed unreliable due to source confusion.

In contrast to this ratio, all FHSC candidates in Serpens South exhibit a ratio S_{450}/S_{24} of at least 200 (the lowest allowed by the uncertainties and upper limits). The only candidate detected, 55, has a ratio $S_{450}/S_{24} \sim 840$.

The use of a smaller 10″ aperture radius for 450 µm photometry was accounted for by using a larger aperture correction, so this method will not artificially lower the 450 µm fluxes for this analysis. A 10″ aperture radius was also tested on the 70 µm map, but it was found to produce less consistent fluxes than a 15″ aperture radius, so an aperture radius of 15″ was maintained.

To test its effect on the extracted flux, the 'companion' of candidate 37 was removed from the 450 µm map, and photometry was carried on on source 37. The flux value thus obtained did not differ substantially, so this companion does not appear to significantly affect the measured flux value of candidate 37.

4.5 Results of the Investigation

Once the full table of fluxes for these five candidates was produced, it was made available to A.Young. Thus, her model SEDs could be fit to these FHSC candidate data. Her models comprise a grid, similar to that of Robitaille et al. (2006), with one or more parameters varying between these models.

To produce these models, radiation magnetohydrodynamical (RMHD) simulations were first implemented. The general method of these simulations is outlined by Bate, Tricco, and Price (2014), with changes explained in Young et al. (2018). A total of six different parameters could be varied to produce the RMHD models: initial temperature, incident interstellar radiation field, mass, rotation, radius, and magnetic field. Each parameter had between two and six possible values. Once the RMHD models were produced, synthetic SEDs were created using the radiative transfer code TORUS (Harries 2000). By varying initial parameters, a total of 1440 synthetic SEDs were produced for two RMHD models.

SEDs for all five candidates in Serpens South were fit by A.Young to her synthetic

SEDs using χ^2. Best-fitting models were obtained, and those with χ^2 within a factor of two of the best model were also considered. Figure 4.4, reproduced from Young et al. (2018), shows SEDs for the five FHSC candidates in Serpens South. The names used are from the literature, so the corresponding numerical designations used in this chapter have been added.

Candidates 131 (Aqu-MM1) and 230 (K242) were fit well by model SEDs with consistent properties, and are likely to be true FHSCs. In addition, candidate 131 is likely to have a high rotation rate and an edge-on inclination. Candidate 37 (Aqu-MM2) was not able to be constrained to the FHSC stage (though this has not been ruled out) due to an overlap between models from different evolutionary phases. No models were able to adequately fit Candidate 55 (SerpS-MM22) due to the relatively bright 24 µm flux, so its evolutionary stage has not been constrained. Finally, Candidate 78 (SerpS-MM19) appears likely to be either a more-evolved FHSC or to be undergoing the second collapse phase.

The scaling factor used to produce synthetic SEDs in Young et al. (2018) is inversely proportional to distance-squared. Therefore, results were examined using both the recent distance estimate to Serpens South of 436.0 pc (Ortiz-León et al. 2017a) and a closer value of 260 pc. This means that mass estimates for the FHSC candidates vary depending on the distance used. For example, candidate 131 has a mass of either 0.4 or 1.9 $M_\odot$ at 260 or 430 pc, respectively.

To summarise, this work was able to successfully identify two new FHSC candidates in Serpens South as probable FHSCs. Fitting model SEDs to potential FHSCs can, therefore, be used as a tool to identify these thus-far rare objects. This information can then allow targeted high-resolution observations of these objects to be undertaken with interferometers such as ALMA.

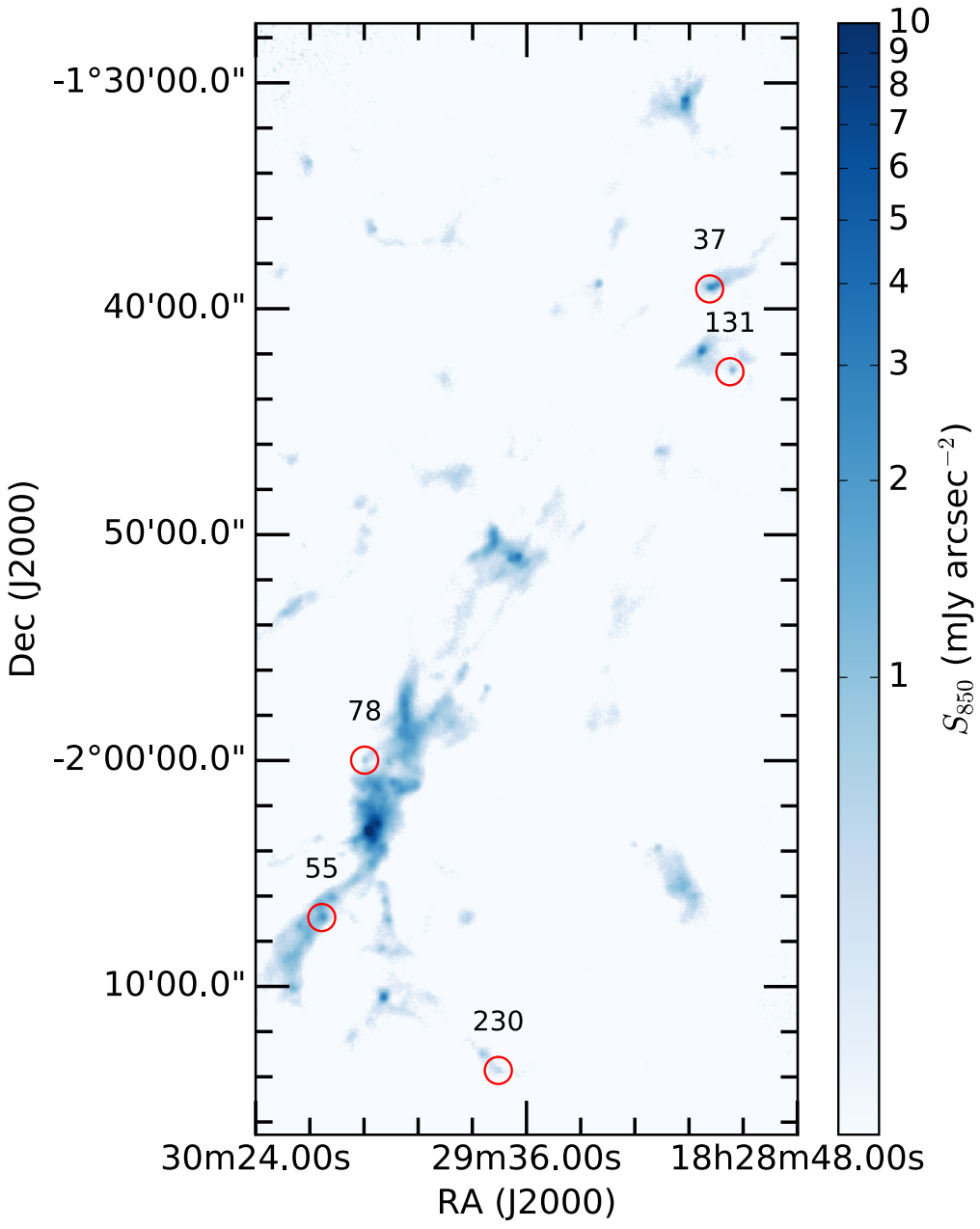

Figure 4.2: SCUBA-2 map of the Serpens South region at 850 µm. FHSC candidates are labelled - and identified using red circles.

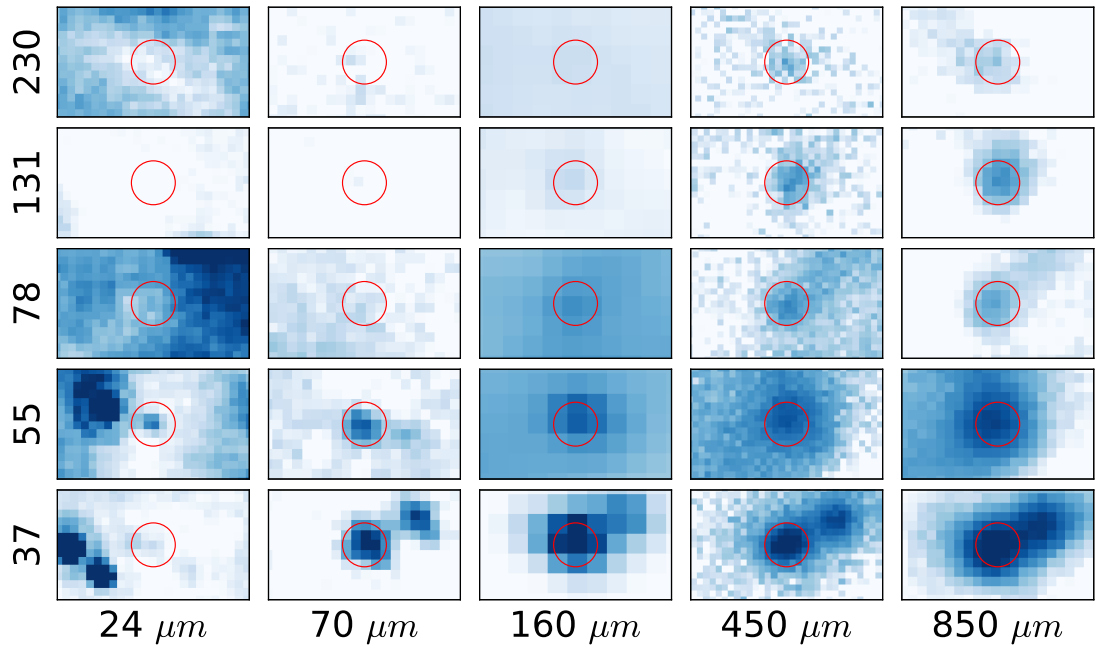

Figure 4.3: Candidate FHSCs in Serpens South, with their positions shown at five wavelengths. Red circles denote the positions of the candidates in each image, and their size represents the size of the aperture used in the photometry (3.5, 15.0, 15.0, 10.0, and 15.0″, respectively). These are centred on the peak flux position when the candidate is detected, and the 450 µm peak position when it is not. The same colour scales are used for all candidates at each wavelength, with the exception of 55 and 78 at 24 µm, as these are in a different map to the others.

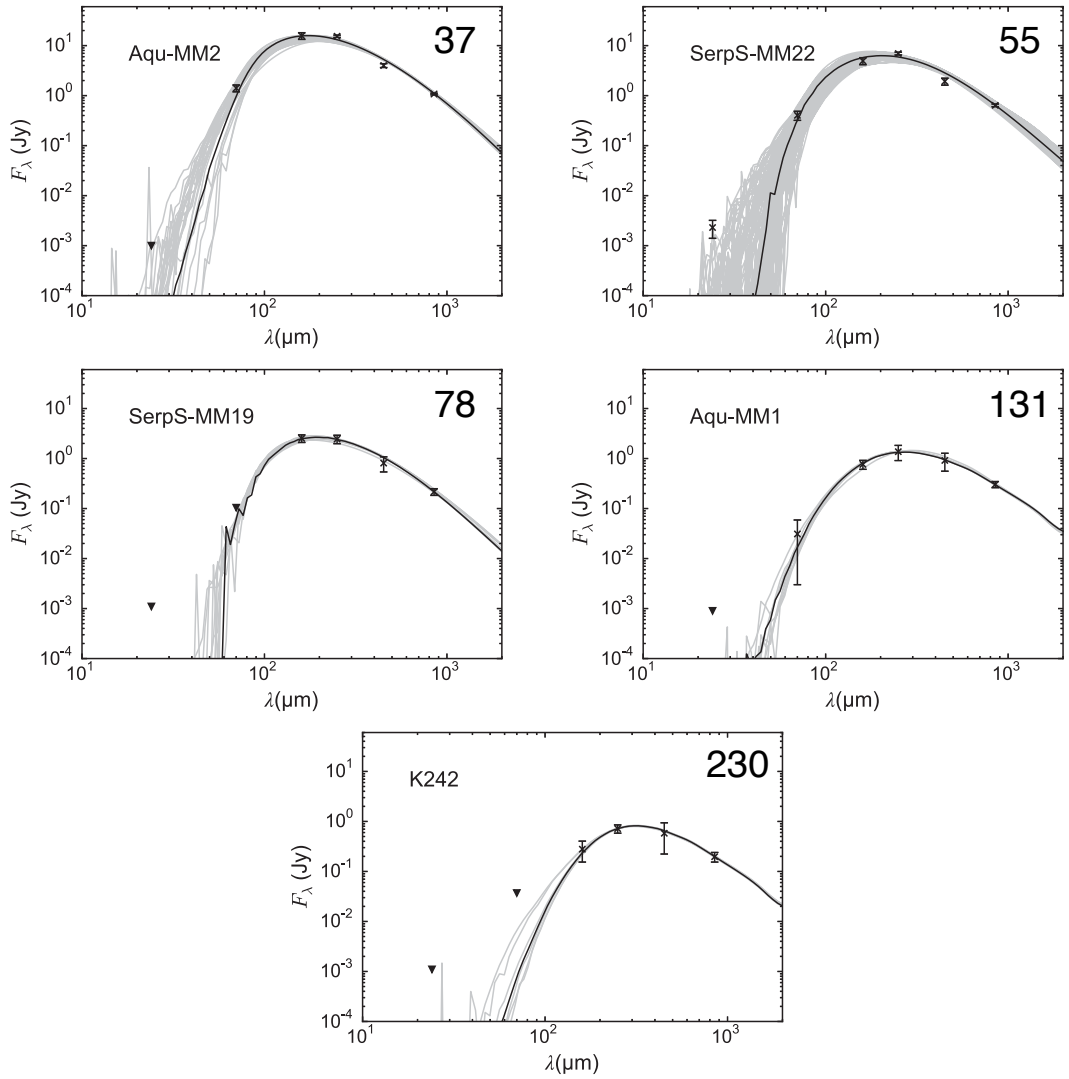

Figure 4.4: Reproduced from Young et al. (2018). SEDs of Candidate FHSCs in Serpens South, with well-fitting models plotted. Best-fit models are shown in black, while models with χ^2 within a factor of two of the best-fitting model are shown in grey. The FHSC SEDs have been labelled with the numerical designations used in this chapter.

Chapter 5

Protostars in the Gould Belt - Identification and Extraction

"Is it about my cube?"

— C.M.Burns

This chapter is the first of two chapters detailing my work - as part of the JCMT GBS - on producing a catalogue of protostars in the Gould Belt observed with SCUBA-2. The JCMT GBS maps enabled long-wavelength (450 and 850 μm) information to be obtained for a larger number of protostars than before. With these submillimetre observations, protostellar properties could be re-examined or calculated for the first time. Such properties include the duration of the protostellar stage of star formation, their luminosities, and the masses of their surrounding envelopes of gas and dust.

To calculate these properties, it was first necessary to define a sample of possible protostars. Their locations in the GBS maps could then be examined, and SCUBA-2 fluxes assigned to these objects. After a brief introduction, the overview of this chapter then details the SCUBA-2 observations and source-finding method in Section 5.2. Section 5.3 defines the sample of possible protostars from previous studies, and how SCUBA-2 sources were matched with these candidates. The results of the inclusion of submillimetre flux will be presented in Chapter 6.

5.1 Introduction

Classification of YSOs is commonly based on their mid-infrared spectral index. Mid-infrared spectral indices were used initially to classify YSOs as either a Class 0/I protostar, a Flat-spectrum object, or a Class II/III T-Tauri star (Wilking, Lada, and Young 1989; Greene et al. 1994). Mid-infrared spectral index, however, is not able to distinguish between Class 0 and Class I sources, so bolometric temperature ($T_{\rm bol}$, Myers and Ladd 1993) is often the preferred discriminator (Enoch et al. 2009; Dunham et al. 2015). Observations at submillimetre wavelengths are required to distinguish between Class 0 and Class I protostars. The Spectral Energy Distributions (SEDs) of protostars have large contributions to flux from the far-infrared to submillimetre wavelength regime (André, Ward-Thompson, and Barsony 1993), so calculations of $T_{\rm bol}$ which do not include wavelengths in this regime will be inaccurate (Enoch et al. 2009).

The YSOs in the Gould Belt have recently been classified based on mid-infrared surveys with the *Spitzer* Space Telescope. A total of 18 molecular clouds in the Gould Belt were observed for the *Spitzer* (Werner et al. 2004) 'From Molecular Cores to Planet-Forming Disks' (c2d, Evans et al. 2003; Evans et al. 2009) and 'Gould Belt' (GB) Legacy surveys. These surveys covered most of the nearby clouds within 500 pc. Taurus and Orion were not included, as they were the subject of dedicated surveys (Rebull et al. 2010; Megeath et al. 2012, respectively). Observations were carried out at 3.6, 4.5, 5.8 and 8.0 µm with the Infrared Array Camera (IRAC, Fazio et al. 2004), and 24, 70 and 160 µm with the Multiband Imaging Photometer for Spitzer (MIPS, Rieke et al. 2004).

Using these observations, Dunham et al. (2013), henceforth referred to as D13, classified 230 YSOs in the 18 Gould Belt regions as protostellar (Class 0 or I) using $T_{\rm bol}$. Unlike the classifications using mid-infrared spectral indices, these are able to distinguish between Class 0 and Class I objects. These sources were subsequently included in the catalogue of the YSOs in the Gould Belt presented by Dunham et al. (2015), hereafter referred to as D15. As part of the catalogue work of D15, durations of each of the protostellar phases were estimated, based on the ratio of Class 0 and Class I objects to a specified reference class. The numbers of Class 0/I objects, however, were based on the $T_{\rm bol}$ calculations of D13, and

many of these (100) were implemented without any available fluxes in the far-infrared and submillimetre regime. Additionally, a YSO was only considered protostellar if it had at least one detection at a wavelength $\lambda \geq 350$ µm. Therefore, despite $T_{\rm bol}$ being a superior method of classifying protostars, protostars were missed as many of the YSO candidates lacked long-wavelength observations.

Observations by SCUBA-2 as part of the JCMT GBS provide the opportunity to improve the sampling of SEDs for many sources across the Gould Belt. Observations were obtained at both 450 and 850 µm of the regions of the Gould Belt accessible to the JCMT. The fluxes these observations provide can be used to update the SEDs of hundreds of YSOs in the regions observed by both SCUBA-2 and the *Spitzer* c2d / GB surveys. Therefore, we examine the YSOs of D15 and present a revised catalogue of Class 0/I objects in Gould Belt clouds.

5.2 SCUBA-2 Submillimetre Fluxes

5.2.1 The GBS SCUBA-2 Dataset

Many SCUBA-2 dust continuum observations of $A_{\rm V} > 3$ Gould Belt regions, at both 450 and 850 µm, have been published previously by the JCMT GBS team. These include The Aquila Rift / Serpens South / MWC 297 (Rumble et al. 2015; Rumble et al. 2016), Auriga-California (Broekhoven-Fiene et al. 2017), Cepheus (Pattle et al. 2017), IC 5146 (Johnstone et al. 2017), Lupus I (Mowat et al. 2017), Ophiuchus (Pattle et al. 2015), Orion (Salji et al. 2015a; Mairs et al. 2016; Kirk et al. 2016; Lane et al. 2016), Perseus (Chen et al. 2016), and Taurus (Buckle et al. 2015; Ward-Thompson et al. 2016). Additionally, some regions have been observed, and will be published in the future, including Corona Australis (Bresnahan et al., in prep.), the Pipe Nebula, and Serpens Main. The region referred to in this chapter as Serpens North is found at the north-eastern edge of the Aquila rift. It was considered as part of Aquila by D15, but it is treated separately in this work. In addition, we consider Serpens South as part of Aquila in this study.

The SCUBA-2 continuum observations of all regions are of the same form as the

Table 5.1: Catalogue of selected JCMT MJLSG33 observations of Serpens Main and Serpens North. τ_{225} is the opacity of the atmosphere at 225 GHz when each observation was undertaken. Approximate coordinates of PONG centres are provided.

	Serpens North $18^h39^m05^s$ $+00°27'55''$			Serpens Main 1 $18^h30^m00^s$ $+01°14'45''$			Serpens NH3 $18^h29^m11^s$ $+00°29'00''$		
Scan #	Date	Obs #	τ_{225}	Date	Obs #	τ_{225}	Date	Obs #	τ_{225}
1	29/09/2013	00016	0.07	18/05/2012	00068	0.05	08/07/2012	00037	0.08
2	29/09/2013	00017	0.07	18/05/2012	00071	0.05	08/07/2012	00040	0.07
3	29/09/2013	00022	0.07	19/05/2012	00059	0.05	18/08/2012	00029	0.02
4	26/02/2014	00072	0.06	19/05/2012	00062	0.05	18/08/2012	00032	0.03
5	01/03/2014	00083	0.04	...	...	...	03/09/2012	00025	0.06
6	01/03/2014	00084	0.04	...	...	...	03/09/2012	00028	0.06
7	05/03/2014	00081	0.06	...	...	...	...	...	...

Lupus I maps detailed in Chapter 2. Details of the observations of most individual regions can be found in the region-specific GBS papers. Observations of Serpens Main and Serpens North, however, have not previously been published by the JCMT GBS. Therefore, details of the individual observations used to produce the maps of these regions are provided in Table 5.1. Most of these observations were completed in dry band 2 weather, with 225 GHz opacity $0.05 < \tau_{225} < 0.08$ (Dempsey et al. 2013). The 450 and 850 µm observations of Serpens Main and Serpens North are provided in Section A.1.

Several of the aforementioned regions were not catalogued by D13 and D15, and so they are excluded from further analysis in this work. Overall, this work looks at the regions observed by SCUBA-2 that were also covered by the *Spitzer* c2d / GB surveys. Therefore, the final list of regions considered in this chapter is: Aquila / Serpens South, Auriga / California, Cepheus, Corona Australis, IC 5146, Lupus I, Ophiuchus, Perseus, Serpens, and Serpens North.

The distances to these regions are given in Table 5.2. Compared to the distances used in D13 and D15, several have been recently updated. For example, distances to Serpens / Aquila, and Ophiuchus, are now quoted from Ortiz-León et al. (2017a), and Ortiz-León et al. (2017b), respectively. Additionally, the distance to Lupus I has been updated using Galli et al. (2013), which was also done in Chapter 3. Distances to certain regions, however, remain uncertain. In particular, there is evidence to suggest that IC 348 in Perseus may be more distant than the western part of the cloud containing, e.g., NGC 1333, with distances

Table 5.2: Molecular Clouds Observed by both the JCMT GBS, and *Spitzer* c2d / GB Survey

Cloud	Distance (pc)	Distance Reference	A_V[a] (mag)	SCUBA-2 Coverage (degree^2)	Number of *Spitzer* YSOs[c] Total	In JCMT GBS maps
Aquila / Serpens South / MWC297	436.0*	1	12.4	2.272	1095	753
Auriga / California	450.0	2	7.5	3.338	133	114
Cepheus (L1228)	200.0	3	5.4	0.562	103	89
Cepheus (L1251)	300.0	3	5.4	0.961	103	89
Cepheus (South)	306.5[b]	4	5.4	2.013	103	89
Corona Australis	130.0	5	7.9	1.511	54	51
IC 5146	950.0	6	3.6	1.562	132	132
Lupus I	182.0*	7	2.9	1.590	13	11
Ophiuchus	137.3	8	9.8	3.952	292	234
Ophiuchus North	130	9	5.6	1.725	10	2
Perseus West	250.0[d]	10	5.9	3.982	385	378
Perseus IC 348	250.0	10	5.9	1.987	385	378
Serpens (Main)	436.0*	1	9.6	1.123	227	206
Serpens North	436.0*	1	12.4	0.570	224	93

References for the provided distances: (1) Ortiz-León et al. (2017a), (2) Lada, Lombardi, and Alves (2009), (3) Kun, Kiss, and Balog (2008), (4) Straizys et al. (1992), (5) Neuhäuser and Forbrich (2008), (6) Harvey et al. (2008), (7) Galli et al. (2013), (8) Ortiz-León et al. (2017b), (9) de Geus, de Zeeuw, and Lub (1989), (10) Enoch et al. (2006).
[a] Mean extinction towards all Class II YSOs in the cloud.
[b] This distance is the mean value of the distances to two sub-regions within Cepheus South, L12(47/58), and L12(72/74).
[c] Values for Cepheus and Perseus are overall totals for the entire regions, with SCUBA-2 sub-regions combined.
[d] Discussed further in the main text.
* The distances to these regions have been updated compared to D15.

of 260 pc and 220 pc, respectively (Ĉernis 1990, 1993)). For the western part of Perseus, we adopt a distance of 250 pc. This is consistent within uncertainties with both the closer distances of Hirota et al. (2008) and Hirota et al. (2011) (235 ± 18 pc and 232 ± 18 pc, respectively) and the greater Gaia parallax distance of 270 pc Herczeg et al. (2017). This distance was also used by D15. Many of these distances will be updated again based on the recent Gaia Data Release 2. Early analysis indicates that the distance to IC 5146 may be approximately 25 % closer than the estimate of 950 pc we use here. However, these results have not yet been published.

The SCUBA-2 observations were reduced with MAKEMAP, using the process explained in Chapter 2. The data were gridded to 3″ pixels at 850 µm and 2″ pixels at 450 µm for all maps. We use the GBS Data Release 3 (DR3, Kirk et al. 2018, in prep.). This is explained in Section 2.3.2

5.2.2 SCUBA-2 Source Identification

Once the reduced 450 and 850 µm maps were obtained, the emission in them was split into separate SCUBA-2 sources using the FellWalker (Berry 2015) clumpfinding algorithm (first detailed in Chapter 3). FellWalker was used separately on the 450 and 850 µm maps, to find individual sources within the large-scale cloud structures. FellWalker was used in preference to the CLUMPFIND algorithm (Williams, de Geus, and Blitz 1994), because CLUMPFIND can create erroneous sources by over-splitting larger cores of emission (Watson 2010).

FellWalker has now been used in analyses by several JCMT GBS papers (e.g., Rumble et al. 2015; Kirk et al. 2016; Mowat et al. 2017; Johnstone et al. 2017), with the exact values of certain parameters varied according to the goals of the study. For this work, the aim of the clumpfinding was to identify emission associated with individual protostars, rather than larger scale cloud substructure. To achieve this degree of specificity, the values of several parameters were changed from the defaults. These parameters are listed in Table 5.3.

A background subtraction was performed on all SCUBA-2 maps prior to the implementation of FellWalker, using the Starlink FINDBACK command. Consequently large-scale extended emission at scales larger than 90" was removed from the maps. Such emission is not expected to be associated with individual protostellar cores. Therefore, it was excluded to prevent additional, unassociated emission from contributing to the flux values of YSOs. This means that our FellWalker cores should represent the more compact structure associated with individual protostars. To run FellWalker an RMS value of 1.0 was used, as the algorithm was implemented on signal-to-noise maps. This choice allowed for the same parameters to be used on all maps, regardless of variations in local noise levels, both between regions and within individual regions.

Once the FellWalker algorithm was applied to all maps - at each wavelength - a catalogue of individual objects was available for each of these maps. The observed properties given for each identified source include the right ascension (RA) and declination (Dec) of the peak (both in degrees), the peak flux density (mJy/arcsec^2), and the total integrated flux over the FellWalker clump area (mJy). Each continuum map also has a corresponding

Table 5.3: FellWalker parameters changed from defaults.

Parameter	Function	Value (Default)
MaxJump	Define how far out to search for higher values once a peak is found. Outside this radius, a new peak is defined.	2.0 (4.0)
MinDip	Gives the minimum value for a drop in signal from a peak before another peak can be defined.	1.0*RMS (3.0*RMS)
MinHeight	Specifies the minimum value a peak can have.	3.0*RMS (2.0*RMS)
MinPix	Defines the minimum number of pixels in a core.	7 (16)

core map, showing the core number assigned to each pixel. This information allowed source boundaries (at 450 and 850 µm) to be plotted over the continuum maps. Figure 5.1 shows the FellWalker source boundaries at 450 and 850 µm plotted over the NGC 1333 region of Perseus. Objects are larger at 850 µm, and almost all 450 µm flux detected is located within the corresponding 850 µm boundary. Occasionally, sources at 450 µm can straddle 850 µm boundaries.

5.3 Assigning Submillimetre Fluxes to Protostellar Candidates

Once FellWalker had provided catalogues of SCUBA-2 sources at 450 and 850 µm, the sources were matched to YSOs previously-identified by selected literature surveys. The 450 and 850 µm catalogues were separately matched to the YSOs of the D15 catalogue.

5.3.1 Literature Sources

The D15 catalogue of Gould Belt YSOs, first introduced in Section 5.1, comprises 2966 sources. Using total YSO counts from D15, some Gould Belt regions are significantly more populated than others. For example, Aquila (1095), Perseus (385) and Ophiuchus (292) have many sources, whereas Lupus I (13), and Ophiuchus North (10) have comparatively

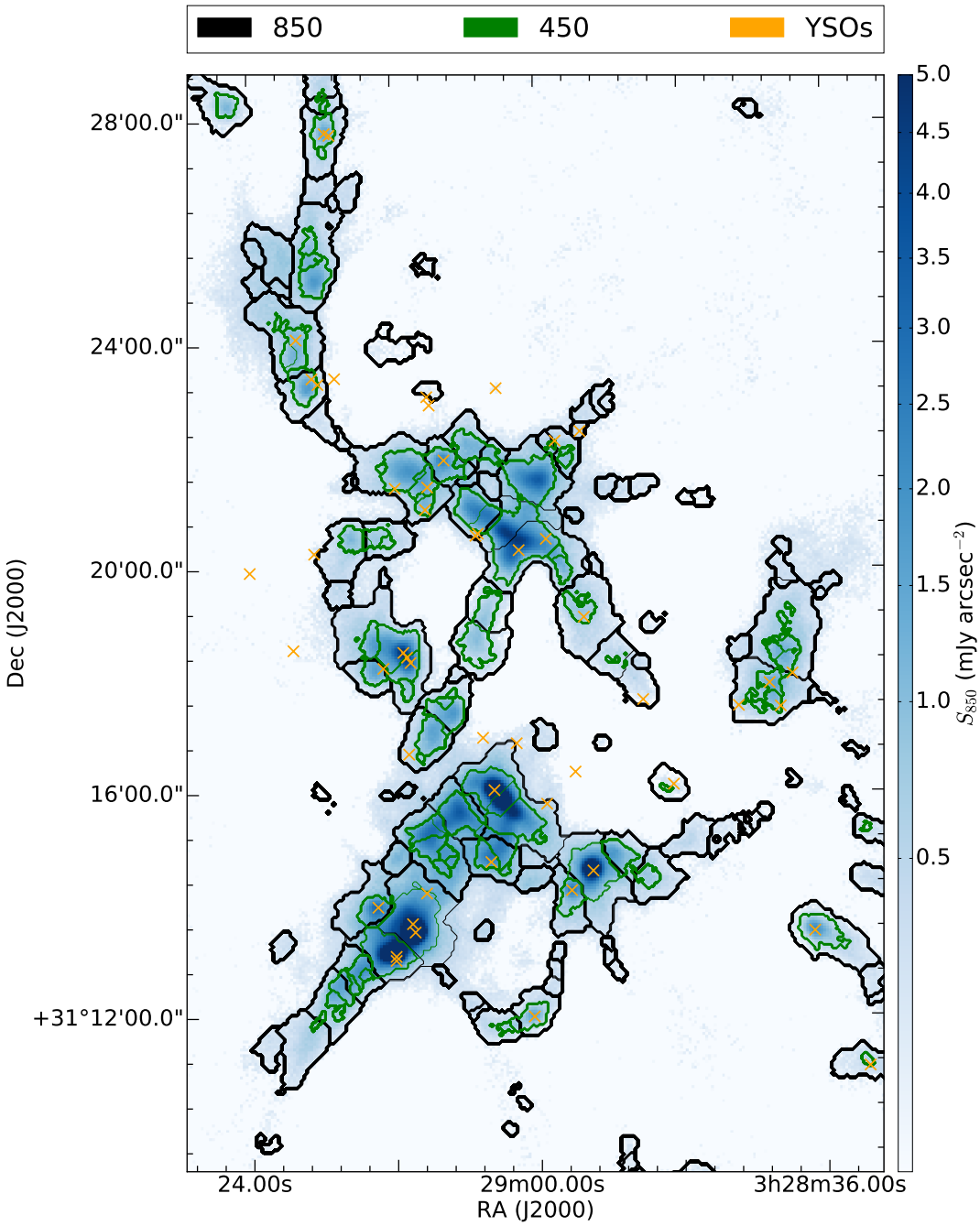

Figure 5.1: FellWalker 450 and 850 µm core boundaries for the NGC 1333 region in Perseus. The 850 µm core boundaries are shown in black, while the 450 µm core boundaries are shown in green. Amber crosses denote the positions of the *Spitzer* candidate protostellar sources from the D15 catalogue. The background image is the SCUBA-2 850 µm continuum map shown with square-root scaling. This image was not background-subtracted.

few sources (see Table 5.2 for source numbers in all regions in this chapter.). These sources have also been observed by other surveys. Therefore, in addition to SCUBA-2 and *Spitzer* fluxes, we incorporate data from many additional surveys also used in D15. Data from the *Wide-field Infrared Survey Explorer* (WISE, Wright et al. 2010) at 12 and 22 µm were taken from the WISE all-sky catalogue (Cutri et al. 2012). The Two Micron All Sky Survey (2MASS, Skrutskie et al. 2006) provided J, H, and K band photometry, obtained from the 2MASS all-sky catalogue (Cutri et al. 2003). Millimetre fluxes, from 1100 µm observations with *Bolocam* (Glenn et al. 2003), were taken for Ophiuchus, Perseus, and Serpens (Enoch et al. 2007). Additionally, 350 µm observations with SHARC-II (Dowell et al. 2003) provided fluxes for some sources in the catalogue (Wu et al. 2007; Suresh, Arce, and Dunham 2015). Further optical and infrared photometric data were used by D15, after being compiled by the authors of individual cloud papers (see Table 1 of D15).

The *Spitzer* fluxes were combined with these literature observations of the candidate YSOs to produce SEDs for each object, following Evans et al. (2009) and D13. After they constructed SEDs, a mid-infrared spectral index was calculated by D15 for each object in the catalogue. The method for calculating the mid-infrared spectral index has already been explained in Section 3.2.3.

Source classifications according to α vary substantially between Gould Belt regions. Referring to D15, Perseus has almost as many Class 0/I sources as Aquila (76 and 83, respectively) whereas it has less than one third the total number of sources of Aquila. It should be noted, however, that the W40 region in Aquila is likely incomplete in the *Spitzer* catalogue due to image saturation (Rumble et al. 2016). Previously undetected YSOs have been discovered here using X-ray observations (Kuhn et al. 2010).

In order to obtain a preliminary list of candidate protostars for our work, we selected every YSO in the D15 catalogue with a value of α > -0.3. As well as Class 0/I YSOs, this criterion includes all the flat-spectrum sources, as such objects may also be protostellar in nature. Additionally, every source with a value of $\alpha \leq -0.3$, but an extinction-corrected bolometric temperature $T_{\rm bol}$ < 650 K (as calculated by the *Spitzer* team), was added to the preliminary list. The value of 650 K is used to distinguish between protostellar and non-protostellar objects, with lower values corresponding to protostars (Enoch et al. 2009).

Finally, sources that fulfilled neither of these criteria, but had at least one available detection longward of 350 µm (defined as a 'core' in D15) were included. Once this initial list was obtained, YSOs outside the fields of view of our SCUBA-2 maps were excluded. These selection criteria resulted in a total of 592 protostellar candidates for which SCUBA-2 fluxes could be sought. We judged that the inclusion of all YSOs from D15 would lead to an unacceptable level of contamination, whereby non-protostellar objects would be classified as protostars due to coincidental association with submillimetre emission. It is possible, however, that this may lead to some genuine protostars being missed.

5.3.2 Cross-matching SCUBA-2 Sources With Protostellar Candidates

Next, the list of 592 *Spitzer* protostellar candidates was cross-matched with the FellWalker sources. This comparison was done separately at 450 and 850 µm. The core peak positions, provided in the FellWalker catalogues, were matched separately to the *Spitzer* catalogue RA and Dec values for each source. Initially, all peak positions within the effective SCUBA-2 beam full-width at half-maximum (FWHM, 9.6 and 14.1″ at 450 and 850 µm, respectively, Dempsey et al. 2013) of a *Spitzer* protostellar candidate position were recorded as matches.

In many cases, a single protostellar candidate matched to a single core, and no further discrimination was required. In this case, the candidate was assigned the total flux of the core. Some cores were matched with more than one candidate, and the candidates were also within a SCUBA-2 beam FWHM of each other. In these cases, the candidates were flagged as 'blended', and each was assigned the total flux of the core. Therefore, the core fluxes act as upper limits for each of the candidates. In cases where a core contained multiple sources separated by a distance greater than one SCUBA-2 beam FWHM, the candidate closest to the peak position was retained as a match, with the farthest given an upper limit (see below). The increased resolution at 450 µm sometimes produces subdivision not seen at 850 µm. In such cases, two *Spitzer* YSOs within a single 850 µm source could be matched to two separate peaks at 450 µm.

The RA and Dec offsets for each YSO that matched to a SCUBA-2 peak position are plotted at 450 and 850 µm in Figure 5.2. The RA offsets visibly have a non-zero mean.

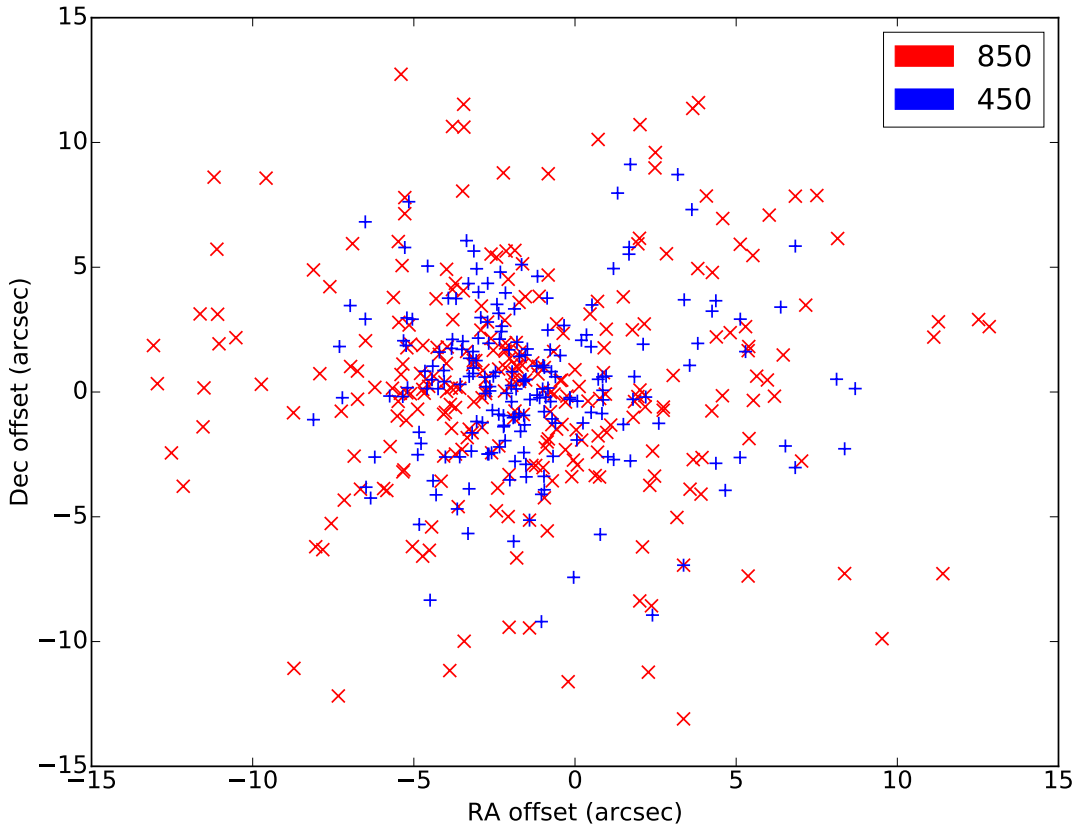

Figure 5.2: Offsets between YSO catalogue positions and FellWalker peaks at 450 and 850 µm. 850 µm points are plotted with red crosses and 450 µm offsets are shown using blue plus symbols.

We investigated whether a correction would be possible, but mean offsets were poorly-constrained in individual regions. For example, the average 850 µm RA offset in Aquila is -0.5 ± 0.8, while in Auriga it is -2.4 ± 0.9. Furthermore, the effect on the number of matched sources would have been minimal. Figure 5.2 shows that most matches are close to the SCUBA-2 peak - few are found one SCUBA-2 FWHM away.

When a source did not match to any peak, but was still within a core boundary (and thus an area of submillimetre emission), we considered the source a match and calculated an upper limit. To calculate this limit, the SCUBA-2 450 and 850 µm maps were smoothed separately over a scale of five pixels (the closest odd-integer number to the beam sizes at both wavelengths) to eliminate local noise spikes. The pixel value at the *Spitzer* RA and Dec position in the smoothed map was then used as the peak value (S_0) of a one-dimensional

Table 5.4: Number of protostellar candidates with each type of SCUBA-2 detection.

Match Type	Flag	N_{sources}		
		450 µm	850 µm	Best
Lone	L	167	219	257
Blended	B	30	54	42
Limit (in core)	U	81	136	112
Limit (noise)	N	314	183	181

Gaussian distribution of flux, where total flux

$$S_{\text{TOT}} = 2\pi \left(\frac{FWHM}{\sqrt{8log2}} \right)^2 S_0 \tag{5.1}$$

is used as an upper limit. The standard SCUBA-2 beam sizes are used to provide the value of $FWHM$.

For candidates which did not lie within the boundaries of any core, Equation 5.1 was again used to estimate an upper limit. In this instance, S_0 was calculated based on the local noise level at the position of the *Spitzer* candidate in the smoothed SCUBA-2 map. A value for S_0 of 3 σ was used for all of these undetected sources, to match the minimum detection criterion for FellWalker (Table 5.3). We consider candidates outside core boundaries at both 450 and 850 µm as undetected by SCUBA-2. Upper limits for these sources are still provided, however, for completeness.

The numbers of sources with each type of match / limit are provided in Table 5.4, at both 450 and 850 µm. If the detection type differed between 450 and 850 µm, the best type was used to label the object (with lone being the best, and noise being the worst). In such a case, both fluxes were still used to construct SEDs for each object.

Once the source matching was implemented on the entire list of protostellar candidates, the new SCUBA-2 fluxes were collated with the previously available fluxes - from the surveys listed in Section 5.2.1 - used in D15. This combination allowed for the creation of a final list of 592 candidate protostars and an updated list of fluxes for each, including their corresponding SCUBA-2 fluxes at 450 and 850 µm. This full table is available in Appendix B as Table B.1, and an example table containing the SCUBA-2 fluxes for 15 assorted

Table 5.5: SCUBA-2 450 and 850 µm fluxes for candidate protostellar YSOs.

Index No.	Cloud	*Spitzer* ID	S_{450} (mJy)	Flag$_{450}$[1] (450 µm)	S_{850} (mJy)	Flag$_{850}$[1] (850 µm)	Core?[2] *Spitzer*	$\alpha'_{\text{protostellar}}$[3] *Spitzer*
8	Aquila	J182847.7-013807	2180	B	404	B	N	Y
24	Aquila	J182912.8-020350	1230	L	348	L	N	Y
71	Aquila	J183003.1-020234	≤ 4430	U	≤ 1410	U	N	Y
92	Aquila	J183015.6-015035	≤ 194	N	178	L	N	N
176	Auriga	J042953.4+351548	≤ 219	N	≤ 187	U	N	N
243	Corona Australis	J190141.5-365831	9820	L	2560	L	Y	N
276	IC 5146	J215214.3+471454	≤ 452	N	≤ 36.6	N	N	Y
321	Ophiuchus	J162625.6-242428	≤ 3580	U	≤ 1070	U	Y	Y
373	Ophiuchus	J162857.8-244054	≤ 433	N	≤ 38.8	N	Y	Y
442	Perseus West	J032910.4+311331	87900	B	16700	B	Y	Y
458	Perseus West	J032918.7+312325	≤ 813	U	1230	B	Y	N
473	Perseus West	J033217.9+304947	15000	L	4020	L	Y	Y
498	Perseus IC348	J034351.0+320308	3530	L	≤ 317	U	Y	N
528	Serpens	J182851.2+001927	≤ 222	N	≤ 30.4	N	Y	N
540	Serpens	J182909.0+003128	15300	B	2580	B	N	N

[1] Flags: L - lone match, B - blended match, U - unmatched, within submillimetre emission, N - not detected.
[2] Denotes whether the candidate had a previously published millimetre or submillimetre detection.
[3] $\alpha'_{\text{protostellar}}$ signifies a value of $\alpha' > 0.3$.
Note: SCUBA-2 uncertainties from flux calibration, not included in the table, are 8 per cent and 12 per cent at 850 µm and 450 µm, respectively (Dempsey et al. 2013).
Note: The full table is available online DETAILS.

protostellar candidates is provided - as Table 5.5. These example YSOs represent a diverse range of source types from the *Spitzer* catalogue. For instance, objects with and without previous submillimetre fluxes are included, and a range of protostellar and non-protostellar mid-infrared spectral indices is also included. Further diversity is provided by including sources with all SCUBA-2 match types detailed in Table 5.4. Photometric uncertainties are not included, as their effect is negligible when compared to the SCUBA-2 calibration uncertainties of 8 % and 12 % per cent at 850 µm and 450 µm, respectively (Dempsey et al. 2013). Figure 5.3 shows 850 µm images of each of the sample SCUBA-2 sources listed in Table 5.5. Figure 5.4 shows 450 µm images of the same sources.

With fluxes now obtained for all protostellar candidates, their properties could be examined. This analysis is detailed in Chapter 6. The final part of this chapter first compares SCUBA-2 fluxes to SCUBA fluxes for each source, when possible. Next, SCUBA-2 FellWalker fluxes are compared to those obtained with the *Getsources* source extraction algorithm.

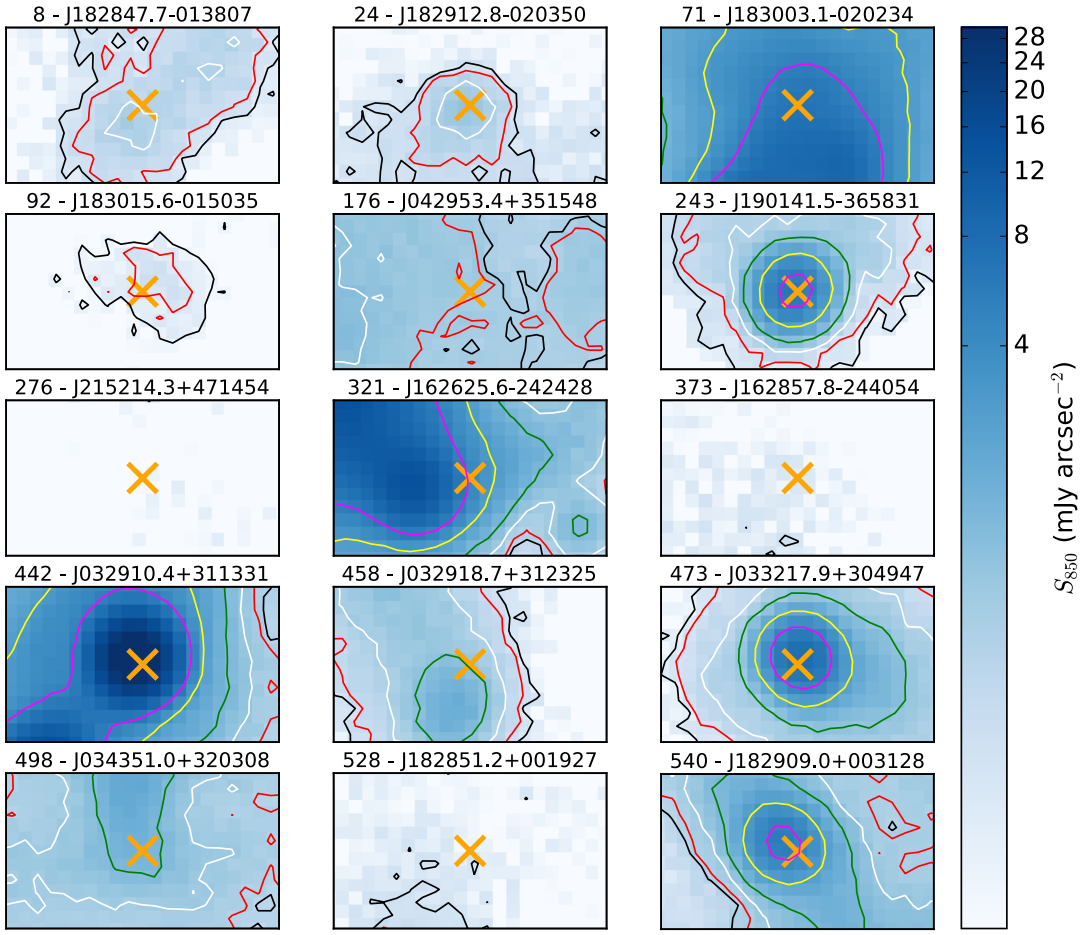

Figure 5.3: 850 µm images of each source in Table 5.5. The literature source positions are marked with amber crosses, and each image is 63″ x 36 ″, with each pixel being 3″ x 3″. Pixel-by-pixel flux is shown with a log scaling, and is the same across all images. Contours are shown at the 3, 5, 10, 20, 50, and 100 σ levels, represented by black, red, white, green, yellow, and cyan, respectively.

5.4 SCUBA-2 Flux Comparisons

5.4.1 Comparing SCUBA-2 fluxes to the SCUBA Legacy Catalogue

We cross-matched all of our protostellar candidates with the sources in the SCUBA Legacy Catalogue (Di Francesco et al. 2008) at 850 µm. A match radius of one SCUBA-2 beam FWHM was used and only candidates which directly matched SCUBA-2 peaks were included (lone and blended sources in Table 5.4). This resulted in a list of 100 sources with directly comparable peak and overall fluxes observed with SCUBA and SCUBA-2.

The comparison between SCUBA and SCUBA-2 fluxes is shown in Figure 5.5. On initial inspection there appears to be a significant amount of variation between SCUBA

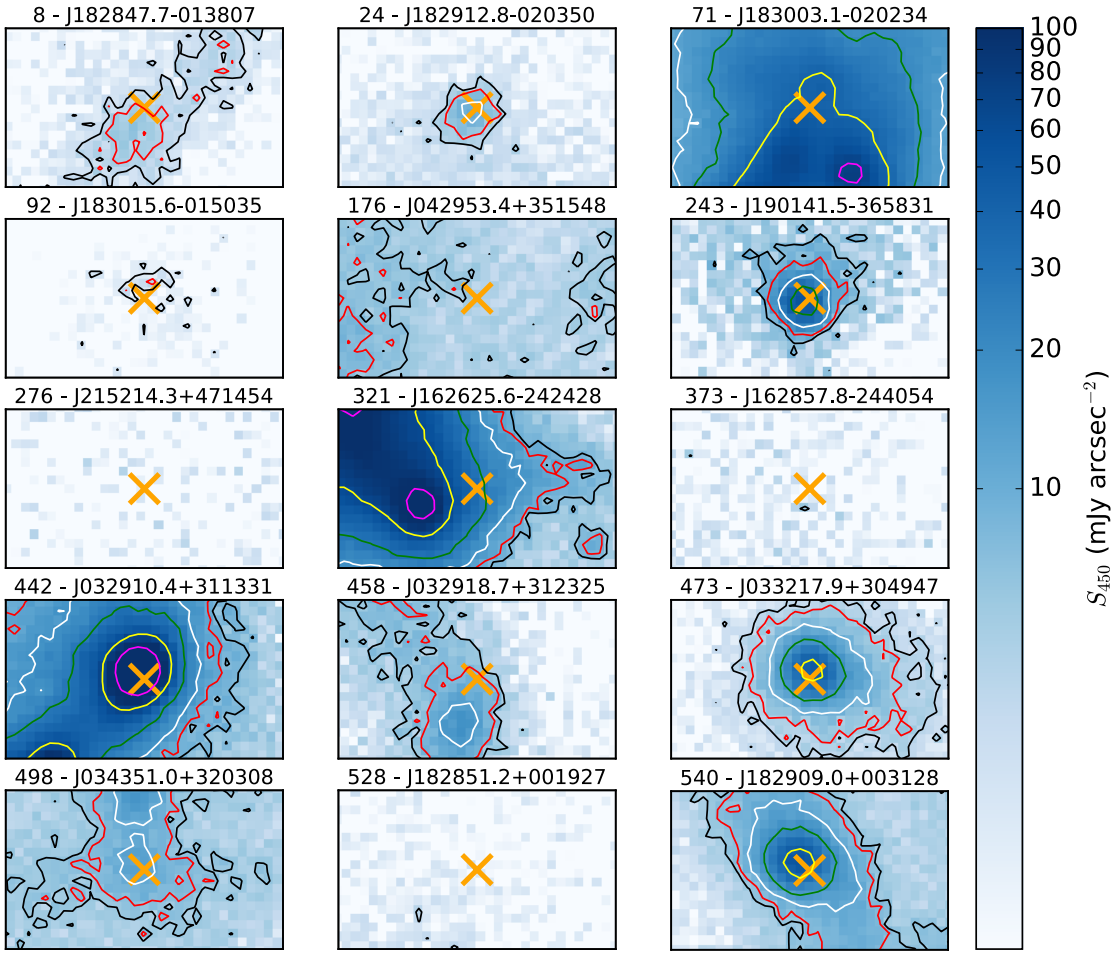

Figure 5.4: 450 µm images of each source in Table 5.5. The literature source positions are marked with amber crosses, and each image is 63″ x 36 ″, with each pixel being 2″ x 2″. Pixel-by-pixel flux is shown with a log scaling, and is the same across all images. Contours are shown at the 3, 5, 10, 20, 50, and 100 σ levels, represented by black, red, white, green, yellow, and cyan, respectively.

and SCUBA-2 fluxes for many sources. As SCUBA and SCUBA-2 have similar wavelength coverage and angular resolution (due to both being on the JCMT), large discrepancies would not be expected. Small variations due to the different observing modes are possible (Holland et al. 1999; Holland et al. 2013). In addition, variations in flux can be caused by different methods of assigning flux to sources. For example, SCUBA legacy fluxes were obtained using CLUMPFIND rather than FellWalker. In addition, 450 µm fluxes in the SCUBA catalogue were found by taking the positions of 850 µm sources identified with CLUMPFIND, rather than being separately identified. Therefore it is unsurprising that fluxes can vary between catalogues.

A comparison of peak fluxes avoids this issue, as peak fluxes do not vary with, for

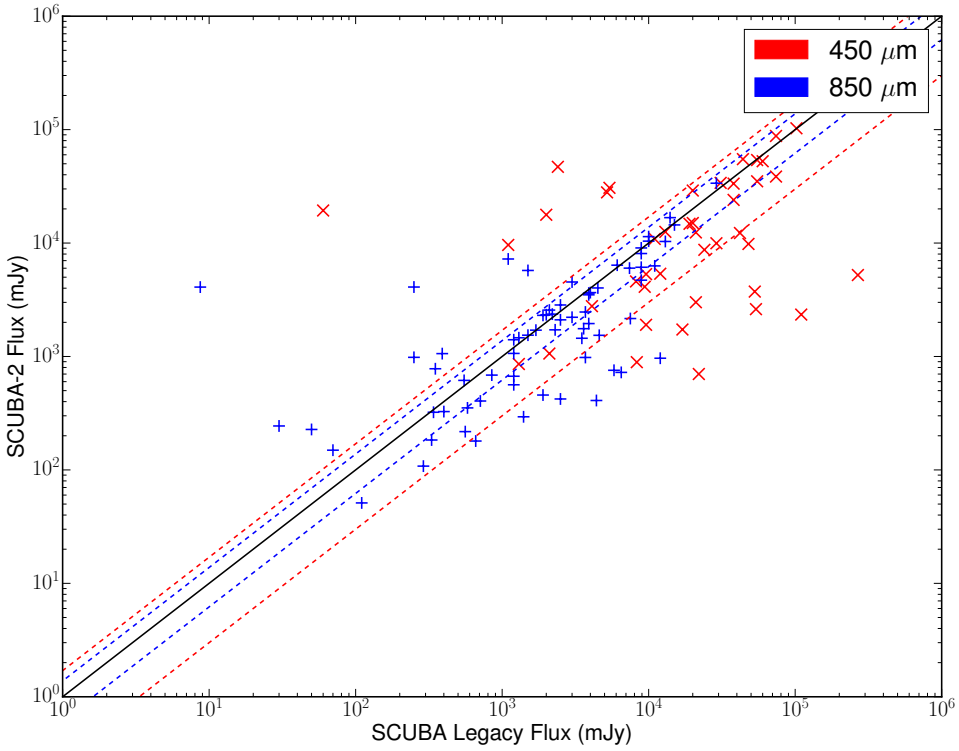

Figure 5.5: SCUBA Legacy and SCUBA-2 850 µm fluxes plotted for 100 protostellar candidates. The solid black line represents a 1:1 flux ratio, with 3 σ uncertainty intervals shown by dashed blue lines and 5 σ uncertainties shown by dashed red lines. Blue plus symbols represent 850 µm fluxes while red crosses are used to show 450 µm fluxes.

example, the size of a clump. Therefore, figure 5.6 shows the relation between SCUBA and SCUBA-2 peak fluxes for these 100 sources, distinguished by molecular cloud. The comparison is only made at 850 µm as this was the wavelength used to identify sources in the SCUBA Legacy Catalogue.

Average SCUBA-2/SCUBA peak flux ratios were calculated for four clouds: Corona Australis, Ophiuchus, Perseus, and Serpens. Only sources with a peak flux greater than 0.35 Jy/beam were compared, following Mairs et al. (2017). The results of these calculations are shown in Table 5.6. SCUBA-2 peak fluxes are on average higher than the SCUBA peak fluxes. A large systematic discrepancy between SCUBA and SCUBA-2 fluxes could indicate an error in data reduction and / or source finding. The majority of the peak fluxes are consistent with a 1:1 ratio within uncertainties. However, some SCUBA-2 peak fluxes are higher than the corresponding SCUBA peaks. Notably, fainter fluxes show the largest discrepancy, while the brightest are all consistent within uncertainties. In individual

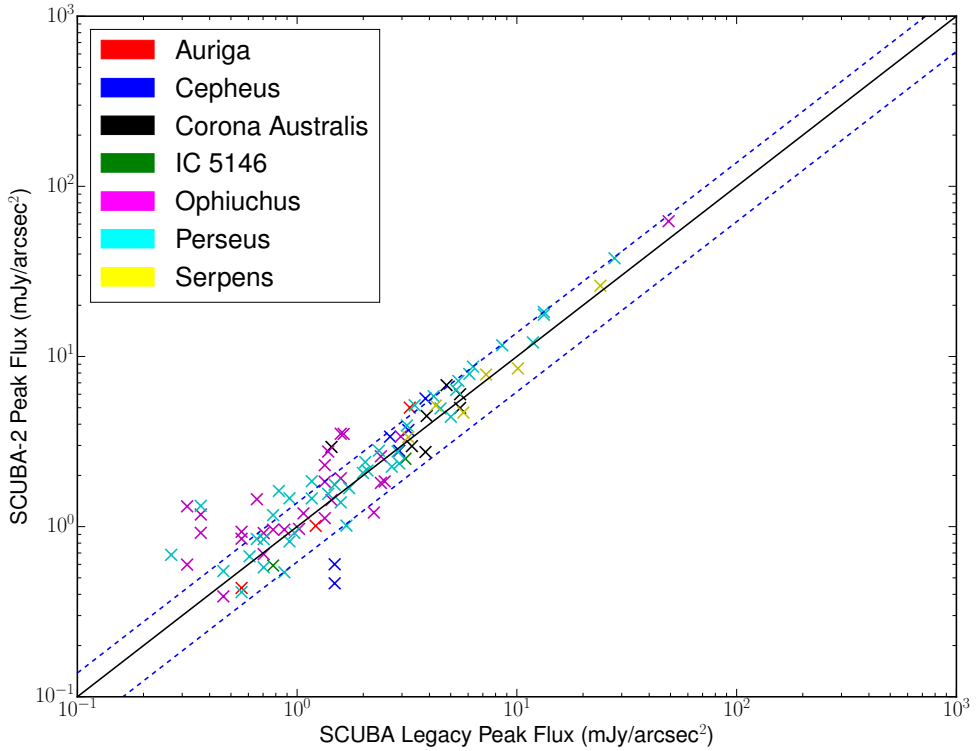

Figure 5.6: SCUBA Legacy and SCUBA-2 850 µm peak fluxes plotted for 100 protostellar candidates. The solid black line represents a 1:1 flux ratio, with 3 σ uncertainty intervals shown by dashed blue lines. Sources in each Gould Belt cloud are plotted using different colours.

regions, Ophiuchus shows the greatest discrepancy between SCUBA and SCUBA-2 peak fluxes, while fluxes in Serpens show an approximately 1:1 relationship. The effective beam FWHM of SCUBA is 22.9″, meaning that more faint, extended emission falls within the SCUBA beam than the SCUBA-2 beam. In addition, differences in background subtraction could mean that the SCUBA-2 peaks sit on more of a 'pedestal' of extended emission than the SCUBA fluxes, despite the 90″ background subtraction.

Table 5.6: SCUBA-2 vs. SCUBA peak flux ratios for four Gould Belt clouds.

Cloud	Mean Ratio
Corona Australis	1.17 ± 0.41
Ophiuchus	1.25 ± 0.48
Perseus	1.17 ± 0.24
Serpens	1.01 ± 0.14

5.4.2 Comparing SCUBA-2 FellWalker Fluxes to *Getsources*

The *Getsources* source extraction algorithm (Men'shchikov et al. 2012) is able to work at multiple wavelengths and multiple scales to produce source catalogues. *Getsources* analyses individual spatial scales and separates significant sources of emission (at least 3σ) from noise and background. By combining the information at individual scales, *Getsources* produces a single scale detectability map which applies to all wavelengths. The spatial scale at which a source is brightest determines its size. Peaks are usually found from the wavelength data with the greatest angular resolution. To provide fluxes for sources, *Getsources* detections are applied to the original maps, which are background subtracted and deblended. Men'shchikov et al. (2012) provides full details of the algorithm. *Getsources* was developed for use with *Herschel* data and has been used for *Herschel* GBS papers (e.g., Könyves et al. 2015). However, it is also able to be used at other wavelengths and on maps from other instruments. Therefore, we investigated the effectiveness of *Getsources* for obtaining fluxes for protostellar candidates.

Getsources was implemented on all SCUBA-2 GBS 450 and 850 µm maps by Jared Keown at the University of Victoria. This produced a catalogue of sources with positions, sizes, and fluxes at 450 and 850 µm. Figure 5.7 shows a zoomed-in SCUBA-2 map of NGC 1333 at 850 µm with *Getsources* objects plotted as ellipses. These sources were then matched with the 592 protostellar candidates with the same criteria used for the FellWalker cross-matching (Section 5.3). The SCUBA-2 maps used to run *Getsources* were reduced using Internal Release 3 parameters, one release before the data used in this Chapter (IR4). However, the comparison between FellWalker and *Getsources* was made before IR4 was available. The main change implemented for IR4 was a correction of pointing offsets, rather than changes that affect flux values.

Getsources objects matched to a total of 268 protostellar candidates, with 199 'lone' matches and 69 'blended' matches. This number is lower than the 299 FellWalker matches, but has the advantage of always matching at both wavelengths. Where *Getsources* is disadvantaged is in assigning fluxes to candidates that did not match a peak ('unmatched' sources in Table 5.4). Whereas with FellWalker we were able to use the presence of a

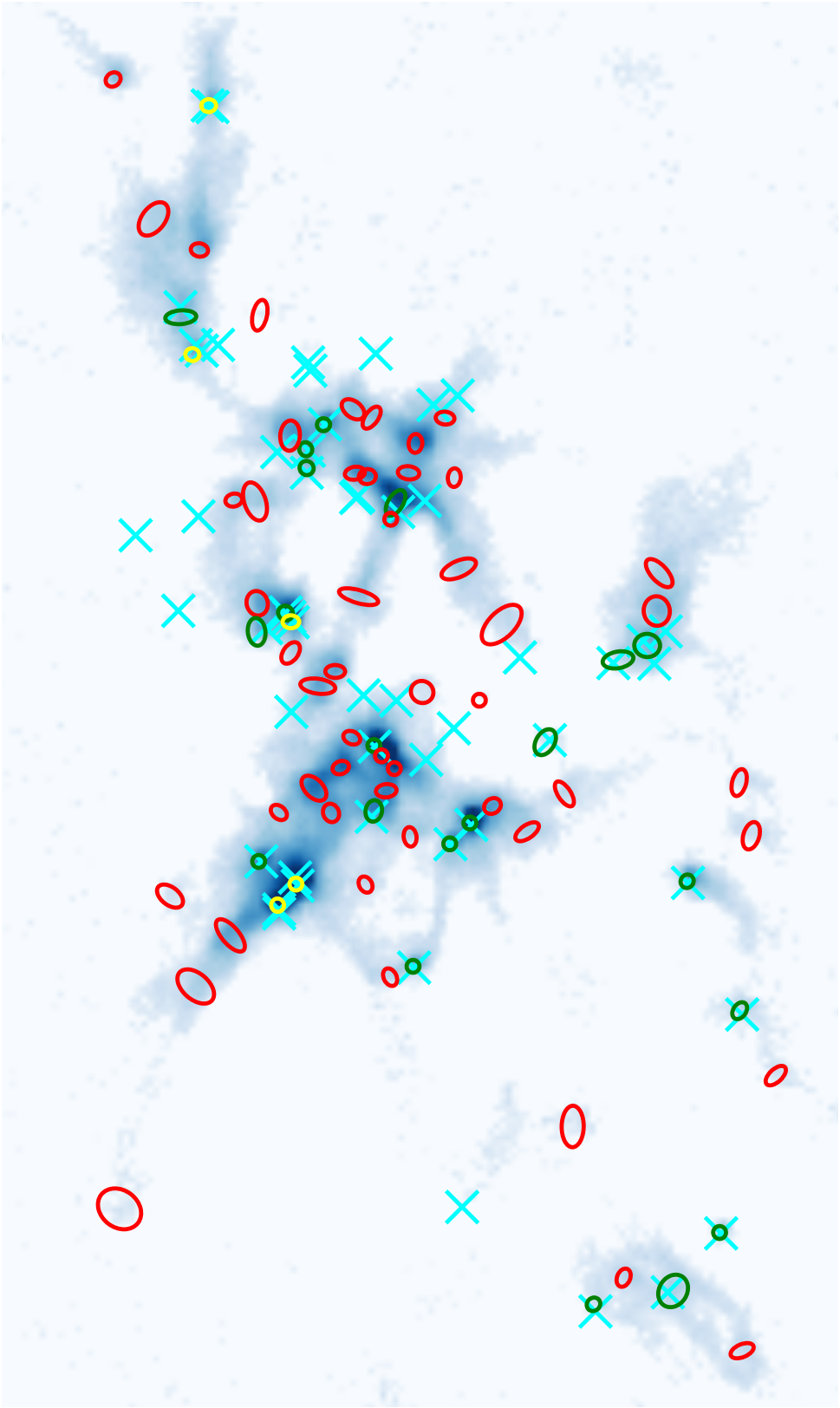

Figure 5.7: *Getsources* objects plotted over 850 µm map of NGC 1333. Ellipses are used to show the position, orientation, and size of *Getsources* objects. *Spitzer* Class 0/I/F YSOs are plotted with cyan crosses. *Getsources* matches to *Spitzer* YSOs are coloured green, with yellow representing blended sources matching more than one YSO. Red denotes *Getsources* objects that do not match to any *Spitzer* YSOs. Flux is shown with square-root scaling.

candidate inside a core boundary to assign it an upper limit to flux based on the local emission, this cannot be done with *Getsources*. Therefore, the overall number of candidates matched to submillimetre emission is much lower when using *Getsources* (268 vs 411 with FellWalker).

Fluxes at both 450 and 850 µm were compared for sources that matched to both FellWalker and *Getsources* objects. Peak and total fluxes are plotted as the first four panels in Figure 5.8. While *Getsources* peak fluxes often lie below those of FellWalker, the two follow each other closely. For brighter objects, there is very little difference. This may be indicative that FellWalker overestimates peak fluxes for dimmer objects due to the presence of background emission. Conversely, *Getsources* may underestimate peak fluxes if the positions of the brightest pixels in the 450 and 850 µm maps do not coincide.

The trend for total fluxes is different, as *Getsources* produces systematically lower fluxes than FellWalker at both wavelengths. However, a significant number of less-bright 450 µm sources have higher *Getsources* fluxes compared to almost none at 850 µm. The bottom panel of Figure 5.8 helps explain this because it shows that *Getsources* objects are consistently smaller than those of FellWalker. In addition, larger FellWalker cores do not correspond to larger *Getsources* objects. Therefore, it seems that for larger, brighter objects, *Getsources* is missing some of the more extended flux. This is a problem for protostars, which are often extended in the SCUBA-2 maps. The line of *Getsources* objects at similar sizes is not at the size of the SCUBA-2 beam area.

To summarise, *Getsources* was able to associate fewer protostellar candidates with submillimetre emission, and does not measure all of the more extended emission of protostellar sources. Therefore, we continued to use FellWalker for this work.

5.5 Summary

Observations of ten clouds in the Gould Belt were obtained at 450 and 850 µm, as part of the James Clerk Maxwell Telescope (JCMT) Gould Belt Legacy Survey (GBS, Ward-Thompson et al. 2007). SCUBA-2 sources within these Gould Belt regions were identified separately

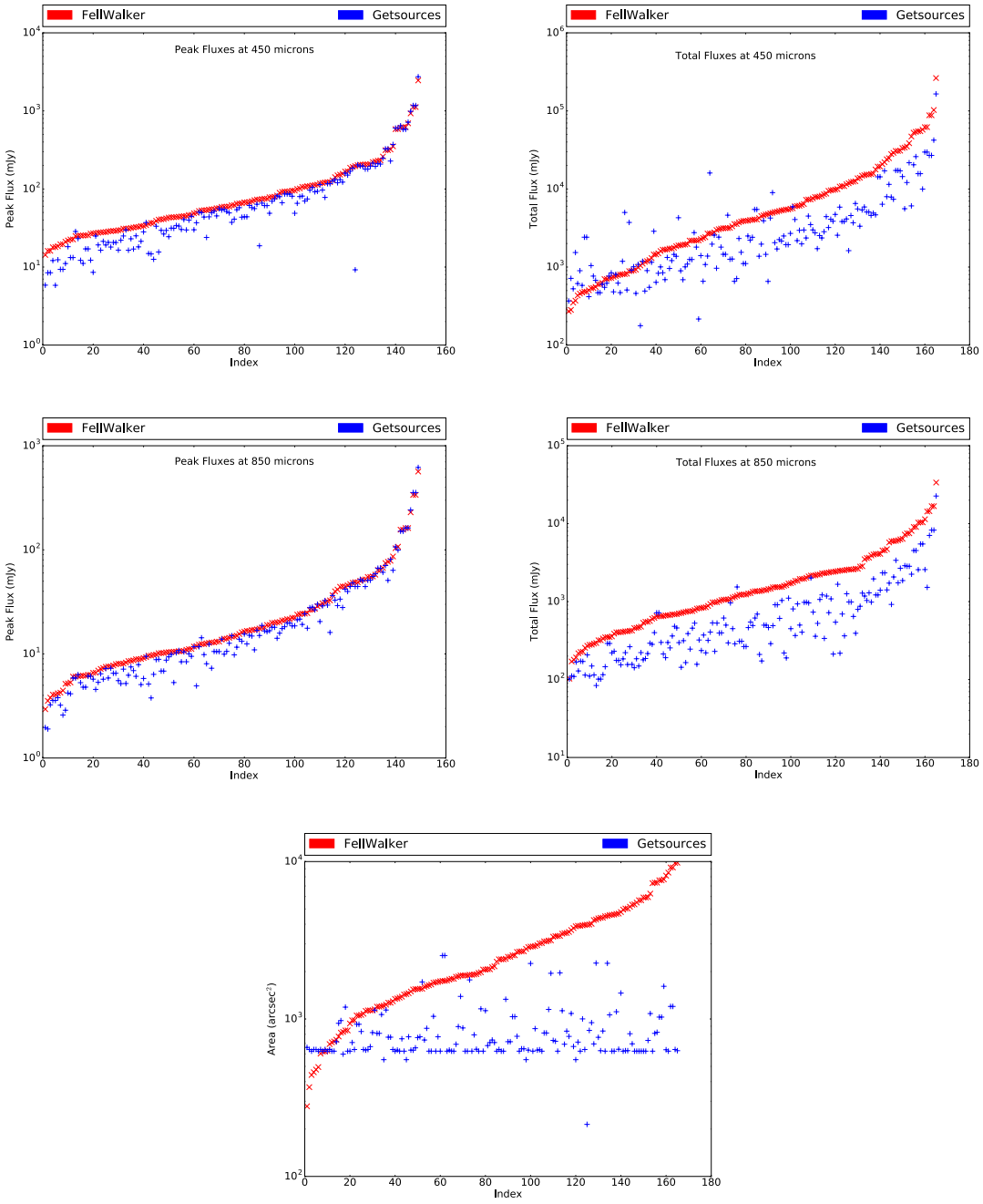

Figure 5.8: Comparison of FellWalker and *Getsources* fluxes for matches sources. The top left panel plots peak fluxes at 450 µm, with total 450 µm fluxes at the top right. Peak and total fluxes at 850 µm are shown middle left and middle right, respectively. The bottom panel plots FellWalker 850 µm core sizes against *Getsources* object sizes. FellWalker objects are plotted in ascending order of flux / size for easy visual comparison.

at each wavelength using the FellWalker clump-finding algorithm (Berry 2015).

Once sources were identified, they were cross-matched with 592 protostellar candidates from the *Spitzer* c2d and Gould Belt catalogue of Dunham et al. (2015). Sources were either matched to a peak in emission or found within dense cores; those not associated with SCUBA-2 emission were ultimately rejected. SCUBA-2 fluxes were combined with the data from *Spitzer* and other published surveys, and spectral energy distributions were constructed for every candidate. Data for each of these protostellar candidates are available as a table in Appendix B.

Chapter 6

Protostars in the Gould Belt - Lifetimes and Other Properties

"Bobo, I know I say this every century, but I'll never leave you behind again."

— C.M.Burns

Using the catalogue of fluxes for protostellar candidates obtained in Chapter 5, this chapter re-examines the properties of these YSOs. The numbers of protostars in Gould Belt regions, their classifications (based on $T_{\rm bol}$), and the durations of the protostellar stages, are recalculated with the addition of SCUBA-2 fluxes. In addition, protostellar luminosities are examined. This includes investigating the luminosity distribution of protostars, characterising objects with very low luminosity, and discussing an alternative method for classifying the evolutionary stage of protostars ($L_{\rm bol}/L_{\rm smm}$). Finally, envelope masses and temperatures are found for a subset of the protostars in this work. This chapter continues to use D13 and D15 to refer to Dunham et al. (2013) and Dunham et al. (2015), respectively.

The structure of this chapter is as follows: Section 6.1 presents the results of the re-evaluation of protostellar candidates, including classifications in Section 6.1.4. Section 6.2 recalculates protostellar properties, including lifetimes in Section 6.2.1, luminosities in Section 6.2.2 and masses in Section 6.2.3. The results of this work are summarised in

Section 6.3.

6.1 Re-evaluation of Protostellar Candidates

In Chapter 5 I presented a catalogue of submillimetre fluxes for 592 protostellar candidates. Using these updated fluxes, SEDs were constructed for every YSO in the candidate list. The process is largely the same as the method employed by the *Spitzer* c2d and GB teams (Evans et al. 2009; Dunham et al. 2013). The key change is that we supplant any previous 450 and 850 µm fluxes from the SCUBA Legacy Catalogue (Di Francesco et al. 2008) with the updated fluxes provided by SCUBA-2.

Figure 6.1 shows the constructed SEDs for the same assorted sources listed in Table 5.5. With a complete list of SCUBA-2 fluxes for the 592 protostellar candidates, we were able to revisit their classifications. In particular, the Class 0/I boundary was investigated. To determine whether or not a candidate lay on the Class 0 or Class I side of the boundary, the extinction-corrected bolometric temperature was calculated (see Section 6.1.2).

6.1.1 Extinction Correction

The assorted candidate SEDs in Figure 6.1 are plotted without extinction corrections, which can be significant in the infrared bands. Such corrections were applied to the literature fluxes for the subsequent calculations of bolometric luminosity and temperature in this work. Following Evans et al. (2009) and D15, the Weingartner and Draine (2001a) $R_V = 5.5$ extinction law was used to de-redden the fluxes for each candidate protostar. This approach has been shown to be an appropriate law for characterising interstellar extinction towards star-forming molecular clouds (Chapman et al. 2009). Extinction was corrected - for all YSOs - with the same values of A_V used in the *Spitzer* catalogue.

All YSOs classified as Class 0/I and Flat-spectrum in a given cloud were given an extinction value, A_V, by D15. They calculated the mean extinction towards all Class II YSOs in the cloud to estimate the typical extinction values for Class 0/I and Flat-spectrum

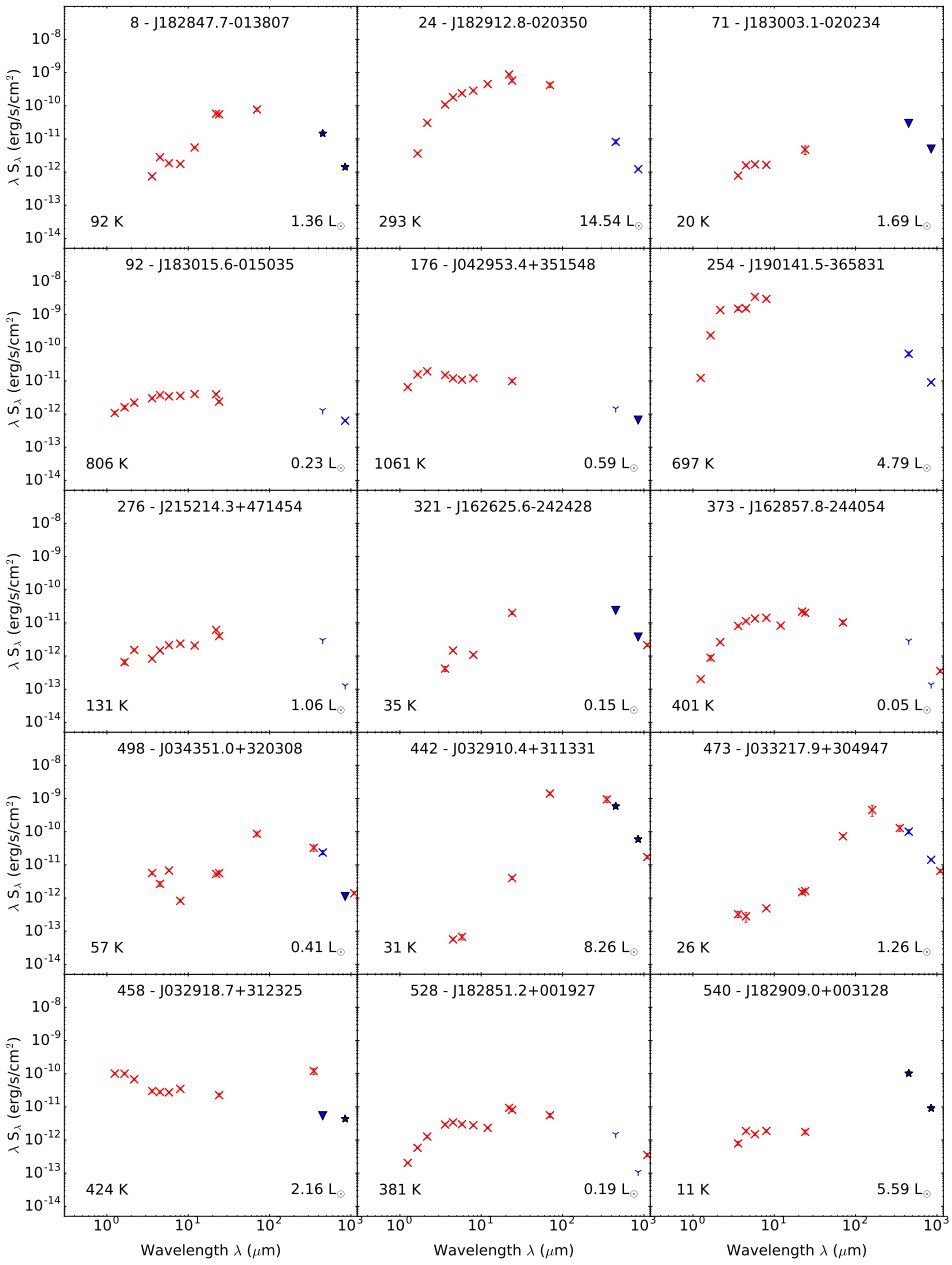

Figure 6.1: SEDs for 15 assorted sources taken from the list of *Spitzer* protostellar candidates. The SEDs are labelled with the *Spitzer* source IDs of each YSO, as well as the running numerical index from the full candidate list. Symbols used to plot the SCUBA-2 fluxes vary depending on the type of detection. Lone matches are plotted using blue crosses, literature fluxes are plotted with red crosses, blended source fluxes are shown as blue star symbols, upper limits for sources with associated submillimetre emission are marked by downward-facing filled blue triangles, and upper limits for undetected objects use three-pointed stars. These detection types can be different at 850 μm compared to 450 μm. Calculated values of $T_{\rm bol}$ and $L_{\rm bol}$ (Table 6.1) are also given.

YSOs. These less-evolved sources comprise most of the protostellar candidates for which SCUBA-2 fluxes have been obtained. Therefore, the extinction values assigned to each of these YSOs were constant for each cloud. The extinction values used for each cloud are provided in Table 5.2.

Some of the protostellar candidates were considered by D15 to be Class II, or occasionally Class III, when looking at their spectral indices. For these sources, they calculated the extinction in one of two ways. If possible, they adopted extinction values for these sources from the literature. If this option was not available, YSOs were de-reddened to the intrinsic near-IR colours of a source with spectral type K7. Both possibilities are explained in D15. Following D15 we use these individual values where available.

6.1.2 Classification of YSOs with Bolometric Temperature

Following D13, the trapezoidal rule was used to calculate the integrals in Equation 1.25, by estimating the area under the SED. The trapezoidal rule was only used within the range of the data points, with no extrapolation outside these areas. Data outside the wavebands covered by *Spitzer* and SCUBA-2 do not contribute significantly to $T_{\rm bol}$ for protostars as they lie far from the SED peak. $T_{\rm bol}$ was then calculated using Equation 1.24. $T_{\rm bol}$ was calculated for every candidate protostar in this work, using every available flux measurement.

Uncertainties in the calculation of $T_{\rm bol}$ can be very large, potentially over 50 % if there is no available flux at 160 µm (near the SED peak, Enoch et al. 2009). Additionally, when upper limits are used at 450 and 850 µm, $T_{\rm bol}$ will be biased low if the values of these limits are significantly higher than the true flux of the relevant YSO. Therefore, whenever the $T_{\rm bol}$ of an individual source lies near a classification boundary (Class 0/I at 70 K, Class I/II at 650 K), caution should be exercised - as the true evolutionary stage of the object is not certain.

As extinction corrections have a much larger effect on short-wavelength fluxes, the use of these corrections causes an increase in $T_{\rm bol}$. The ramification of this increase is a decrease in the measured fraction of Class 0/I protostars that are Class 0 (Enoch et al. 2009).

Indeed, a drop in the overall number of Class 0/I protostars due to this would imply a decrease in a deduced protostellar duration. Conversely, a lack of extinction correction could lead to an overestimation of protostellar lifetimes.

6.1.3 Protostellar Candidates

Once $T_{\rm bol}$ was calculated for every protostellar candidate, the sources were classified. Two requirements were enforced in order for a source to be classified as protostellar. First, $T_{\rm bol}$ had to be below 650 K. Second, the source had to be associated with SCUBA-2 emission at least at the 3σ level. In other words, the source had to be found within an identified FellWalker core (see Section 5.2.2) for at least one of the SCUBA-2 wavebands. This means that YSOs with lone (L), blended (B), and unmatched, within submillimetre emission (U) flags pass this latter criterion, while those with undetected (N) flags do not (see Table 5.4). $T_{\rm bol}$ and protostellar classification are shown for all protostellar candidates in Table B.1. Table 6.1 shows these quantities for the assorted sources from Table 5.5. Candidates that fulfil the criteria to be Class 0 or Class I are labelled as such, while other sources are simply labelled as non-protostellar. Whether the object is Class II, Class III, or not even a YSO, is not considered in this work.

A total of 362 out of 592 (61 %) candidates are protostellar, according to the above criteria. The remaining 230 candidates were rejected due to either a non-detection with SCUBA-2 (31 %), or having a value of $T_{\rm bol} > 650$ K (8 %). Rejection based on $T_{\rm bol}$ was only used for candidates that were detected by SCUBA-2. 266 of the 362 protostellar sources are matched to SCUBA-2 peaks, with the remainder found within SCUBA-2 core boundaries.

D15 classified YSOs as Class 0/I (without differentiating between the two) using mid-infrared spectral indices only. This approach produced a total of 326 Class 0/I sources, of which 314 lie within the clouds observed by SCUBA-2. 286 of these 314 sources are found within the boundaries of the SCUBA-2 maps. This means of classification provided the numbers they used when calculating Class 0/I durations (see Section 6.2.1). Therefore, it is prudent to compare their number of Class 0/I sources with ours, as these represent the total protostellar counts used in the respective studies. The 362 protostars found with

Table 6.1: $T_{\rm bol}$, $L_{\rm bol}$, and classifications, for candidate protostellar YSOs.

Index	Cloud	*Spitzer* ID	D15 Class[1]	$T_{\rm bol}$ (K)	$L_{\rm bol}$ ($L_\odot$)	Detection? (SCUBA-2)	Class
8	Aquila	J182847.7-013807	0/I	92	1.36	Y	I
24	Aquila	J182912.8-020350	0/I	293	14.5	Y	I
71	Aquila	J183003.1-020234	0/I	20	1.69	Y	0
92	Aquila	J183015.6-015035	II	806	0.23	Y	NP[2]
176	Auriga	J042953.4+351548	II	1060	0.59	Y	NP
243	Corona Australis	J190141.5-365831	II	697	4.79	Y	NP
276	IC 5146	J215214.3+471454	0/I	131	1.06	N	NP
321	Ophiuchus	J162625.6-242428	0/I	35	0.15	Y	0
373	Ophiuchus	J162857.8-244054	0/I	401	0.05	N	NP
442	Perseus	J032910.4+311331	0/I	31	8.26	Y	0
458	Perseus	J032918.7+312325	II	424	2.16	Y	I
473	Perseus	J033217.9+304947	0/I	26	1.26	Y	0
498	Perseus	J034351.0+320308	II	57	0.41	Y	0
528	Serpens	J182851.2+001927	II	381	0.19	N	NP
540	Serpens	J182909.0+003128	II	11	5.59	Y	0

[1] Classes based on mid-infrared spectral index value from D15
[2] Non-protostellar.
Note: The full table is available in the Appendix as Table B.1.

the inclusion of SCUBA-2 fluxes represent an increase of 27 % compared to the 286 in D15. This difference demonstrates that using the mid-infrared spectral index alone to classify protostars can result in an undercount compared to classifying with $T_{\rm bol}$. Many candidates classified as Class II/III by spectral index are found to be Class 0/I by $T_{\rm bol}$. In addition only 286 out of 314 Class 0/I sources identified by *Spitzer*, in the clouds also observed by SCUBA-2, actually lie within the JCMT GBS fields-of-view. This difference of 8.4 % suggests that approximately 10 % of the protostars in the Gould Belt clouds investigated by us may have been missed by SCUBA-2, due to lying outside of the SCUBA-2 observational areas.

D15 separately classified a total of 230 protostellar candidates using $T_{\rm bol}$. These candidates had required at least one detection with a wavelength $\lambda \geq 350$ µm - signifying the presence of a dense core. As some of these 230 sources lie outside the clouds observed by the JCMT GBS, a total of 204 candidate protostars within those clouds is used for comparative purposes. Of these 204 YSOs, D15 classified 179 (88 %) as Class 0 or Class I protostars, according to $T_{\rm bol}$ The remainder had $T_{\rm bol} > 650$ K. A visual breakdown of these numbers is provided in Figure 6.2.

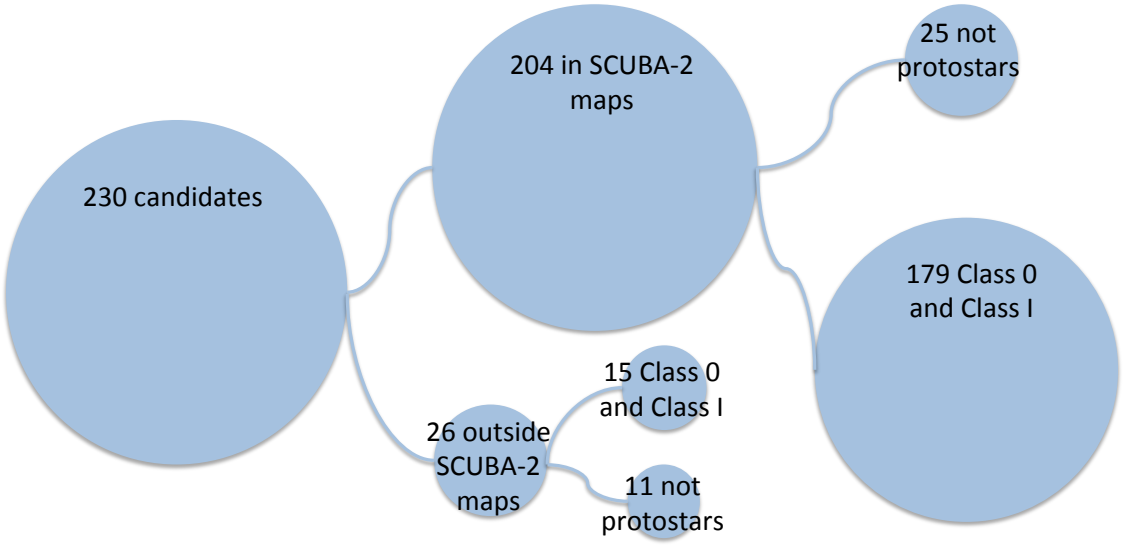

Figure 6.2: Visual breakdown of classifications of protostellar candidates from D15. All objects had a detection longward of 350 µm before the addition of SCUBA-2 fluxes (Original list given by D13). Circles are in proportional size to the number of sources in each group.

Many of the sources classified as Class 0/I by mid-infrared spectral index in D15 did not have a detection longward of 350 µm. Therefore, many possible protostars were missed, due to a lack of wavelength coverage. The improvement in long-wavelength coverage with SCUBA-2 has enabled many of these Class 0/I sources to be confirmed as protostars. Moreover, the inclusion of submillimetre fluxes has caused many $T_{\rm bol}$ values to decrease, in many cases below the Class I/II threshold of 650 K. Therefore, the number of Class 0 and Class I protostars (in the Gould Belt clouds in Table 5.2) classified using $T_{\rm bol}$ has increased from 179 to 362, over twice as many.

Of the 204 candidates within the JCMT GBS maps, we classify 164 as protostellar (80 %). Among these protostars, 152 (91 %) are directly matched to a SCUBA-2 peak. The remainder are found within SCUBA-2 core boundaries and are assigned SCUBA-2 upper limits. Of the sources we do not classify as protostellar in nature, 17 were not detected by SCUBA-2 (8 %) and the remaining 23 had $T_{\rm bol} > 650$ K.

The rejection of some candidates is no surprise. These candidates were originally identified by D13, who solely required a detection at $\lambda \geq 350$ µm to select a candidate, so disk sources in the vicinity of a dense core were not ruled out (as acknowledged by them). Five of the 17 undetected cores have $T_{\rm bol} > 650$ K, so the lack of a 3 σ SCUBA-2

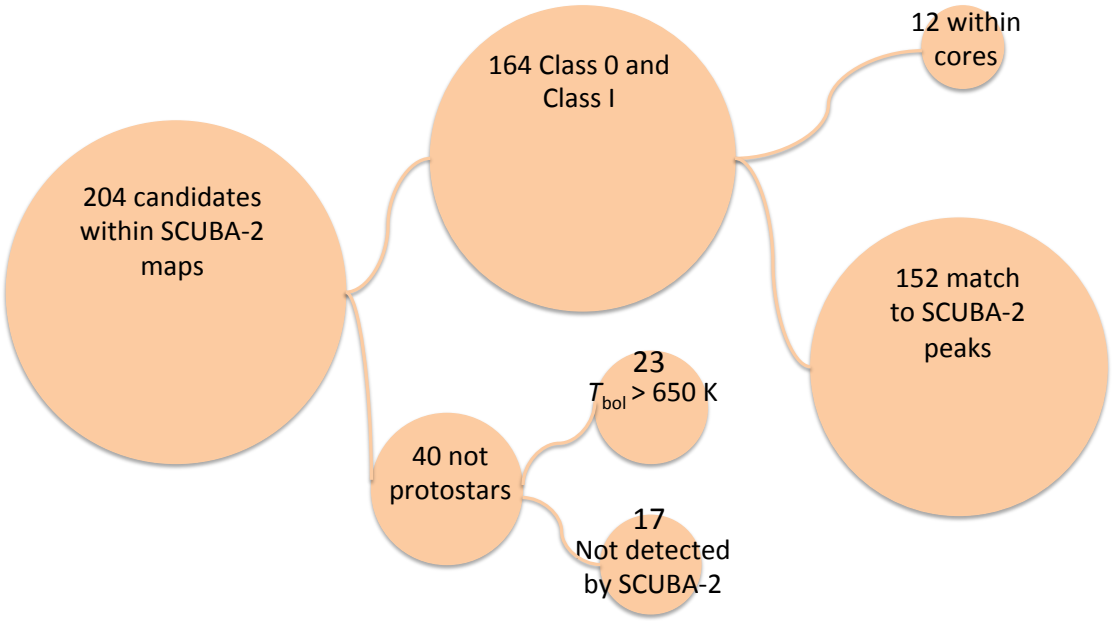

Figure 6.3: Visual breakdown of our updated classifications of previous candidates from D13 / D15. Circles are in proportional size to the number of sources in each group.

detection means that these YSOs are likely to be more evolved T-Tauri stars, rather than protostars viewed through outflow cavities. The remaining twelve sources (6 %) of the dense core sources within the JCMT GBS maps have $T_{bol} \leq 650$ K. These sources lie within the extended areas of large-scale emission filtered out during the SCUBA-2 data reduction process. Therefore, the level of emission in the vicinity of these sources was reduced below the 3 σ threshold.

6.1.4 Class 0 and Class I objects

Table 6.2 shows the breakdown of protostellar sources into Class 0 and Class I objects from this work, and how these numbers compare to those from D15. The overall numbers of objects D15 classify as Class 0 and Class I using T_{bol} are 65 and 129, respectively. Not all of these, however, lie within the JCMT GBS maps. Excluding those objects for comparative purposes leaves 63 Class 0 objects and 116 Class I objects. Including the SCUBA-2 data has increased these numbers to 115 Class 0 objects and 247 Class I objects. In total, 198 YSOs

Table 6.2: Number of protostars found in this work compared to D15.

Classification	$N_{sources}$ *Spitzer*[1]	SCUBA-2 (peaks only)[2]		SCUBA-2 (with limits)[3]	
		$N_{sources}$	Change	$N_{sources}$	Change
Class 0	63	109	+46	115	+52
Class I	116	157	+41	247	+131

[1] Excludes sources outside JCMT GBS SCUBA-2 maps (2 Class 0 and 13 Class I sources).
[2] Sources that did not match to SCUBA-2 peaks are excluded.
[3] Full count of sources, including those found within SCUBA-2 cores that did not match to peaks and that were thus assigned upper limits.

that were not previously associated with a dense core are now known to be associated with emission at 450 µm and / or 850 µm, and are Class 0 or Class I according to T_{bol}. 118 of these sources are matched to a SCUBA-2 peak (60 %), with the rest being assigned upper limits.

The increase in numbers of both Class 0 and Class I sources indicates that the addition of 450 and 850 µm fluxes has had a significant effect on the calculated T_{bol} values of the protostellar candidates compared to the previous literature values. Figure 6.4 compares T_{bol} values for all protostellar candidates associated with emission at 450 or 850 µm between D15 and our work. 207 sources saw a reduction in T_{bol} by greater than 10 %, while comparatively few (20) experienced an increase of greater than 10 %. Specifically, 49 candidates had T_{bol} reduced below 650 K, while only three had T_{bol} increase above 650 K. The effect on the total number of Class II/III objects is small, however, with a reduction of approximately 2 %. Furthermore, 52 YSOs previously with 70 K $< T_{bol} \leq$ 650 K had T_{bol} reduced below 70 K, with only five sources having the opposite occur. The vast majority of these sources did not have previously available fluxes at 350 or 1100 µm. For sources that did have available 1100 µm data, our T_{bol} values are much more consistent with those of D15 (shown in Figure 6.4). Thus, it is clear that T_{bol} values were previously overestimated due to the lack of available submillimetre data.

We cannot, however, exclude the possibility that the addition of SCUBA-2 fluxes will cause T_{bol} to be underestimated. This is of particular concern for the candidates with large gaps in wavelength coverage. Observations by the *Herschel* Space Observatory (Pilbratt

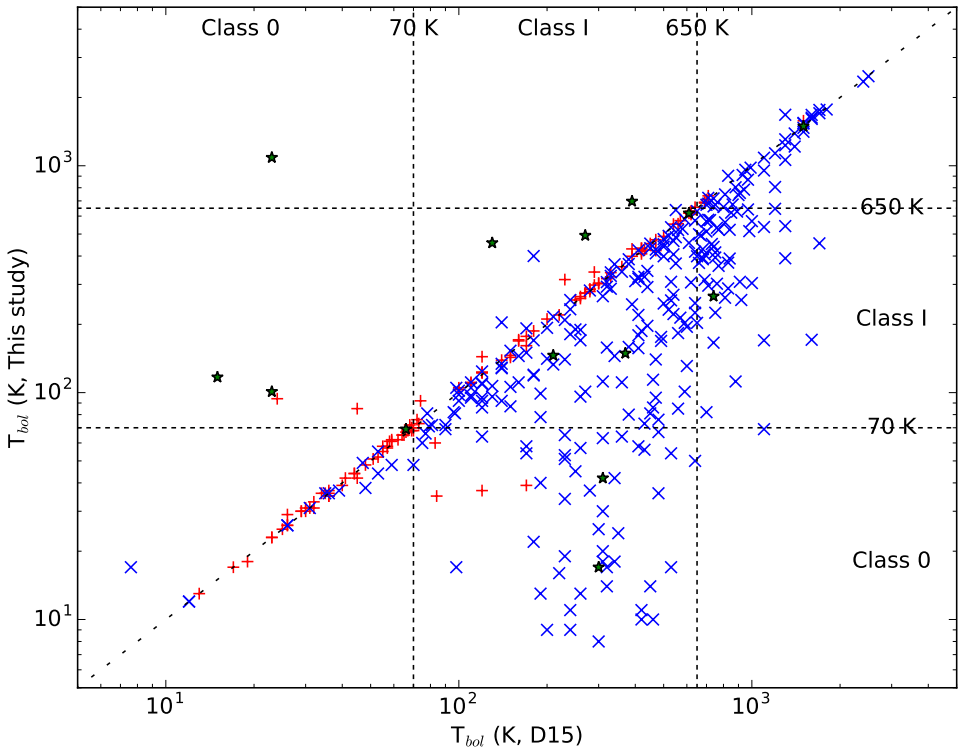

Figure 6.4: Comparison of $T_{\rm bol}$ values calculated, for protostellar candidates, with and without SCUBA-2 450 and 850 µm fluxes. Only sources associated with SCUBA-2 emission are included. Class boundaries are shown with double-dashed lines. The single-dashed diagonal line shows the points where a *Spitzer* (literature) $T_{\rm bol}$ is equivalent to a newly-calculated $T_{\rm bol}$ including SCUBA-2 fluxes. Points plotted with red plus symbols represent YSOs that previously had 1100 µm fluxes available, while blue cross symbols represent those that did not. Green stars are used to mark YSOs in Corona Australis, as many previously had unreliable SCUBA Legacy 450 µm fluxes

et al. 2010) could provide superior wavelength sampling for hundreds of the protostellar candidates in our sample. This will require the reconciliation of *Herschel* and SCUBA-2 fluxes, which is beyond the scope of the JCMT GBS SCUBA-2 catalogue. Future analysis including *Herschel* data will, however, be required to ensure that the classification of our protostellar candidates is accurate.

Several YSOs in Figure 6.4 can be seen with D15 $T_{\rm bol}$ values much lower than those from SCUBA-2. Some of the most outlying of these objects are found in Corona Australis, and all had SCUBA Legacy Catalogue fluxes available at 450 and 850 µm Di Francesco et al. (2008). The 450 µm fluxes for these objects, taken at 850 µm source positions, are unreliably high in the SCUBA Legacy catalogue due to saturation. These high 450 µm fluxes caused very low values of $T_{\rm bol}$ to be calculated. These values have now been corrected

Table 6.3: Cloud-by-cloud comparison of protostellar numbers from this work and D15.

Cloud	Class 0 (D15)	Class 0 (SCUBA-2)	Class I (D15)	Class I (SCUBA-2)
Aquila	1	25	16	78
Auriga / California	0	8	3	24
Cepheus	6	6	11	14
Corona Australis	4	3	6	8
IC 5146	0	4	2	23
Lupus I	0	0	0	1
Ophiuchus	3	5	25	31
Perseus West	29	36	28	36
Perseus IC 348	6	8	7	7
Serpens	14	20	18	23
Serpens North	0	0	0	2
Total	63	115	116	247

Note: Excludes sources outside SCUBA-2 maps (2 Class 0 and 13 Class I sources).

with the addition of 450 µm fluxes from SCUBA-2.

Table 6.3 and Figure 6.5 show the changes in source numbers cloud-by-cloud for all sources within the boundaries of JCMT GBS coverage. The starkest differences in protostellar counts are in Aquila, Auriga / California and IC 5146. The number of protostars in Aquila has increased from 17 to 103, in Auriga / California the amount has increased from 3 to 32 and in IC 5146 the count has changed from 2 to 27. None of these clouds were surveyed by Bolocam (Enoch et al. 2009) and the SCUBA Legacy Catalogue observed few protostars in these regions. As a result many protostellar candidates lacked any detection at $\lambda \geq 350$ µm. Detection of such emission (signifying a dense core) was required by D15 before a source could be classified as Class 0 or Class I.

Cepheus and Corona Australis were not observed by the Bolocam survey, yet in these clouds the numbers of Class 0/I sources have not changed significantly with the addition of SCUBA-2 fluxes. In Cepheus, the cloud had already been well-covered by SHARC-II at 350 µm. In Corona Australis, much of the previous submillimetre coverage came from the SCUBA Legacy Catalogue at 450 and 850 µm. Ophiuchus, Perseus and Serpens were covered by the Bolocam and SCUBA Legacy surveys. Hence, many sources had fluxes available at 1.1 mm as well as 450 and 850 µm. Despite this, there has still been a significant increase in the numbers of protostellar sources in these clouds due to the addition of SCUBA-2 fluxes. Firstly, the superior resolution (Bolocam has an effective beam

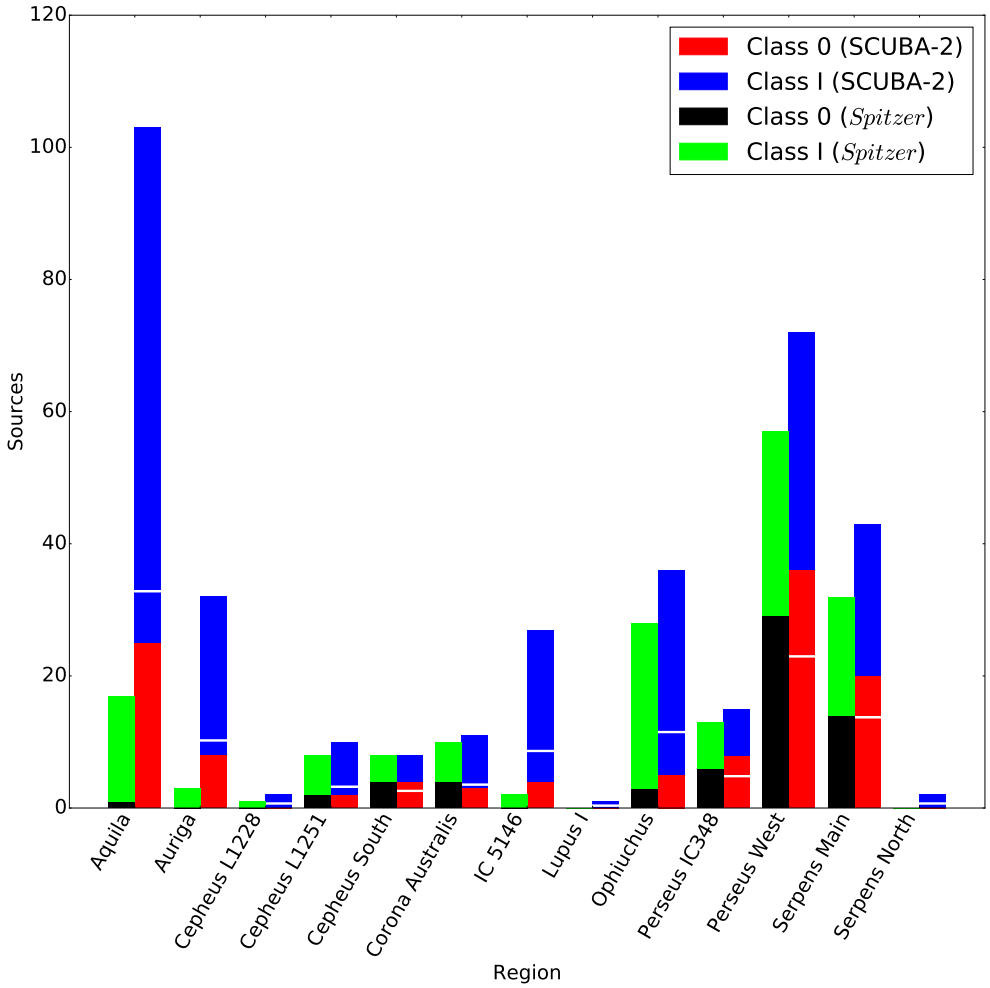

Figure 6.5: Cloud-by-cloud comparison of protostellar numbers from this work and D15. D15 numbers are represented by the left bars, with SCUBA-2 numbers shown by the right bars, for each region. A horizontal white line is used on the SCUBA-2 bars for each cloud to show the average ratio of Class 0 to Class I sources across all clouds (Section 6.1.4.1).

FWHM of 31″) and coverage of SCUBA-2 has allowed more sources to be matched to peaks of emission. In addition, knowledge of the location of protostellar candidates has enabled fluxes to be assigned to objects within dense cores that do not necessarily match to peaks of emission. As the SCUBA, Bolocam and SHARC-II studies predate the *Spitzer* c2d and GB surveys, they were unable to do this.

6.1.4.1 Protostellar Fractions

Of the 362 Class 0/I objects, 115 are Class 0, a fraction of 31.8 %. This percentage is consistent with the value of 33.5 % found by D15. It is lower, however, than the 42 %

found by the *Herschel* Orion Protostar Survey (Furlan et al. 2016; Fischer et al. 2017). Note, however, that Orion may naturally have a higher Class 0 fraction than the clouds we have studied. When including every Class 0 to Class III YSO from D15 that lies within the SCUBA-2 maps, the overall fraction of sources that are protostellar (Class 0/I) is 17.5 %. If extending to include every D15 YSO within regions we have observed, the fraction is 13.8 % - higher than the value of 11.6 % calculated using source counts from D15. The overall fraction of Class 0 sources is shown in Figure 6.5, plotted over the region-by-region fractions.

In order to test whether or not individual Gould Belt molecular clouds have statistically significant fractions of YSOs that are protostellar compared to the overall value as a whole, a binomial test was implemented on the sample from each cloud. The binomial test can be used to examine whether a number of occurrences of a particular event is likely, given an overall probability for the event to occur. In this case, the overall protostellar fraction provides a probability (p, 13.8 %) that can be used for the binomial test. The number of protostars in an individual region (X) out of n total protostars in that region was used to calculate a cumulative probability - the probability of up to X protostars occurring in that region, given the overall probability for all regions. The probability of a specific number k of protostars is calculated as

$$Pr(k; n, p) = \frac{n!}{k!(n-k)!} p^k (1-p)^{n-k}. \tag{6.1}$$

The cumulative probability is then the sum of all probabilities calculated with integer values of $k \leq X$. If the cumulative probability lies outside the specified confidence interval, the distribution of the individual region is statistically different to the overall distribution. In this case, we used a 3 σ level of significance. Therefore, if the cumulative probability for a region is less than 0.003 or greater than 0.997, the number of protostars in that region is statistically different from the overall population. Comparisons between the ratios of Class 0 to Class I objects were implemented in the same manner.

In Perseus the overall protostellar fraction is 22.6 %. We have been able to compare the eastern and western regions of Perseus, since SCUBA-2 observations of IC 348 and B5

were examined separately from the rest of Perseus. In IC 348, the protostellar fraction is very low, with only 6.4 % of YSOs being protostellar. Conversely, in the western region of Perseus, including NGC 1333, the protostellar fraction of 36.2 % is unusually high for a Gould Belt region. In addition, the fraction of protostars that are Class 0 is high (50 %). This contrast is indicative of a significant difference between eastern and western Perseus. Indeed, previous work has suggested that IC 348 is older, and has perhaps already undergone the majority of its star formation activity (Luhman et al. 1998; Bally et al. 2008; Sadavoy et al. 2014). No unusual source distributions were seen in the remaining Gould Belt regions. Ophiuchus has a low number of Class 0 objects, with only 13.9 % of protostars being Class 0 and the rest being Class I. This percentage supports similar findings by André and Montmerle (1994) and Enoch et al. (2009). Despite this, the percentage is not inconsistent with the overall fraction of Class 0s at a level of 3 σ.

6.1.5 Comparison to HCO^+ Observations.

Centrally-concentrated dense gas, which is a characteristic of protostellar envelopes, is traced by HCO^+ emission. For example, higher-level transitions are sensitive to critical densities of $> 10^6$ cm^{-3} (van Kempen et al. 2009). Heiderman and Evans (2015) observed the HCO^+ J = 3 $\rightarrow$ 2 transition towards 89 % of the Class 0/I and Flat-spectrum YSOs of the D15 catalogue. They used the criteria of van Kempen et al. (2009) for identifying protostars based on HCO^+ integrated main beam intensity being above a certain threshold, modified to the J = 3 $\rightarrow$ 2 transition ($I_{MB} \geq 0.68$ K km s^{-1}). A total of 455 of the sources they observed match with our initial list of protostellar candidates (Section 6.1). Of these matching protostellar candidates, they classified 300 sources as protostars, while we classify 303 of these sources as protostellar with SCUBA-2 data. Thus, both methods of protostellar classification produce broadly consistent numbers of protostellar sources. Note, however, that $T_{\rm bol}$ has an advantage in being able to offer a distinction between Class 0 and Class I objects.

Within the bounds of the JCMT GBS SCUBA-2 maps, the number of Class 0/I objects found by HCO^+ emission (300) is 83 % of the 362 sources classified as protostellar using

SCUBA-2 data. Note that Heiderman and Evans (2015) did not observe *Spitzer* Class II YSOs in their survey. This nuance helps explain the different protostellar counts of their study and ours because 32 YSOs, previously classified as Class II according to mid-infrared spectral index, are now classified as protostellar after the addition of SCUBA-2 fluxes. Although we cannot rule out the possibility that these are contaminants, Class II YSOs were only selected as candidates if they already had $T_{\rm bol} \leq 650$ K or a dense core detection in the D15 catalogue.

A total of 47 sources are classified as protostellar by SCUBA-2, but not by HCO^+, while 44 sources are classified as protostellar by HCO^+, but not SCUBA-2. YSOs classified as protostellar by $T_{\rm bol}$ that lack HCO^+ detections may be more evolved disk sources (Carney et al. 2016). Some YSOs which were detected by HCO^+ are not classified as protostellar by $T_{\rm bol}$. Some of these sources may merit further investigation, but others simply lie at the boundary of extended HCO^+ filament / cloud emission. Overall, 364 out of 455 classifications of the initial protostellar candidates agree between both methods (80 %), with 91 disagreements. Of the 303 sources classified as protostellar by SCUBA-2, 256 (84.5 %) are also classified as protostellar by HCO^+. A visual breakdown of the comparison between our work and the HCO^+ classifications is provided as Figure 6.6.

If, for example, the physical conditions of a specific cloud caused $T_{\rm bol}$ classifications to be inaccurate, an unusually high number of disagreements between classifications with HCO^+ and $T_{\rm bol}$ would be expected in that cloud. Therefore, a binomial test was run on the number of agreements and disagreements between classifications with HCO^+ and with $T_{\rm bol}$ in each individual cloud. This analysis showed that none of these Gould Belt regions display an unusually high probability of disagreement at the 3 σ level. This result suggests that $T_{\rm bol}$ classifications are not significantly affected by the properties of individual clouds in the Gould Belt (such as source inclinations).

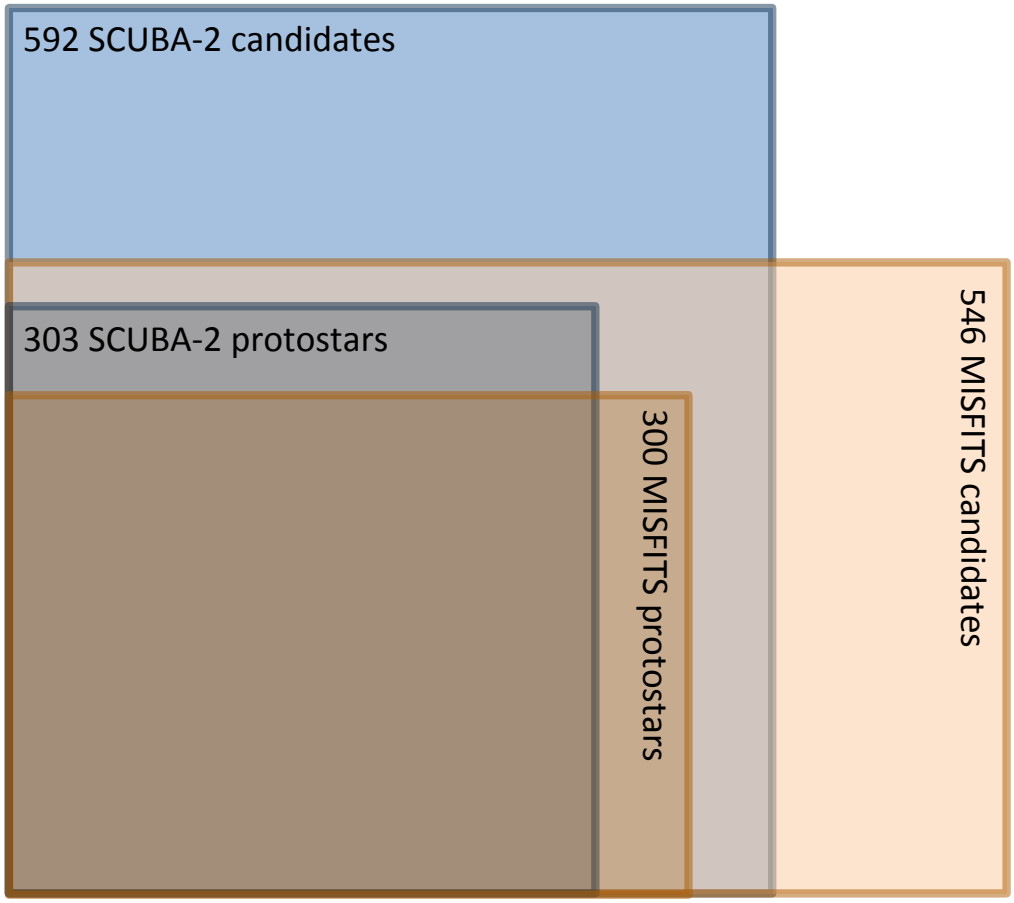

Figure 6.6: Visual representation of the numbers of sources in this work compared to Heiderman and Evans (2015). Box sizes are scaled to the number of sources in each group.

6.2 Protostellar Properties

6.2.1 Class 0/I Lifetimes

Typically, the duration of the Class 0/I phases is calculated by comparing the numbers of YSOs in these classes to the amount in a different, more-evolved reference class, for which a duration is better constrained (Wilking, Lada, and Young 1989; Evans et al. 2009; Dunham et al. 2015; Heiderman and Evans 2015). The ratio of the number of protostars to the number of objects in the reference class, multiplied by the duration of the reference class, will provide an estimate for the duration of the Class 0/I phase:

$$\tau_{0/\mathrm{I}} = \tau_{\mathrm{ref}} \frac{N_{0/\mathrm{I}}}{N_{\mathrm{ref}}} \tag{6.2}$$

The term 'duration' (rather than lifetime) is used because characterising a source as Class 0 or Class I is fundamentally observational in nature. These classifications are based on theory, but are not necessarily indicative of the true evolutionary stage of a protostar. Initially, a protostellar evolutionary sequence was proposed by Adams, Lada, and Shu (1987). They combined previous theoretical treatments (e.g., Shu 1977; Terebey, Shu, and Cassen 1984) with the observational work of Lada and Wilking (1984). An observational classification scheme, based on spectral indices, was then provided by Lada (1987), which formally defined Class I, Class II, and Class III YSOs. André, Ward-Thompson, and Barsony (1993) then introduced Class 0 to describe the very youngest sources. Flat-spectrum objects (Greene et al. 1994) are found between Class I and Class II YSOs. This classification does not represent a physical stage; Flat-spectrum objects are split approximately evenly between protostars and more evolved sources (Heiderman and Evans 2015).

As discussed in Section 5.1, Class 0/I objects will not always be Stage 0/I protostars. This issue served as the motivation for the use of alternative observational characteristics, such as the HCO^+ observations by Heiderman and Evans (2015) already discussed in Section 6.1.5. As noted by D15, these observations provided a number of protostars in Gould Belt clouds very similar to the *Spitzer* work, where classification was based on spectral indices. In addition, the number of protostars classified by HCO^+ emission is very close to that found using T_{bol} among matching sources (Section 6.1.5). Therefore, while caution should be exercised about the correspondence between 'Class' and 'Stage', this work continues to use the duration of the Class 0/I phase interchangeably with protostellar lifetime.

Respective numbers of Class 0 and Class I objects can provide separate duration estimates for each stage of evolution. This method fundamentally relies on the assumption that the star formation rate has been constant over the lifetime of the reference class. This assumption, however, is unlikely to be valid in individual regions. For example, Perseus West has a large protostellar fraction (see Section 6.1.4.1), which implies that the local star formation rate has seen an increase in recent times. It is also possible for the different subregions within clouds to have the same star formation rates, but different star formation start times Sadavoy et al. (2014) and Mercimek et al. (2017). L1448 in Perseus, for example,

has no known Class II or III objects. This means that star formation is likely to have triggered very recently in this subregion. However, the individual variations in certain clouds should average out when looking at the entire Gould Belt dataset.

Various assumptions can be made about both the duration and constituent YSOs of the chosen reference class. By using several of these assumptions, a range of values of protostellar durations can be obtained. This work follows D15 in using five separate reference class definitions to calculate durations for Class 0/I sources. This approach allows for consistency and easy comparison with previous work. The results from each of the five assumptions are shown in Table 6.4.

The simplest assumption is to use Class II sources as the reference class, which is the method used by Evans et al. (2009). A Class II duration of 2 Myr can be also assumed, consistent with disk dissipation timescales found in young clusters (Wyatt 2008; Galli et al. 2015). However, recent studies have indicated that a disk dissipation time of 2 Myr may be too short (e.g., Bell et al. 2013), a point discussed in more detail in D15. Due to this, D15 suggest that 3 Myr may be a superior choice of reference class duration. Hence, the first two definitions of reference class are Class II objects only with 2 Myr and 3 Myr durations.

As the above two assumptions solely involve Class II objects to define a reference class, Class III objects that still possess primordial disks are excluded. This distinction is important, because disk dissipation times calculated by previous studies (Ribas et al. 2014; Ribas, Bouy, and Merín 2015) do not specifically refer to Class II YSOs. Class III YSOs still show a modest infrared excess on their SEDs (or they would not be classified as such). Thus, whether or not a source is technically Class II or Class III is immaterial, and leaving out Class III objects from the reference class may artificially increase any subsequently calculated Class 0/I durations. Therefore, the remaining three reference class definitions include both Class II and Class III objects.

The third definition includes the full number of available Class II and III objects and a 3 Myr disk dissipation duration. The use of the full number of Class II and III objects available will produce the most numerous reference class, and a concomitantly shorter

Class 0/I duration. However, the Class III sample from D15 is significantly contaminated by background AGB stars, at levels between 25 and 90 %. Accordingly, the fourth and fifth reference class definitions attempt to account for this contamination. The fourth includes all Class II and 75 % of Class III objects to create the reference class. The fifth includes all Class II and only 10 % of Class III sources. The fourth and fifth definitions act as lower and upper limits for contamination correction, respectively. Both also include a 3 Myr disk dissipation lifetime. The fourth and fifth definitions are our preferred assumptions, due to their greater level of physical motivation.

Table 6.4 provides lifetimes for the Class 0, Class I, and Class 0 + I phases for each of the five reference class definitions discussed above. The numbers of Class II and Class III sources within the JCMT GBS SCUBA-2 maps are 1097 and 603, respectively. However, the JCMT GBS maps represent a narrower sky coverage per cloud than often seen with *Spitzer*, so many previously-identified Class III sources and some Class II sources within these clouds lie outside the JCMT GBS SCUBA-2 maps. Class 0/I YSOs are much more likely to be concentrated in areas with high extinction (Heiderman and Evans 2015), and these are the areas specifically targeted by the JCMT GBS (Ward-Thompson et al. 2007). In contrast, Class II and III sources are more likely to be dispersed (Salji et al. 2015b; Mairs et al. 2016; Megeath et al. 2016). This distribution of sources would bias our YSO counts to higher values of protostars relative to Class II and III objects. Therefore, all known Class II and Class III YSOs within the clouds observed by SCUBA-2 were used to construct the reference classes, even if such objects fall outside the boundaries of the JCMT GBS SCUBA-2 maps.

However, Class II and III objects are not the only YSOs that lie outside SCUBA-2 coverage areas. Of the 314 *Spitzer* Class 0/I objects within SCUBA-2-observed clouds, only 286 are actually found within the JCMT GBS map boundaries. Therefore, a correction factor of 1.084 is applied to the numbers of Class 0 and Class I objects used to calculate lifetimes. Not using this correction would cause calculated lifetimes to be about 10 % lower, due to the protostars presumably missing from the calculations. Inherent in this correction factor is the assumption that the population of *Spitzer* Class 0/I objects that lies exterior to the JCMT GBS SCUBA-2 maps is indistinct from the main group within the maps.

Using all five assumptions, the range of lifetimes for Class 0 objects is 0.17 – 0.31

Table 6.4: Durations of YSO Protostellar Classes

Reference Class Constituents	τ_{ref} (Myr)	N_{ref}	τ_0 (Myr)	τ_I (Myr)	$\tau_{0/I}$ (Myr)
Class II	2.0	1214	0.21	0.44	0.65
Class II	3.0	1214	0.31	0.66	0.97
Class II + III	3.0	2253	0.17	0.36	0.52
Class II + 0.75*III	3.0	1993	0.19	0.40	0.59
Class II + 0.1*III	3.0	1318	0.28	0.61	0.89

Myr, and the range for Class I objects is 0.36 – 0.66 Myr. Together, these values yield a range for protostellar (Class 0/I) lifetimes of 0.52 – 0.97 Myr. Using just the preferred definitions previously mentioned, the range of protostellar lifetimes is 0.59 – 0.89 Myr. These derived lifetimes are longer than the range of 0.46 – 0.72 Myr found by D15 using the same preferred definitions. The increase is approximately 25 %, if averaging the extremes of the ranges. If only the Class II and III objects within the JCMT GBS maps are included, the derived lifetime is approximately 50 % greater than those of D15.

Using the ranges obtained from the latter two, preferred reference class definitions, Class 0 lifetime has increased from 0.15 – 0.24 Myr to 0.19 – 0.28 Myr. This represents an averaged increase of approximately 21 %. By comparison, Class I lifetimes have increased by approximately 28 % (from 0.31 - 0.48 Myr to 0.40 - 0.61 Myr). Therefore, the majority of the increase in protostellar lifetime is due to the increase in the number of Class I sources. A higher fraction of Class I objects was found once SCUBA-2 fluxes were included (see Section 6.1.4.1). In addition, the overall number of Class 0/I sources is also greater compared to D15 (see Section 6.1.3). The increased Class 0 lifetime means that protostars will remain in an envelope-dominated stage for longer. As this has no bearing on the initial mass of a protostellar envelope, this allows for a reduced mass accretion rate.

In their MISFITS study, Heiderman and Evans (2015) also calculated protostellar lifetimes. To construct a reference class, they used only the first definition, i.e., the reference class consisted of only Class II sources with an assumed disk dissipation timescale of 2 Myr. Using this assumption, they calculated a combined Stage 0/I lifetime of 0.54 Myr. In comparison, when using the same reference class, D15 found a lifetime of 0.52 Myr, and we determine a lifetime of 0.65 Myr. The value of 0.65 Myr is 25 % higher than the D15

value, and 20 % higher than the Heiderman and Evans (2015) MISFITS value. The JCMT GBS protostellar count is larger, leading to an increase in calculated lifetimes.

The lifetime estimates of D15, Heiderman and Evans (2015) and our work were found using three different methods. D15 used the total number of Class 0/I sources according to the extinction-corrected mid-infrared spectral index, Heiderman and Evans (2015) identified Stage 0/I YSOs based on their HCO^+ emission, and we classify protostellar objects using both T_{bol} and a SCUBA-2 detection.

As discussed in Section 6.1.5, the total number of protostars from the matching candidates found using HCO^+ (300) differs very little from the 303 found using 450 and 850 µm fluxes. For large numbers of sources, either method can be used to broadly identify most protostellar YSOs. Note that this statement is only true when looking at a large number of YSOs across multiple molecular clouds. The derived Class 0/I lifetimes presented by the studies, however, differ by approximately 25 %. This is because Heiderman and Evans (2015) did not observe as many sources. Consequently, their number of confirmed protostars is lower, leading to a shorter Stage 0/I lifetime. The D15 lifetime estimate is not lower because of a lower source count; our analysis used their source list. Instead, the use of mid-infrared spectral index alone to classify Class 0/I objects appears to underestimate the true number of protostars, leading to shorter derived lifetimes.

6.2.2 Bolometric Luminosity

We calculated L_{bol} for all candidate protostars using available extinction-corrected fluxes. The trapezium rule was used to calculate the integral in Equation 1.26, using the same method as Section 6.1.2. Values of L_{bol} are shown alongside T_{bol} for the sample of assorted YSOs in Table 6.1 and online. The distances used to calculate L_{bol} within each region are provided in Table 5.2.

The mean and median luminosites of all protostars are 3.53 $L_\odot$ and 1.13 $L_\odot$, respectively. We find that 173 out of 362 protostars (48 %) are low-luminosity, with $L_{bol} \leq 1$ $L_\odot$. A cloud-by-cloud breakdown of mean and median luminosities for all protostars in the

Table 6.5: Region-by-region comparison of protostellar luminosity averages.

Region	$N_{\rm sources}$ Total	$L_{\rm bol,\ mean}$ $L_\odot$	$L_{\rm bol,\ median}$ $L_\odot$	$N_{\rm sources}$ $L_{\rm bol} \leq L_\odot$
Aquila	103	2.50	0.98	53
Auriga / California	32	2.66	1.11	15
Cepheus L1228	2	1.39	1.39	1
Cepheus L1251	10	2.14	0.52	6
Cepheus South	8	8.64	1.17	3
Corona Australis	11	3.04	1.21	5
IC 5146	27	8.04	3.58	1
Lupus I	1	0.07	0.07	1
Ophiuchus	36	2.15	0.21	26
Perseus West	72	2.98	0.93	38
Perseus IC 348	15	1.19	0.58	9
Serpens	43	6.44	3.58	14
Serpens North	2	2.67	2.67	1
Total	362	3.53	1.13	173

sample is provided in Table 6.5. A binomial test was implemented on each cloud in turn, at a 3σ level of significance, to compare the numbers of low-luminosity sources to the overall fraction (48 %). Ophiuchus was found to have a high fraction of low-luminosity sources (72 %) and IC 5146 has a low fraction of low-luminosity sources (3.7 %). For example, the mean and median luminosities in IC 5146 (8.04 and 3.58 $L_\odot$, respectively) are higher than those in Ophiuchus (2.15 and 0.21 $L_\odot$, respectively). Due to the distance-square dependence of luminosity, this result is not surprising. Ophiuchus is one of the closest Gould Belt regions to Earth, and IC 5146 is the furthest (see Table 5.2).

D13 found mean and median luminosities for their protostellar sample of 4.3 and 1.3 $L_\odot$, respectively. They predicted that the addition of photometry between 70 and 850 µm would increase these numbers. With the addition of the SCUBA-2 data, however, the mean luminosity has dropped to 3.53 $L_\odot$. This indicates that the sources newly added to the list of Gould Belt protostars have, on average, lower luminosities. Indeed, the mean luminosity for these 'new' protostars is lower, at 2.39 $L_\odot$. The median luminosity of all protostars in our sample is now 1.13 $L_\odot$, thus it has decreased by 13 %.

Figure 6.7 plots luminosity distribution of our current work and that of D13 / D15.

The K-sample Anderson-Darling test can be used to model whether two separate distributions could have come from the same population. A significance value is returned, with larger values indicating that the distributions could originate from the same population (and vice-versa). An Anderson-Darling test - calculated using the SciPy stats module - run on our distribution and the D13 / D15 distribution returned a significance value of 0.33. Therefore, the two distributions are not statistically different. This demonstrates that the protostars we have added have not had a significant effect on the overall distribution of protostellar luminosities.

The completeness limit for the *Spitzer* c2d / Gould Belt surveys is $L_{\rm bol}$ = 0.2 $L_{\odot}$ at a distance of 1 kpc (IC 5146, D13). Therefore, the shape of the distribution to the left of the line plotted in Figure 6.7 begins to be driven by completeness, rather than physical reasons such as the shape of the IMF. Regions closer than 1 kpc will still be complete to the left of this line (Enoch et al. 2009).

Figure 6.8 plots $L_{\rm bol}$ against $T_{\rm bol}$ (A 'BLT' diagram, Myers and Ladd 1993) for all objects we classify as protostellar. YSOs previously classified as Class 0 or Class I using $T_{\rm bol}$ by D15 are distinguished from the objects we newly classify as such. The two populations of protostars appear visually indistinct, suggesting no significant difference between the 'old' and 'new' populations of Class 0 and Class I protostars. Such a difference would be expected if the 'new' sources consisted of many contaminants, rather than true protostars. In addition, although we use a further distance for Aquila this has not substantially affected the luminosity distribution compared to D13 / D15. This is because 86/103 of the protostars in Aquila are 'new' sources not previously included in the D13 / D15 luminosity distribution.

6.2.2.1 Use of $L_{\rm bol}/L_{\rm smm}$ as an Evolutionary Indicator

An alternative approach to differentiate between Class 0 and Class I protostars is to use the ratio of $L_{\rm bol}$ to submillimetre luminosity ($L_{\rm smm}$), where $L_{\rm smm}$ is calculated for wavelengths longward of 350 μm (Figure 6.9 shows these ranges on an example SED). Since Class 0 protostars are more deeply embedded than Class I objects, they should have lower ratios

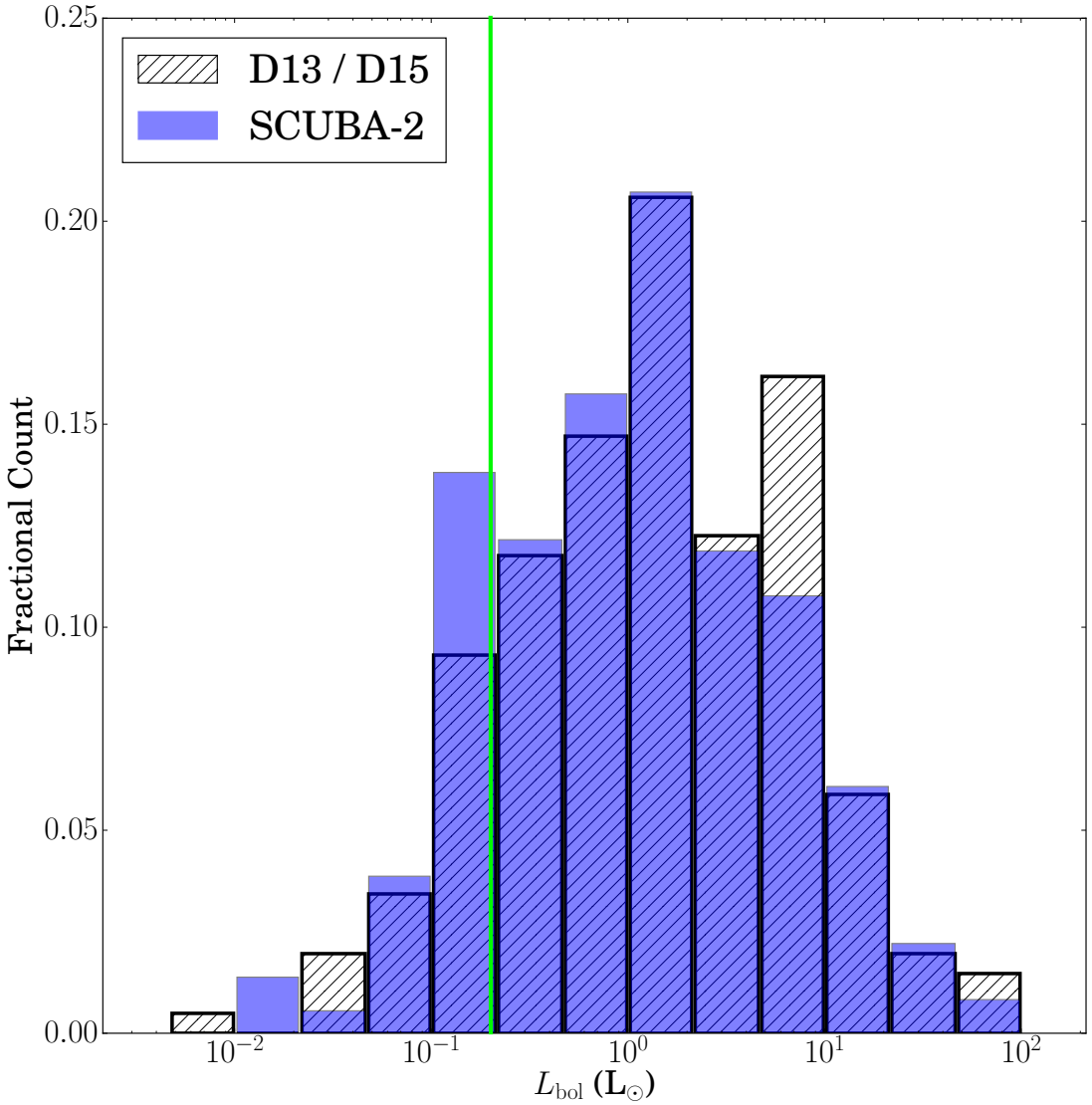

Figure 6.7: Histogram of protostellar $L_{\rm bol}$ distributions, plotted with 1/3 dex bins. Solid blue shading is used to show our luminosity distribution, while black hatching and edges are used to show the distribution of D13 / D15. The vertical green line at $L_{\rm bol}$ = 0.2 $L_\odot$ marks the D13 completeness limit.

of $L_{\rm bol}/L_{\rm smm}$. André, Ward-Thompson, and Barsony (1993) define Class 0 objects as those with the ratio $L_{\rm bol}/L_{\rm smm} < 200$. This value was revised to $L_{\rm bol}/L_{\rm smm} < 175$ by Young and Evans (2005) using SED models. Although the ratio of $L_{\rm bol}$ to $L_{\rm smm}$ has been suggested as a superior discriminator between Class 0 and Class I sources compared to $T_{\rm bol}$ (Young and Evans 2005; Dunham et al. 2010b), we continue to use $T_{\rm bol}$ rather than $L_{\rm bol}/L_{\rm smm}$ to distinguish between Class 0 and Class I sources. This is because we are still unable to use observational $L_{\rm bol}/L_{\rm smm}$ values to reliably distinguish between protostars at different evolutionary stages.

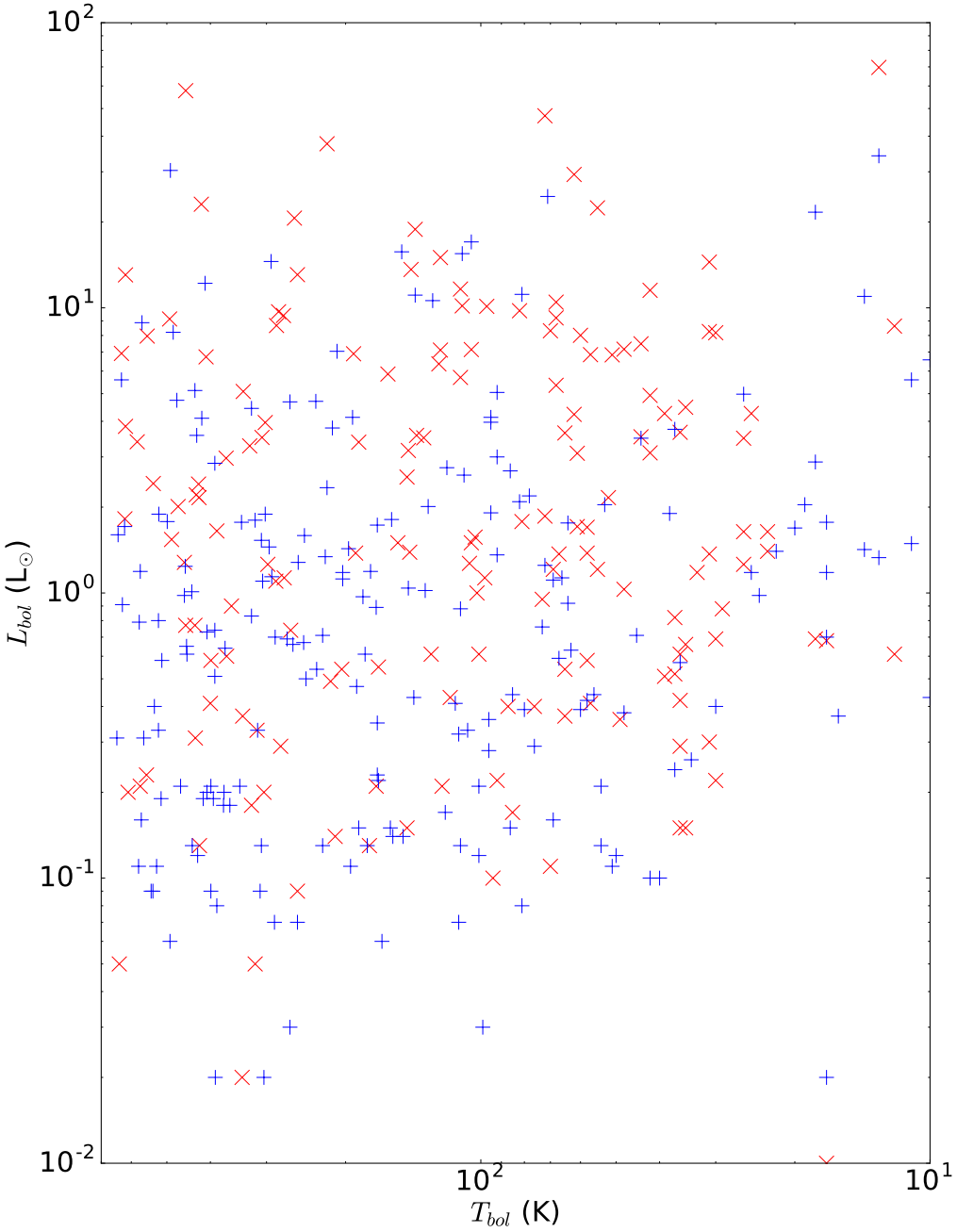

Figure 6.8: 'BLT' diagram for 362 Gould Belt protostars. Red crosses show objects with $T_{\rm bol} \leq 650$ K and a dense core detection in D15. Blue plus symbols show the objects we newly classify with this method.

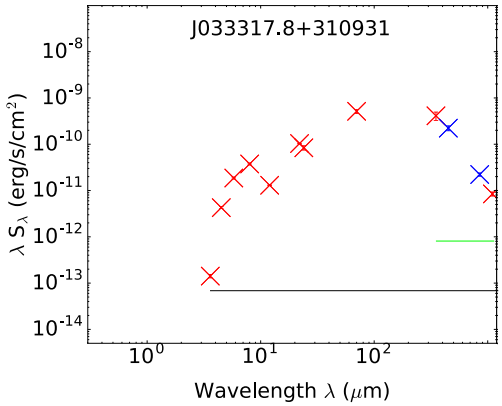

Figure 6.9: Example SED showing wavelength ranges for $L_{\rm bol}$ and $L_{\rm smm}$. $L_{\rm bol}$ encompasses the full wavelength range of available data (black line) while $L_{\rm smm}$ is calculated for wavelengths longward of 350 µm (green line).

$L_{\rm bol}/L_{\rm smm}$ values were calculated for every protostellar candidate in Section 6.1.3. The calculation of $L_{\rm bol}$ has already been detailed in Section 6.2.2. A value for $L_{\rm smm}$ was obtained using a similar method which included only data at wavelengths $\lambda \geq 350$ µm. For candidates that did not have available 350 µm data, the value of $L_{\rm smm}$ was likely underestimated. Conversely, candidates with only upper limits to flux at 450 and 850 µm will have overestimated $L_{\rm smm}$ values.

Figure 6.10 plots $L_{\rm bol}/L_{\rm smm}$ against $T_{\rm bol}$ for every protostellar candidate. 83 % of the protostellar candidates have a value of $L_{\rm bol}/L_{\rm smm} < 175$, used to identify Class 0 objects. This includes objects classified as non-protostellar by $T_{\rm bol}$. In fact, 49 % of the candidates have $L_{\rm bol}/L_{\rm smm} < 35$. Young and Evans (2005) use this as the boundary between pre-protostellar-core and Class 0 objects. In addition, there is a large degeneracy of $T_{\rm bol}$ values among sources with approximately equal values of $L_{\rm bol}/L_{\rm smm}$. Therefore, we conclude that we are unable to use $L_{\rm bol}/L_{\rm smm}$ to distinguish between Class 0 and Class I sources. This remains true even when only those candidates with available 160 µm data are included. This finding suggests that a revision to the $L_{\rm bol}/L_{\rm smm} < 175$ boundary may be required for observational data. We do not attempt to make such a revision, however, due to the importance of fully-sampled SEDs when calculating this quantity.

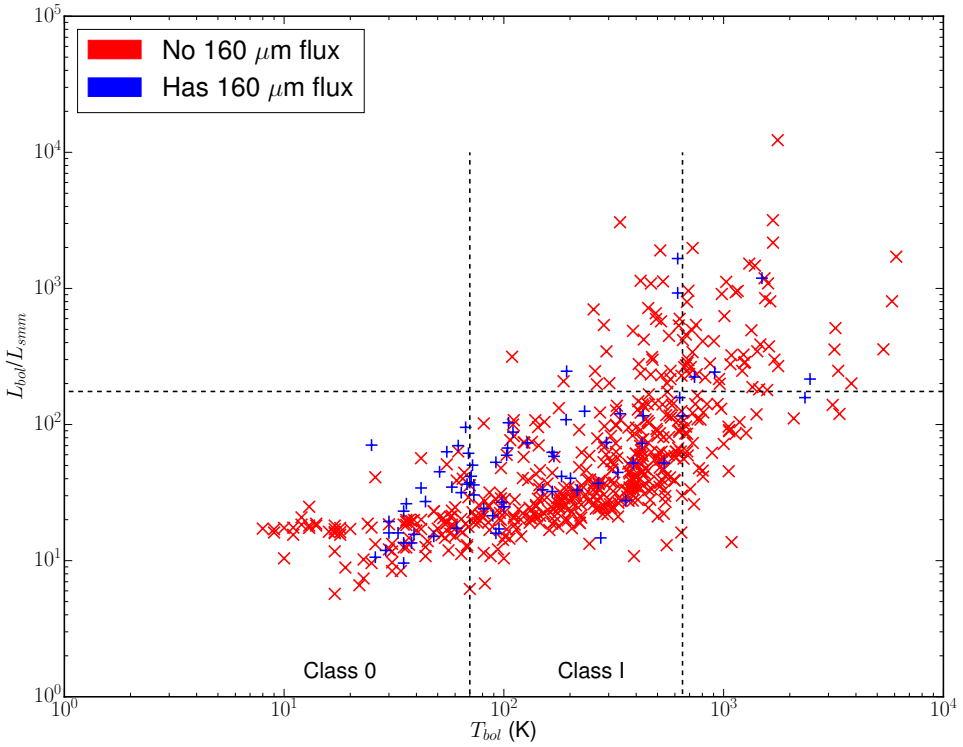

Figure 6.10: $L_{\rm bol}/L_{\rm smm}$ against $T_{\rm bol}$ for each of 592 protostellar candidates. Candidates with and without available 160 µm data are plotted with blue plus symbols and red crosses, respectively. Vertical dashed lines represent the Class 0:I boundary at $T_{\rm bol}$ = 70 K and the Class I:II boundary at $T_{\rm bol}$ = 650 K. The horizontal dashed line marks the theoretical Class 0:I boundary at $L_{\rm bol}/L_{\rm smm}$ = 175. Class 0 objects are expected to lie below this line.

6.2.2.2 Very Low Luminosity Objects

Very Low Luminosity Objects (VeLLOs) were first discovered by Young et al. (2004). VeLLOs are protostars with an internal luminosity, $L_{\rm int} \leq 0.1$ L$_\odot$ (Di Francesco et al. 2007). A total of 24 VeLLOs was found from the list of protostellar candidates: four Class 0 and twenty Class I objects. This count represents just 6.6 % of the total protostellar sample. The majority of these sources are located in Ophiuchus and Perseus, among the nearest Gould Belt molecular clouds (see Table 5.2, and references therein). Three VeLLOs, however, are present in Aquila and Serpens at a distance of 436 pc. The luminosities of these objects range from 0.01 to 0.1 L$_\odot$. The 24 sources should provide a lower limit on the number of VeLLOs among the total number of protostars, as it is possible for $L_{\rm int}$ to be below 0.1 L$_\odot$ even if $L_{\rm bol}$ is not (e.g., due to external heating, see Young et al. 2004 and D13).

Dunham et al. (2008) identified 15 VeLLOs from the *Spitzer* c2d and Gould Belt surveys, all of which have luminosities recalculated by D13. As three are located in Chamaeleon I, a region too far south to be observed with the JCMT, twelve are located within our SCUBA-2 Gould Belt maps. Of the twelve, only five still have $L_{\rm bol} \leq 0.1$ $L_\odot$, and a SCUBA-2 detection. Table 6.6 shows the 24 VeLLOs identified in this work. Of these VeLLOs, 19 are newly identified as such by us. All but one of the 24 objects have $L_{\rm bol} \leq 0.1$ $L_\odot$ in the D15 catalogue. Therefore, the increase in the number of VeLLOs is due to the increased number of submillimetre detections by SCUBA-2. The extra SED coverage also means that our luminosities are larger or the same within uncertainties for 22 of the 24 VeLLOs.

The previously-identified VeLLOs located in Aquila no longer have $L_{\rm bol} \leq 0.1$ $L_\odot$. The distance-squared dependence of $L_{\rm bol}$ means that the change in distance used for Aquila, from 260 to 436 pc (D13 and D15 vs. our work), leads approximately to a factor of 3 increase in luminosity for all sources located there. Thus, had the larger distance been used by D13, both sources would have had $L_{\rm bol} > 0.1$ $L_\odot$, even without SCUBA-2 fluxes. The previously-identified VeLLO in the IC 348 region of Perseus is excluded by us as its location in the 850 µm map contains no emission. Two of the previous VeLLOs in Ophiuchus are also not detected by us, while two more now have $L_{\rm bol} > 0.1$ $L_\odot$. As already mentioned, however, such sources may still be VeLLOs if $L_{\rm int} \leq 0.1$ $L_\odot$.

6.2.2.3 Effect of SCUBA-2 Fluxes on Luminosities

D13 conclude that a lack of far-infrared or submillimetre photometry for a given source will cause $L_{\rm bol}$ to be underestimated by a factor of approximately 2.5 on average. Of the 100 sources previously lacking such data, 46 now have available SCUBA-2 fluxes at both 450 and 850 µm. The remainder were either not detected by SCUBA-2, or lie outside our SCUBA-2 maps. Of these 46 sources, 37 are matched to a FellWalker peak at 450 µm, with the remaining nine having upper limits. Comparing previously determined values of $L_{\rm bol}$ for the matched YSOs to the ones calculated here, the average $L_{\rm bol}$ value increased by a factor of 2.5. This factor is consistent with the predictions of D13.

Table 6.6: VeLLOs identified / confirmed by SCUBA-2.

Cloud	*Spitzer* ID	L_{bol} ($L_\odot$)	Previously identified?
Aquila	J182939.1-015021	0.1	N
Aquila	J183031.4-015609	0.08	N
Cepheus	J222933.3+751316	0.09	Y
Corona Australis	J190256.8-370719	0.02	N
Corona Australis	J190301.0-370753	0.03	N
Lupus	J154301.2-340915	0.07	N
Ophiuchus	J162546.6-242336	0.02	N
Ophiuchus	J162614.6-242507	0.01	Y
Ophiuchus	J162658.2-243740	0.02	N
Ophiuchus	J162702.9-242614	0.05	Y
Ophiuchus	J162715.5-243053	0.08	N
Ophiuchus	J162716.3-243114	0.06	N
Ophiuchus	J162721.8-242727	0.02	Y
Ophiuchus	J162730.9-242733	0.09	N
Perseus	J032838.7+311806	0.07	N
Perseus	J032848.7+311608	0.06	N
Perseus	J032851.2+311739	0.07	N
Perseus	J032856.6+310737	0.07	N
Perseus	J032905.1+312036	0.09	N
Perseus	J032910.8+311642	0.09	N
Perseus	J032918.2+312319	0.1	N
Perseus	J033309.5+310531	0.05	Y
Perseus	J034359.4+320035	0.09	N
Serpens	J182856.6+003008	0.1	N

6.2.3 Protostellar Masses

A calculation of protostellar envelope mass can be implemented by fitting an opacity-modified blackbody to long-wavelength emission ($\lambda \geq 70$ µm). Any protostars with fluxes available at a minimum of 70, 450, and 850 µm were fit with single temperature modified blackbody SEDs, using the same method as Section 3.2.5. Only sources with non-confused matches to FellWalker peaks at both 450 and 850 µm (flag 'L' in Table 5.4) were included. This resulted in mass fits being made for a total of 90 well-sampled protostars, of which 33 are Class 0 and 57 are Class I.

A grid of possible protostellar masses and temperatures was used to produce model SEDs, which were then fitted to the long-wavelength data for each of the 90 protostars. In addition to fluxes at the mandatory wavelengths, data at 160, 350, 1100, 1200, and 1300 µm

Table 6.7: Envelope masses and temperatures for well-sampled protostars.

Protostars	$N_{\rm sources}$	Envelope Mass $M_\odot$		Temperature (K)	
		mean	median	mean	median
Overall	90	$0.75^{+2.19}_{-0.56}$	0.32	20.0 ± 3.3	19.4
Class 0	33	$1.14^{+2.45}_{-0.78}$	0.63	18.2 ± 2.3	17.7
Class I	57	$0.53^{+1.53}_{-0.39}$	0.26	21.0 ± 3.3	20.1
Class I ($T_{\rm bol} \leq 200$ K)	29	$0.69^{+1.84}_{-0.50}$	0.28	20.4 ± 3.3	19.6
Class I ($T_{\rm bol} > 200$ K)	28	$0.35^{+0.99}_{-0.26}$	0.19	21.6 ± 3.2	20.7

Table 6.8: Mean envelope masses and temperatures for well-sampled protostars.

Region	$N_{\rm sources}$	Mean Envelope Mass $M_\odot$	Mean Temperature K
Aquila	19	$0.79^{+1.10}_{-0.46}$	20.0 ± 3.3
Auriga	11	$0.50^{+0.89}_{-0.32}$	20.1 ± 3.0
Cepheus	6	$0.33^{+0.51}_{-0.20}$	19.1 ± 1.6
Ophiuchus	11	$0.23^{+0.63}_{-0.17}$	23.6 ± 4.3
Perseus	28	$0.54^{+1.21}_{-0.37}$	19.4 ± 3.3
Serpens	8	$2.33^{+4.47}_{-1.53}$	18.7 ± 1.1

were used. Further details can be found in Section 3.2.5, where the same fitting procedure was used for the YSOs in Lupus I.

The mean and median envelope masses for all 90 protostars are given in Table 6.7. Mean and median values are also given for Class 0 and Class I sources. These numbers are also plotted as a histogram in Figure 6.11, and the full table is provided in the Appendix as Table B.2. The Class I sources are further split into those with $T_{\rm bol} \leq 200$ K, and those with $T_{\rm bol} > 200$ K. Figure 6.12 is a histogram showing the envelope masses for both types of Class I source. The corresponding temperature values are also provided. A histogram of Class 0 and Class I envelope temperatures is provided as Figure 6.13. Mean masses and temperatures were also calculated for every region with more than five well-sampled protostars. These are provided in Table 6.8. The least massive envelope of the 90 protostars is 0.01 $M_\odot$, and the most massive envelope is 8 $M_\odot$.

Overall, the envelopes of Class 0 sources are more massive than those of Class I

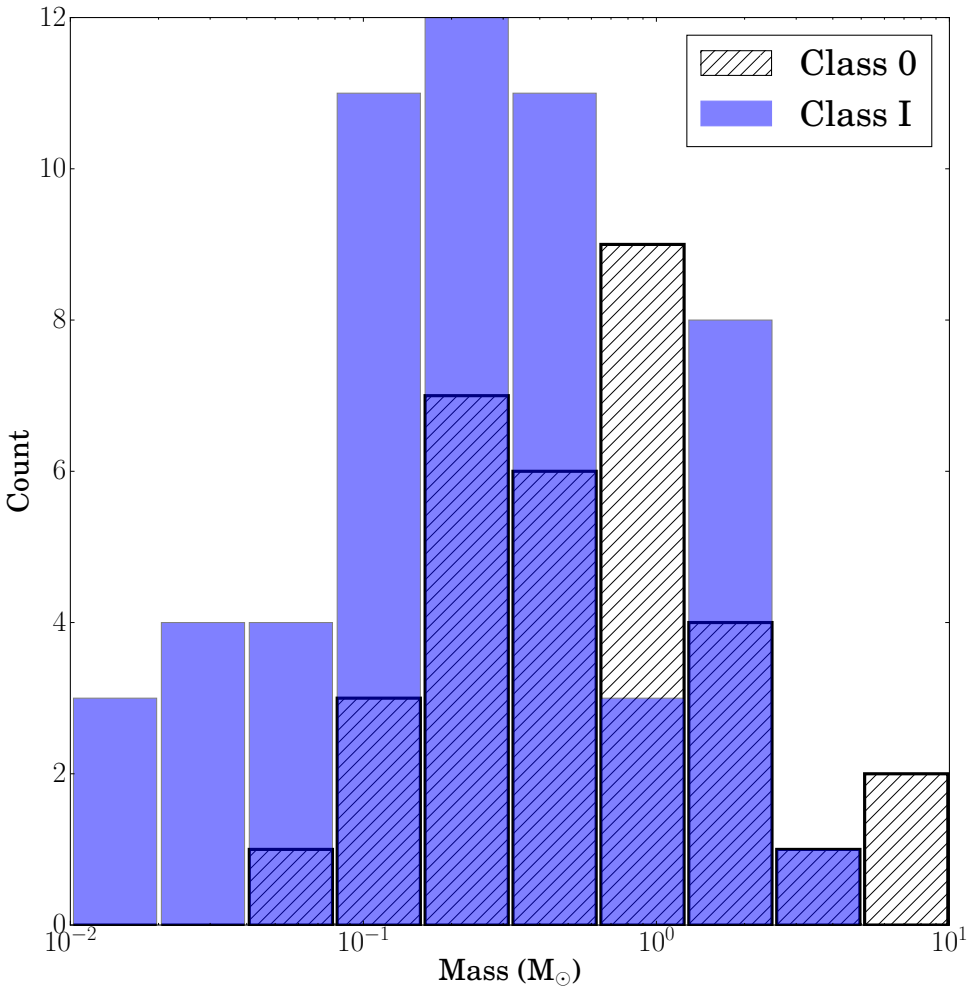

Figure 6.11: Envelope masses for 90 well-sampled Class 0 and Class I protostars. Class 0 objects are plotted using hatched bars and Class Is using solid blue bars.

sources, particularly for Class Is with $T_{\rm bol} > 200$ K. The average Class 0 protostar has an envelope approximately three times as massive as a late-type Class I protostar. This is unsurprising; a Class I protostar is expected to have accreted more material from its envelope than a Class 0 by definition (André, Ward-Thompson, and Barsony 2000). Protostellar envelopes in Serpens are more massive than in other regions. This is true even when compared to Aquila, which is the same distance away (Table 5.2). Serpens has a high fraction of Class 0 sources along with Perseus (Table 6.3). The mean envelope mass in Perseus, however, is much lower than in Serpens, but this is consistent with the difference in distances (see Table 5.2).

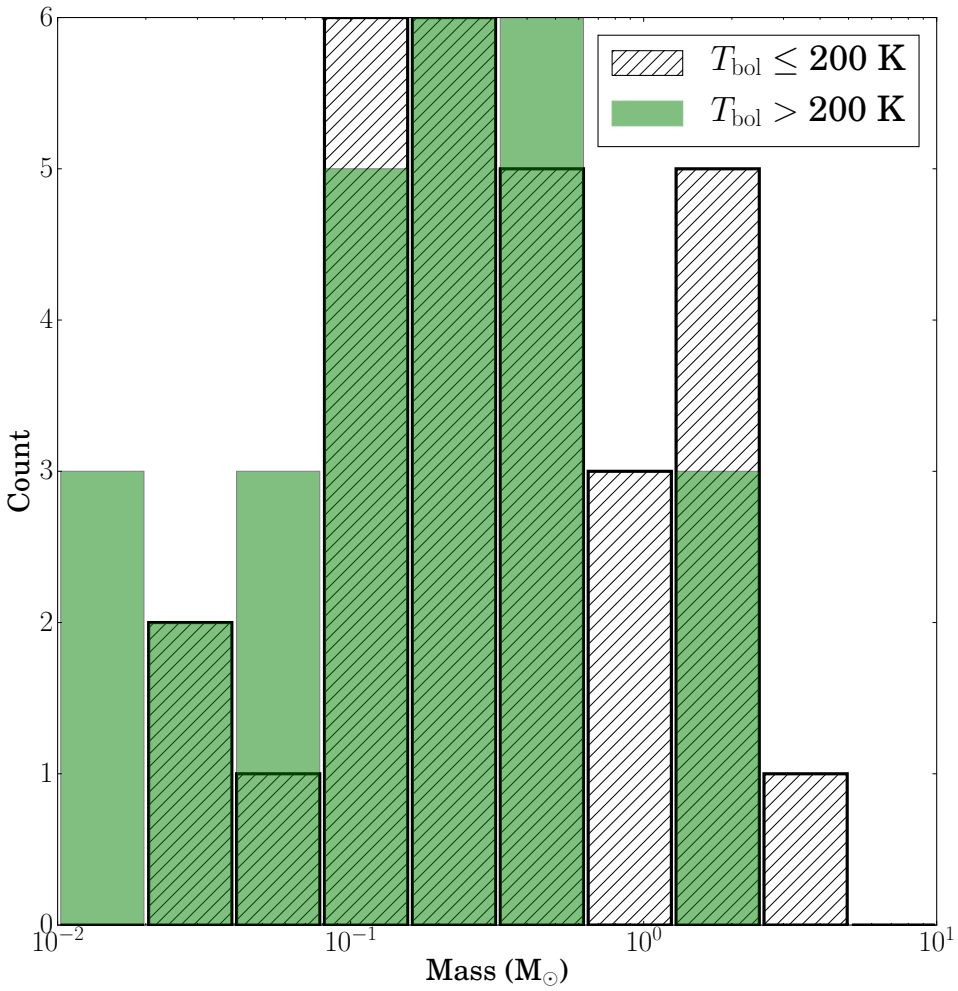

Figure 6.12: Envelope masses for Class I protostars, split by $T_{\rm bol}$. Class I protostars with $T_{\rm bol} \leq 200$ K are plotted using hatched bars and those with $T_{\rm bol} > 200$ K are shown with solid green bars.

Models by, e.g., Shirley, Evans, and Rawlings (2002) and Young et al. (2003) indicated a protostellar temperature of approximately 15 K. The average temperature derived here, however, is 20 K. One explanation for this is that the model SED fitting here incorporates wavelengths shorter than the submillimetre regime (i.e., 70 µm). These wavelengths also sample hotter emitters and can, therefore, bias temperatures towards higher values. Our estimates are consistent with the temperature maps of Rumble et al. (2015) and Rumble et al. (2016) that only used 450 and 850 µm fluxes. Those calculations were implemented in regions where YSOs are externally heated by OB stars, whereas many of the regions we have obtained temperatures in do not experience such heating. This may mean that

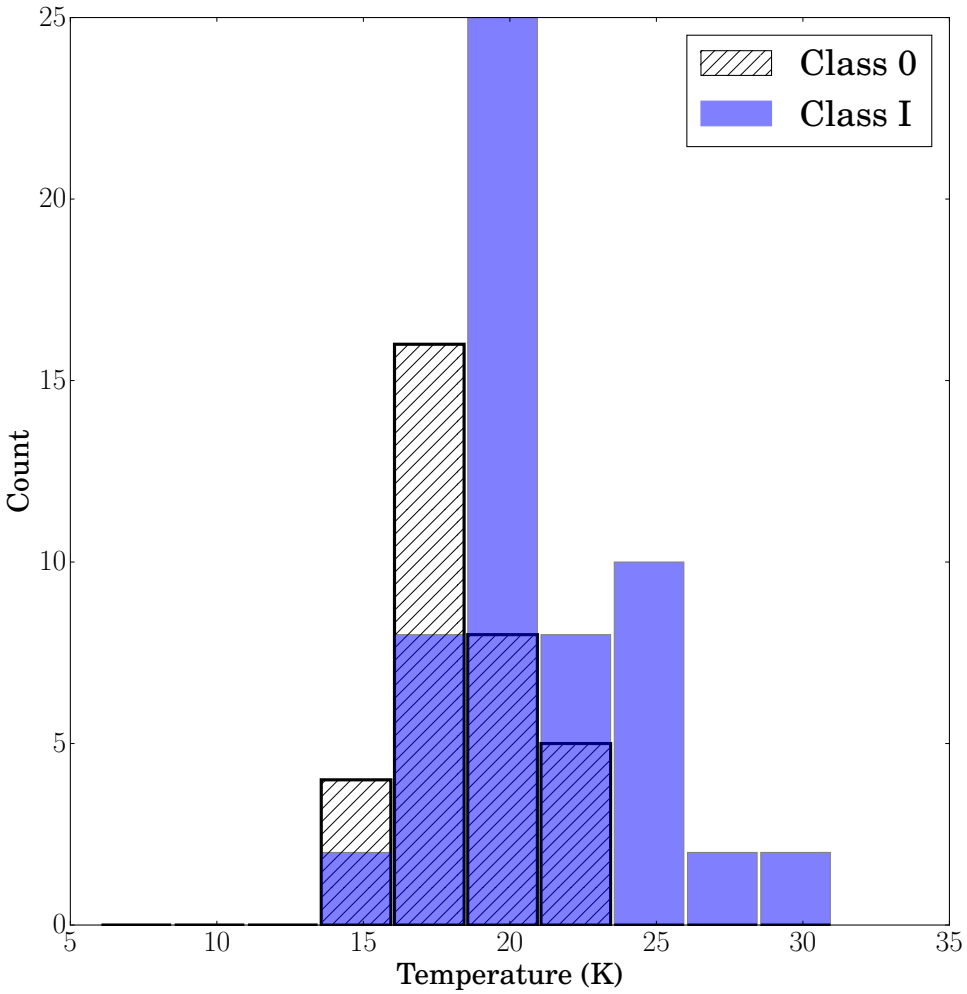

Figure 6.13: Envelope temperatures for 90 well-sampled Class 0 and Class I protostars - derived from single temperature opacity modified blackbody fits to SEDs. Class 0 objects are plotted using hatched bars and Class Is using solid blue bars.

our single-temperature fits are overestimating protostellar temperatures. For example, the Ossenkopf and Henning (1994) model 5 opacities assume a dust opacity spectral index $\beta = 1.8$. If this is too low, it will increase the temperatures of the model SEDs.

Figure 6.14 plots envelope masses against temperatures for all 90 protostars in the sample. The highest-temperature objects all have low envelope masses, but colder objects can also have low masses. With the exception of the warmer protostars, envelope masses show very little correlation to temperature.

The correlation between envelope mass and temperature was also examined using

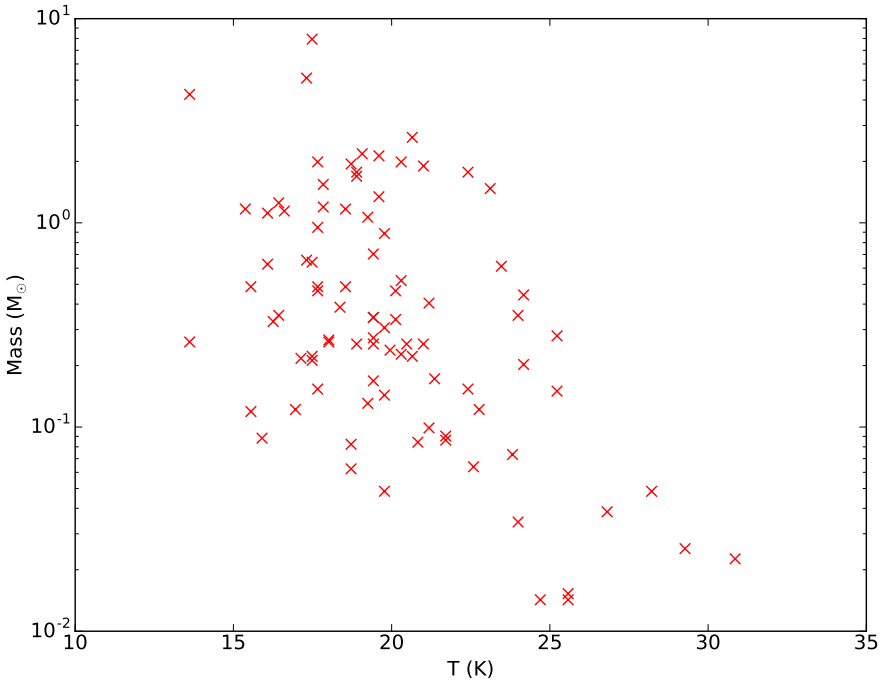

Figure 6.14: Envelope temperatures and masses for 90 well-sampled Class 0 and Class I protostars - derived from single temperature opacity modified blackbody fits to SEDs.

the Pearson correlation coefficient (Pearson 1895). This quantity is found using the relation

$$\rho_{X,Y} = \frac{\mathrm{cov}(X,Y)}{\sigma_X \sigma_Y} \tag{6.3}$$

where $\mathrm{cov}(X,Y)$ is the covariance of two variables X and Y, and σ is the standard deviation. The Pearson correlation coefficient was calculated for all well-sampled protostars. A value of -0.47 was returned, with a p value of 3.5×10^{-6}, indicating a moderate negative correlation between envelope mass and temperature. As sources evolve from Class 0 to Class I, envelope mass decreases and temperature increases.

Figure 6.15 plots derived envelope mass against bolometric temperature for each of the 90 protostars. Expected masses for Class 0 and Class I objects are plotted for the mean, minimum, and maximum temperatures derived in this section. These act as detection limits. At low values of T_{bol}, there is a region with no sources that lies above the mass limit at which SCUBA-2 can detect objects. This void indicates that we are being limited by *Spitzer* completeness for our youngest protostars.

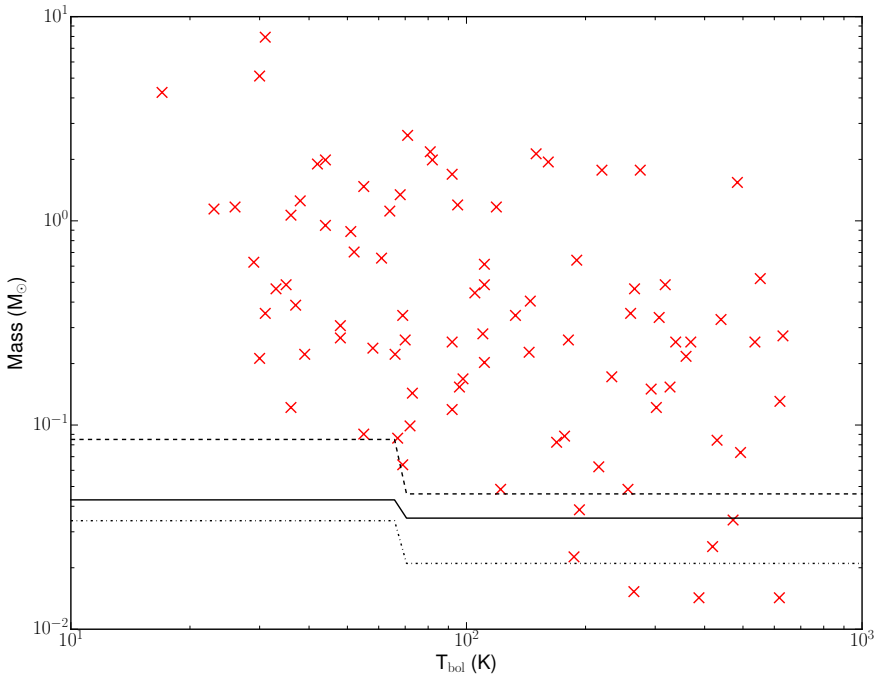

Figure 6.15: Envelope masses plotted against $T_{\rm bol}$ for 90 well-sampled Class 0 and Class I protostars. Masses were derived from single temperature opacity modified blackbody fits to SEDs. The solid black line shows the expected mass for the mean Class 0 then Class I temperatures derived in this section using a 3σ point source detection threshold (18.2 and 21.0 K, respectively). The dotted and dot-dashed lines use the minimum and maximum temperatures derived for each class.

6.2.4 Source Concentrations

We also calculated the concentration parameter at 850 µm for all YSOs matched to a SCUBA-2 peak (either lone or blended sources were permitted). The calculation was largely the same as Equation 4.1, with one modification. Rather than using $\pi R^2_{\rm core}$ to provide an area, the total area of the FellWalker core was used. Concentration parameters were then plotted against $T_{\rm bol}$ for each object, shown in Figure 6.16.

There is very little correlation between concentration and $T_{\rm bol}$. The value of the Pearson correlation coefficient was calculated for the two sets of variables, returning a value of -0.21. This indicates a very weak (negative) correlation. Therefore, there appears to be no relation between the evolutionary class of an object and how centrally concentrated its emission is.

The majority of sources have concentration values between 0.33 and 0.72, correspond-

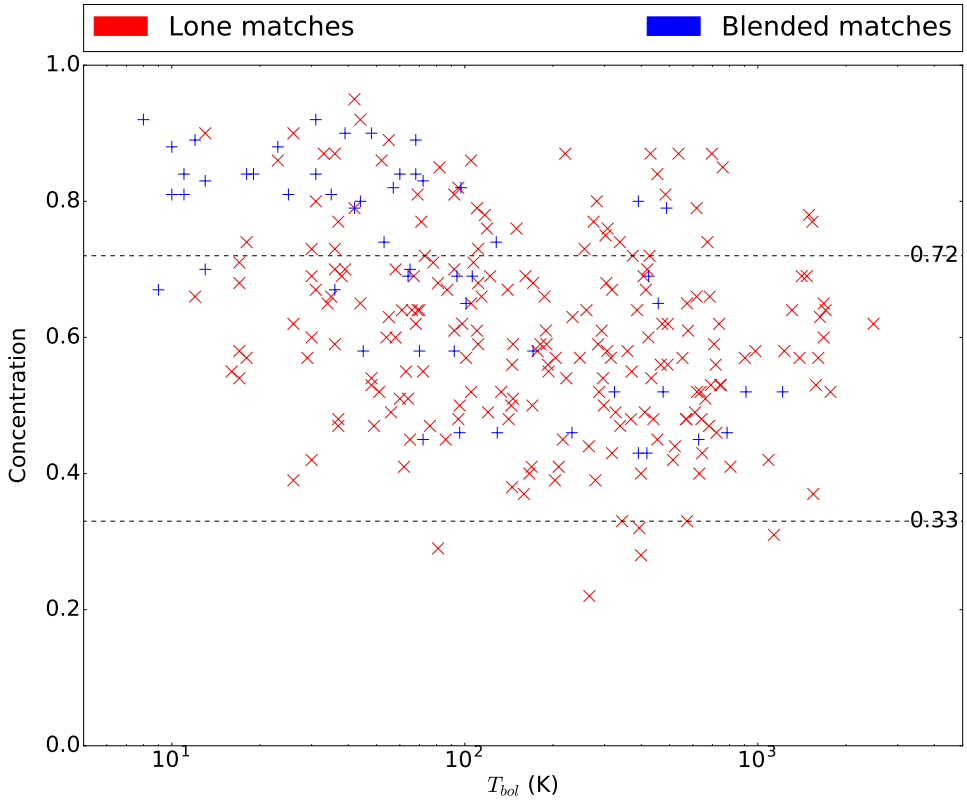

Figure 6.16: Concentrations plotted against $T_{\rm bol}$ for peak-matched sources. Lone matches are plotted with red crosses and blended matches are plotted with blue plus symbols. Dashed lines at concentration values of 0.33 and 0.72 represent the minimum and maximum concentration values expected of a Bonnor-Ebert sphere (Johnstone et al. 2000).

ing to the minimum and maximum values expected for a Bonnor-Ebert sphere (Johnstone et al. 2000). A large number of sources have a concentration of > 0.72, the boundary for critically self-gravitating objects. This may either mean that these objects are undergoing collapse, or that they are being supported by additional mechanisms such as magnetic fields (Kirk, Johnstone, and Di Francesco 2006). Protostars are undergoing collapse, so it would be expected that most sources would have a concentration of > 0.72. It is possible that this is not the case because FellWalker clump areas include more extended material than the central protostellar cores themselves. Larger areas cause correspondingly smaller concentrations to be calculated.

6.3 Summary

In this chapter, the properties of 592 protostellar candidates identified in Chapter 5 were examined. Extinction-corrected bolometric temperatures ($T_{\rm bol}$) were calculated for each of the protostellar candidates. $T_{\rm bol}$ was used to classify these sources, with the additional requirement that protostellar sources must be associated with dense cores at or above a 3 σ level of detection for at least one SCUBA-2 wavelength (450 or 850 µm). Sources were classified as Class 0, Class I, or non-protostellar-objects.

A total of 362 protostellar candidates are Class 0/I protostars according to our classification, with 115 Class 0 objects and 247 Class I objects. The overall number is approximately 27 % higher than the number of Class 0/I sources found within the same clouds by mid-infrared spectral index in the Dunham et al. (2015) catalogue. Our number of separately classified Class 0 and Class I protostars, requiring both $T_{\rm bol} \leq 650$ K and a detection at $\lambda \geq 350$ µm, is a factor of two greater, due to the addition of SCUBA-2 fluxes to our dataset.

We find that Class 0 objects comprise 32 % of the total number of protostars. This value is consistent with the 33.5 % found by Dunham et al. (2015), but lower than the 42 % found by the *Herschel* Orion Protostar Survey (Furlan et al. 2016; Fischer et al. 2017). Overall, 17.5 % of the YSOs within the SCUBA-2 maps are protostellar. 80 % of classifications made with SCUBA-2 agree with those determined from observations of the HCO^+ J = 3 $\rightarrow$ 2 transition by Heiderman and Evans (2015).

Based on our source counts, we derived lifetimes of 0.19-0.28 Myr and 0.40-0.61 Myr for the Class 0 and Class I protostellar stages, respectively, giving an overall protostellar lifetime of 0.59-0.89 Myr. Averaging between the two extremes, the overall lifetime is approximately 25 % longer than calculated by Dunham et al. (2015). The majority of this increase applies to the Class I sources, for which the (averaged) Class I lifetime is approximately 28 % larger. By contrast, the averaged Class 0 lifetime is approximately 21 % longer. This increase means that Class 0 protostars will remain in this envelope-dominated stage for longer, allowing a reduced mass accretion rate.

An extinction-corrected bolometric luminosity ($L_{\rm bol}$) was also calculated for every protostellar source in the SCUBA-2 dataset. The mean luminosity of the protostars in this sample is 3.53 $L_\odot$, and the median luminosity is 1.13 $L_\odot$. 173 protostars (48 %) are low luminosity, with $L_{\rm bol} \leq L_\odot$. The addition of SCUBA-2 fluxes to protostars previously without any submillimetre coverage caused luminosities to increase by an average factor of 2.5, as predicted by Dunham et al. (2013).

$L_{\rm bol}/L_{\rm smm}$ values were calculated for every protostellar candidate. We find that this quantity cannot be used to distinguish between Class 0 and Class I objects in our list of candidates. In addition, the Young and Evans (2005) boundary between Class 0 and Class I objects ($L_{\rm bol}/L_{\rm smm} < 175$) may require revision when applied to observational datasets.

We found 24 Very Low Luminosity Objects (VeLLOs) from the list of protostellar candidates, comprising 6.6 % of the total sample. Of these objects, 19 are newly-identified as such, and several previously-published VeLLOs now have $L_{\rm bol} > 0.1$ $L_\odot$, excluding them from that type.

Chapter 7

The Conclusion

"Oh, very well, it's time for your bribe. Now, you can either have the washer and dryer where the lovely Smithers is standing, or you can trade it all in for what's in this box."
— C.M.Burns

7.1 Concluding Remarks

In this thesis I have discussed the work I have done as part of the JCMT GBS (Ward-Thompson et al. 2007). I began by focusing on the Lupus I molecular cloud. Before analysing the SCUBA-2 data of this cloud, I investigated the data reduction process in Chapter 2. This investigation resulted in changes being made to the default GBS reductions, which improved the recovery of faint submillimetre emission in Lupus I.

Once the newly-reduced maps were available, I studied the star formation in Lupus I in depth to produce a GBS first look paper on Lupus I. This work is outlined in Chapter 3, where we studied both individual YSOs and prestellar / starless cores. We detected eleven YSOs with SCUBA-2, including two Class 0/I protostars, one Flat-Spectrum YSO, and eight Class II objects. Including YSOs not detected by SCUBA-2, we found a high proportion of protostellar objects in Lupus I compared to clouds such as Ophiuchus.

We calculated disk masses for the more evolved YSOs and found that one has a disk mass greater than the minimum mass Solar nebula. We found a mean disk mass for Class

F and II objects of 5.9×10^{-3} $M_{\odot}$. We also used modified blackbody SED fits to calculate envelope masses and temperatures for three protostars, finding that all had low envelope masses and temperatures higher than 19 K. We calculated luminosities and found at least two VeLLOs, with two other possible. We used the SED models of Robitaille et al. (2006) to fit our data and found that they were able to constrain interstellar extinction, but not masses.

In Lupus I we found a mean core mass of 0.73 $M_{\odot}$, two of which are starless but have a mass greater than the Jeans mass. Virial stability estimates also show that a starless core of 2.99 $M_{\odot}$ may be undergoing collapse. Overall, although the number of YSOs is low, we found evidence for an ongoing low-mass star formation event in Lupus I that has possibly been triggered by a shock front.

In Chapter 4 I used observations by SCUBA-2, *Spitzer* and *Herschel* to construct SEDs for five FHSC candidates in Serpens South, in collaboration with other members of the University of Exeter's Astrophysics Department. These observations were then used by Alison Young (Young et al. 2018) to investigate the nature of the FHSC candidates by fitting to FHSC models. We found that modelling can be used to constrain the properties of FHSC candidates, and that two of the candidates are probable FHSCs.

Moving on from FHSCs, I began producing a GBS catalogue of protostars in the Gould Belt using the YSO list of Dunham et al. (2015). This work first required sources to be identified in the SCUBA-2 maps of ten Gould Belt regions, which is explained in Chapter 5. Once a list of 592 candidate protostars had been produced, with SCUBA-2 fluxes assigned, these objects could be examined.

We used $T_{\rm bol}$ to classify the 592 candidates and found a total of 362 protostars. This is twice the number of protostars classified using $T_{\rm bol}$ by Dunham et al. (2015), as $T_{\rm bol}$ was previously underestimates due to lack of submillimetre data. The ratio of Class 0 to Class I protostars is 32 %, which is consistent with previous estimates. We used our updated source counts to recalculate the lifetime of the protostellar phase. We found lifetimes of 0.19-0.28 Myr and 0.40-0.61 Myr for the Class 0 and Class I protostellar stages, respectively, giving an overall protostellar lifetime of 0.59-0.89 Myr. These numbers are approximately

25 % greater than previously calculated, a significant result.

We also investigated the luminosity distribution of protostars, finding an average luminosity of 3.53 $L_\odot$. The luminosity distribution of our updated list of protostars does not differ from the distribution of Dunham et al. (2013), meaning that our newly added sources are robust. We also calculated the ratio $L_{\rm bol}/L_{\rm smm}$, finding that we were not able to use it to classify our protostars. This may be because we require more fluxes at the SED peak, or it may be that this ratio is not able to observationally classify sources. Finally, we identified 24 VeLLOs with $L_{\rm bol} \leq 0.1$ $L_\odot$, 19 of which were not previously known to be VeLLOs. This number is a factor of two greater than previously known.

To sum up, my work has improved the understanding of protostars. We now know them to be more numerous and longer-lived than previously thought.

7.2 Future Work

The work of this thesis has involved constructing the SEDs of YSOs using data from several surveys. Ensuring that SEDs are well-sampled is important; data at a wide range of wavelengths should be used. In particular, detections at the SED peak for YSOs are necessary to accurately calculate properties such as the bolometric luminosity ($L_{\rm bol}$). For protostars, this peak lies at approximately 100 µm (see Figure 6.1). Although MIPS 2 and 3 observe at 70 and 160 µm, respectively, there are issues with using MIPS fluxes. Coverage is often not as complete as in the IRAC bands due, for example, to saturation. In addition, the resolution of MIPS 3 is approximately 40", so individual sources may not be resolved by these observations.

Therefore, one of my immediate research goals would be to further improve the sampling of the SEDs of the protostars investigated in Chapter 6 by including data from the *Herschel* Space Observatory. *Herschel* was able to observe continuum emission at six wavelengths between 70 µm and 500 µm, including higher resolution images at 70 and 160 µm compared to MIPS. Therefore, combining fluxes from *Herschel* with the protostar catalogue presented in this work would improve the SEDs for hundreds of protostars. Full

coverage from *Spitzer*, *Herschel* and SCUBA-2 would improve the calculation of several protostellar properties including $T_{\rm bol}$ and $L_{\rm bol}$.

Unfortunately, it is not trivial to combine fluxes from different surveys. In particular, the *Herschel* GBS use *Getsources* for their source-finding (see Section 5.4.2, whereas we used FellWalker in Chapter 5. Therefore, I would like to collaborate with both the JCMT GBS and *Herschel* teams, with the aim of reconciling these separate datasets. Their combination would allow the properties of YSOs such as $L_{\rm bol}$ to be calculated with improved accuracy.

To determine the evolutionary class of protostars, we used $T_{\rm bol}$ in Chapter 6. A combined dataset would mean that the evolutionary status of more YSOs than ever before could be accurately calculated. In turn, the lifetimes of these objects could be ascertained with greater accuracy than we were able to in Chapter 6.

Another question that these calculations could help answer is the luminosity problem. The magnitude of the problem will not be certain until protostellar luminosities, as well as the duration of the protostellar stage, are known accurately. Compared to observational work by Dunham et al. (2013), I would be able to improve protostellar statistics with both a greater number of sources, and more accurate luminosities, by incorporating *Herschel* fluxes.

I also demonstrated in Section 6.2.2.1 that we have been unable to use the ratio of $L_{\rm bol}/L_{\rm smm}$ to determine the evolutionary stage of protostars. To calculate this quantity accurately, a fully-sampled SED is required. This will be possible when *Herschel* fluxes are incorporated into our dataset. Therefore, we will be able to determine whether $L_{\rm bol}/L_{\rm smm}$ can be used to observationally classify protostars, and whether the evolutionary boundary between Class 0 and Class I sources requires adjustment.

Furthermore, *Herschel* observations may also be able to identify new protostars that were missed from the Dunham et al. (2015) catalogue. Such new information could then be used to revisit the SCUBA-2 sources identified in Chapter 5 and provide an updated catalogue of protostars in the Gould belt regions we have studied.

7.3 Acknowledgements

The JCMT has historically been operated by the Joint Astronomy Centre on behalf of the Science and Technology Facilities Council of the United Kingdom, the National Research Council of Canada and the Netherlands Organisation for Scientific Research. Additional funds for the construction of SCUBA-2 were provided by the Canada Foundation for Innovation. The identification number for the programme under which the SCUBA-2 data used in Chapter 3 was obtained is MJLSG34. In addition, the data provided in Section A.1 was obtained under the program with the identification number MJLSG33. Chris Mowat was supported by an STFC studentship.

This research has made use of NASA's Astrophysics Data System. This research used the services of the Canadian Advanced Network for Astronomy Research (CANFAR) which in turn is supported by CANARIE, Compute Canada, University of Victoria, the National Research Council of Canada, and the Canadian Space Agency. This research used the facilities of the Canadian Astronomy Data Centre operated by the National Research Council of Canada with the support of the Canadian Space Agency.

Starlink software (Currie et al. 2014) is supported by the East Asian Observatory. Matplotlib is a 2D graphics package used for Python for application development, interactive scripting, and publication-quality image generation across user interfaces and operating systems. This research made use of APLpy (Robitaille and Bressert 2012), an open-source plotting package for Python hosted at http://aplpy.github.com.

This publication makes use of data products from the Wide-field Infrared Survey Explorer, which is a joint project of the University of California, Los Angeles, and the Jet Propulsion Laboratory/California Institute of Technology, funded by the National Aeronautics and Space Administration. This publication makes use of data products from the Two Micron All Sky Survey, which is a joint project of the University of Massachusetts and the Infrared Processing and Analysis Center/California Institute of Technology, funded by the National Aeronautics and Space Administration and the National Science Foundation. This research uses observations with AKARI, a JAXA project with the participation of ESA. Herschel is an ESA space observatory with science instruments provided by European-led

Principal Investigator consortia and with important participation from NASA.

The authors wish to recognize and acknowledge the very significant cultural role and reverence that the summit of Maunakea has always had within the indigenous Hawaiian community. We are most fortunate to have the opportunity to conduct observations from this mountain.

The Appendices

Appendix A

Additional SCUBA-2 Maps

"Oh, and one more thing; You must find the jade monkey before the next full moon."

— C.M.Burns

A.1 SCUBA-2 Maps of Serpens

In Section 5.2.1, I discussed the SCUBA-2 observations of the Serpens Main and Serpens North molecular clouds. The following figures present the 450 and 850 μm SCUBA-2 maps of these clouds, which have not yet been published. The fluxes for these maps are shown with square root scaling.

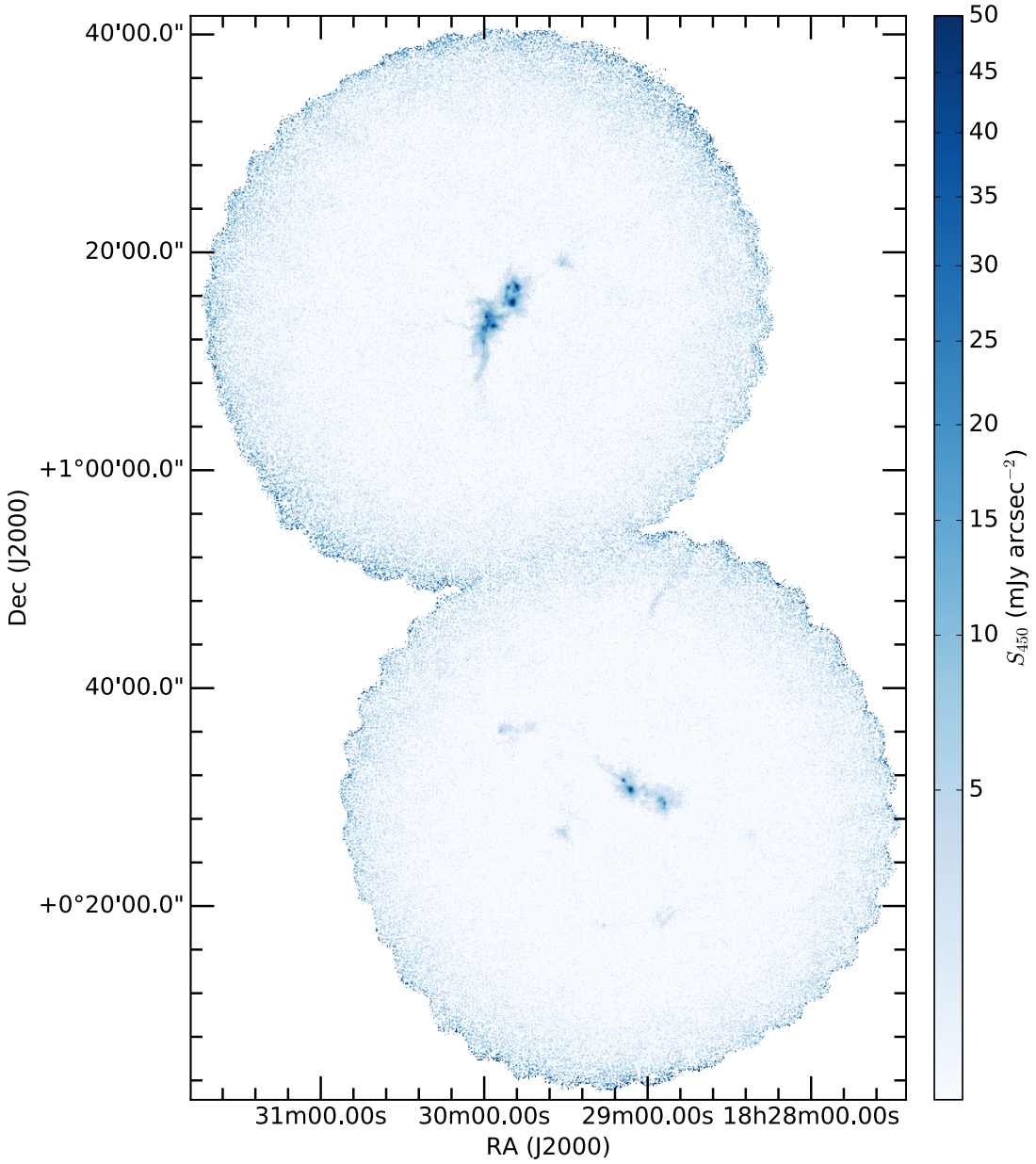

Figure A.1: SCUBA-2 450 µm map of the Serpens Main molecular cloud.

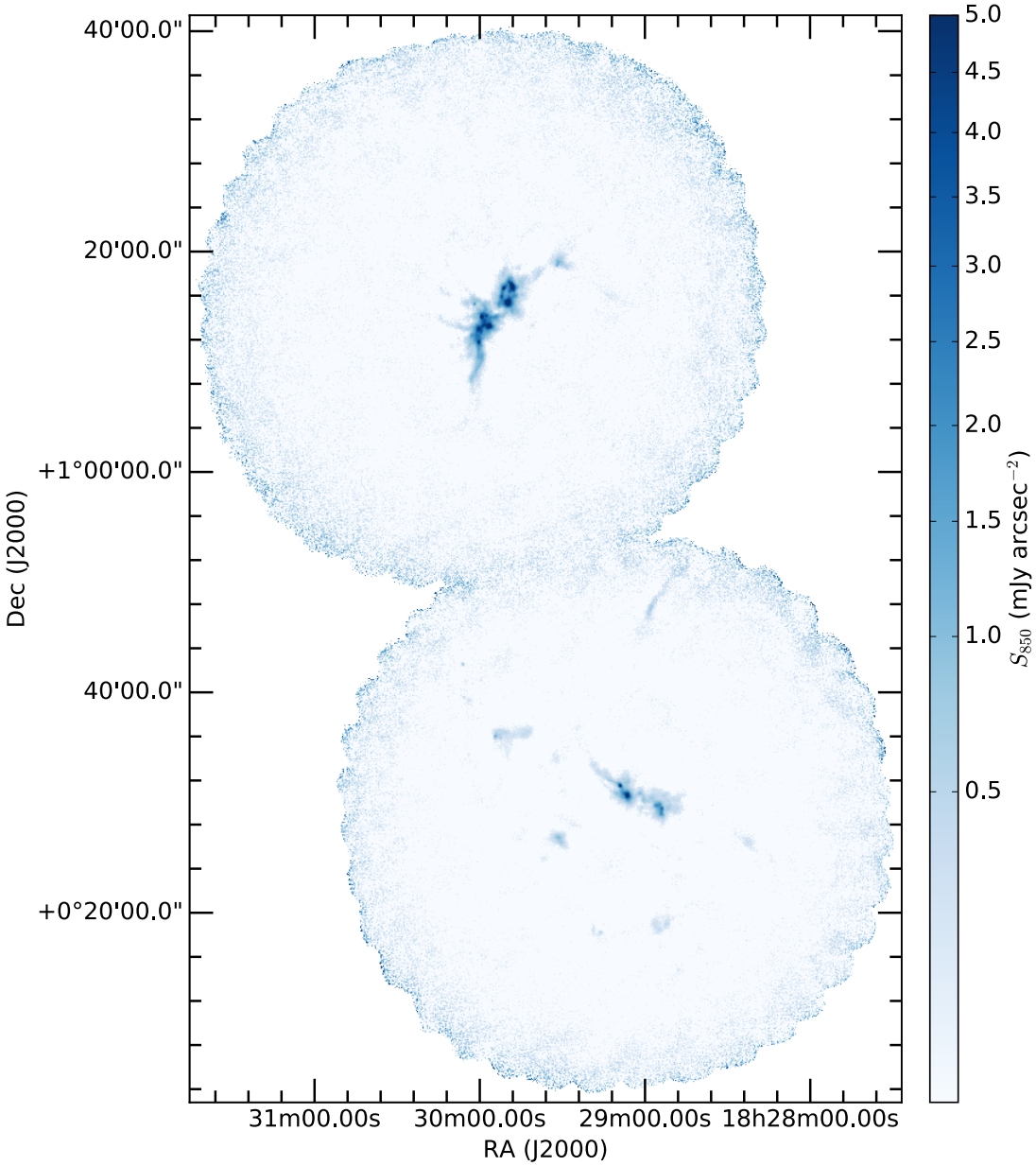

Figure A.2: SCUBA-2 850 µm map of the Serpens Main molecular cloud.

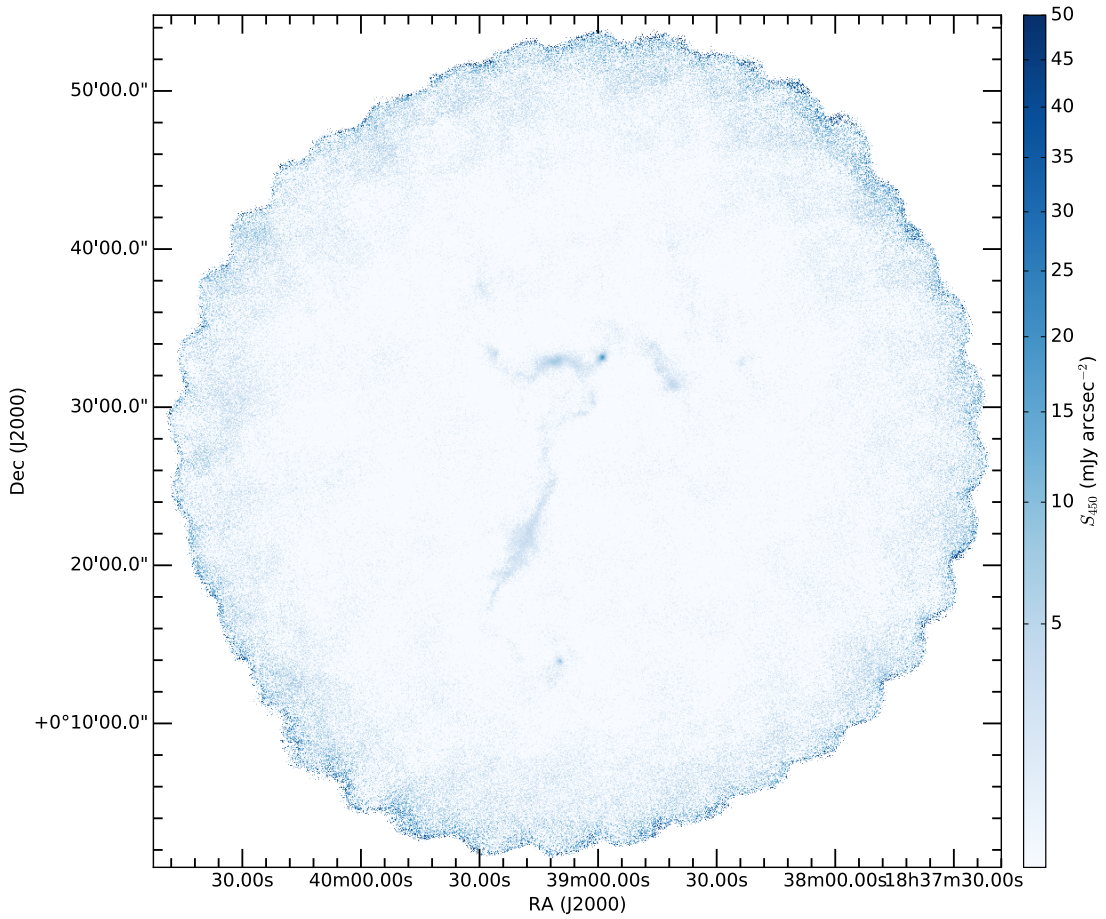

Figure A.3: SCUBA-2 450 µm map of the Serpens North molecular cloud.

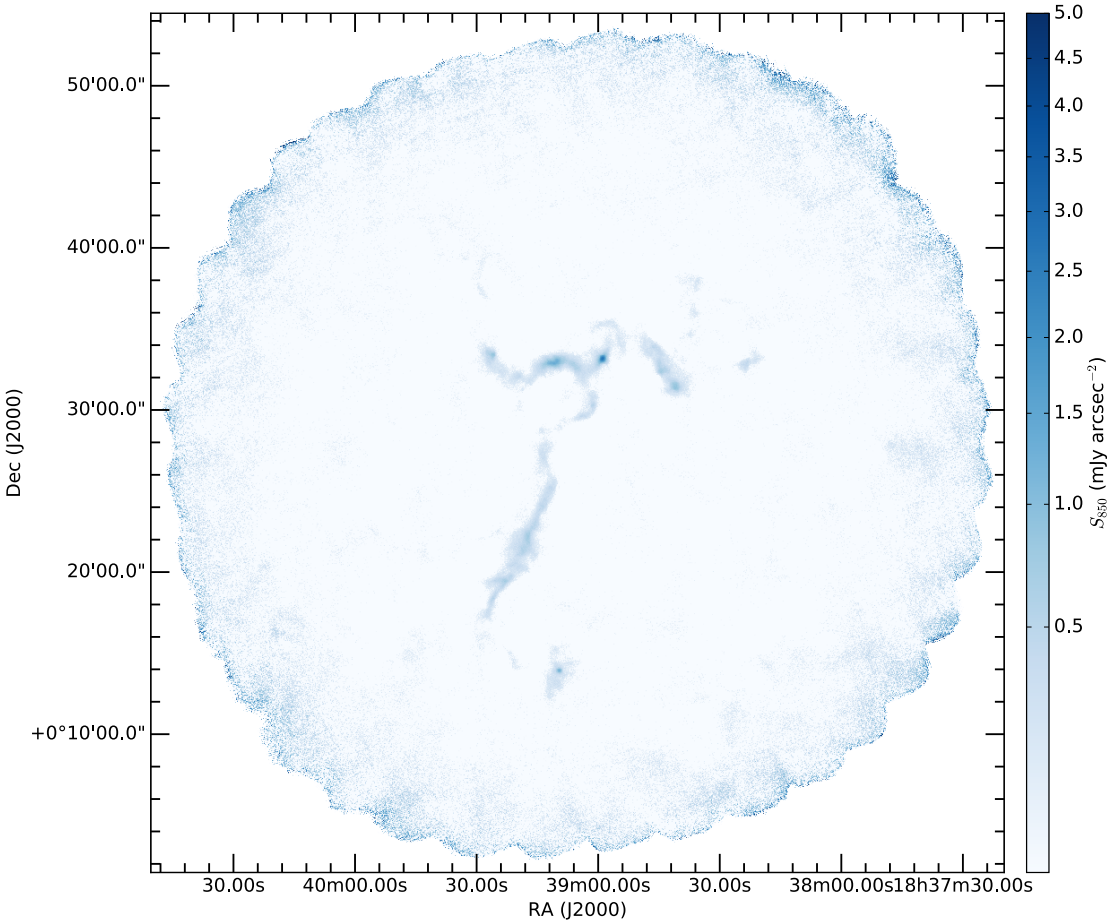

Figure A.4: SCUBA-2 850 µm map of the Serpens North molecular cloud.

Appendix B

Tables

B.1 Full Table of Protostellar Candidates

Here I present the full table of 592 protostellar candidate sources. Table 5.5 and Table 6.1 presented 450 and 850 µm fluxes and flags, $T_{\rm bol}$, $L_{\rm bol}$, and classifications for a sample of 15 candidates. This information is now provided for every candidate in a single reference table.

The running indices used to identify candidates in Chapter 5 and Chapter 6 are provided alongside each *Spitzer* source ID from Dunham et al. (2015) and the source's parent molecular cloud. For further explanations of fluxes and flags, refer to Table 5.5 and Section 5.3. Classifications, as well as values of $T_{\rm bol}$ and $L_{\rm bol}$, are detailed in Table 6.1 and Section 6.1 and Section 6.2.2.

Note also that SEDs for all candidates are provided on a CD as supplementary material. In addition, this disk contains the full catalogue of all fluxes used to construct SEDs for the protostellar candidates in this work.

Table B.1: Full table of source properties for 592 protostellar candidates.

Source index	ID	Cloud	S_{450} (mJy)	Flag_{450}	S_{850} (mJy)	Flag_{850}	T_{bol} (K)	L_{bol} ($L_{\odot}$)	Class
1	J182632.8-034627	Aquila	15905.0458333	D	70.6036202748	U	82	2.09	I
2	J182713.2-034014	Aquila	585.645736719	N	81.3637681159	D	1630	11.65	NP
3	J182736.7-035004	Aquila	536.067650401	N	36.9601055254	N	385	0.94	I
4	J182750.1-034913	Aquila	521.710929408	N	266.140170851	D	743	1.89	NP
5	J182754.7-034238	Aquila	6413.41944444	D	2225.03327499	D	484	8.21	I
6	J182805.4-034659	Aquila	515.766434631	N	34.8721591951	N	178	2.09	I
7	J182842.6-012951	Aquila	616.513979501	N	78.4249435588	N	292	0.33	I
8	J182847.7-013807	Aquila	2181.90277778	C	403.995437252	C	92	1.36	I
9	J182847.7-013814	Aquila	2181.90277778	C	403.995437252	C	171	0.89	I
10	J182854.8-013727	Aquila	230.252886748	N	63.2783396235	U	51	0.11	0
11	J182855.8-013734	Aquila	237.856604095	N	168.125328068	D	287	0.7	I
12	J182855.8-014313	Aquila	252.201618694	N	36.0224409045	N	288	0.2	I
13	J182857.1-013715	Aquila	235.275509036	N	35.5442399005	N	458	0.19	I
14	J182857.7-014230	Aquila	257.252763671	N	35.9352442824	N	198	0.13	I
15	J182858.3-013834	Aquila	822.383333333	D	560.867447404	D	440	1.01	I
16	J182901.8-013902	Aquila	387.584401392	U	194.134863332	U	169	0.22	I
17	J182905.3-014156	Aquila	15771.5187286	D	2812.3474261	D	82	9.77	I
18	J182905.4-034245	Aquila	529.05212666	N	542.740954498	D	189	0.47	I
19	J182905.9-013025	Aquila	346.735970378	N	147.909737422	U	245	0.5	I
20	J182908.0-020221	Aquila	251.223987077	N	36.1822878295	N	605	0.34	I
21	J182908.1-020538	Aquila	2196.05972222	D	2492.81423173	D	296	1.45	I
22	J182911.1-020430	Aquila	253.703115278	N	104.559183464	U	673	3.32	NP
23	J182912.1-014845	Aquila	242.852097883	N	34.5494309076	N	131	0.1	I
24	J182912.8-020350	Aquila	1229.63333333	D	347.905394048	D	293	14.54	I
25	J182913.0-014617	Aquila	1969.79583333	D	828.379704651	D	318	1.8	I
26	J182913.1-020502	Aquila	244.196297763	N	32.9429590553	N	81	0.11	I
27	J182916.6-020339	Aquila	229.511368734	N	42.7390996771	U	157	0.14	I

Source index	ID	Cloud	S_{450} (mJy)	Flag_{450}	S_{850} (mJy)	Flag_{850}	T_{bol} (K)	L_{bol} ($L_\odot$)	Class
28	J182920.9-013714	Aquila	249.732479508	N	199.195653798	D	521	1.89	I
29	J182923.4-013855	Aquila	1668.59583333	D	667.54647815	D	307	3.51	I
30	J182925.1-014737	Aquila	239.665938481	N	125.010144928	D	344	0.21	I
31	J182925.8-020317	Aquila	211.897789948	N	29.1925596194	N	273	0.17	I
32	J182936.6-015059	Aquila	643.563651846	U	225.86875053	U	868	4.51	NP
33	J182938.1-015100	Aquila	15544.8138889	D	2637.95479967	C	57	6.85	0
34	J182938.6-015100	Aquila	8015.00555556	D	2637.95479967	C	97	10.12	I
35	J182939.1-015021	Aquila	241.725112842	N	125.964490001	U	42	0.1	0
36	J182940.2-014032	Aquila	233.841619395	N	33.5115998017	N	179	0.12	I
37	J182940.2-015127	Aquila	239.285266797	N	161.617531921	U	225	0.13	I
38	J182941.6-015129	Aquila	235.758321457	N	36.2693981948	N	974	0.66	NP
39	J182941.9-015011	Aquila	812.379166667	D	2309.20654874	D	87	0.4	I
40	J182943.3-015651	Aquila	1303.45138889	D	415.655125215	D	369	2.97	I
41	J182943.9-021255	Aquila	1498.42083333	D	663.683590823	D	69	1.11	0
42	J182945.9-013312	Aquila	264.980419881	N	36.9647350626	N	264	0.17	I
43	J182947.0-015548	Aquila	800.918055556	D	289.27826087	D	327	3.28	I
44	J182947.3-015603	Aquila	433.110353141	U	585.904151363	D	371	0.64	I
45	J182952.1-015736	Aquila	221.510084843	N	212.802898551	D	159	0.15	I
46	J182952.3-015745	Aquila	224.877388187	N	174.672981453	U	111	0.13	I
47	J182953.7-015746	Aquila	226.608985401	N	30.9400517726	N	468	0.3	I
48	J182954.3-015823	Aquila	662.527960303	U	256.394196808	U	76	0.29	I
49	J182957.0-015945	Aquila	4769.06805556	D	1844.54270612	D	17	1.77	0
50	J182957.9-020103	Aquila	198.40327613	N	343.208743938	U	407	0.2	I
51	J182958.3-015740	Aquila	8641.06388889	D	4444.33361408	D	17	1.18	0
52	J182958.8-020004	Aquila	195.286099304	N	178.124357517	U	195	0.11	I
53	J182958.9-020125	Aquila	1026.10603273	U	1876.64899708	D	56	0.44	0
54	J182959.0-020157	Aquila	191.057122007	N	91.5217391304	D	415	0.19	I
55	J182959.4-020106	Aquila	1182.84980912	U	1098.35224893	D	65	0.54	0

Source index	ID	Cloud	S_{450} (mJy)	Flag_{450}	S_{850} (mJy)	Flag_{850}	T_{bol} (K)	L_{bol} ($L_\odot$)	Class
56	J183000.0-015715	Aquila	219.092787194	N	31.410133681	N	324	0.31	I
57	J183000.2-020052	Aquila	2558.55555556	D	309.625800313	U	24	0.98	0
58	J183000.5-020211	Aquila	1229.86465103	U	404.7222038	U	225	0.71	I
59	J183000.6-020204	Aquila	1060.80222692	U	352.838316326	U	248	0.67	I
60	J183001.0-020608	Aquila	3826.59305556	D	652.49112563	D	145	3.16	I
61	J183001.1-020127	Aquila	1019.93342183	U	338.483545224	U	85	0.44	I
62	J183001.2-020148	Aquila	2358.68194444	D	846.756697128	D	266	4.68	I
63	J183001.3-020342	Aquila	1180.65183813	U	1632.91340575	D	411	12.19	I
64	J183002.2-020159	Aquila	1589.32988543	U	487.144791308	U	255	1.28	I
65	J183002.4-020257	Aquila	38195.7305556	D	1490.93669276	U	140	18.85	I
66	J183002.7-020259	Aquila	4248.7862967	U	1554.71369996	U	131	2.01	I
67	J183002.8-020222	Aquila	3018.96574115	U	923.241384866	U	25	1.18	0
68	J183002.8-020240	Aquila	4974.46945122	U	14307.6343901	C	19	2.04	0
69	J183002.9-020133	Aquila	3859.42361111	D	410.820333407	U	14	1.42	0
70	J183003.0-013632	Aquila	767.902777778	D	738.258463177	D	66	1.13	0
71	J183003.1-020234	Aquila	4425.46021658	U	1412.19104639	U	20	1.69	0
72	J183003.2-020326	Aquila	29708.3698945	D	1388.68621483	U	14	10.97	0
73	J183003.3-020245	Aquila	57493.8840029	D	14307.6343901	C	18	21.65	0
74	J183004.3-020138	Aquila	952.982937993	U	289.937397772	U	499	1.78	I
75	J183004.4-020415	Aquila	575.141700654	U	196.750358458	U	391	0.51	I
76	J183004.7-020227	Aquila	1867.47306553	U	555.658890741	U	17	0.7	0
77	J183004.9-020142	Aquila	844.265566563	U	249.86192334	U	270	0.69	I
78	J183005.1-020141	Aquila	834.425554622	U	237.148061135	U	292	1.14	I
79	J183005.2-020206	Aquila	1400.74343443	U	483.375797031	U	67	0.59	0
80	J183005.2-020234	Aquila	1117.00139186	U	387.540808226	U	621	1.71	I
81	J183005.2-020325	Aquila	1737.21043615	U	668.621922717	U	73	0.76	I
82	J183005.5-020107	Aquila	845.416747612	U	252.390494371	U	80	0.39	I
83	J183005.8-020144	Aquila	821.048425912	U	239.403405079	U	491	30.33	I

Source index	ID	Cloud	S_{450} (mJy)	Flag_{450}	S_{850} (mJy)	Flag_{850}	T_{bol} (K)	L_{bol} ($L_{\odot}$)	Class
84	J183006.2-020219	Aquila	195.42295093	N	195.947388924	U	373	0.2	I
85	J183006.2-020304	Aquila	193.08989594	N	147.215747541	U	179	0.13	I
86	J183006.7-020337	Aquila	815.138200309	U	890.905001747	D	114	0.41	I
87	J183008.7-020610	Aquila	214.23953915	N	86.5869876784	U	187	0.15	I
88	J183010.8-020354	Aquila	196.143302999	N	129.371215383	D	399	0.21	I
89	J183011.3-020656	Aquila	578.116649756	U	2148.72940926	D	34	0.26	0
90	J183013.0-012536	Aquila	-82.1572524015	U	212.220740876	N	1762	6.61	NP
91	J183015.6-015035	Aquila	193.685354041	N	178.369565217	D	806	0.23	NP
92	J183015.6-020719	Aquila	3562.55	D	1375.40886616	D	64	0.92	0
93	J183016.2-015252	Aquila	932.755555556	D	488.287253558	D	48	0.38	0
94	J183016.6-022936	Aquila	243.823604713	N	34.1112989971	N	495	0.49	I
95	J183017.0-020958	Aquila	3900.29583333	C	1232.82810217	C	64	1.76	0
96	J183017.4-020958	Aquila	3900.29583333	C	1232.82810217	C	106	1.27	I
97	J183021.2-021112	Aquila	229.188516524	N	32.3701439553	N	180	0.15	I
98	J183021.8-015200	Aquila	174.650763752	N	26.9309640974	N	419	1.16	I
99	J183021.9-020912	Aquila	225.600515288	N	99.3116603302	D	394	0.19	I
100	J183024.1-021029	Aquila	225.829818161	N	32.9629083093	N	420	0.21	I
101	J183024.5-015410	Aquila	1036.80277778	D	146.460415476	U	582	3.39	I
102	J183025.7-021115	Aquila	410.0875	D	120.597075404	U	457	0.98	I
103	J183025.8-021042	Aquila	5111.27916667	D	978.326059826	D	111	11.64	I
104	J183025.9-021142	Aquila	231.170875262	N	33.413715225	N	564	2.56	I
105	J183026.8-015327	Aquila	163.791760716	N	25.9821320976	N	565	0.29	I
106	J183027.1-021056	Aquila	3145.43055556	C	647.435028075	C	391	2.85	I
107	J183027.2-021100	Aquila	3145.43055556	C	647.435028075	C	418	4.1	I
108	J183027.5-015439	Aquila	163.206065605	N	30.0072463768	D	107	0.33	I
109	J183027.9-021037	Aquila	223.838960107	N	63.8198412989	U	515	0.19	I
110	J183029.0-020720	Aquila	204.16254635	N	31.1680195823	N	606	0.24	I
111	J183029.2-015642	Aquila	558.541613695	U	792.999687824	D	722	7.55	NP

Source index	ID	Cloud	S_{450} (mJy)	Flag_{450}	S_{850} (mJy)	Flag_{850}	T_{bol} (K)	L_{bol} ($L_\odot$)	Class
112	J183031.1-021032	Aquila	217.379000326	N	32.2933516869	N	1132	0.39	NP
113	J183031.4-015609	Aquila	164.518513915	N	388.578214693	D	81	0.08	I
114	J183031.5-021136	Aquila	225.874817936	N	32.4823924166	N	369	0.13	I
115	J183031.5-021606	Aquila	239.459279907	N	33.914339226	N	332	0.13	I
116	J183031.7-015613	Aquila	298.781944444	D	107.305120009	U	576	0.79	I
117	J183032.9-015252	Aquila	163.954874255	N	26.9990118874	N	74	0.07	I
118	J183033.2-021125	Aquila	224.685915135	N	32.5732399688	N	761	0.52	NP
119	J183034.4-022708	Aquila	248.904660484	N	34.8223172535	N	167	0.12	I
120	J183037.5-020853	Aquila	193.550042023	U	225.581164982	C	324	0.83	I
121	J183037.6-020840	Aquila	534.748611111	D	225.581164982	C	475	4.74	I
122	J183038.3-020843	Aquila	203.186752997	N	37.7963802783	U	101	0.12	I
123	J183041.2-022019	Aquila	249.351662798	N	33.758584148	N	240	0.23	I
124	J183046.9-015645	Aquila	603.466666667	C	319.10295676	C	129	0.61	I
125	J183046.9-015651	Aquila	603.466666667	C	319.10295676	C	96	0.36	I
126	J183048.7-015601	Aquila	3152.31111111	D	820.562003905	D	190	1.38	I
127	J183048.8-020713	Aquila	177.577686349	N	28.2142155317	N	534	0.17	I
128	J183054.9-020401	Aquila	173.766225363	N	61.3898550725	D	570	0.16	I
129	J183100.2-020338	Aquila	179.632311727	N	30.0459923548	N	1060	0.34	NP
130	J183102.7-020959	Aquila	607.154195309	U	240.294767081	U	452	0.65	I
131	J183111.0-020600	Aquila	2214.33668675	U	560.266521643	U	158	1.81	I
132	J183114.6-021144	Aquila	193.776413853	N	27.6146388638	N	938	0.59	NP
133	J183115.0-020105	Aquila	196.274835697	N	33.6171600902	N	422	0.28	I
134	J183119.4-020739	Aquila	1305.18565708	U	355.276278193	U	170	1.73	I
135	J183120.4-021553	Aquila	232.699640159	N	26.382574043	N	1055	0.22	NP
136	J183121.3-015335	Aquila	206.612757276	N	35.5058404684	N	387	0.15	I
137	J183129.8-020744	Aquila	195.774188075	N	58.7304347826	D	1135	5.29	NP
138	J183130.5-020055	Aquila	195.01223093	N	34.8395570213	N	188	0.14	I
139	J183133.8-021229	Aquila	232.336891786	N	27.1256673499	N	687	0.29	NP

Source index	ID	Cloud	S_{450} (mJy)	Flag_{450}	S_{850} (mJy)	Flag_{850}	T_{bol} (K)	L_{bol} ($L_\odot$)	Class
140	J183134.5-021512	Aquila	273.029505118	N	84.1860741487	U	675	0.6	NP
141	J183135.3-021254	Aquila	237.193205607	N	26.9912471097	N	1353	0.94	NP
142	J183135.9-021330	Aquila	245.608239745	N	27.2547254032	N	643	1.28	I
143	J183136.1-021448	Aquila	3966.4125	D	212.379504253	U	86	2.68	I
144	J183136.3-022120	Aquila	334.796134777	N	30.3331758388	N	545	0.28	I
145	J183137.5-020503	Aquila	197.937931754	N	32.2652638202	N	1240	1.22	NP
146	J183137.6-021455	Aquila	564.811514897	U	160.582528706	U	522	0.8	I
147	J183140.4-020814	Aquila	193.25611769	N	52.4906254683	U	1085	1.42	NP
148	J183144.2-021621	Aquila	313.565436946	N	30.5145193277	N	431	0.51	I
149	J183144.4-020745	Aquila	196.038906307	N	28.1180145985	N	226	0.15	I
150	J183148.5-021737	Aquila	356.892809266	N	347.252764225	D	646	0.31	I
151	J183152.1-020126	Aquila	2686.95694444	D	729.446381921	D	58	1.38	0
152	J183152.4-020031	Aquila	211.750713017	N	36.2237971034	N	417	0.32	I
153	J183201.5-023814	Aquila	368.81117476	N	33.465049991	N	285	0.23	I
154	J183206.2-021725	Aquila	338.029170862	N	30.2315201363	N	385	0.23	I
155	J183212.7-022237	Aquila	348.443923027	N	29.4837849235	N	427	0.35	I
156	J183213.1-015730	Aquila	1941.30972222	D	460.113043478	D	48	1.03	0
157	J183215.1-023453	Aquila	494.268063661	U	172.615224414	U	112	0.32	I
158	J183215.9-023443	Aquila	6102.84027778	D	1523.89331487	D	119	2.75	I
159	J183238.1-022905	Aquila	358.683814298	N	31.0993398658	N	803	0.33	NP
160	J183242.4-024756	Aquila	3993.72831718	N	2304.4689639	D	642	1.6	I
161	J183245.6-024657	Aquila	10844.2	D	353.359587696	N	22	1.4	0
162	J183303.4-020842	Aquila	715.553913098	N	57.4363745358	N	323	1.07	I
163	J041000.6+400236	Auriga	317.615492809	N	259.793354004	D	86	0.15	I
164	J041002.6+400248	Auriga	498.885613027	U	458.150473632	D	26	4.98	0
165	J041008.4+400224	Auriga	5581.78055556	D	1015.39227541	D	105	17.03	I
166	J041011.1+400126	Auriga	371.425	D	647.68628534	D	54	0.21	0
167	J041041.6+380805	Auriga	793.617481564	U	2305.09441397	D	105	7.14	I

Source index	ID	Cloud	S_{450} (mJy)	Flag_{450}	S_{850} (mJy)	Flag_{850}	T_{bol} (K)	L_{bol} ($L_{\odot}$)	Class
168	J042140.8+373359	Auriga	1670.89861111	D	713.00041054	D	111	0.88	I
169	J042538.4+370701	Auriga	4882.83888889	D	2430.68063805	D	38	1.9	0
170	J042539.7+370708	Auriga	275.672407584	N	176.092580845	U	631	5.59	I
171	J042940.0+352108	Auriga	225.814315957	N	62.4420289855	D	573	1.19	I
172	J042944.2+351230	Auriga	227.012223844	N	34.6232040724	N	1001	0.37	NP
173	J042949.2+351422	Auriga	219.851898442	N	34.749820935	N	754	1.22	NP
174	J042950.8+351558	Auriga	223.174012007	N	335.984084153	C	785	0.89	NP
175	J042951.0+351547	Auriga	700.604166667	D	335.984084153	C	232	0.54	I
176	J042953.4+351548	Auriga	219.219577246	N	187.440727024	U	1061	0.59	NP
177	J042954.1+351021	Auriga	218.065088861	N	35.04411422	N	175	0.14	I
178	J042956.2+351742	Auriga	227.758674323	N	35.9371300228	N	398	0.31	I
179	J043003.6+351420	Auriga	886.883333333	D	1282.68909744	D	204	0.54	I
180	J043008.2+351410	Auriga	222.409104347	N	188.884073148	U	400	0.41	I
181	J043009.5+351440	Auriga	221.375655329	N	54.9376811594	D	407	0.73	I
182	J043014.5+351332	Auriga	224.370150759	N	107.997101449	D	1545	5.17	NP
183	J043014.9+360008	Auriga	354.123103803	N	358.33761954	D	120	0.17	I
184	J043019.5+350821	Auriga	237.929738978	N	38.4057971014	D	374	0.18	I
185	J043023.8+352112	Auriga	228.952002545	N	35.6357803561	N	211	0.15	I
186	J043024.6+354520	Auriga	433.1125	D	102.542028986	D	193	4.13	I
187	J043027.0+354550	Auriga	333.594260033	N	38.8601112717	N	544	0.2	I
188	J043027.4+350917	Auriga	4067.48611111	C	1533.59610759	C	128	10.6	I
189	J043027.7+354615	Auriga	331.113644804	N	38.7420579234	N	189	1.43	I
190	J043028.0+350916	Auriga	4067.48611111	C	1533.59610759	C	53	2.04	0
191	J043028.4+354917	Auriga	328.472679277	N	38.3188691947	N	1266	0.63	NP
192	J043030.1+350639	Auriga	234.206030963	N	37.3673954278	N	256	0.19	I
193	J043030.5+355144	Auriga	725.8625	D	550.507596512	D	181	0.61	I
194	J043031.5+354513	Auriga	340.455613215	N	95.3806859584	U	341	1.77	I
195	J043036.8+355436	Auriga	9455.41388889	D	2586.3188685	D	95	3.97	I

Source index	ID	Cloud	S_{450} (mJy)	Flag_{450}	S_{850} (mJy)	Flag_{850}	T_{bol} (K)	L_{bol} ($L_\odot$)	Class
196	J043037.8+355101	Auriga	906.252777778	D	387.494202899	D	16	0.37	0
197	J043038.2+354959	Auriga	1726.39305556	D	477.023188406	D	133	1.02	I
198	J043038.6+355439	Auriga	423.744986366	U	137.416011786	U	314	0.33	I
199	J043039.1+355203	Auriga	484.458333333	C	350.452365065	C	1215	3.6	NP
200	J043039.3+355200	Auriga	484.458333333	C	350.452365065	C	911	6.49	NP
201	J043041.1+352941	Auriga	3553.425	D	1362.36151788	D	44	3.49	0
202	J043044.2+355951	Auriga	1167.45555556	D	534.416281717	D	233	4.7	I
203	J043046.2+345856	Auriga	445.182445903	N	555.048927709	D	60	0.39	0
204	J043048.5+353753	Auriga	1847.49583333	D	602.748916344	D	92	3.0	I
205	J043048.6+345853	Auriga	474.221574674	N	192.171779355	U	433	5.13	I
206	J043049.2+345610	Auriga	910.123223692	N	141.385302478	N	373	0.9	I
207	J043053.5+345627	Auriga	951.840041617	N	222.475362319	D	30	0.4	0
208	J043055.9+345647	Auriga	902.558868924	N	130.020289855	D	141	0.43	I
209	J043056.6+353004	Auriga	785.856944444	D	170.584057971	D	72	1.25	I
210	J205706.7+773656	Cepheus L1228	256.386111111	D	68.4048240144	U	2349	0.6	NP
211	J205707.9+773659	Cepheus L1228	246.213650133	N	119.685507246	D	170	0.35	I
212	J205713.0+773543	Cepheus L1228	9621.87638889	D	2333.4070557	D	536	2.42	I
213	J222933.3+751316	Cepheus L1251	255.686480135	N	65.9801568898	U	256	0.09	I
214	J222959.4+751403	Cepheus L1251	260.874721736	N	89.7768115942	D	339	0.37	I
215	J223031.8+751409	Cepheus L1251	1073.15199838	U	1022.85035167	D	36	0.42	0
216	J223105.6+751337	Cepheus L1251	2468.425	D	1175.34393201	D	31	0.3	0
217	J223440.5+751744	Cepheus L1251	361.347000462	N	37.5971014493	D	1412	0.43	NP
218	J223500.8+751536	Cepheus L1251	422.684933961	N	32.0474202447	N	886	0.25	NP
219	J223514.1+751502	Cepheus L1251	458.623993276	N	33.2646374288	N	220	0.08	I
220	J223523.4+751707	Cepheus L1251	13921.4916667	D	2510.9422957	D	282	9.69	I
221	J223526.6+751636	Cepheus L1251	483.502355501	N	144.707965514	U	563	0.31	I
222	J223605.6+751832	Cepheus L1251	539.934800508	N	34.3320138726	N	3227	2.72	NP
223	J223842.8+751136	Cepheus L1251	1061.33628821	U	352.190305838	U	81	1.78	I

Source index	ID	Cloud	S_{450} (mJy)	Flag_{450}	S_{850} (mJy)	Flag_{850}	T_{bol} (K)	L_{bol} ($L_\odot$)	Class
224	J223846.9+751133	Cepheus L1251	3008.21495262	U	755.659117762	U	124	6.36	I
225	J223853.0+751123	Cepheus L1251	858.172735863	U	322.335897808	U	153	1.5	I
226	J223913.3+751215	Cepheus L1251	545.154701399	N	91.9581308443	U	451	0.61	I
227	J203546.3+675302	Cepheus South	891.105555556	D	669.567022117	D	55	1.21	0
228	J203619.8+675631	Cepheus South	644.447344022	N	56.6260869565	D	2481	4.47	NP
229	J203906.2+680215	Cepheus South	12555.1319444	D	2844.8883957	D	36	3.66	0
230	J204553.9+675738	Cepheus South	5364.02083333	D	1541.02394345	D	454	57.75	I
231	J210020.7+681316	Cepheus South	3108.99861111	D	932.045373753	D	98	1.13	I
232	J210022.1+681258	Cepheus South	622.726890995	U	201.415694466	U	102	1.0	I
233	J210132.8+681120	Cepheus South	4115.33888889	D	294.025764527	U	26	3.49	0
234	J210143.9+681403	Cepheus South	290.560080111	N	42.4482201203	N	3322	0.78	NP
235	J210202.5+681158	Cepheus South	306.196444545	N	44.2225678467	N	3365	0.38	NP
236	J210214.1+680730	Cepheus South	294.548775637	N	41.3363914649	N	682	0.2	NP
237	J210221.2+675420	Cepheus South	457.294444444	D	280.488518403	D	216	0.49	I
238	J210227.3+675418	Cepheus South	500.606819057	N	328.426148877	D	49	0.36	0
239	J210259.5+680632	Cepheus South	299.329689516	N	40.388594969	N	5836	2.48	NP
240	J185943.9-370400	Corona Australis	4146.91627424	N	188.436287924	N	55	0.14	0
241	J190015.5-365757	Corona Australis	759.446074787	N	41.2612346915	N	152	0.03	I
242	J190108.6-365720	Corona Australis	2194.5875	D	982.916856367	D	1494	7.16	NP
243	J190141.5-365831	Corona Australis	9820.07083333	D	2564.72410662	D	697	4.79	NP
244	J190148.0-365722	Corona Australis	2341.77230037	U	3620.57317741	C	457	1.28	I
245	J190148.4-365714	Corona Australis	13697.9430556	D	3620.57317741	C	101	0.61	I
246	J190150.6-365809	Corona Australis	5224.63055556	D	2160.75890191	D	493	9.14	I
247	J190153.7-370033	Corona Australis	617.111327003	N	396.476763121	D	1087	0.02	NP
248	J190155.3-365721	Corona Australis	46982.3007178	D	7235.62501724	D	42	4.93	0
249	J190155.6-365651	Corona Australis	2386.33245196	U	696.177394444	U	149	0.14	I
250	J190156.4-365728	Corona Australis	27976.2555556	D	5733.04880607	D	146	2.55	I
251	J190158.5-365708	Corona Australis	8541.42222222	D	3904.8722395	D	117	0.43	I

Source index	ID	Cloud	S_{450} (mJy)	Flag_{450}	S_{850} (mJy)	Flag_{850}	T_{bol} (K)	L_{bol} ($L_\odot$)	Class
252	J190256.8-370719	Corona Australis	654.337213763	N	99.7010626857	U	17	0.02	0
253	J190258.6-370735	Corona Australis	8716.225	D	2466.13852901	D	69	1.21	0
254	J190301.0-370753	Corona Australis	645.109382674	N	86.6824441647	U	266	0.03	I
255	J190306.8-371249	Corona Australis	4588.375	D	1706.22852534	D	618	13.05	I
256	J190355.2-370935	Corona Australis	734.860844572	N	40.2806648021	N	100	0.01	I
257	J214443.0+474643	IC 5146	1602.82222222	D	688.523792015	D	18	2.88	0
258	J214448.3+474459	IC 5146	425.29648279	N	87.4492753623	D	37	3.75	0
259	J214451.7+474044	IC 5146	479.101943587	U	149.863798151	U	455	1.24	I
260	J214452.0+474030	IC 5146	4505.87638889	D	1359.80898539	D	71	24.58	I
261	J214453.9+474543	IC 5146	413.82544473	N	32.1312481554	N	599	1.54	I
262	J214457.0+474152	IC 5146	420.815077362	N	42.2476153088	U	203	1.18	I
263	J214502.6+473307	IC 5146	431.283707499	N	249.772463768	D	95	4.13	I
264	J214508.3+473305	IC 5146	4018.83611111	D	837.802702496	D	150	15.72	I
265	J214527.8+474550	IC 5146	418.57693441	N	32.0354988396	N	501	0.84	I
266	J214531.2+473621	IC 5146	418.379981894	N	155.65942029	D	209	7.04	I
267	J214558.5+473601	IC 5146	271.263888889	D	409.303838132	D	192	6.9	I
268	J214703.0+473314	IC 5146	278.870139135	N	44.4136027452	U	308	1.53	I
269	J214706.0+473939	IC 5146	284.417487869	N	264.27880286	D	63	0.63	0
270	J214721.2+473226	IC 5146	868.945177583	U	312.664661135	U	95	1.91	I
271	J214722.6+473205	IC 5146	19364.4816234	C	4091.01336755	C	13	34.13	0
272	J214722.7+473214	IC 5146	19364.4816234	C	4091.01336755	C	72	47.16	I
273	J214728.7+473217	IC 5146	294.624590193	N	35.115942029	D	306	1.1	I
274	J214755.6+473711	IC 5146	307.216460043	N	47.7507246377	D	145	1.04	I
275	J214759.2+473626	IC 5146	4002.90138889	D	755.803811421	D	81	11.15	I
276	J215214.3+471454	IC 5146	451.747594489	N	36.5542800897	N	131	1.06	I
277	J215237.7+471438	IC 5146	990.85	D	415.868813681	D	110	15.49	I
278	J215246.5+471249	IC 5146	434.420131897	N	34.1134143391	N	3813	8.43	NP
279	J215306.9+471434	IC 5146	429.631244435	N	216.071545408	D	203	1.12	I

Source index	ID	Cloud	S_{450} (mJy)	Flag_{450}	S_{850} (mJy)	Flag_{850}	T_{bol} (K)	L_{bol} ($L_\odot$)	Class
280	J215325.0+471622	IC 5146	417.731475184	N	32.9373864604	N	705	1.34	NP
281	J215328.3+471543	IC 5146	416.196506448	N	32.6557023144	N	386	2.17	I
282	J215328.6+471551	IC 5146	415.561965268	N	32.6354332501	N	441	4.75	I
283	J215330.4+471310	IC 5146	418.216526406	N	33.0617477861	N	5334	14.38	NP
284	J215331.4+472217	IC 5146	418.809287782	N	97.8444512152	U	324	4.44	I
285	J215333.0+471439	IC 5146	416.965057967	N	32.615908595	N	772	1.92	NP
286	J215333.1+471418	IC 5146	2183.36388889	D	1063.05184181	D	140	11.08	I
287	J215333.9+471724	IC 5146	418.062843502	N	53.5216407961	U	197	1.43	I
288	J215334.7+472044	IC 5146	410.311262969	N	762.398769758	D	568	8.87	I
289	J215336.2+471027	IC 5146	417.663502854	N	33.0831380422	N	417	1.38	I
290	J215336.3+471903	IC 5146	732.70757471	U	740.069803098	D	78	2.19	I
291	J215337.0+471817	IC 5146	418.500449018	N	32.4333333333	D	247	1.59	I
292	J215338.3+471935	IC 5146	614.280689485	U	178.324931892	U	429	3.57	I
293	J215342.0+471426	IC 5146	408.550716659	N	31.9341530077	N	387	1.53	I
294	J215349.7+471351	IC 5146	409.685294221	N	749.912813473	D	222	1.34	I
295	J215355.7+472030	IC 5146	423.368684901	N	33.5226563051	N	3136	5.86	NP
296	J215358.1+471445	IC 5146	414.493724227	N	32.8931031466	N	85	0.99	I
297	J215418.7+471209	IC 5146	411.370543255	N	32.4070112712	N	6101	72.29	NP
298	J153848.3-344038	Lupus I	1577.78437365	N	42.7926886566	N	166	0.27	I
299	J153927.7-344617	Lupus I	1607.66490427	N	42.7761566242	N	3194	1.98	NP
300	J153928.2-344618	Lupus I	1581.7701619	N	41.8685321768	N	2085	0.6	NP
301	J154214.5-341025	Lupus I	521.513134361	N	35.9772809099	N	270	0.07	I
302	J154301.2-340915	Lupus I	962.603579296	U	367.20687449	U	112	0.07	I
303	J154506.3-341738	Lupus I	881.917474242	N	40.2997382566	N	535	0.07	I
304	J162332.2-242553	Ophiuchus	1396.9706567	N	127.319871903	N	134	0.06	I
305	J162527.5-243647	Ophiuchus	376.320072741	N	33.5489522045	N	1182	0.08	NP
306	J162538.1-242236	Ophiuchus	556.068055556	D	191.814492754	D	1608	0.48	NP
307	J162539.5-242634	Ophiuchus	348.710098824	N	31.6578297884	N	1159	0.83	NP

Source index	ID	Cloud	S_{450} (mJy)	Flag_{450}	S_{850} (mJy)	Flag_{850}	T_{bol} (K)	L_{bol} ($L_\odot$)	Class
308	J162546.6-242336	Ophiuchus	354.598620634	N	34.9927536232	D	304	0.02	I
309	J162556.1-242048	Ophiuchus	346.444787194	N	149.276811594	D	1388	1.65	NP
310	J162610.3-242054	Ophiuchus	700.659722222	D	422.166666667	D	1678	4.2	NP
311	J162614.6-242507	Ophiuchus	344.505350847	N	544.786798072	D	17	0.01	0
312	J162617.2-242345	Ophiuchus	331.14212123	N	172.67826087	D	466	0.21	I
313	J162618.8-242819	Ophiuchus	318.42674578	N	244.072463768	D	1676	3.29	NP
314	J162618.9-242414	Ophiuchus	337.069465305	N	31.160087897	N	723	0.08	NP
315	J162621.3-242304	Ophiuchus	1728.82916667	D	2362.72393006	D	256	13.07	I
316	J162622.2-242407	Ophiuchus	336.397928441	N	31.2702511615	N	511	0.02	I
317	J162623.5-242439	Ophiuchus	339.111792063	N	249.623188406	D	748	0.57	NP
318	J162623.6-244314	Ophiuchus	1190.03333333	D	617.398550725	D	1704	0.9	NP
319	J162624.0-241613	Ophiuchus	2277.95	D	1059.97899381	D	1535	7.09	NP
320	J162625.4-242301	Ophiuchus	1691.74482116	U	510.848587706	U	211	0.14	I
321	J162625.6-242428	Ophiuchus	3579.4974761	U	1066.26113953	U	35	0.15	0
322	J162625.9-242340	Ophiuchus	3387.55674354	U	819.486804315	U	54	0.13	0
323	J162636.8-241551	Ophiuchus	385.609915908	N	37.3056800236	N	1008	0.55	NP
324	J162640.4-242714	Ophiuchus	625.366666667	D	270.710144928	D	423	0.13	I
325	J162644.1-243448	Ophiuchus	924.375	D	404.947040223	D	387	1.65	I
326	J162645.0-242307	Ophiuchus	1681.94305556	D	779.510144928	D	1469	1.57	NP
327	J162648.4-242838	Ophiuchus	312.821117937	N	63.0260869565	D	573	0.21	I
328	J162651.9-243039	Ophiuchus	316.973630563	N	33.4676935612	N	520	0.04	I
329	J162653.4-243236	Ophiuchus	338.683656726	N	35.0272096601	N	507	0.04	I
330	J162654.2-242437	Ophiuchus	315.553429764	N	32.3017895137	N	512	0.03	I
331	J162656.4-243301	Ophiuchus	334.462903951	N	34.644271571	N	140	0.02	I
332	J162658.2-243740	Ophiuchus	338.262281894	N	59.9503643798	U	390	0.02	I
333	J162658.4-244531	Ophiuchus	344.694891595	N	615.610144928	D	1308	3.37	NP
334	J162659.1-243503	Ophiuchus	332.246119095	N	236.603832211	U	109	2.59	I
335	J162702.3-243727	Ophiuchus	335.476383896	N	35.0170207509	N	530	5.85	I

Source index	ID	Cloud	S_{450} (mJy)	Flag_{450}	S_{850} (mJy)	Flag_{850}	T_{bol} (K)	L_{bol} ($L_\odot$)	Class
336	J162702.9-242614	Ophiuchus	312.868353433	N	231.871628092	D	638	0.05	I
337	J162703.5-242005	Ophiuchus	390.351672946	N	36.8592421401	N	471	0.03	I
338	J162704.1-242829	Ophiuchus	290.883606628	N	31.2561141457	N	691	0.2	NP
339	J162705.2-243629	Ophiuchus	1931.63472222	D	812.736488827	D	122	0.21	I
340	J162706.7-243814	Ophiuchus	337.581553198	N	177.468115942	D	433	0.77	I
341	J162709.3-244022	Ophiuchus	326.047305626	N	31.8275362319	D	759	0.11	NP
342	J162709.4-243718	Ophiuchus	6057.29444444	D	1064.18118163	D	419	23.09	I
343	J162711.1-244046	Ophiuchus	328.002957207	N	92.3420289855	D	718	0.42	NP
344	J162713.8-244331	Ophiuchus	337.757705469	N	39.2782608696	D	1231	0.25	NP
345	J162714.4-242645	Ophiuchus	303.911766064	N	31.4734858733	N	642	0.08	I
346	J162715.5-243053	Ophiuchus	923.883677877	U	309.11795545	U	387	0.08	I
347	J162715.8-242513	Ophiuchus	315.075807314	N	32.4349252752	N	511	0.04	I
348	J162715.8-243843	Ophiuchus	349.990277778	D	179.727536232	D	903	1.39	NP
349	J162716.3-243114	Ophiuchus	282.625	D	468.048082498	D	492	0.06	I
350	J162717.5-242856	Ophiuchus	808.311111111	D	278.74057971	D	265	0.74	I
351	J162718.3-243914	Ophiuchus	333.994986623	N	59.752173913	D	578	0.11	I
352	J162719.2-242843	Ophiuchus	305.845146708	N	123.228985507	D	662	0.2	NP
353	J162721.4-244143	Ophiuchus	328.861642927	N	35.5383636037	N	723	2.26	NP
354	J162721.7-242953	Ophiuchus	303.813827773	N	32.6254978039	N	467	1.51	I
355	J162721.8-242727	Ophiuchus	295.074204806	N	175.333103388	U	340	0.02	I
356	J162724.5-244103	Ophiuchus	1766.86666667	D	2407.83035503	D	315	0.33	I
357	J162726.2-244246	Ophiuchus	329.511352642	N	35.96693355	N	532	0.06	I
358	J162726.9-244050	Ophiuchus	6258.37361111	D	1950.6075205	D	302	3.96	I
359	J162727.9-243933	Ophiuchus	2702.31527778	D	562.988349338	D	285	8.67	I
360	J162728.4-242721	Ophiuchus	1901.41829868	U	4559.88170136	D	454	0.77	I
361	J162730.1-242743	Ophiuchus	7336.58888889	D	1536.85542612	D	620	1.82	I
362	J162730.8-242455	Ophiuchus	332.373678297	N	33.9887561705	N	1422	0.26	NP
363	J162730.9-242733	Ophiuchus	309.978580204	N	317.016431027	U	399	0.09	I

Source index	ID	Cloud	S_{450} (mJy)	Flag_{450}	S_{850} (mJy)	Flag_{850}	T_{bol} (K)	L_{bol} ($L_\odot$)	Class
364	J162737.2-244237	Ophiuchus	539.093055556	D	97.2355265511	U	555	0.23	I
365	J162738.9-244020	Ophiuchus	330.540943278	N	56.431884058	D	427	0.12	I
366	J162739.8-244315	Ophiuchus	336.981871862	N	217.55942029	D	691	1.38	NP
367	J162741.6-244644	Ophiuchus	335.76075253	N	36.6123598107	N	429	0.04	I
368	J162741.7-244336	Ophiuchus	341.905714327	N	35.8121170789	N	644	0.07	I
369	J162745.7-244453	Ophiuchus	335.216092342	N	45.8465903174	U	527	0.11	I
370	J162748.2-244225	Ophiuchus	331.325952391	N	36.0055243542	N	237	0.03	I
371	J162751.7-243145	Ophiuchus	316.673587487	N	199.316008619	D	681	1.42	NP
372	J162821.6-243623	Ophiuchus	4234.62083333	D	1341.03149426	D	36	0.29	0
373	J162857.8-244054	Ophiuchus	432.726719601	N	38.8232278759	N	401	0.05	I
374	J163129.2-240431	Ophiuchus	547.165729973	N	35.401823714	N	724	0.08	NP
375	J163133.8-240446	Ophiuchus	538.715401822	N	34.6611277498	N	1251	0.31	NP
376	J163134.2-240325	Ophiuchus	538.853368357	N	84.3478607657	U	804	0.5	NP
377	J163135.6-240129	Ophiuchus	3734.18055556	D	1758.61053102	D	430	2.21	I
378	J163136.7-240419	Ophiuchus	543.316008376	N	32.3623188406	D	171	0.21	I
379	J163143.7-245524	Ophiuchus	799.538743571	N	35.3942028986	D	685	0.5	NP
380	J163145.8-243909	Ophiuchus	522.285658774	N	31.729843753	N	338	3.17	I
381	J163152.0-245726	Ophiuchus	769.031955445	N	37.9352586783	N	58	0.03	0
382	J163152.1-245615	Ophiuchus	797.067774266	N	732.965805253	D	981	2.68	NP
383	J163152.4-245536	Ophiuchus	762.050480492	N	162.425226399	U	324	0.18	I
384	J163200.9-245642	Ophiuchus	2777.69027778	D	685.315362591	D	187	3.38	I
385	J163222.6-242831	Ophiuchus	263568.660505	D	33692.6204923	D	42	11.52	0
386	J163355.6-244205	Ophiuchus	559.839961606	N	205.549275362	D	1770	0.37	NP
387	J163952.9-241931	Ophiuchus	528.868776068	N	36.1511146655	N	223	0.02	I
388	J032519.5+303424	Perseus West	188.273312097	N	27.4099320483	N	364	0.04	I
389	J032522.3+304513	Perseus West	20844.3015755	D	4095.19324917	D	52	2.16	0
390	J032536.2+304515	Perseus West	61962.5597222	C	10396.0774194	C	12	8.63	0
391	J032536.4+304522	Perseus West	61962.5597222	C	10396.0774194	C	68	5.35	0

Source index	ID	Cloud	S_{450} (mJy)	Flag_{450}	S_{850} (mJy)	Flag_{850}	T_{bol} (K)	L_{bol} ($L_{\odot}$)	Class
392	J032538.8+304406	Perseus West	30684.1263889	C	4536.10892152	C	48	7.16	0
393	J032539.1+304358	Perseus West	30684.1263889	C	4536.10892152	C	39	4.26	0
394	J032637.4+301528	Perseus West	3174.95972222	D	749.876214572	D	73	0.95	I
395	J032738.2+301358	Perseus West	3051.9375	D	685.457618644	D	359	0.9	I
396	J032738.8+301257	Perseus West	10868.2583333	C	1405.05994881	C	13	1.33	0
397	J032739.0+301303	Perseus West	10868.2583333	C	1405.05994881	C	65	3.64	0
398	J032743.2+301228	Perseus West	5320.5875	D	1462.43729029	D	58	1.7	0
399	J032747.6+301204	Perseus West	2317.98194444	D	183.50539134	U	960	3.65	NP
400	J032800.3+300801	Perseus West	261.429531982	N	229.485741196	D	279	0.29	I
401	J032832.5+311105	Perseus West	719.2375	D	424.739177448	D	92	0.22	I
402	J032834.4+310051	Perseus West	526.278455671	N	74.8826086957	D	298	1.26	I
403	J032834.5+310705	Perseus West	538.533333333	D	357.376811594	D	177	0.13	I
404	J032834.9+305454	Perseus West	532.408057738	N	35.2633344289	N	137	0.08	I
405	J032835.0+302009	Perseus West	247.705230174	N	28.7073713813	N	97	0.33	I
406	J032837.0+311330	Perseus West	12403.0680556	D	1717.79033945	D	110	10.16	I
407	J032838.7+311806	Perseus West	379.864729478	N	153.898705037	U	288	0.07	I
408	J032839.1+310601	Perseus West	382.080289879	N	467.749702312	D	30	0.22	0
409	J032839.7+311731	Perseus West	383.450034632	N	138.469048806	U	304	0.2	I
410	J032840.6+311756	Perseus West	2693.80277778	D	2157.24876493	D	12	0.61	0
411	J032843.2+311732	Perseus West	388.678854577	N	101.689936218	U	656	1.98	NP
412	J032845.3+310541	Perseus West	394.348570391	N	214.723442085	D	76	0.4	I
413	J032848.7+311608	Perseus West	378.190265762	N	270.397390062	D	166	0.06	I
414	J032850.6+304244	Perseus West	509.429202483	N	33.885231196	N	733	0.09	NP
415	J032851.2+311739	Perseus West	385.10391518	N	29.9377455187	U	256	0.07	I
416	J032855.5+311436	Perseus West	53921.9611111	D	6010.13177746	D	55	22.42	0
417	J032856.1+311908	Perseus West	1447.3625	D	1595.2015612	D	101	0.21	I
418	J032856.3+312227	Perseus West	377.123999507	N	81.7623188406	D	610	0.2	I
419	J032856.6+310737	Perseus West	337.768061783	N	23.3891653423	U	99	0.03	I

Source index	ID	Cloud	S_{450} (mJy)	Flag_{450}	S_{850} (mJy)	Flag_{850}	T_{bol} (K)	L_{bol} ($L_\odot$)	Class
420	J032856.9+311622	Perseus West	369.379258221	N	31.5792362525	N	1053	0.24	NP
421	J032857.3+311415	Perseus West	7270.86805556	D	1270.643206	D	111	5.7	I
422	J032858.4+312217	Perseus West	391.110032122	N	145.264169865	U	286	1.1	I
423	J032859.2+312032	Perseus West	1264.0792531	U	360.71170031	U	69	0.16	0
424	J032859.3+311548	Perseus West	384.671656114	N	117.926789123	U	134	3.5	I
425	J032900.5+311200	Perseus West	5074.28055556	D	879.436334218	D	30	0.69	0
426	J032901.5+312020	Perseus West	52633.8254658	D	8083.72672736	D	275	9.4	I
427	J032901.8+311653	Perseus West	391.089476832	N	31.542787031	N	188	0.06	I
428	J032903.3+312314	Perseus West	379.198138113	N	33.0035133564	N	284	0.14	I
429	J032903.7+311603	Perseus West	38568.6027778	D	11393.2667675	D	220	37.62	I
430	J032903.8+305629	Perseus West	529.66613241	N	34.3195359074	N	282	0.08	I
431	J032904.0+311446	Perseus West	4951.04722222	D	2399.99939722	D	18	0.69	0
432	J032904.6+311659	Perseus West	394.046675862	N	32.1497040186	N	596	0.1	I
433	J032904.9+312038	Perseus West	383.703297049	N	190.933494025	U	439	0.13	I
434	J032905.1+312036	Perseus West	391.367376861	N	150.412359838	U	542	0.09	I
435	J032906.0+303039	Perseus West	532.446201361	N	37.456177716	N	245	0.05	I
436	J032907.7+312157	Perseus West	9957.39861111	D	1447.68984606	D	260	20.64	I
437	J032908.9+312256	Perseus West	389.214408282	N	32.3190450895	N	669	0.23	NP
438	J032909.1+312128	Perseus West	5261.9875	D	318.281428611	U	183	0.97	I
439	J032909.1+312305	Perseus West	383.077189939	N	32.3609281459	N	628	0.23	I
440	J032909.3+312104	Perseus West	1578.15555556	D	200.977213772	U	170	0.23	I
441	J032909.4+311413	Perseus West	941.671362771	U	338.509782749	U	50	0.12	0
442	J032910.4+311331	Perseus West	87916.7555556	C	16747.7662254	C	31	8.26	0
443	J032910.6+311340	Perseus West	87916.7555556	C	16747.7662254	C	8	10.5	0
444	J032910.6+311820	Perseus West	12257.8111111	C	724.115196251	U	61	3.09	0
445	J032910.8+311642	Perseus West	388.702330692	N	106.731753219	U	537	0.09	I
446	J032910.9+311826	Perseus West	12257.8111111	C	5968.95986382	C	11	1.49	0
447	J032911.2+311831	Perseus West	24785.3055556	D	5968.95986382	C	31	1.37	0

Source index	ID	Cloud	S_{450} (mJy)	Flag_{450}	S_{850} (mJy)	Flag_{850}	T_{bol} (K)	L_{bol} ($L_{\odot}$)	Class
448	J032911.8+312127	Perseus West	779.815980562	U	185.019040583	U	362	0.18	I
449	J032912.0+311301	Perseus West	54942.1166667	C	9056.57301056	C	10	6.57	0
450	J032912.0+311305	Perseus West	54942.1166667	C	9056.57301056	C	25	4.26	0
451	J032912.9+311814	Perseus West	858.210383612	U	309.047126573	U	274	1.13	I
452	J032913.5+311358	Perseus West	7885.92777778	D	1954.25268248	D	37	0.82	0
453	J032916.8+312325	Perseus West	385.851185077	N	33.2429115875	N	463	0.07	I
454	J032917.1+312746	Perseus West	5465.61527778	C	1224.34572625	C	36	0.61	0
455	J032917.5+312748	Perseus West	5465.61527778	C	1224.34572625	C	9	0.66	0
456	J032918.2+312319	Perseus West	537.548870969	U	1229.72076432	C	94	0.1	I
457	J032918.6+312017	Perseus West	389.425480246	N	32.8292945552	N	178	0.06	I
458	J032918.7+312325	Perseus West	812.836945327	U	1229.72076432	C	424	2.16	I
459	J032920.0+312407	Perseus West	916.265743185	U	229.027803883	U	103	1.57	I
460	J032920.4+311834	Perseus West	378.875216148	N	31.9587624094	N	825	0.57	NP
461	J032923.4+313329	Perseus West	744.25	D	157.87476238	U	65	0.37	0
462	J032924.0+311957	Perseus West	384.096498041	N	32.4109157077	N	407	0.09	I
463	J032946.0+310439	Perseus West	538.246533882	N	39.5487870917	N	331	0.08	I
464	J032951.8+313906	Perseus West	3925.30277778	D	1129.48314576	D	39	0.51	0
465	J033015.1+302349	Perseus West	538.894158418	N	326.804879066	D	105	1.5	I
466	J033022.4+313240	Perseus West	694.388043325	N	60.1134752774	N	146	0.1	I
467	J033027.1+302829	Perseus West	483.748500248	N	36.1348389063	N	419	0.33	I
468	J033032.6+302626	Perseus West	526.06232781	N	744.45255832	D	36	0.15	0
469	J033035.4+311558	Perseus West	740.417535371	N	73.5926695713	N	551	0.06	I
470	J033038.2+303211	Perseus West	360.953838975	N	30.8088797217	N	386	0.07	I
471	J033114.7+304955	Perseus West	317.327203964	N	33.9940974665	N	840	0.31	NP
472	J033120.9+304530	Perseus West	7576.2875	D	2104.42701868	D	33	1.18	0
473	J033217.9+304947	Perseus West	15016.6805556	D	4019.60402224	D	26	1.26	0
474	J033229.1+310240	Perseus West	750.1375	D	255.231884058	D	169	0.55	I
475	J033241.6+311044	Perseus West	191.768479834	N	29.6202642069	N	271	0.05	I

Source index	ID	Cloud	S_{450} (mJy)	Flag_{450}	S_{850} (mJy)	Flag_{850}	T_{bol} (K)	L_{bol} ($L_\odot$)	Class
476	J033257.8+310608	Perseus West	196.250846305	N	31.2111475017	N	103	0.02	I
477	J033306.4+310804	Perseus West	195.637841871	N	30.5560294447	N	598	0.08	I
478	J033309.5+310531	Perseus West	192.673446013	N	180.286391253	D	318	0.05	I
479	J033312.8+312124	Perseus West	135.425	D	51.1710144928	D	618	3.84	I
480	J033313.8+312005	Perseus West	1889.35555556	D	1077.19570478	D	70	0.11	0
481	J033314.3+310710	Perseus West	6003.07916667	D	2517.07630982	D	35	0.66	0
482	J033316.4+310652	Perseus West	8203.85694444	D	2021.87150291	D	29	0.88	0
483	J033316.6+310755	Perseus West	1901.90833333	D	980.271879789	D	144	1.39	I
484	J033317.8+310931	Perseus West	33408.6666308	D	6290.46094425	D	44	3.53	0
485	J033320.3+310721	Perseus West	1187.06173966	U	547.544741528	U	58	0.58	0
486	J033327.2+310710	Perseus West	821.238888889	D	457.163859426	D	67	1.37	0
487	J034141.0+314804	Perseus IC 348	410.68842059	N	34.0775747099	N	213	0.07	I
488	J034153.2+315019	Perseus IC 348	426.651530821	N	35.6096985274	N	270	0.07	I
489	J034155.7+314811	Perseus IC 348	422.406705338	N	35.0421157118	N	532	0.16	I
490	J034158.6+314821	Perseus IC 348	419.065515508	N	34.5993297378	N	199	0.08	I
491	J034202.1+314802	Perseus IC 348	421.731119398	N	35.1283486194	N	211	0.09	I
492	J034256.0+315644	Perseus IC 348	310.904219734	N	30.5090143667	N	243	0.06	I
493	J034329.4+315219	Perseus IC 348	249.303367606	N	29.3185282532	N	498	0.16	I
494	J034336.0+315009	Perseus IC 348	261.01223003	N	32.0878386513	N	455	0.06	I
495	J034344.4+314309	Perseus IC 348	486.542290294	N	61.7921625412	N	1074	0.97	NP
496	J034345.1+320358	Perseus IC 348	238.378116567	N	33.4043938614	N	653	0.94	NP
497	J034350.9+320324	Perseus IC 348	4702.56388889	D	2312.07226337	D	17	0.68	0
498	J034351.0+320308	Perseus IC 348	3532.64027778	D	316.980426999	U	57	0.41	0
499	J034356.5+320052	Perseus IC 348	29034.0765566	D	6382.05674169	C	23	1.64	0
500	J034356.8+320304	Perseus IC 348	14783.5875	D	3657.58097846	D	23	1.4	0
501	J034357.2+320047	Perseus IC 348	3461.8543117	U	6382.05674169	C	10	0.43	0
502	J034357.8+320312	Perseus IC 348	1925.35365614	U	706.439456462	U	9	0.23	0
503	J034359.4+320035	Perseus IC 348	230.925016572	N	75.7657157135	U	310	0.09	I

Source index	ID	Cloud	S_{450} (mJy)	Flag_{450}	S_{850} (mJy)	Flag_{850}	T_{bol} (K)	L_{bol} ($L_\odot$)	Class
504	J034359.6+320154	Perseus IC 348	233.212747176	N	33.9883934862	N	1338	6.68	NP
505	J034402.4+320204	Perseus IC 348	776.138965189	U	244.760320332	U	85	0.17	I
506	J034402.6+320159	Perseus IC 348	1738.55972222	D	261.315176204	U	37	0.24	0
507	J034409.2+320237	Perseus IC 348	240.855591074	N	34.4232978814	N	419	0.21	I
508	J034412.9+320135	Perseus IC 348	503.870833333	D	227.365217391	D	472	2.01	I
509	J034418.2+320732	Perseus IC 348	238.258590245	N	34.774709105	N	78	0.03	I
510	J034419.2+320734	Perseus IC 348	234.204064912	N	34.1815058321	N	254	0.05	I
511	J034421.3+315932	Perseus IC 348	230.597702178	N	67.6612423379	U	432	0.31	I
512	J034424.8+321348	Perseus IC 348	249.824736309	N	35.2394316238	N	77	0.04	I
513	J034430.3+321135	Perseus IC 348	242.779276597	N	35.6452801266	N	337	0.05	I
514	J034431.1+320558	Perseus IC 348	241.550012176	N	34.3123412667	N	224	0.05	I
515	J034432.0+321143	Perseus IC 348	246.750203253	N	35.5078173723	N	1593	2.03	NP
516	J034434.0+320657	Perseus IC 348	229.638444451	N	34.0464569142	N	122	0.03	I
517	J034434.6+321600	Perseus IC 348	244.913504094	N	35.8365189453	N	682	0.15	NP
518	J034435.9+320924	Perseus IC 348	241.729163694	N	35.1696038899	N	548	0.21	I
519	J034442.1+320902	Perseus IC 348	244.548108712	N	34.4185878561	N	328	0.1	I
520	J034443.3+320131	Perseus IC 348	678.906398992	U	1359.37246229	C	488	1.54	I
521	J034443.9+320136	Perseus IC 348	9693.99444444	D	1359.37246229	C	42	3.1	0
522	J034513.8+321210	Perseus IC 348	252.809247824	N	36.8159629528	N	312	0.09	I
523	J034705.4+324308	Perseus IC 348	370.948882412	N	184.623396356	D	399	0.58	I
524	J034741.5+325144	Perseus IC 348	3321.75	D	1154.76142964	D	338	5.09	I
525	J182844.0+005337	Serpens	31533.8425654	N	703.635259522	N	38	12.06	0
526	J182844.7+005125	Serpens	1265.67043178	N	888.26399504	D	37	0.52	0
527	J182844.9+005203	Serpens	1842.20972222	D	611.049275362	D	62	4.23	0
528	J182851.2+001927	Serpens	222.310592068	N	30.4017073088	N	381	0.19	I
529	J182852.7+002846	Serpens	224.274446243	N	105.796226823	U	308	0.13	I
530	J182854.0+002930	Serpens	11490.4361111	D	1847.72278942	D	68	9.22	0
531	J182854.8+002952	Serpens	7344.67361111	D	1046.2455733	D	51	6.84	0

Source index	ID	Cloud	S_{450} (mJy)	Flag_{450}	S_{850} (mJy)	Flag_{850}	T_{bol} (K)	L_{bol} ($L_{\odot}$)	Class
532	J182854.9+001832	Serpens	226.162635338	N	239.15956135	D	146	0.15	I
533	J182855.7+002944	Serpens	5662.99861111	D	1185.97622287	D	26	1.64	0
534	J182856.6+003008	Serpens	222.778835165	N	183.184810392	U	40	0.1	0
535	J182902.1+003120	Serpens	222.974306854	N	29.5242437538	N	97	0.17	I
536	J182902.8+003009	Serpens	231.05367281	N	29.641451682	N	808	0.74	NP
537	J182904.3+003324	Serpens	230.674028137	N	30.5618956521	N	625	3.06	I
538	J182906.2+003043	Serpens	30948.8023223	D	7515.10840574	C	68	10.47	0
539	J182906.7+003034	Serpens	22010.7291667	D	7515.10840574	C	60	8.01	0
540	J182909.0+003128	Serpens	15311.4652778	C	2583.39685305	C	11	5.59	0
541	J182909.0+003132	Serpens	15311.4652778	C	2583.39685305	C	35	4.48	0
542	J182916.1+001822	Serpens	1103.63333333	D	217.150724638	D	631	6.92	I
543	J182927.3+003849	Serpens	229.346111342	N	30.2680201901	N	383	0.14	I
544	J182931.9+011842	Serpens	1453.42916667	D	1622.22342466	D	737	21.76	NP
545	J182940.2+001513	Serpens	263.368328106	N	34.9560269203	N	657	0.31	NP
546	J182947.0+011626	Serpens	1202.16725713	U	425.150360961	U	262	0.66	I
547	J182947.6+010422	Serpens	298.842713024	N	39.9782433245	N	143	0.18	I
548	J182948.1+011644	Serpens	35028.8180556	D	10326.160669	D	31	14.47	0
549	J182949.1+011619	Serpens	5397.33194444	D	681.176160223	U	143	13.63	I
550	J182949.2+011631	Serpens	1989.57182958	U	774.993417056	U	220	2.34	I
551	J182949.5+011706	Serpens	6171.01527778	D	780.972527691	U	214	3.79	I
552	J182949.6+011456	Serpens	2032.53544352	U	586.436801625	U	176	1.19	I
553	J182949.6+011521	Serpens	102745.755067	D	14448.0032489	D	13	69.68	0
554	J182951.1+011640	Serpens	17761.3875	D	3495.75094574	D	161	5.86	I
555	J182952.0+003643	Serpens	222.12832837	N	30.1238703498	N	430	0.16	I
556	J182952.2+011547	Serpens	7913.67916667	D	2216.54675138	C	70	8.31	0
557	J182952.2+011559	Serpens	1571.6172983	U	2216.54675138	C	45	0.71	0
558	J182952.5+003611	Serpens	396.135265146	U	122.252173913	C	72	1.86	I
559	J182952.8+011456	Serpens	1040.14305556	D	268.890689185	U	139	3.57	I

Source index	ID	Cloud	S_{450} (mJy)	Flag_{450}	S_{850} (mJy)	Flag_{850}	T_{bol} (K)	L_{bol} ($L_\odot$)	Class
560	J182953.0+003606	Serpens	432.582520061	U	122.252173913	C	628	0.91	I
561	J182954.3+003601	Serpens	2980.11666667	D	705.142135884	D	61	1.71	0
562	J182955.6+011431	Serpens	296.014431496	N	165.114219456	U	953	1.65	NP
563	J182956.6+011239	Serpens	292.066176554	N	295.44635912	U	533	0.4	I
564	J182956.8+011446	Serpens	295.082069992	N	39.1980235515	N	519	22.02	I
565	J182957.5+011300	Serpens	2613.73399335	U	965.309394048	U	62	29.36	0
566	J182957.6+011304	Serpens	2919.25913388	U	1121.5050212	U	302	1.89	I
567	J182957.7+011405	Serpens	11832.1666667	D	2174.09530819	D	709	67.86	NP
568	J182957.8+011251	Serpens	1643.89192844	U	566.407388024	U	409	6.73	I
569	J182958.7+011426	Serpens	1840.16084891	U	548.463285812	U	425	2.41	I
570	J182959.0+011225	Serpens	983.867315809	U	401.285236047	U	58	0.42	0
571	J182959.2+011401	Serpens	33922.3945618	D	4707.44905724	C	44	7.48	0
572	J182959.3+011041	Serpens	1456.74166667	D	288.563391223	U	36	0.57	0
573	J182959.5+011159	Serpens	1295.32637872	U	472.76750767	U	123	15.01	I
574	J182959.9+011311	Serpens	1959.65459608	U	788.455195847	U	123	7.11	I
575	J183000.1+011403	Serpens	1284.03153316	U	4707.44905724	C	391	0.74	I
576	J183000.3+010944	Serpens	480.938888889	D	232.978463435	U	368	0.6	I
577	J183000.7+011301	Serpens	24011.0811383	D	6118.36956879	D	30	8.18	0
578	J183001.1+011324	Serpens	294.139882324	N	273.646983728	U	522	0.33	I
579	J183002.0+011359	Serpens	290.510210464	N	90.5855072464	D	513	0.58	I
580	J183002.7+011228	Serpens	1046.20138889	D	754.219103616	D	553	7.96	I
581	J183005.2+004104	Serpens	361.367701591	N	46.0666399559	N	97	0.24	I
582	J183005.7+003931	Serpens	321.467421209	N	67.2449275362	D	1578	1.34	NP
583	J183018.1+011416	Serpens	305.540191117	N	40.8412037067	N	1451	1.17	NP
584	J183747.8+002415	Serpens North	396.005296069	N	52.1250070796	N	376	0.4	I
585	J183755.7+002331	Serpens North	299.714604644	N	38.162499854	N	515	13.16	I
586	J183858.8+003309	Serpens North	10728.7236111	D	1968.02270465	D	92	5.05	I
587	J183901.3+003015	Serpens North	473.255555556	D	294.219940724	D	96	0.28	I

Source index	ID	Cloud	S_{450} (mJy)	Flag_{450}	S_{850} (mJy)	Flag_{850}	T_{bol} (K)	L_{bol} ($L_{\odot}$)	Class
588	J183909.5+001354	Serpens North	2410.63888889	D	550.553586902	D	673	17.39	NP
589	J183909.7+003245	Serpens North	471.779166667	D	184.153475426	U	658	1.18	NP
590	J183929.8+003740	Serpens North	212.796336876	N	28.9159563288	N	226	0.3	I
591	J184012.0+002927	Serpens North	261.268117476	N	35.729683299	N	1028	7.72	NP
592	J184017.6+001613	Serpens North	578.670079846	N	92.7104015072	N	452	2.04	I

B.2 Full Table of Envelope Masses and Temperatures

Envelope masses and temperatures were calculated for 90 protostars with detections at 70, 450, and 850 μm in Section 6.2.3 of Chapter 6. The full table of masses and temperatures for all 90 sources is provided as Table B.2 below. The running protostellar candidate index is provided for each protostar, along with their *Spitzer* ID, parent cloud, envelope temperature, and envelope mass. Refer to Section 6.2.3 for information on the calculation of these quantities.

Table B.2: Full table of envelope masses and temperatures for 90 protostars.

Source index	Cloud	ID	T (K)	M ($M_\odot$)
5	Aquila	J182754.7-034238	17.8391959799	1.54212959393
15	Aquila	J182858.3-013834	16.256281407	0.328683714322
17	Aquila	J182905.3-014156	20.3015075377	1.98765640439
24	Aquila	J182912.8-020350	25.2261306533	0.150001921865
25	Aquila	J182913.0-014617	18.5427135678	0.486540354772
29	Aquila	J182923.4-013855	20.1256281407	0.336355261958
40	Aquila	J182943.3-015651	19.4221105528	0.255010313542
41	Aquila	J182943.9-021255	19.4221105528	0.344205865144
43	Aquila	J182947.0-015548	22.4120603015	0.153502998551
51	Aquila	J182958.3-015740	13.6180904523	4.25600995393
60	Aquila	J183001.0-020608	21.1809045226	0.404537277
62	Aquila	J183001.2-020148	20.1256281407	0.464599552675
70	Aquila	J183003.0-013632	20.6532663317	0.222043213889
92	Aquila	J183015.6-020719	16.0804020101	1.1164526538
93	Aquila	J183016.2-015252	18.0150753769	0.267053224023
103	Aquila	J183025.8-021042	23.4673366834	0.612800721958
126	Aquila	J183048.7-015601	17.4874371859	0.641740352416
156	Aquila	J183213.1-015730	19.7738693467	0.306703029549
158	Aquila	J183215.9-023443	18.5427135678	1.16917734238
165	Auriga	J041008.4+400224	24.1708542714	0.44364818299
168	Auriga	J042140.8+373359	17.6633165829	0.486540354772
169	Auriga	J042538.4+370701	16.432160804	1.25296953264
186	Auriga	J043024.6+354520	26.8090452261	0.0384516037918
193	Auriga	J043030.5+355144	18.0150753769	0.260962308371
195	Auriga	J043036.8+355436	17.8391959799	1.19646618964
197	Auriga	J043038.2+354959	19.4221105528	0.344205865144
201	Auriga	J043041.1+352941	17.6633165829	0.949948431065
202	Auriga	J043044.2+355951	21.3567839196	0.172272939384
204	Auriga	J043048.5+353753	21.0050251256	0.255010313542
209	Auriga	J043056.6+353004	21.1809045226	0.0990230051006
212	Cepheus L1228	J205713.0+773543	18.8944723618	0.255010313542
216	Cepheus L1251	J223105.6+751337	16.432160804	0.352239703074
227	Cepheus South	J203546.3+675302	21.7085427136	0.0902933864707

Source index	Cloud	ID	T (K)	M ($M_\odot$)
229	Cepheus South	J203906.2+680215	19.2462311558	1.06610561375
231	Cepheus South	J210020.7+681316	19.4221105528	0.168343760297
237	Cepheus South	J210221.2+675420	18.7185929648	0.0624216580629
246	Corona Australis	J190150.6-365809	23.8190954774	0.0733627463555
253	Corona Australis	J190258.6-370735	22.5879396985	0.0638785928075
260	IC 5146	J214452.0+474030	20.6532663317	2.62169275153
264	IC 5146	J214508.3+473305	19.5979899497	2.13010706399
275	IC 5146	J214759.2+473626	19.0703517588	2.17982421485
315	Ophiuchus	J162621.3-242304	28.216080402	0.0484300435369
325	Ophiuchus	J162644.1-243448	24.6984924623	0.0142578071182
339	Ophiuchus	J162705.2-243629	19.7738693467	0.0484300435369
342	Ophiuchus	J162709.4-243718	29.2713567839	0.0253836304966
350	Ophiuchus	J162717.5-242856	25.5778894472	0.0152796306204
358	Ophiuchus	J162726.9-244050	22.7638190955	0.121875514661
361	Ophiuchus	J162730.1-242743	19.2462311558	0.13061004615
372	Ophiuchus	J162821.6-243623	16.959798995	0.121875514661
377	Ophiuchus	J163135.6-240129	20.8291457286	0.0842550268607
384	Ophiuchus	J163200.9-245642	30.8542713568	0.0226179654754
385	Ophiuchus	J163222.6-242831	21.0050251256	1.89802195705
500	PerseusIC348	J034356.8+320304	16.608040201	1.14251089564
508	PerseusIC348	J034412.9+320135	23.9949748744	0.0342621220851
524	PerseusIC348	J034741.5+325144	20.4773869347	0.255010313542
389	PerseusWest	J032522.3+304513	19.4221105528	0.703784193665
394	PerseusWest	J032637.4+301528	19.7738693467	0.14323750356
395	PerseusWest	J032738.2+301358	17.135678392	0.21697888077
398	PerseusWest	J032743.2+301228	19.9497487437	0.23795652879
401	PerseusWest	J032832.5+311105	15.5527638191	0.119095793568
403	PerseusWest	J032834.5+310705	15.9045226131	0.0882339865032
406	PerseusWest	J032837.0+311330	25.2261306533	0.279664863238
416	PerseusWest	J032855.5+311436	23.1155778894	1.47258642059
421	PerseusWest	J032857.3+311415	24.1708542714	0.202468443616
425	PerseusWest	J032900.5+311200	17.4874371859	0.212030054312
426	PerseusWest	J032901.5+312020	18.8944723618	1.77109196171
429	PerseusWest	J032903.7+311603	22.4120603015	1.77109196171
436	PerseusWest	J032907.7+312157	23.9949748744	0.352239703074
452	PerseusWest	J032913.5+311358	18.3668341709	0.386294448325
464	PerseusWest	J032951.8+313906	17.4874371859	0.222043213889
472	PerseusWest	J033120.9+304530	17.6633165829	0.464599552675
473	PerseusWest	J033217.9+304947	15.3768844221	1.16917734238
474	PerseusWest	J033229.1+310240	18.7185929648	0.082333349024
479	PerseusWest	J033312.8+312124	25.5778894472	0.0142578071182
480	PerseusWest	J033313.8+312005	13.6180904523	0.260962308371
481	PerseusWest	J033314.3+310710	15.5527638191	0.486540354772
482	PerseusWest	J033316.4+310652	16.0804020101	0.62710362084
483	PerseusWest	J033316.6+310755	20.3015075377	0.227225749617
484	PerseusWest	J033317.8+310931	17.6633165829	1.98765640439
486	PerseusWest	J033327.2+310710	21.7085427136	0.0862215570658
530	SerpensMain	J182854.0+002930	19.5979899497	1.3427669121

Source index	Cloud	ID	T (K)	M ($M_\odot$)
531	SerpensMain	J182854.8+002952	19.7738693467	0.886420741364
542	SerpensMain	J182916.1+001822	19.4221105528	0.273286302938
548	SerpensMain	J182948.1+011644	17.4874371859	7.93494127876
554	SerpensMain	J182951.1+011640	18.7185929648	1.94232219228
561	SerpensMain	J182954.3+003601	17.3115577889	0.656718708414
577	SerpensMain	J183000.7+011301	17.3115577889	5.11873864445
580	SerpensMain	J183002.7+011228	20.3015075377	0.521409557672
586	SerpensN	J183858.8+003309	18.8944723618	1.69122360578
587	SerpensN	J183901.3+003015	17.6633165829	0.153502998551

Bibliography

Adams, F. C., C. J. Lada, and F. H. Shu. 1987. 'Spectral evolution of young stellar objects.' ApJ 312 (January): 788–806.

Allison, R. J., S. P. Goodwin, R. J. Parker, R. de Grijs, S. F. Portegies Zwart, and M. B. N. Kouwenhoven. 2009. 'Dynamical Mass Segregation on a Very Short Timescale.' ApJL 700 (August): L99–L103.

Alves, J. F., C. J. Lada, and E. A. Lada. 2001. 'Internal structure of a cold dark molecular cloud inferred from the extinction of background starlight.' Nature 409 (January): 159–161.

Alves, J., M. Lombardi, and C. J. Lada. 2008. 'The Pipe Nebula: A Young Molecular Cloud Complex.' In *Handbook of Star Forming Regions, Volume II,* edited by B. Reipurth, 415. December.

André, P., A. Men'shchikov, S. Bontemps, et al. 2010. 'From filamentary clouds to prestellar cores to the stellar IMF: Initial highlights from the Herschel Gould Belt Survey.' A&A 518, L102 (July): L102.

André, P., and T. Montmerle. 1994. 'From T Tauri stars to protostars: Circumstellar material and young stellar objects in the rho Ophiuchi cloud.' ApJ 420 (January): 837–862.

André, P., D. Ward-Thompson, and M. Barsony. 1993. 'Submillimeter continuum observations of Rho Ophiuchi A - The candidate protostar VLA 1623 and prestellar clumps.' ApJ 406 (March): 122–141.

André, P., D. Ward-Thompson, and M. Barsony. 2000. 'From Prestellar Cores to Protostars: the Initial Conditions of Star Formation.' *Protostars and Planets IV* (May): 59.

Andrews, S. M., and J. P. Williams. 2005. 'Circumstellar Dust Disks in Taurus-Auriga: The Submillimeter Perspective.' ApJ 631 (October): 1134–1160.

———. 2007. 'High-Resolution Submillimeter Constraints on Circumstellar Disk Structure.' ApJ 659, no. 1 (April): 23.

Aniano, G., B. T. Draine, K. D. Gordon, and K. Sandstrom. 2011. 'Common-Resolution Convolution Kernels for Space- and Ground-Based Telescopes.' PASP 123 (October): 1218–1236.

Antoniucci, S., T. Giannini, G. Li Causi, and D. Lorenzetti. 2014. 'On the Mid-infrared Variability of Candidate Eruptive Variables (EXors): A Comparison between Spitzer and WISE Data.' ApJ 782, 51 (February): 51.

Azimlu, M., J. R. Martínez-Galarza, and A. A. Muench. 2015. 'A WISE Census of Young Stellar Objects in the Perseus OB2 Association.' AJ 150, 95 (September): 95.

Baade, D., K. Meisenheimer, O. Iwert, et al. 1999. 'The Wide Field Imager at the 2.2-m MPG/ESO telescope: first views with a 67-million-facette eye.' *The Messenger* 95 (March): 15–16.

Baldry, I. K., and K. Glazebrook. 2003. 'Constraints on a Universal Stellar Initial Mass Function from Ultraviolet to Near-Infrared Galaxy Luminosity Densities.' ApJ 593 (August): 258–271.

Ballesteros-Paredes, J. 2006. 'Six myths on the virial theorem for interstellar clouds.' MNRAS 372 (October): 443–449.

Bally, J. 2008. 'Overview of the Orion Complex.' In *Handbook of Star Forming Regions, Volume I*, edited by B. Reipurth, 459. Handbook of Star Forming Regions Vol I. Astronomical Society of the Pacific, December.

Bally, J., J. Walawender, D. Johnstone, H. Kirk, and A. Goodman. 2008. 'The Perseus Cloud.' In *Handbook of Star Forming Regions, Volume I*, edited by B. Reipurth, 308. Handbook of Star Forming Regions Vol I. Astronomical Society of the Pacific, December.

Balog, Zoltan, Thomas Müller, Markus Nielbock, et al. 2014. 'The Herschel-PACS photometer calibration.' *Experimental Astronomy* 37 (2): 129–160.

Barnard, E. E. 1919. 'On the dark markings of the sky, with a catalogue of 182 such objects.' ApJ 49 (January).

———. 1927. *Catalogue of 349 dark objects in the sky. University of Chicago Press.*

Bastien, P., E. Bissonnette, A. Simon, et al. 2011. 'POL-2: The SCUBA-2 Polarimeter.' In *Astronomical Polarimetry 2008: Science from Small to Large Telescopes,* edited by P. Bastien, N. Manset, D. P. Clemens, and N. St-Louis, 449:68. Astronomical Society of the Pacific Conference Series. November.

Basu, S. 1997. 'A Semianalytic Model for Supercritical Core Collapse: Self-Similar Evolution and the Approach to Protostar Formation.' ApJ 485 (August): 240–253.

Bate, M. R. 2009. 'The dependence of star formation on initial conditions and molecular cloud structure.' MNRAS 397 (July): 232–248.

———. 2012. 'Stellar, brown dwarf and multiple star properties from a radiation hydrodynamical simulation of star cluster formation.' MNRAS 419 (February): 3115–3146.

Bate, M. R., T. S. Tricco, and D. J. Price. 2014. 'Collapse of a molecular cloud core to stellar densities: stellar-core and outflow formation in radiation magnetohydrodynamic simulations.' MNRAS 437 (January): 77–95.

Beckwith, S. V. W., and A. I. Sargent. 1991. 'Particle emissivity in circumstellar disks.' ApJ 381 (November): 250–258.

Beckwith, S. V. W., A. I. Sargent, R. S. Chini, and R. Guesten. 1990. 'A survey for circumstellar disks around young stellar objects.' AJ 99 (March): 924–945.

Beichman, C. A., G. Neugebauer, H. J. Habing, P. E. Clegg, and T. Chester. 1988. 'Infrared astronomical satellite (IRAS) catalogs and atlases. Volume 1: Explanatory supplement.' *Infrared astronomical satellite (IRAS) catalogs and atlases. Volume 1: Explanatory supplement.*

Bell, C. P. M., T. Naylor, N. J. Mayne, R. D. Jeffries, and S. P. Littlefair. 2013. 'Pre-main-sequence isochrones – II. Revising star and planet formation time-scales.' MNRAS 434 (July): 806–831.

Benedettini, M., S. Pezzuto, M. G. Burton, S. Viti, S. Molinari, P. Caselli, and L. Testi. 2012. 'Multiline spectral imaging of dense cores in the Lupus molecular cloud.' MNRAS 419 (January): 238–250.

Berry, D. S. 2015. 'FellWalker-A clump identification algorithm.' *Astronomy and Computing* 10 (April): 22–31.

Berry, D. S., K. Reinhold, T. Jenness, and F. Economou. 2013. *CUPID: Clump Identification and Analysis Package.* Astrophysics Source Code Library, record ascl:1311.007, November.

Bertoldi, F., and C. F. McKee. 1992. 'Pressure-confined clumps in magnetized molecular clouds.' ApJ 395 (August): 140–157.

Bessell, M. S. 1979. 'UBVRI photometry. II - The Cousins VRI system, its temperature and absolute flux calibration, and relevance for two-dimensional photometry.' PASP 91 (October): 589–607.

Bok, B. J., and E. F. Reilly. 1947. 'Small Dark Nebulae.' ApJ 105 (March): 255.

Bonnell, I. A., M. R. Bate, C. J. Clarke, and J. E. Pringle. 1997. 'Accretion and the stellar mass spectrum in small clusters.' MNRAS 285 (February): 201–208.

Bonnell, I. A., C. J. Clarke, M. R. Bate, and J. E. Pringle. 2001. 'Accretion in stellar clusters and the initial mass function.' MNRAS 324 (June): 573–579.

Bonnell, I. A., and M. B. Davies. 1998. 'Mass segregation in young stellar clusters.' MNRAS 295 (April): 691.

Bonnor, W. B. 1956. 'Boyle's Law and gravitational instability.' MNRAS 116:351.

Bontemps, S., P. André, V. Könyves, et al. 2010a. 'The Herschel first look at protostars in the Aquila rift.' A&A 518, L85 (July): L85.

Bontemps, S., F. Motte, T. Csengeri, and N. Schneider. 2010b. 'Fragmentation and mass segregation in the massive dense cores of Cygnus X.' A&A 524, A18 (December): A18.

Booth, R. S., G. Delgado, M. Hagstrom, et al. 1989. 'The Swedish-ESO Submillimetre Telescope (SEST).' A&A 216 (June): 315–324.

Boss, A. P., and H. W. Yorke. 1995. 'Spectral energy of first protostellar cores: Detecting 'class -I' protostars with ISO and SIRTF.' ApJL 439 (February): L55–L58.

Broekhoven-Fiene, H., B. C. Matthews, P. M. Harvey, et al. 2014. 'The Spitzer Survey of Interstellar Clouds in the Gould Belt. VI. The Auriga-California Molecular Cloud Observed with IRAC and MIPS.' ApJ 786, 37 (May): 37.

Broekhoven-Fiene, H., B. C. Matthews, P. Harvey, et al. 2017. 'The JCMT Gould Belt Survey: A first look at the Auriga-California Molecular Cloud with SCUBA-2.' ApJ accepted.

Buckle, J. V., E. Drabek-Maunder, J. Greaves, et al. 2015. 'The JCMT Gould Belt Survey: SCUBA-2 observations of circumstellar discs in L 1495.' MNRAS 449 (May): 2472–2488.

Buckle, J. V., R. E. Hills, H. Smith, et al. 2009. 'HARP/ACSIS: a submillimetre spectral imaging system on the James Clerk Maxwell Telescope.' MNRAS 399 (October): 1026–1043.

Bustamante, I., B. Merín, Á. Ribas, H. Bouy, T. Prusti, G. L. Pilbratt, and P. André. 2015. 'Identification of new transitional disk candidates in Lupus with Herschel.' A&A 578, A23 (June): A23.

Cambrésy, L. 1999. 'Mapping of the extinction in giant molecular clouds using optical star counts.' A&A 345 (May): 965–976.

Carney, M. T., U. A. Yıldız, J. C. Mottram, E. F. van Dishoeck, J. Ramchandani, and J. K. Jørgensen. 2016. 'Classifying the embedded young stellar population in Perseus and Taurus and the LOMASS database.' A&A 586, A44 (February): A44.

Ceraski, W. 1906. 'Deux nouvelles variables.' *Astronomische Nachrichten* 170 (March): 339.

Ĉernis, K. 1990. 'Interstellar extinction in the vicinity of the reflection nebula NGC 1333 in Perseus.' Ap&SS 166 (April): 315–330.

———. 1993. 'Interstellar extinction in the direction of the open cluster IC 348 and the Per OB2 association.' *Baltic Astronomy* 2 (January): 214.

Chabrier, G. 2003. 'Galactic Stellar and Substellar Initial Mass Function.' PASP 115 (July): 763–795.

Chabrier, G. 2005. 'The Initial Mass Function: from Salpeter 1955 to 2005.' In *The Initial Mass Function 50 Years Later,* edited by E. Corbelli, F. Palla, and H. Zinnecker, 327:41. Astrophysics and Space Science Library. January.

Chabrier, G., and P. Hennebelle. 2011. 'Dimensional argument for the impact of turbulent support on the stellar initial mass function.' A&A 534, A106 (October): A106.

Chapin, E. L., D. S. Berry, A. G. Gibb, T. Jenness, D. Scott, R. P. J. Tilanus, F. Economou, and W. S. Holland. 2013. 'SCUBA-2: iterative map-making with the Sub-Millimetre User Reduction Facility.' MNRAS 430 (April): 2545–2573.

Chapman, N. L., S.-P. Lai, L. G. Mundy, et al. 2007. 'The Spitzer c2d Survey of Large, Nearby, Interstellar Clouds. IV. Lupus Observed with MIPS.' ApJ 667 (September): 288–302.

Chapman, N. L., L. G. Mundy, S.-P. Lai, and N. J. Evans II. 2009. 'The Mid-Infrared Extinction Law in the Ophiuchus, Perseus, and Serpens Molecular Clouds.' ApJ 690, 496-511 (January): 496–511.

Chen, H., P. C. Myers, E. F. Ladd, and D. O. S. Wood. 1995. 'Bolometric temperature and young stars in the Taurus and Ophiuchus complexes.' ApJ 445 (May): 377–392.

Chen, M., J. Di Francesco, D. Johnstone, et al. 2016. 'The JCMT Gould Belt Survey: Evidence for Dust Grain Evolution in Perseus Star-forming Clumps.' ApJ 826 (May): 95.

Clausius, R. 1870. 'Ueber einen auf die Wärme anwendbaren mechanischen Satz.' *Annalen der Physik* 217:124–130.

Clube, S. V. M. 1967. 'The kinematics of Gould's Belt.' MNRAS 137:189.

Cohen, M., W. A. Wheaton, and S. T. Megeath. 2003. 'Spectral Irradiance Calibration in the Infrared. XIV. The Absolute Calibration of 2MASS.' ApJ 126, no. 2 (August): 1090–1096.

Collins, G. W., II. 1978. *The Virial Theorem in Stellar Astrophysics. Tucson, Ariz., Pachart Publishing House (Astronomy and Astrophysics Series. Volume 7).*

Comerón, F., L. Spezzi, and B. López Martı. 2009. 'A new population of cool stars and brown dwarfs in the Lupus clouds.' A&A 500 (June): 1045–1063.

Comeron, F., and J. Torra. 1994. 'The origin of the Gould Belt by the impact of a high velocity cloud on the galactic disk.' A&A 281 (January): 35–45.

Comerón, F., and J. Torra. 1992. 'The oblique impact of a high velocity cloud on the galactic disk.' A&A 261 (July): 94–104.

Comeron, Fernando. 2008. 'The Lupus Clouds.' In *The Lupus Clouds,* edited by B. Reipurth, II:295. Handbook of Star Forming Regions. ASP.

Correia, S., H. Zinnecker, T. Ratzka, and M. F. Sterzik. 2006. 'A VLT/NACO survey for triple and quadruple systems among visual pre-main sequence binaries.' A&A 459 (December): 909–926.

Crapsi, A., E. F. van Dishoeck, M. R. Hogerheijde, K. M. Pontoppidan, and C. P. Dullemond. 2008. 'Characterizing the nature of embedded young stellar objects through silicate, ice and millimeter observations.' A&A 486 (July): 245–254.

Currie, M. J., D. S. Berry, T. Jenness, A. G. Gibb, G. S. Bell, and P. W. Draper. 2014. *Starlink Software in 2013.* Edited by N. Manset and P. Forshay. Astrophysics Source Code Library, record ascl:1110.012, May.

Curtis, E. I., J. S. Richer, and J. V. Buckle. 2010. 'A submillimetre survey of the kinematics of the Perseus molecular cloud - I. Data.' MNRAS 401 (January): 455–472.

Cutri, R. M., M. F. Skrutskie, S. van Dyk, et al. 2003. 'VizieR Online Data Catalog: 2MASS All-Sky Catalog of Point Sources (Cutri+ 2003).' *VizieR Online Data Catalog* 2246 (June).

———. 2012. 'VizieR Online Data Catalog: WISE All-Sky Data Release (Cutri+ 2012).' *VizieR Online Data Catalog* 2311 (March).

Dame, T. M., D. Hartmann, and P. Thaddeus. 2001. 'The Milky Way in Molecular Clouds: A New Complete CO Survey.' ApJ 547 (February): 792–813.

Dame, T. M., and P. Thaddeus. 1985. 'A wide-latitude CO survey of molecular clouds in the northern Milky Way.' ApJ 297 (October): 751–765.

de Geus, E. J. 1992. 'Interactions of stars and interstellar matter in Scorpio Centaurus.' A&A 262 (August): 258–270.

de Geus, E. J., P. T. de Zeeuw, and J. Lub. 1989. 'Physical parameters of stars in the Scorpio-Centaurus OB association.' A&A 216 (June): 44–61.

de Zeeuw, P. T., R. Hoogerwerf, J. H. J. de Bruijne, A. G. A. Brown, and A. Blaauw. 1999. 'A HIPPARCOS Census of the Nearby OB Associations.' AJ 117, no. 1 (January): 354.

Dempsey, J. T., P. Friberg, T. Jenness, et al. 2013. 'SCUBA-2: on-sky calibration using submillimetre standard sources.' MNRAS 430 (April): 2534–2544.

Dempsey, J. T., W. S. Holland, A. Chrysostomou, et al. 2012. 'A new era of wide-field submillimetre imaging: on-sky performance of SCUBA-2.' In *Millimeter, Submillimeter, and Far-Infrared Detectors and Instrumentation for Astronomy VI,* edited by W. S. Holland, 8452:2. Proc. SPIE. September.

Di Francesco, J., N. J. Evans II, P. Caselli, P. C. Myers, Y. Shirley, Y. Aikawa, and M. Tafalla. 2007. 'An Observational Perspective of Low-Mass Dense Cores I: Internal Physical and Chemical Properties.' *Protostars and Planets V:* 17–32.

Di Francesco, J., D. Johnstone, H. Kirk, T. MacKenzie, and E. Ledwosinska. 2008. 'The SCUBA Legacy Catalogues: Submillimeter-Continuum Objects Detected by SCUBA.' ApJS 175, 277-295 (March): 277–295.

Dobashi, K., H. Uehara, R. Kandori, T. Sakurai, M. Kaiden, T. Umemoto, and F. Sato. 2005. 'Atlas and Catalog of Dark Clouds Based on Digitized Sky Survey I.' PASJ 57 (February): 1.

Dodds, P., J. S. Greaves, A. Scholz, J. Hatchell, W. S. Holland, and JCMT Gould Belt Survey Team. 2015. 'The JCMT Gould Belt Survey: low-mass protoplanetary discs from a SCUBA-2 census of NGC 1333.' MNRAS 447 (February): 722–727.

Dowell, C. D., C. A. Allen, R. S. Babu, et al. 2003. 'SHARC II: a Caltech submillimeter observatory facility camera with 384 pixels.' In *Millimeter and Submillimeter Detectors for Astronomy,* edited by T. G. Phillips and J. Zmuidzinas, 4855:73–87. Proc. SPIE. February.

Drabek-Maunder, E., J. Hatchell, J. V. Buckle, J. Di Francesco, and J. Richer. 2016. 'The JCMT Gould Belt Survey: Understanding the influence of outflows on Gould Belt clouds.' MNRAS 457 (March): L84–L88.

Drabek, E., J. Hatchell, P. Friberg, J. Richer, S. Graves, J. V. Buckle, D. Nutter, D. Johnstone, and J. Di Francesco. 2012. 'Molecular line contamination in the SCUBA-2 450 and 850 μm continuum data.' MNRAS 426 (October): 23–39.

Draine, B. T. 2006. 'On the Submillimeter Opacity of Protoplanetary Disks.' ApJ 636 (January): 1114–1120.

Draper, P. W., D. S. Berry, T. Jenness, and F. Economou. 2009. 'GAIA – Version 4.' In *Astronomical Data Analysis Software and Systems XVIII*, edited by D. A. Bohlender, D. Durand, and P. Dowler, 411:575. ASP Conf. Ser. September.

Dreyer, J. L. E. 1895. 'Index Catalogue of Nebulæ found in the years 1888 to 1894, with Notes and Corrections to the New General Catalogue.' MmRAS 51:185.

Dunham, M. K., E. Rosolowsky, N. J. Evans II, et al. 2010a. 'The Bolocam Galactic Plane Survey. III. Characterizing Physical Properties of Massive Star-forming Regions in the Gemini OB1 Molecular Cloud.' ApJ 717, 1157 (July): 1157–1180.

Dunham, M. M., L. E. Allen, N. J. Evans II, et al. 2015. 'Young Stellar Objects in the Gould Belt.' ApJS 220, 11 (September): 11.

Dunham, M. M., H. G. Arce, L. E. Allen, et al. 2013. 'The Luminosities of Protostars in the Spitzer c2d and Gould Belt Legacy Clouds.' AJ 145, 94 (April): 94.

Dunham, M. M., A. Crapsi, N. J. Evans II, T. L. Bourke, T. L. Huard, P. C. Myers, and Jens Kauffmann. 2008. 'Identifying the Low-Luminosity Population of Embedded Protostars in the c2d Observations of Clouds and Cores.' ApJS 179, no. 1 (November): 249–282.

Dunham, M. M., N. J. Evans II, S. Terebey, C. P. Dullemond, and C. H. Young. 2010b. 'Evolutionary Signatures in the Formation of Low-Mass Protostars. II. Toward Reconciling Models and Observations.' ApJ 710, 470-502 (February): 470–502.

Dunham, M. M., and E. I. Vorobyov. 2012. 'Resolving the Luminosity Problem in Low-mass Star Formation.' ApJ 747, 52 (March): 52.

Dzib, S., L. Loinard, A. J. Mioduszewski, A. F. Boden, L. F. Rodrı guez, and R. M. Torres. 2010. 'VLBA Determination of the Distance to Nearby Star-forming Regions. IV. A Preliminary Distance to the Proto-Herbig AeBe Star EC 95 in the Serpens Core.' ApJ 718 (August): 610–619.

Ebert, R. 1955. 'Uber die Verdichtung von H I-Gebieten. Mit 5 Textabbildungen.' ZAp 37:217.

Economou, F., T. Jenness, M. J. Currie, and D. S. Berry. 2014. 'Advantages of Extensible Self-described Data Formats: Lessons Learned from NDF.' In *Astronomical Data Analysis Software and Systems XXIII,* edited by N. Manset and P. Forshay, 485:355. Astronomical Society of the Pacific Conference Series. May.

Eiroa, C., and M. M. Casali. 1992. 'Near-infrared images of the Serpens cloud core - The stellar cluster.' A&A 262 (September): 468–482.

Eiroa, C., A. A. Djupvik, and M. M. Casali. 2008. 'The Serpens Molecular Cloud.' In *Handbook of Star Forming Regions, Volume II,* edited by B. Reipurth, 693. Handbook of Star Forming Regions Vol II. Astronomical Society of the Pacific, December.

Engelbracht, C. W., M. Blaylock, K. Y. L. Su, et al. 2007. 'Absolute Calibration and Characterization of the Multiband Imaging Photometer for Spitzer. I. The Stellar Calibrator Sample and the 24 μm Calibration.' PASP 119 (September): 994–1018.

Enoch, M. L., N. J. Evans II, A. I. Sargent, and J. Glenn. 2009. 'Properties of the Youngest Protostars in Perseus, Serpens, and Ophiuchus.' ApJ 692, 973 (February): 973–997.

Enoch, M. L., J. Glenn, N. J. Evans II, A. I. Sargent, K. E. Young, and T. L. Huard. 2007. 'Comparing Star Formation on Large Scales in the c2d Legacy Clouds: Bolocam 1.1 mm Dust Continuum Surveys of Serpens, Perseus, and Ophiuchus.' ApJ 666 (September): 982–1001.

Enoch, M. L., K. E. Young, J. Glenn, et al. 2006. 'Bolocam Survey for 1.1 mm Dust Continuum Emission in the c2d Legacy Clouds. I. Perseus.' ApJ 638 (February): 293–313.

Evans, N. J., II, L. E. Allen, G. A. Blake, et al. 2003. 'From Molecular Cores to Planet-forming Disks: An SIRTF Legacy Program.' PASP 115 (August): 965–980.

Evans, N., Dunham M. M., J. K. Jørgensen, et al. 2009. 'The Spitzer c2d Legacy Results: Star-Formation Rates and Efficiencies; Evolution and Lifetimes.' ApJS 181, 321 (April): 321–350.

Faimali, A., M. A. Thompson, L. Hindson, et al. 2012. 'The G305 star-forming complex: embedded massive star formation discovered by Herschel Hi-GAL.' MNRAS 426 (October): 402–415.

Fazio, G. G., J. L. Hora, L. E. Allen, et al. 2004. 'The Infrared Array Camera (IRAC) for the Spitzer Space Telescope.' ApJS 154 (September): 10–17.

Fischer, W. J., S. T. Megeath, E. Furlan, et al. 2017. 'The Herschel Orion Protostar Survey: Luminosity and Envelope Evolution.' ApJ 840, 69 (May): 69.

Forbrich, J., A. Tappe, T. Robitaille, A. A. Muench, P. S. Teixeira, E. A. Lada, A. Stolte, and C. J. Lada. 2010. 'Disentangling Protostellar Evolutionary Stages in Clustered Environments Using Spitzer-IRS Spectra and Comprehensive Spectral Energy Distribution Modeling.' ApJ 716 (June): 1453–1477.

Furlan, E., W. J. Fischer, B. Ali, et al. 2016. 'The Herschel Orion Protostar Survey: Spectral Energy Distributions and Fits Using a Grid of Protostellar Models.' ApJS 224, 5 (May): 5.

Gaczkowski, B., T. Preibisch, T. Stanke, et al. 2015. 'Squeezed between shells? The origin of the Lupus I molecular cloud. APEX/LABOCA, Herschel, and Planck observations.' A&A 584, A36 (December): A36.

Galli, P. A. B., C. Bertout, R. Teixeira, and C. Ducourant. 2013. 'A kinematic study and membership analysis of the Lupus star-forming region.' A&A 558, A77 (October): A77.

———. 2015. 'Evolution of the T Tauri star population in the Lupus association.' A&A 580, A26 (August): A26.

Gardner, J. P., J. C. Mather, M. Clampin, et al. 2006. 'The James Webb Space Telescope.' Space Sci. Rev. 123 (April): 485–606.

Ghez, A. M., D. W. McCarthy, J. L. Patience, and T. L. Beck. 1997. 'The Multiplicity of Pre-Main-Sequence Stars in Southern Star Forming Regions.' ApJ 481, no. 1 (May): 378–385.

Gibb, A. G., T. Jenness, and F. Economou. 2013. 'PICARD - A PIpeline for Combining and Analyzing Reduced Data.' *Starlink User Note* 265 (March).

Glenn, J., P. A. R. Ade, M. Amarie, et al. 2003. 'Current status of Bolocam: a large-format millimeter-wave bolometer camera.' In *Millimeter and Submillimeter Detectors for Astronomy*, edited by T. G. Phillips and J. Zmuidzinas, 4855:30–40. Proc. SPIE. February.

Goodwin, S. P., D. Nutter, P. Kroupa, D. Ward-Thompson, and A. P. Whitworth. 2008. 'The relationship between the prestellar core mass function and the stellar initial mass function.' A&A 477 (January): 823–827.

Gould, B. A. 1874. 'On the Number and Distribution of the Bright Fixed Stars.' *American Journal of Science and Arts* 8 (November): 325–334.

Gould, R. J., and E. E. Salpeter. 1963. 'The Interstellar Abundance of the Hydrogen Molecule. I. Basic Processes.' ApJ 138 (August): 393.

Graves, S. F., J. S. Richer, J. V. Buckle, et al. 2010. 'The JCMT Legacy Survey of the Gould Belt: a first look at Serpens with HARP.' MNRAS 409 (December): 1412–1428.

Greene, T. P., B. A. Wilking, P. Andre, E. T. Young, and C. J. Lada. 1994. 'Further mid-infrared study of the rho Ophiuchi cloud young stellar population: Luminosities and masses of pre-main-sequence stars.' ApJ 434 (October): 614–626.

Griffin, M. J., A. Abergel, A. Abreu, et al. 2010. 'The Herschel-SPIRE instrument and its in-flight performance.' A&A 518, L3 (July): L3.

Gutermuth, R. A., T. L. Bourke, L. E. Allen, et al. 2008. 'The Spitzer Gould Belt Survey of Large Nearby Interstellar Clouds: Discovery of a Dense Embedded Cluster in the Serpens-Aquila Rift.' ApJL 673, L151 (February): L151.

Hara, A., K. Tachihara, A. Mizuno, T. Onishi, A. Kawamura, A. Obayashi, and Y. Fukui. 1999. 'A Study of Dense Cloud Cores and Star Formation in Lupus: $C^{18}O$ J = 1-0 Observations with NANTEN.' PASJ 51 (December): 895–910.

Harries, T. J. 2000. 'Synthetic line profiles of rotationally distorted hot-star winds.' MNRAS 315 (July): 722–734.

Harvey, P. M., C. Fallscheer, A. Ginsburg, et al. 2013. 'A First Look at the Auriga-California Giant Molecular Cloud with Herschel and the CSO: Census of the Young Stellar Objects and the Dense Gas.' ApJ 764, 133 (February): 133.

Harvey, P. M., T. L. Huard, J. K. Jørgensen, et al. 2008. 'The Spitzer Survey of Interstellar Clouds in the Gould Belt. I. IC 5146 Observed With IRAC and MIPS.' ApJ 680, 495-516 (June): 495–516.

Harvey, P. M., B. A. Wilking, and M. Joy. 1984. 'Infrared observations of dust cloud structure in young R associations - NGC 1333, S68, and NGC 7129.' ApJ 278 (March): 156–169.

Harvey, P., B. Merín, T. L. Huard, L. M. Rebull, N. Chapman, N. J. Evans II, and P. C. Myers. 2007. 'The Spitzer c2d Survey of Large, Nearby, Interstellar Clouds. IX. The Serpens YSO Population as Observed with IRAC and MIPS.' ApJ 663 (July): 1149–1173.

Hatchell, J., and G. A. Fuller. 2008. 'Star formation in Perseus. IV. Mass-dependent evolution of dense cores.' A&A 482 (May): 855–863.

Hatchell, J., G. A. Fuller, J. S. Richer, T. J. Harries, and E. F. Ladd. 2007. 'Star formation in Perseus. II. SEDs, classification, and lifetimes.' A&A 468 (June): 1009–1024.

Hatchell, J., J. S. Richer, G. A. Fuller, C. J. Qualtrough, E. F. Ladd, and C. J. Chandler. 2005. 'Star formation in Perseus. Clusters, filaments and the conditions for star formation.' A&A 440 (September): 151–161.

Hatchell, J., S. Terebey, T. Huard, et al. 2012. 'The Spitzer Survey of Interstellar Clouds in the Gould Belt. V. Ophiuchus North Observed with IRAC and MIPS.' ApJ 754, 104 (August): 104.

Hatchell, J., T. Wilson, E. Drabek, E. Curtis, J. Richer, D. Nutter, J. Di Francesco, D. Ward-Thompson, and JCMT GBS Consortium. 2013. 'The JCMT Gould Belt Survey: SCUBA-2 observations of radiative feedback in NGC 1333.' MNRAS 429 (February): L10–L14.

Heiderman, A., and N. J. Evans II. 2015. 'The Gould Belt 'MISFITS' Survey: The Real Solar Neighborhood Protostars.' ApJ 806, 231 (June): 231.

Heiderman, A., N. J. Evans II, L. E. Allen, T. Huard, and M. Heyer. 2010. 'The Star Formation Rate and Gas Surface Density Relation in the Milky Way: Implications for Extragalactic Studies.' ApJ 723, 1019 (November): 1019–1037.

Herbig, G. H. 1960. 'The Spectra of Be- and Ae-Type Stars Associated with Nebulosity.' ApJS 4 (March): 337.

Herbig, G. H., and B. Reipurth. 2008. 'Young Stars and Molecular Clouds in the IC 5146 Region.' In *Handbook of Star Forming Regions, Volume I,* edited by B. Reipurth, 108. December.

Herbst, W. 2008. 'Star Formation in IC 348.' In *Handbook of Star Forming Regions, Volume I,* edited by B. Reipurth, 372. December.

Herczeg, G. J., D. Johnstone, S. Mairs, et al. 2017. 'How Do Stars Gain Their Mass? A JCMT/SCUBA-2 Transient Survey of Protostars in Nearby Star-forming Regions.' ApJ 849, 43 (November): 43.

Herschel, J. F. W., Sir. 1847. *Results of astronomical observations made during the years 1834, 5, 6, 7, 8, at the Cape of Good Hope; being the completion of a telescopic survey of the whole surface of the visible heavens, commenced in 1825.*

Heyer, M. H., and J. A. Graham. 1989. 'Newborn stars and stellar winds in Barnard 228.' PASP 101 (September): 816–831.

Hildebrand, R. H. 1983. 'The Determination of Cloud Masses and Dust Characteristics from Submillimetre Thermal Emission.' QJRAS 24 (September): 267.

Hillenbrand, L. A., and L. W. Hartmann. 1998. 'A Preliminary Study of the Orion Nebula Cluster Structure and Dynamics.' ApJ 492 (January): 540–553.

Hillenbrand, L. A., S. E. Strom, F. J. Vrba, and J. Keene. 1992. 'Herbig Ae/Be stars - Intermediate-mass stars surrounded by massive circumstellar accretion disks.' ApJ 397 (October): 613–643.

Hirota, T., T. Bushimata, Y. K. Choi, et al. 2008. 'Astrometry of H_2O Masers in Nearby Star-Forming Regions with VERA. II. SVS13 in NGC1333.' PASJ 60 (February): 37–44.

Hirota, T., M. Honma, H. Imai, K. Sunada, Y. Ueno, H. Kobayashi, and N. Kawaguchi. 2011. 'Astrometry of H_2O Masers in Nearby Star-Forming Regions with VERA. IV. L 1448 C.' PASJ 63 (February): 1–8.

Hogerheijde, M. R., E. F. van Dishoeck, J. M. Salverda, and G. A. Blake. 1999. 'Envelope Structure of Deeply Embedded Young Stellar Objects in the Serpens Molecular Cloud.' ApJ 513 (March): 350–369.

Holland, W. S., D. Bintley, E. L. Chapin, et al. 2013. 'SCUBA-2: the 10 000 pixel bolometer camera on the James Clerk Maxwell Telescope.' MNRAS 430 (April): 2513–2533.

Holland, W. S., E. I. Robson, W. K. Gear, et al. 1999. 'SCUBA: a common-user submillimetre camera operating on the James Clerk Maxwell Telescope.' MNRAS 303 (March): 659–672.

Hubble, E. 1934. 'The Distribution of Extra-Galactic Nebulae.' ApJ 79 (January): 8.

Hubble, E. P. 1922a. 'A general study of diffuse galactic nebulae.' ApJ 56 (October).

———. 1922b. 'The source of luminosity in galactic nebulae.' ApJ 56 (December).

Hughes, J., P. Hartigan, J. Krautter, and J. Kelemen. 1994. 'The stellar population of the Lupus clouds.' AJ 108 (September): 1071–1090.

Isella, Andrea. 2006. 'Interferometric observations of pre-main sequence disks.' *PhD thesis, Univ. Milan.*

Ishihara, D., T. Onaka, H. Kataza, et al. 2010. 'The AKARI/IRC mid-infrared all-sky survey.' A&A 514, A1 (May): A1.

Jarrett, T. H., M. Cohen, F. Masci, et al. 2011. 'The Spitzer-WISE Survey of the Ecliptic Poles.' ApJ 735, 112 (July): 112.

Jeans, J. H. 1902. 'The Stability of a Spherical Nebula.' *Royal Society of London Philosophical Transactions Series A* 199:1–53.

Johnstone, D., S. Ciccone, H. Kirk, et al. 2017. 'The JCMT Gould Belt Survey: A First Look at IC 5146.' ApJ 836, 132 (February): 132.

Johnstone, D., M. Fich, G. F. Mitchell, and G. Moriarty-Schieven. 2001. 'Large Area Mapping at 850 Microns. III. Analysis of the Clump Distribution in the Orion B Molecular Cloud.' ApJ 559 (September): 307–317.

Johnstone, D., C. D. Wilson, G. Moriarty-Schieven, G. Joncas, G. Smith, E. Gregersen, and M. Fich. 2000. 'Large-Area Mapping at 850 Microns. II. Analysis of the Clump Distribution in the ρ Ophiuchi Molecular Cloud.' ApJ 545 (December): 327–339.

Jørgensen, J. K., P. M. Harvey, N. J. Evans II, et al. 2006. 'The Spitzer c2d Survey of Large, Nearby, Interstellar Clouds. III. Perseus Observed with IRAC.' ApJ 645 (July): 1246–1263.

Jørgensen, J., D. Johnstone, H. Kirk, and P. C. Myers. 2007. 'Current Star Formation in the Perseus Molecular Cloud: Constraints from Unbiased Submillimeter and Mid-Infrared Surveys.' ApJ 656, no. 1 (February): 293.

Juvela, M., K. Demyk, Y. Doi, et al. 2015. 'Galactic cold cores. VI. Dust opacity spectral index.' A&A 584, A94 (December): A94.

Kackley, R., D. Scott, E. Chapin, and P. Friberg. 2010. 'JCMT Telescope Control System upgrades for SCUBA-2.' In *Software and Cyberinfrastructure for Astronomy*, edited by N. Radziwill and A. Bridger, 7740:1. Proc. SPIE. July.

Kauffmann, J., F. Bertoldi, T. L. Bourke, N. J. Evans II, and C. W. Lee. 2008. 'MAMBO mapping of Spitzer c2d small clouds and cores.' A&A 487 (September): 993–1017.

Kauffmann, J., T. Pillai, and P. F. Goldsmith. 2013. 'Low Virial Parameters in Molecular Clouds: Implications for High-mass Star Formation and Magnetic Fields.' ApJ 779, 185 (December): 185.

Kawada, M., H. Baba, P. D. Barthel, et al. 2007. 'The Far-Infrared Surveyor (FIS) for AKARI.' PASJ 59 (October): 389.

Kelly, B. C., R. Shetty, A. M. Stutz, J. Kauffmann, A. A. Goodman, and R. Launhardt. 2012. 'Dust Spectral Energy Distributions in the Era of Herschel and Planck: A Hierarchical Bayesian-fitting Technique.' ApJ 752, 55 (June): 55.

Kennicutt, R. C., Jr. 1983. 'The rate of star formation in normal disk galaxies.' ApJ 272 (September): 54–67.

Kenyon, S. J., M. Gómez, and B. A. Whitney. 2008. 'Low Mass Star Formation in the Taurus-Auriga Clouds.' In *Handbook of Star Forming Regions, Volume I,* edited by B. Reipurth, 405. Handbook of Star Forming Regions Vol I. Astronomical Society of the Pacific, December.

Kenyon, S. J., L. W. Hartmann, K. M. Strom, and S. E. Strom. 1990. 'An IRAS survey of the Taurus-Auriga molecular cloud.' AJ 99 (March): 869–887.

Kim, S.-H., P. G. Martin, and P. D. Hendry. 1994. 'The size distribution of interstellar dust particles as determined from extinction.' ApJ 422 (February): 164–175.

Kirk, H., J. Di Francesco, D. Johnstone, et al. 2016. 'The JCMT Gould Belt Survey: A First Look at Dense Cores in Orion B.' ApJ 817, 167 (February): 167.

Kirk, H., D. Johnstone, and J. Di Francesco. 2006. 'The Large- and Small-Scale Structures of Dust in the Star-forming Perseus Molecular Cloud.' ApJ 646 (August): 1009–1023.

Kirk, H., and P. C. Myers. 2011. 'Young Stellar Groups and Their Most Massive Stars.' ApJ 727, 64 (February): 64.

Kirk, H., P. C. Myers, T. L. Bourke, R. A. Gutermuth, A. Hedden, and G. W. Wilson. 2013. 'Filamentary Accretion Flows in the Embedded Serpens South Protocluster.' ApJ 766, 115 (April): 115.

Kirk, J. M., D. Ward-Thompson, J. Di Francesco, et al. 2009. 'The Spitzer Survey of Interstellar Clouds in the Gould Belt. II. The Cepheus Flare Observed with IRAC and MIPS.' ApJS 185, 198-249 (November): 198–249.

Könyves, V., P. André, A. Men'shchikov, et al. 2015. 'A census of dense cores in the Aquila cloud complex: SPIRE/PACS observations from the Herschel Gould Belt survey.' A&A 584, A91 (December): A91.

Kramer, C., J. Stutzki, R. Rohrig, and U. Corneliussen. 1998. 'Clump mass spectra of molecular clouds.' A&A 329 (January): 249–264.

Krasnopolsky, R., and A. Königl. 2002. 'Self-similar Collapse of Rotating Magnetic Molecular Cloud Cores.' ApJ 580 (December): 987–1012.

Kristensen, L. E., E. F. van Dishoeck, E. A. Bergin, et al. 2012. 'Water in star-forming regions with Herschel (WISH). II. Evolution of 557 GHz 1_{10}-1_{01} emission in low-mass protostars.' A&A 542, A8 (June): A8.

Kritsuk, A. G., C. T. Lee, and M. L. Norman. 2013. 'A supersonic turbulence origin of Larson's laws.' MNRAS 436 (December): 3247–3261.

Kroupa, P. 2001. 'On the variation of the initial mass function.' MNRAS 322 (April): 231–246.

Kroupa, P., C. A. Tout, and G. Gilmore. 1993. 'The distribution of low-mass stars in the Galactic disc.' MNRAS 262 (June): 545–587.

Krumholz, M.R., M.R. Bate, H.G. Arce, J.E. Dale, R. Gutermuth, R.I. Klein, Z.Y. Li, F. Nakamura, and Q. Zhang. 2014. 'Star Cluster Formation and Feedback.' *Protostars and Planets VI* (January): 243–266.

Kryukova, E., S. T. Megeath, J. L. Hora, et al. 2014. 'The Dependence of Protostellar Luminosity on Environment in the Cygnus-X Star-Forming Complex.' AJ 148, no. 1 (April): 11.

Kuhn, M. A., K. V. Getman, E. D. Feigelson, B. Reipurth, S. A. Rodney, and G. P. Garmire. 2010. 'A Chandra Observation of the Obscured Star-forming Complex W40.' ApJ 725 (December): 2485–2506.

Kukarkin, B. V., P. N. Kholopov, Y. P. Pskovsky, Y. N. Efremov, N. P. Kukarkina, N. E. Kurochkin, and G. I. Medvedeva. 1971. 'The third edition containing information on 20437 variable stars discovered and designated till 1968.' In *General Catalogue of Variable Stars, 3rd ed. (1971).*

Kun, M., Z. T. Kiss, and Z. Balog. 2008. 'Star Forming Regions in Cepheus.' In *Handbook of Star Forming Regions, Volume I*, edited by B. Reipurth, 136. December.

Lada, C. J. 1987. 'Star formation - From OB associations to protostars.' In *Star Forming Regions*, edited by M. Peimbert and J. Jugaku, 115:1–17. IAU Symposium.

Lada, C. J., M. Lombardi, and J. F. Alves. 2009. 'The California Molecular Cloud.' ApJ 703 (September): 52–59.

Lada, C. J., and B. A. Wilking. 1984. 'The nature of the embedded population in the Rho Ophiuchi dark cloud - Mid-infrared observations.' ApJ 287 (December): 610–621.

Lane, J., H. Kirk, D. Johnstone, et al. 2016. 'The JCMT Gould Belt Survey: Dense Core Clusters in Orion A.' ApJ 833, 44 (December): 44.

Larson, R. B. 1969. 'Numerical calculations of the dynamics of collapsing proto-star.' MNRAS 145:271.

———. 1981. 'Turbulence and star formation in molecular clouds.' MNRAS 194 (March): 809–826.

———. 2003. 'The physics of star formation.' *Reports on Progress in Physics* 66 (October): 1651–1697.

Leavitt, H. S., and E. C. Pickering. 1907. '71 New Variable Stars in Harvard Maps Nos. 9, 12, 21, 48, and 51.' *Harvard College Observatory Circular* 130 (July): 1–4.

Lewis, B. T., and M. R. Bate. 2017. 'The dependence of protostar formation on the geometry and strength of the initial magnetic field.' MNRAS 467 (May): 3324–3337.

Lombardi, M., C. J. Lada, and J. Alves. 2008. 'Hipparcos distance estimates of the Ophiuchus and the Lupus cloud complexes.' A&A 480 (March): 785–792.

Luhman, K. L., G. H. Rieke, C. J. Lada, and E. A. Lada. 1998. 'Low-Mass Star Formation and the Initial Mass Function in IC 348.' ApJ 508 (November): 347–369.

Lynds, B. T. 1962. 'Catalogue of Dark Nebulae.' ApJS 7 (May): 1.

Mac Low, M.-M., and R. S. Klessen. 2004. 'Control of star formation by supersonic turbulence.' *Reviews of Modern Physics* 76 (January): 125–194.

Mairs, S., D. Johnstone, H. Kirk, et al. 2015. 'The JCMT Gould Belt Survey: a quantitative comparison between SCUBA-2 data reduction methods.' MNRAS 454 (December): 2557–2579.

Mairs, S., D. Johnstone, H. Kirk, et al. 2016. 'The JCMT Gould Belt Survey: a first look at Southern Orion A with SCUBA-2.' MNRAS 461 (October): 4022–4048.

Mairs, S., J. Lane, D. Johnstone, et al. 2017. 'The JCMT Transient Survey: Data Reduction and Calibration Methods.' ApJ 843, 55 (July): 55.

Mallick, K. K., M. S. N. Kumar, D. K. Ojha, R. Bachiller, M. R. Samal, and L. Pirogov. 2013. 'The W40 Region in the Gould Belt: An Embedded Cluster and H II Region at the Junction of Filaments.' ApJ 779, 113 (December): 113.

Matthews, H. E., and J. Leech. 2004. 'Overview of the JCMT.' (November). Accessed 2004.

Maury, A. J., P. André, A. Men'shchikov, V. Könyves, and S. Bontemps. 2011. 'The formation of active protoclusters in the Aquila rift: a millimeter continuum view.' A&A 535, A77 (November): A77.

McKee, C. F., and E. C. Ostriker. 2007. 'Theory of Star Formation.' ARA&A 45 (September): 565–687.

McKee, C. F., and J. C. Tan. 2003. 'The Formation of Massive Stars from Turbulent Cores.' ApJ 585 (March): 850–871.

McMullin, J. P., L. G. Mundy, G. A. Blake, B. A. Wilking, J. G. Mangum, and W. B. Latter. 2000. 'A Spectral Line Study of Serpens S68 FIRS1 Region.' ApJ 536 (June): 845–856.

Megeath, S. T., R. Gutermuth, J. Muzerolle, et al. 2016. 'The Spitzer Space Telescope Survey of the Orion A and B Molecular Clouds. II. The Spatial Distribution and Demographics of Dusty Young Stellar Objects.' AJ 151, no. 6, 5 (January): 5.

Megeath, S.T., R. Gutermuth, J. Muzerolle, et al. 2012. 'The Spitzer Space Telescope Survey of the Orion A and B Molecular Clouds. I. A Census of Dusty Young Stellar Objects and a Study of Their Mid-infrared Variability.' AJ 144, no. 6 (December): 27.

Men'shchikov, A., P. André, P. Didelon, F. Motte, M. Hennemann, and N. Schneider. 2012. 'A multi-scale, multi-wavelength source extraction method: getsources.' A&A 542, A81 (June): A81.

Mercimek, S., P. C. Myers, K. I. Lee, and S. I. Sadavoy. 2017. 'An Estimation of the Star Formation Rate in the Perseus Complex.' AJ 153, 214 (May): 214.

Merín, B., J. Jørgensen, L. Spezzi, et al. 2008. 'The Spitzer c2d Survey of Large, Nearby, Interstellar Clouds. XI. Lupus Observed with IRAC and MIPS.' ApJS 177 (August): 551–583.

Miller, G. E., and J. M. Scalo. 1979. 'The initial mass function and stellar birthrate in the solar neighborhood.' ApJS 41 (November): 513–547.

Motte, F., P. Andre, and R. Neri. 1998. 'The initial conditions of star formation in the rho Ophiuchi main cloud: wide-field millimeter continuum mapping.' A&A 336 (August): 150–172.

Mottram, J. C., M. G. Hoare, J. S. Urquhart, S. L. Lumsden, R. D. Oudmaijer, T. P. Robitaille, T. J. T. Moore, B. Davies, and J. Stead. 2011. 'The Red MSX Source survey: the bolometric fluxes and luminosity distributions of young massive stars.' A&A 525, A149 (January): A149.

Mottram, J. C., E. F. van Dishoeck, M. Schmalzl, L. E. Kristensen, R. Visser, M. R. Hogerheijde, and S. Bruderer. 2013. 'Waterfalls around protostars. Infall motions towards Class 0/I envelopes as probed by water.' A&A 558, A126 (October): A126.

Mowat, C., J. Hatchell, D. Rumble, et al. 2017. 'The JCMT Gould Belt Survey: A First Look at SCUBA-2 Observations of the Lupus I Molecular Cloud.' MNRAS 467 (May): 812–835.

Murakami, H., H. Baba, P. Barthel, et al. 2007. 'The Infrared Astronomical Mission AKARI.' PASJ 59 (October): 369.

Murphy, D. C., R. Cohen, and J. May. 1986. 'CO observations of dark clouds in Lupus.' A&A 167 (October): 234–238.

Myers, P. C. 2005. 'Centrally Condensed Collapse of Starless Cores.' ApJ 623 (April): 280–290.

———. 2011. 'Filamentary Condensations in a Young Cluster.' ApJ 735, 82 (July): 82.

Myers, P. C., T. M. Dame, P. Thaddeus, R. S. Cohen, R. F. Silverberg, E. Dwek, and M. G. Hauser. 1986. 'Molecular clouds and star formation in the inner galaxy - A comparison of CO, H II, and far-infrared surveys.' ApJ 301 (February): 398–422.

Myers, P. C., and G. A. Fuller. 1992. 'Density structure and star formation in dense cores with thermal and nonthermal motions.' ApJ 396 (September): 631–642.

Myers, P. C., and E. F. Ladd. 1993. 'Bolometric temperatures of young stellar objects.' ApJ 413 (August): L47–L50.

Nakamura, F., K. Sugitani, Y. Shimajiri, et al. 2011. 'Molecular Outflows from the Protocluster Serpens South.' ApJ 737, 56 (August): 56.

Neugebauer, G., H. J. Habing, R. van Duinen, et al. 1984. 'The Infrared Astronomical Satellite (IRAS) mission.' ApJL 278 (March): L1–L6.

Neuhäuser, R., and J. Forbrich. 2008. 'The Corona Australis Star Forming Region.' In *Handbook of Star Forming Regions, Volume II,* edited by B. Reipurth, 735. December.

Nuernberger, D., R. Chini, and H. Zinnecker. 1997. 'A 1.3mm dust continuum survey of Halpha selected T Tauri stars in Lupus.' A&A 324 (August): 1036–1045.

Olano, C. A. 1982. 'On a model of local gas related to Gould's belt.' A&A 112 (August): 195–208.

———. 2001. 'The Origin of the Local System of Gas and Stars.' AJ 121, no. 1 (January): 295.

Onaka, T., H. Matsuhara, T. Wada, et al. 2007. 'The Infrared Camera (IRC) for AKARI – Design and Imaging Performance.' PASJ 59 (October): 401.

Ortiz-León, G. N., S. A. Dzib, M. A. Kounkel, et al. 2017a. 'The Gould's Belt Distances Survey (GOBELINS). III. The Distance to the Serpens/Aquila Molecular Complex.' ApJ 834, 143 (January): 143.

Ortiz-León, G. N., L. Loinard, M. A. Kounkel, et al. 2017b. 'The Gould's Belt Distances Survey (GOBELINS). I. Trigonometric Parallax Distances and Depth of the Ophiuchus Complex.' ApJ 834, 141 (January): 141.

Ossenkopf, V., and T. Henning. 1994. 'Dust opacities for protostellar cores.' A&A 291 (November): 943–959.

Oya, Y., N. Sakai, T. Sakai, et al. 2014. 'A Substellar-mass Protostar and its Outflow of IRAS 15398-3359 Revealed by Subarcsecond-resolution Observations of H_2CO and CCH.' ApJ 795, 152 (November): 152.

Padgett, D. L., L. M. Rebull, K. R. Stapelfeldt, et al. 2008. 'The Spitzer c2d Survey of Large, Nearby, Interstellar Clouds. VII. Ophiuchus Observed with MIPS.' ApJ 672, 1013-1037 (January): 1013–1037.

Padgett, D., L. Cieza, K. R. Stapelfeldt, et al. 2006. 'The SPITZER c2d Survey of Weak-Line T Tauri Stars. I. Initial Results.' ApJ 645, no. 2 (July): 1283.

Padoan, P., C. Federrath, G. Chabrier, N. J. Evans II, D. Johnstone, J. K. Jørgensen, C. F. McKee, and Å. Nordlund. 2013. 'The Star Formation Rate of Molecular Clouds.' *ArXiv e-prints 1312.5365* (December).

Padoan, P., and Å. Nordlund. 2002. 'The Stellar Initial Mass Function from Turbulent Fragmentation.' ApJ 576 (September): 870–879.

Pattle, K., D. Ward-Thompson, J. M. Kirk, et al. 2015. 'The JCMT Gould Belt Survey: first results from the SCUBA-2 observations of the Ophiuchus molecular cloud and a virial analysis of its prestellar core population.' MNRAS 450 (June): 1094–1122.

Pattle, K., D. Ward-Thompson, J. M. Kirk, et al. 2017. 'The JCMT Gould Belt Survey: first results from SCUBA-2 observations of the Cepheus Flare region.' MNRAS 464, no. 4 (February): 4255–4281.

Pearson, K. 1895. 'Note on Regression and Inheritance in the Case of Two Parents.' *Proceedings of the Royal Society of London Series I* 58:240–242.

Pecaut, M., E. Mamajek, and E. Bubar. 2012. 'A Revised Age for Upper Scorpius and the Star Formation History among the F-type Members of the Scorpius-Centaurus OB Association.' ApJ 746, no. 2 (February): 22.

Penston, M. V. 1969. 'Dynamics of self-gravitating gaseous spheres-III. Analytical results in the free-fall of isothermal cases.' MNRAS 144:425.

Peretto, N., G. A. Fuller, A. Duarte-Cabral, et al. 2013. 'Global collapse of molecular clouds as a formation mechanism for the most massive stars.' A&A 555, A112 (July): A112.

Peretto, N., G. A. Fuller, R. Plume, et al. 2010. 'Mapping the column density and dust temperature structure of IRDCs with Herschel.' A&A 518, L98 (July): L98.

Perrot, C. A., and I. A. Grenier. 2003. '3D dynamical evolution of the interstellar gas in the Gould Belt.' A&A 404 (June): 519–531.

Peterson, D. E., A. Caratti o Garatti, T. L. Bourke, et al. 2011. 'The Spitzer Survey of Interstellar Clouds in the Gould Belt. III. A Multi-wavelength View of Corona Australis.' ApJS 194, 43 (June): 43.

Pilbratt, G. L., J. R. Riedinger, T. Passvogel, et al. 2010. 'Herschel Space Observatory. An ESA facility for far-infrared and submillimetre astronomy.' A&A 518, L1 (July): L1.

Poglitsch, A., C. Waelkens, N. Geis, et al. 2010. 'The Photodetector Array Camera and Spectrometer (PACS) on the Herschel Space Observatory.' A&A 518, L2 (July): L2.

Pogson, N. 1856. 'Magnitudes of Thirty-six of the Minor Planets for the first day of each month of the year 1857.' MNRAS 17 (November): 12–15.

Polychroni, D., E. Schisano, D. Elia, et al. 2013. 'Two Mass Distributions in the L 1641 Molecular Clouds: The Herschel Connection of Dense Cores and Filaments in Orion A.' ApJL 777, L33 (November): L33.

Prato, L., T. P. Greene, and M. Simon. 2003. 'Astrophysics of Young Star Binaries.' ApJ 584 (February): 853–874.

Preibisch, T., A. G. A. Brown, T> Bridges, E. Guenther, and H. Zinnecker. 2002. 'Exploring the Full Stellar Population of the Upper Scorpius OB Association.' ApJ 124, no. 1 (July): 13.

Preibisch, T., and E. Mamajek. 2008. 'The Nearest OB Association: Scorpius-Centaurus (Sco OB2).' In *Handbook of Star Forming Regions, Volume II*, edited by B. Reipurth, 235. December.

Reach, W. T., S. T. Megeath, M. Cohen, et al. 2005. 'Absolute Calibration of the Infrared Array Camera on the Spitzer Space Telescope.' PASP 117 (September): 978–990.

Rebull, L. M., D. L. Padgett, C.-E. McCabe, et al. 2010. 'The Taurus Spitzer Survey: New Candidate Taurus Members Selected Using Sensitive Mid-Infrared Photometry.' ApJS 186 (February): 259–307.

Rebull, L. M., K. R. Stapelfeldt, N. J. Evans II, et al. 2007. 'The Spitzer c2d Survey of Large, Nearby, Interstellar Clouds. VI. Perseus Observed with MIPS.' ApJS 171 (August): 447–477.

Reid, M. A., and C. D. Wilson. 2005. 'High-Mass Star Formation. I. The Mass Distribution of Submillimeter Clumps in NGC 7538.' ApJ 625 (June): 891–905.

Reipurth, B., R. Chini, E. Krugel, E. Kreysa, and A. Sievers. 1993. 'Cold Dust around Herbig-Haro Energy Sources - a 1300-MICRON Survey.' A&A 273 (June): 221.

Ribas, Á., H. Bouy, and B. Merín. 2015. 'Protoplanetary disk lifetimes vs. stellar mass and possible implications for giant planet populations.' A&A 576, A52 (April): A52.

Ribas, Á., B. Merín, H. Bouy, and L. T. Maud. 2014. 'Disk evolution in the solar neighborhood. I. Disk frequencies from 1 to 100 Myr.' A&A 561, A54 (January): A54.

Richards, P. L. 1994. 'Bolometers for infrared and millimeter waves.' *Journal of Applied Physics* 76 (July): 1–24.

Rieke, G. H., M. Blaylock, L. Decin, et al. 2008. 'Absolute Physical Calibration in the Infrared.' AJ 135 (June): 2245–2263.

Rieke, G. H., E. T. Young, C. W. Engelbracht, et al. 2004. 'The Multiband Imaging Photometer for Spitzer (MIPS).' ApJS 154 (September): 25–29.

Robitaille, T. P., B. A. Whitney, R. Indebetouw, and K. Wood. 2007. 'Interpreting Spectral Energy Distributions from Young Stellar Objects. II. Fitting Observed SEDs Using a Large Grid of Precomputed Models.' ApJS 169 (April): 328–352.

Robitaille, T. P., B. A. Whitney, R. Indebetouw, K. Wood, and P Denzmore. 2006. 'Interpreting Spectral Energy Distributions from Young Stellar Objects. I. A Grid of 200,000 YSO Model SEDs.' ApJS 167, no. 2 (December): 256–285.

Robitaille, T., and E. Bressert. 2012. *APLpy: Astronomical Plotting Library in Python.* Astrophysics Source Code Library, record ascl:1208.017, August.

Rodney, S. A., and B. Reipurth. 2008. 'The W40 Cloud Complex.' In *Handbook of Star Forming Regions, Volume II*, edited by B. Reipurth, 683. December.

Rumble, D., J. Hatchell, R. A. Gutermuth, et al. 2015. 'The JCMT Gould Belt Survey: evidence for radiative heating in Serpens MWC 297 and its influence on local star formation.' MNRAS 448 (April): 1551–1573.

Rumble, D., J. Hatchell, K. Pattle, et al. 2016. 'The JCMT Gould Belt Survey: evidence for radiative heating and contamination in the W40 complex.' MNRAS 460 (August): 4150–4175.

Rygl, K. L. J., M. Benedettini, E. Schisano, et al. 2013. 'Recent star formation in the Lupus clouds as seen by Herschel.' A&A 549, L1 (January): L1.

Sadavoy, S. I., J. Di Francesco, P. André, et al. 2014. 'Class 0 Protostars in the Perseus Molecular Cloud: A Correlation Between the Youngest Protostars and the Dense Gas Distribution.' ApJL 787, L18 (June): L18.

Sadavoy, S. I., J. Di Francesco, and D. Johnstone. 2010. '"Starless" Super-Jeans Cores in Four Gould Belt Clouds.' ApJL 718 (July): L32–L37.

Sadavoy, S. I., J. Di Francesco, D. Johnstone, et al. 2013. 'The Herschel and JCMT Gould Belt Surveys: Constraining Dust Properties in the Perseus B1 Clump with PACS, SPIRE, and SCUBA-2.' ApJ 767, 126 (April): 126.

Saigo, K., and K. Tomisaka. 2011. 'Spectrum Energy Distribution and Submillimeter Image of a Rotating First Core.' ApJ 728, 78 (February): 78.

Salji, C. J., J. S. Richer, J. V. Buckle, et al. 2015a. 'The JCMT Gould Belt Survey: constraints on prestellar core properties in Orion A North.' MNRAS 449 (May): 1769–1781.

Salji, C. J., J. S. Richer, J. V. Buckle, et al. 2015b. 'The JCMT Gould Belt Survey: properties of star-forming filaments in Orion A North.' MNRAS 449 (May): 1782–1796.

Salpeter, E. E. 1955. 'The Luminosity Function and Stellar Evolution.' ApJ 121 (January): 161.

Scalo, J. M. 1986. 'The stellar initial mass function.' Fund. Cosmic Phys. 11 (May): 1–278.

Schnee, S., B. Mason, J. Di Francesco, R. Friesen, D. Li, S. Sadavoy, and T. Stanke. 2014. 'Evidence for large grains in the star-forming filament OMC 2/3.' MNRAS 444 (November): 2303–2312.

Shirley, Y. L., N. J. Evans II, and J. M. C. Rawlings. 2002. 'Tracing the Mass during Low-Mass Star Formation. III. Models of the Submillimeter Dust Continuum Emission from Class 0 Protostars.' ApJ 575 (August): 337–353.

Shu, F. H. 1977. 'Self-similar collapse of isothermal spheres and star formation.' ApJ 214 (June): 488–497.

Shu, F. H., F. C. Adams, and S. Lizano. 1987. 'Star formation in molecular clouds - Observation and theory.' ARA&A 25:23–81.

Simpson, J. P., A. S. Cotera, M. G. Burton, M. R. Cunningham, N. Lo, and I. Bains. 2012. 'A Spitzer Space Telescope survey of massive young stellar objects in the G333.2-0.4 giant molecular cloud.' MNRAS 419 (January): 211–237.

Siringo, G., E. Kreysa, A. Kovács, et al. 2009. 'The Large APEX BOlometer CAmera LABOCA.' A&A 497 (April): 945–962.

Skrutskie, M. F., R. M. Cutri, R. Stiening, et al. 2006. 'The Two Micron All Sky Survey (2MASS).' AJ 131 (February): 1163–1183.

Smith, J., A. Bentley, M. Castelaz, R. D. Gehrz, G. L. Grasdalen, and J. A. Hackwell. 1985. 'Infrared sources and excitation of the W40 complex.' ApJ 291 (April): 571–580.

Spezzi, L., J. M. Alcalá, E. Covino, et al. 2008. 'The Young Population of the Chamaeleon II Dark Cloud.' ApJ 680, 1295-1318 (June): 1295–1318.

Stothers, R., and J. A. Frogel. 1974. 'The local complex of O and B stars. I. Distribution of stars and interstellar dust.' AJ 79 (April): 456.

Straizys, V., K. Cernis, and S. Bartasiūtė. 2003. 'Interstellar extinction in the direction of the Aquila Rift.' A&A 405 (July): 585–590.

Straizys, V., K. Cernis, A. Kazlauskas, and E. Meistas. 1992. 'On the distance of dark clouds in the vicinity of the reflection nebula NGC 7023 in Cepheus.' *Baltic Astronomy* 1 (January): 149.

Strom, S. E., G. L. Grasdalen, and K. M. Strom. 1974. 'Infrared and optical observations of Herbig-Haro objects.' ApJ 191 (July): 111–142.

Suresh, A., H. G. Arce, and M. Dunham. 2015. 'A Catalog of Low-Mass Star-Forming Cores Observed with SHARC-II at 350 μm,' 225:444.01. January.

Tachihara, K., K. Dobashi, A. Mizuno, H. Ogawa, and Y. Fukui. 1996. '13CO (J= 1–0) Observations of the Lupus Molecular Clouds.' PASJ 48 (June): 489–502.

Tachihara, K., S. Toyoda, T. Onishi, A. Mizuno, Y. Fukui, and R. Neuhäuser. 2001. '^{12}CO Molecular Cloud Survey and Global Star Formation in Lupus.' PASJ 53 (December): 1081–1096.

Terebey, S., F. H. Shu, and P. Cassen. 1984. 'The collapse of the cores of slowly rotating isothermal clouds.' ApJ 286 (November): 529–551.

Thomas, H. S. 2015. 'The SCUBA-2 Data Reduction Cookbook.' *http://starlink.eao.hawaii.edu/docs/sc21.htx/sc21.html*, no. 1.3 (December).

van Gent, H. 1933. 'Discussion of 122, mostly new, variable stars in or near the constellation Corona Australis.' Bull. Astron. Inst. Netherlands 7 (March): 21.

van Kempen, T. A., E. F. van Dishoeck, D. M. Salter, M. R. Hogerheijde, J. K. Jørgensen, and A. C. A. Boogert. 2009. 'The nature of the Class I population in Ophiuchus as revealed through gas and dust mapping.' A&A 498 (April): 167–194.

Vilas-Boas, J. W. S., P. C. Myers, and G. A. Fuller. 2000. 'Dense Cores of Dark Clouds. XII. ^{13}CO and C^{18}O in Lupus, Corona Australis, Vela, and Scorpius.' ApJ 532 (April): 1038–1050.

Walawender, J., J. Bally, J. D. Francesco, J. Jørgensen, and K. =. Getman. 2008. 'NGC 1333: A Nearby Burst of Star Formation.' In *Handbook of Star Forming Regions, Volume I*, edited by B. Reipurth, 346. December.

Ward-Thompson, D., J. Di Francesco, J. Hatchell, et al. 2007. 'The James Clerk Maxwell Telescope Legacy Survey of Nearby Star-forming Regions in the Gould Belt.' PASP 119 (August): 855–870.

Ward-Thompson, D., K. Pattle, P. Bastien, et al. 2017. 'First results from BISTRO – a SCUBA-2 polarimeter survey of the Gould Belt.' ApJ 842 (June).

Ward-Thompson, D., K. Pattle, J. M. Kirk, et al. 2016. 'The JCMT and Herschel Gould Belt Surveys: A comparison of SCUBA-2 and Herschel data of dense cores in the Taurus dark cloud L1495.' MNRAS 463, no. 1 (November): 1008–1025.

Ward-Thompson, D., P. F. Scott, R. E. Hills, and P. Andre. 1994. 'A Submillimetre Continuum Survey of Pre Protostellar Cores.' MNRAS 268 (May): 276.

Watson, M. 2010. 'Assessing the Performance of Sub-Millimetre Compact Object Detection Algorithms.' Master's thesis, University of Hertfordshire.

Weingartner, J. C., and B. T. Draine. 2001a. 'Dust Grain-Size Distributions and Extinction in the Milky Way, Large Magellanic Cloud, and Small Magellanic Cloud.' ApJ 548 (February): 296–309.

———. 2001b. 'Photoelectric Emission from Interstellar Dust: Grain Charging and Gas Heating.' ApJS 134 (June): 263–281.

Werner, M. W., T. L. Roellig, F. J. Low, et al. 2004. 'The Spitzer Space Telescope Mission.' ApJS 154, no. 1 (September): 1–9.

Westerhout, G. 1958. 'A survey of the continuous radiation from the Galactic System at a frequency of 1390 Mc/s.' Bull. Astron. Inst. Netherlands 14 (December): 215.

Whitney, B. A., K. Wood, J. E. Bjorkman, and M. Cohen. 2003. 'Two-dimensional Radiative Transfer in Protostellar Envelopes. II. An Evolutionary Sequence.' ApJ 598 (December): 1079–1099.

Wilking, B. A., M. Gagné, and L. E. Allen. 2008. 'Star Formation in the ρ Ophiuchi Molecular Cloud.' In *Handbook of Star Forming Regions, Volume II,* edited by B. Reipurth, 351. Handbook of Star Forming Regions Vol II. Astronomical Society of the Pacific, December.

Wilking, B. A., C. J. Lada, and E. T. Young. 1989. 'IRAS observations of the Rho Ophiuchi infrared cluster - Spectral energy distributions and luminosity function.' ApJ 340 (May): 823–852.

Williams, J. P., E. J. de Geus, and L. Blitz. 1994. 'Determining structure in molecular clouds.' ApJ 428 (June): 693–712.

Wolf, M. 1904. 'Remarkable nebula in Cygnus.' MNRAS 64 (June): 838.

Wootten, A., and A. R. Thompson. 2009. 'The Atacama Large Millimeter-Submillimeter Array.' *IEEE Proceedings* 97 (August): 1463–1471.

Wright, E. L., P. R. M. Eisenhardt, A. K. Mainzer, et al. 2010. 'The Wide-field Infrared Survey Explorer (WISE): Mission Description and Initial On-orbit Performance.' AJ 140, 1868 (December): 1868–1881.

Wright, N. J., R. J. Parker, S. P. Goodwin, and J. J. Drake. 2014. 'Constraints on massive star formation: Cygnus OB2 was always an association.' MNRAS 438 (February): 639–646.

Wu, J., M. M. Dunham, N. J. Evans II, T. L. Bourke, and C. H. Young. 2007. 'SHARC-II Mapping of Spitzer c2d Small Clouds and Cores.' AJ 133 (April): 1560–1584.

Wyatt, M. C. 2008. 'Evolution of Debris Disks.' ARA&A 46 (September): 339–383.

Yamamura, I., S. Makiuti, N. Ikeda, Y. Fukuda, S. Oyabu, T. Koga, and G. J. White. 2010. 'VizieR Online Data Catalog: AKARI/FIS All-Sky Survey Point Source Catalogues (ISAS/JAXA, 2010).' *VizieR Online Data Catalog* 2298 (April).

Yang, Y.-L., N. J. Evans II, J. D. Green, M. M. Dunham, and J. K. Jørgensen. 2017. 'The Class 0 Protostar BHR71: Herschel Observations and Dust Continuum Models.' ApJ 835, 259 (February): 259.

Young, A. K., M. R. Bate, C. F. Mowat, J. Hatchell, and T. J. Harries. 2018. 'What can the SEDs of first hydrostatic core candidates reveal about their nature?' MNRAS 474 (February): 800–823.

Young, C. H., and N. J. Evans II. 2005. 'Evolutionary Signatures in the Formation of Low-Mass Protostars.' ApJ 627 (July): 293–309.

Young, C. H., J. K. Jørgensen, Y. L. Shirley, et al. 2004. 'A "Starless" Core that Isn't: Detection of a Source in the L1014 Dense Core with the Spitzer Space Telescope.' ApJS 154 (September): 396–401.

Young, C. H., Y. L. Shirley, N. J. Evans II, and J. M. C. Rawlings. 2003. 'Tracing the Mass during Low-Mass Star Formation. IV. Observations and Modeling of the Submillimeter Continuum Emission from Class I Protostars.' ApJS 145 (March): 111–145.

Zacharias, N., D. G. Monet, S. E. Levine, S. E. Urban, R. Gaume, and G. L. Wycoff. 2005. 'VizieR Online Data Catalog: NOMAD Catalog (Zacharias+ 2005).' *VizieR Online Data Catalog* 1297 (November).

Zinnecker, H., and H. W. Yorke. 2007. 'Toward Understanding Massive Star Formation.' ARA&A 45 (September): 481–563.

Index